GYROFLUID MODELS OF TURBULENT TRANSPORT IN TOKAMAKS

Michael Alan Beer

January 1995

GYROFLUID MODELS OF TURBULENT TRANSPORT IN TOKAMAKS

Michael Alan Beer

A DISSERTATION
PRESENTED TO THE FACULTY
OF PRINCETON UNIVERSITY
IN CANDIDACY FOR THE DEGREE
OF DOCTOR OF PHILOSOPHY

RECOMMENDED FOR ACCEPTANCE
BY THE DEPARTMENT OF ASTROPHYSICAL
SCIENCES

January 1995

To Jason, with love.

Abstract

MICROINSTABILITY DRIVEN TURBULENCE IN TOKAMAKS is studied via numerical simulation of a comprehensive fluid model. For the ions, toroidal gyrofluid equations are derived which contain accurate models of the kinetic effects arising from toroidal ∇B and curvature drifts, parallel Landau damping and its inverse, finite Larmor radius effects, and trapped ion effects. For the electrons, sophisticated bounce averaged trapped electron fluid equations are derived which model the toroidal precession resonance and use a Lorentz collision operator for pitch angle scattering. These coupled ion and electron equations can simultaneously describe the nonlinear evolution of toroidal ion temperature gradient driven instabilities and trapped electron modes, and provide realistic nonlinear calculations of ion and electron heat fluxes and particle fluxes. These equations are solved in a reduced flux tube geometry, formulated in general magnetic coordinates. This technique exploits the elongated nature of microinstability driven turbulence, which has long parallel scales and short perpendicular scales. The reduced simulation volume allows high resolution simulations in realistic tokamak geometry, fully retaining important toroidal effects such as good and bad curvature. These toroidal simulations predict much larger thermal transport than found in simplified sheared slab geometry, bringing the predictions up to experimentally measured levels. The turbulent fluctuation spectrum is peaked at long wavelengths compared to the fastest growing linear modes, and the fluctuation spectrum is anisotropic in k_r and k_θ, as seen in experimental fluctuation measurements. The nonlinear generation of sheared $\mathbf{E} \times \mathbf{B}$ flows is found to play an important role in the development and saturation of this turbulence, and the damping of these flows is carefully investigated. Finally, the predicted transport from these simulations is compared with experiment. The simulations underestimate the transport near the plasma edge, but encouraging agreement is found between the predicted and measured ion and electron heat transport in the core.

Contents

Figures

Acknowledgements

I owe thanks to many people who made this thesis possible. Foremost, I thank my thesis advisor Greg Hammett. His foresight, physical intuition, and integrity have been a constant and dependable guide throughout this entire work. Personally, he has been an inspiration as a true scientist, and has kindly insulated me from much of the politics surrounding a new approach to an old problem.

The flux-tube coordinate system in Chapter 4 was suggested by Steve Cowley, and I thank him for hours of enlightening discussions. He has been a great resource for many physics issues that arose during the course of this work.

The toroidal nonlinear gyrofluid code developed in this thesis grew out of the earlier slab gyrofluid code developed by Bill Dorland, whom I thank for providing helpful computational advice and physics discussions. I also thank Bill for laying much of the groundwork, encouraging me to work on this project, and for keeping me from wandering too deeply into theory.

Many teachers at Princeton have helped and inspired me, especially Liu Chen, Taik Soo Hahm, John Krommes, Rip Perkins, Greg Rewoldt, and Bill Tang. Special thanks to my readers Bill Tang and Taik Soo Hahm for many useful suggestions.

I thank Steve Scott, Mike Zarnstorff, and the TFTR team for the experimental data in Chapter 6 and useful discussions.

I thank Jason Rudy for making the past year so interesting. I never dreamed I would share such a mutual understanding with anyone—you have made me very happy. Thank you for being so tolerant the past few months. I am especially grateful to Rex Hatfield, Temple Gill, and Barbara Sarfaty, who kept me relatively sane while writing this thesis. I thank my parents, Larry and Mary Ann Beer, my sisters, Carolyn, Angela, and Stephanie, and my family for their support, en-

couragement, and understanding. I also thank plasma physics graduate students past and present for making lunch the high point of my day, especially Mehmet Artun, David Coster, Cary Forest, Ted Jones, Karl Krushelnick, Q. P. Liu, Mark Herrmann, Alex MacAulay, Jon Menard, David Moore, and Sherrie Preische. I would particularly like to acknowledge useful (and disgusting) conversations with Stephen Smith.

I thank the TFTR project for supporting this work, and the National Energy Research Supercomputer Center for computing resources. This work was also supported in part by the High Performance Computing and Communications Initiative (HPCCI) Grand Challenge Numerical Tokamak Project, by USDoE contract No. DE-AC02-76-CH0-3073, and by a National Science Foundation Graduate Fellowship.

And finally, thanks to the person who first realized it would be a good idea to pour hot water over beans and drink it.

Chapter 1

Introduction

DEVELOPING AN UNDERSTANDING of turbulent transport in tokamaks has been a primary goal of magnetic confinement fusion research for decades. The main goal of this thesis is to develop techniques for making quantitative predictions of tokamak turbulence. These predictions can then be compared with present experiments, and used to aid in the design of future fusion reactors. While much progress has been made in both the theory of microinstabilities and experimental measurements of turbulent fluctuations in tokamaks, quantitative comparisons between experiment and non-empirical theories have been unsatisfactory in the past. This thesis presents new toroidal gyrofluid equations and nonlinear simulations which provide perhaps the most promising direct comparisons between first principles theory and experiment to date, both in levels of transport and fluctuation spectra, for actual tokamak parameters. Several advances are presented in this thesis which have been ignored in previous simulations and make these comparisons favorable, primarily: the inclusion of destabilizing toroidal effects ignored in slab theories, the use of an efficient flux tube simulation geometry for three dimensional high resolution nonlinear simulations in realistic tokamak geometry, the self-consistent evolution of small-scale turbulence generated sheared flows and realistic damping of these flows, and the inclusion of nonadiabatic electron dynamics with a sophisticated trapped electron fluid model.

1.1 Motivation

In all tokamak experiments, the particle and heat losses greatly exceed the neoclassical predictions which result from collisional diffusion. However, fluctuation measurements in tokamaks invariably see small scale (compared to the size of the tokamak, but large compared to the Debye length, λ_D) and low frequency (compared to the plasma frequency, ω_{pe}) fluctuations which apparently enhance transport above collisional levels. These fluctuations are believed to arise from microinstabilities primarily driven by the temperature and density gradients inherent in any confinement device. The fastest growing microinstabilities typically have perpendicular scales on the order of the ion gyroradius, $k_\perp \rho_i \sim 1/2$, where the ion gyroradius, $\rho_i = v_{ti}/\Omega_i$, and frequency and growth rate scales on the order of the diamagnetic drift frequency, $\omega_* = k_\theta \rho_i v_{ti}/L_n$. Here $v_{ti}^2 = T_i/m_i$ is the ion thermal velocity and $L_n = -(d \ln n_0/dr)^{-1}$ is the equilibrium density scale length. Based on mixing length estimates, the simplest description of the nonlinear saturation of these instabilities, these fluctuations should lead to particle diffusivities, D, and heat diffusivities, χ, which scale as

$$D, \chi \sim \frac{\Delta x^2}{\Delta t} \sim \frac{\gamma}{k_\perp^2} \sim \frac{1}{k_\perp \rho_i} \frac{\rho_i^2 v_{ti}}{L_n}.$$

Assuming that the dominant fluctuation scale is set by the fastest growing modes ($k_\perp \rho_i \sim 1$) yields the "gyro-Bohm" diffusivity, $D_{\rm gB} \sim \rho_i^2 v_{ti}/L_n$. While this leads to reasonable estimates for global energy confinement times [Perkins, 1990], it has several problems. The most striking disagreement is in the variation of fluctuation levels and diffusivities with minor radius. Experiments show that χ and fluctuation levels increase with increasing minor radius, while the gyro-Bohm χ decreases, because of the $T^{3/2}$ dependence. The gyro-Bohm χ is thus too high in the core, and too low at the edge, see [Horton *et al.*, 1992]. Additionally, using γ and $k_\perp$ from the fastest growing mode usually predicts diffusivities less than those measured in experiments. Another problem is that the experimentally measured fluctuation spectra peak at $k_\perp \rho_i \approx 0.1 - 0.2$ [Fonck *et al.*, 1993], not at the fastest growing wavelengths. The mixing length formula above shows that the largest eddies (smallest $k_\perp$) are the most dangerous and cause the most transport. This emphasizes the need to understand where the fluctuation spectrum peaks, i.e. why the dominant scale is at $k_\perp \rho_i \sim 0.1 - 0.2$, and not at the fastest growing scales or the longest

possible scales, $k_\perp \rho_i \sim \rho_i/a \sim 0.003$. Many versions of this mixing length estimate have been proposed which compensate for the long wavelength peak in the spectrum, for example, using the maximum $\gamma/k_\perp^2$ rather than γ and $k_\perp$ for the fastest growing mode. An understanding of the nonlinear dynamics at a level beyond the simplest mixing length estimates is clearly needed, and nonlinear simulations can help sort out these various possible scaling relations.

Theoretical predictions of turbulent transport beyond this simple estimate are quite challenging. The evolution of the turbulence is intrinsically nonlinear and three dimensional. In addition, microinstabilities are strongly influenced by kinetic (velocity space) effects, since present day tokamak plasmas are in the long mean free path regime. Future experiments and reactor grade plasmas will also be in this regime. Either velocity space effects must be accurately modeled in fluid equations, or a kinetic approach which resolves velocity space is necessary, making the problem five dimensional. Our approach has been to develop simplified fluid equations which retain accurate models of the important physics for tokamak transport; primarily, long mean free path effects leading to Landau damping and its inverse, from both parallel free streaming and toroidal ∇B and curvature drifts. These reduced equations allow the use of high resolution, three dimensional, nonlinear computer simulations to investigate the turbulent dynamics in realistic tokamak geometry without further approximation. Most previous theories of tokamak turbulence have necessarily used either simplified dynamics, simplified geometry, or simplified nonlinear analysis: mixing length or quasilinear estimates, weak turbulence theory, or lower resolution computer simulations.

The combination of more accurate fluid models and fully nonlinear three dimensional simulations in toroidal geometry have resolved some of the aforementioned discrepancies between theory and experiment. In the simulations presented here, the peak in the fluctuation spectrum is at longer wavelengths than the fastest growing wavelengths (also seen in full torus gyrokinetic particle simulations [Parker *et al.*, 1993]). These toroidal gyrofluid simulations find much higher transport levels than the simplest mixing length estimates or sheared slab simulations, and bring the predictions up to the measured levels. Finally, part of the discrepancy in the radial dependence of χ is remedied by our toroidal gyrofluid equations, which give more accurate linear growth rates than have previous fluid theories. If the instabilities are

nearly stable in the core and strongly unstable in the edge, or if some dependence on local parameters causes nonlinear saturation levels to increase near the edge, the radial variation of predicted and measured transport is in much better agreement. Recent comparisons between experiment and a transport model based on simulations with our toroidal gyrofluid code and linear fully kinetic calculations indicate that this is the case in the core ($r/a < 0.85$) of L-mode type discharges [Dorland *et al.*, 1994b; Kotschenreuther *et al.*, 1994a]. Direct comparisons of the nonlinear toroidal simulations developed here with a TFTR L-mode discharge, presented in Chapter 6, show reasonable agreement, which encourages us to continue adding more physics to this code to try to explain a wider range of experimental conditions.

1.2 Brief Historical Review

The host of different of plasma instabilities can make a first foray into the microinstability literature quite daunting. An important guide to understanding this zoo is that all microinstabilities which may be considered relevant for tokamak turbulence are accurately described by the nonlinear electromagnetic toroidal gyrokinetic equation [Frieman and Chen, 1982] (with an appropriate collision operator) for all plasma species: ions, impurities, beams, and electrons (though the drift kinetic equation can be used for the electrons since the electron gyroradius is small). The wide range of instabilities in the literature arises from making assumptions that simplify this fundamental equation: each simplification generally isolates an instability, and it is given a new name. Even linearly, the complexity of the gyrokinetic equation makes it difficult to solve, and full solutions are only available numerically [Rewoldt *et al.*, 1987; Kotschenreuther *et al.*, 1994b]. Before proceeding chronologically, it is useful to have the basic results from these comprehensive numerical solutions in mind. These kinetic calculations show that for realistic tokamak parameters (low β and low collisionality) the dominant instability is either the toroidal Ion Temperature Gradient (ITG) driven instability (also called the η_i mode) or the Trapped Electron Mode (TEM), and that either the toroidal ITG mode or the TEM is linearly unstable or nearly unstable for measured tokamak parameters. Some of the distinction between the ITG and TEM is artificial, since ion and trapped electron dynamics affect both modes. The distinction arises because the toroidal ITG mode is primarily driven by the ion temperature gradi-

ent and the TEM is primarily driven by the trapped electron toroidal precession resonance. At higher β, kinetic versions of ideal MHD ballooning modes can be driven unstable [REWOLDT *et al.*, 1987], but tokamaks usually operate below this β limit, and electromagnetic corrections to the basic electrostatic instabilities are usually small. The toroidal ITG and TEM are thus the most promising candidates for explaining anomalous transport in tokamaks, and have been the focus of much work in this area. Variations of these instabilities are the most likely cause of the observed density and temperature fluctuations in large tokamak experiments, with the possible exception of the extreme edge.

Some of the major simplifications which have been used in the past are local vs. nonlocal treatment, simplified magnetic geometry, and fluid vs. kinetic treatment. In the local approximation, each Fourier harmonic of the perturbations is assumed to be independent, while physical inhomogeneities may couple these harmonics. Nonlocal treatment takes this coupling into account, and turns the local algebraic dispersion relation (zero-dimensional) into a one- or two-dimensional differential or integral equation in space. The nonlocal eigenmode is then a superposition of many coupled Fourier harmonics. The simplest magnetic geometry is an unsheared slab where B is straight and constant. The next level of complication is a sheared slab, where B is still constant, but the field lines twist. This couples the radial and parallel directions (k_r and $k_\parallel$) and makes the linear problem spatially one dimensional. In more realistic toroidal geometry where B also varies with major radius, toroidal ∇B and curvature drifts become an important destabilization mechanism, both through fluid-like and kinetic effects. In addition, the poloidal variation of the ∇B and curvature drifts introduce coupling of different poloidal harmonics (k_θ's), making the problem two dimensional. Fully nonlocal investigations in toroidal geometry awaited the development of the ballooning representation [CONNOR *et al.*, 1979], which reduces the problem back to one dimension by exploiting the perpendicular scale separation between the equilibrium and the fluctuations. Finally, to avoid the additional complexity of resolving velocity space, many earlier works were based on fluid equations which did not capture the kinetic effects of phase mixing and wave-particle resonances. Kinetic effects are often important for microinstabilities, and accurate stability calculations based on fluid equations require models of these effects.

The ITG mode can be isolated from the TEM by assuming that the electrons are adiabatic, which removes the trapped electron drive. The earliest investigations of the ITG instability were in simplified magnetic geometry, first in an unsheared slab [RUDAKOV and SAGDEEV, 1961] and later in a sheared slab [COPPI *et al.*, 1967]. The magnetic shear and T_i/T_e dependence of the threshold for instability was fully treated by [HAHM and TANG, 1989] in the small ion gyroradius limit, including kinetic effects. In an unsheared or sheared slab, the ITG mode is basically an ion acoustic wave driven unstable by the ion temperature gradient. Later investigations revealed that in more realistic toroidal geometry the ITG mode can be strongly destabilized by ∇B and curvature drifts, and becomes the interchange-like toroidal ITG mode [HORTON *et al.*, 1981; COPPI and PEGORARO, 1977]. The toroidal ITG mode is unstable if $\eta_i > \eta_i^{\rm crit}$, where $\eta_i = L_{ni}/L_{Ti}$. In these early oversimplified fluid limits $\eta_i^{\rm crit} \approx -1$ [HORTON *et al.*, 1981], although $\eta_i^{\rm crit}$ also depends on $k_\perp^2\rho_i^2$ and $\epsilon_n = L_{ni}/R$. Later work began including the kinetic effects of parallel and toroidal drift resonances, usually keeping either parallel or toroidal drifts, but not both. [GUZDAR *et al.*, 1983] retained the parallel resonance in a nonlocal treatment, while [TERRY *et al.*, 1982; BIGLARI *et al.*, 1989; ROMANELLI, 1989] retained the toroidal resonance in the local limit. Both of these approaches show that the kinetic $\eta_i^{\rm crit} \approx 1$, demonstrating the importance of kinetic effects on the toroidal ITG mode. In the flat density limit where $\epsilon_n \to \infty$, the stability criterion actually becomes a criterion on L_{ti}/R instead of η_i [TANG *et al.*, 1986], and $L_{ti}/R < L_{ti}^{\rm crit}/R$ for instability. In the purely toroidal local kinetic limit (ignoring $k_\parallel$ and parallel Landau damping), [BIGLARI *et al.*, 1989; DOMINGUEZ and ROSENBLUTH, 1989] find $L_{ti}^{\rm crit}/R \approx 0.35$. The fully toroidal nonlocal kinetic calculations by [DONG *et al.*, 1992] are very complete within the context of adiabatic electrons and ignoring trapped ion effects. These results clearly demonstrate inadequacies in the local approximation. For example, in the local approximation the safety factor, q, and magnetic shear parameter, $\hat{s} = (r/q)\partial q/\partial r$, do not enter (although a q dependence can be introduced by assuming $k_\parallel = 1/qR$ in local calculations). Fig. 7 of [DONG *et al.*, 1992] shows a strong dependence of the toroidal ITG growth rate on $\hat{s}$, an effect which is completely missed within the local approximation.

Impurities and beams can also affect the toroidal ITG mode. If the impurity density is outwardly peaked (inverted), impurities can be strongly destabilizing, as was first shown in an unsheared slab by [COPPI *et al.*, 1966]. Later nonlocal in-

vestigations in sheared slab geometry [TANG *et al.*, 1980] confirmed that inverted impurity density profiles can be strongly destabilizing, and that inwardly peaked impurity density profiles are strongly stabilizing. That these trends persist in toroidal geometry was shown in the fully toroidal kinetic calculations of [DONG *et al.*, 1994]. Thus the radial variation of $Z_{\rm eff}$ is potentially an important stability parameter, and if $Z_{\rm eff}$ is peaked near the edge, this impurity destabilization may increase theoretical transport predictions in the edge, bringing them into closer agreement with experiment, as pointed out by [DORLAND *et al.*, 1994a]. The effects of impurities (strongly stabilizing with flat $Z_{\rm eff}$) and beam ions (weakly stabilizing) have also been demonstrated in comprehensive toroidal kinetic calculations of the toroidal ITG mode [KOTSCHENREUTHER *et al.*, 1993], and the effects of a non-Maxwellian beam distribution have been investigated by [REWOLDT and TANG, 1990] for both the toroidal ITG mode and TEM.

Another complication is the effect of trapped ions. When the mode time scales fall below the ion bounce frequency $\omega_{bi} = \sqrt{\epsilon} v_{ti}/qR$, trapped ion effects become destabilizing. Since the toroidal ITG mode typically has $\omega \sim k_\theta \rho_i v_{ti}/R$, trapped ion effects are important for long wavelengths, $k_\theta \rho_i \ll \sqrt{\epsilon}/q$. Although the trapped-ion mode and toroidal ITG mode are often considered distinct, the toroidal ITG mode gradually evolves into the trapped ion mode at long wavelengths. The work of [XU and ROSENBLUTH, 1991] includes trapped ions, but assumes adiabatic electrons.

For more complete instability calculations, the adiabatic electron assumption must be relaxed. The dominant contribution to the nonadiabatic electron response comes from the bounce averaged trapped electron response; the passing electrons and non-bounce-averaged trapped electron response are usually weak [REWOLDT and TANG, 1990]. The early work on electron driven instabilities usually isolated the effects of electrons by either assuming cold ions, which considerably simplifies the analysis but removes the ITG mode, or by using a fluid ion approximation. The TEM was first investigated in the local approximation, with fluid ions and kinetic trapped electrons, with [ADAM *et al.*, 1976] and without [LIU *et al.*, 1976] electron toroidal precession drifts. The nonlocal calculation with fluid ions, neglecting ion toroidal drifts, was performed by [CATTO and TSANG, 1978]. A nonlocal calculation using the ballooning representation including ion toroidal drifts, for small $k_\perp \rho_i$

was presented in [CHENG and CHEN, 1981]. There is a somewhat artificial distinction between the dissipative (DTEM) and collisionless (CTEM) trapped electron modes, since the transition between them is smooth, and they are slightly different versions of the same instability.

The "ubiquitous mode" of [COPPI and REWOLDT, 1974; COPPI and PEGORARO, 1977] is the short wavelength ($k_\perp \rho_i \gtrsim 1$) version of the instabilities considered above.

In toroidal geometry, when full kinetic ions and electrons are both considered, whether the toroidal ITG mode or TEM will dominate is primarily a function of the parameters η_i, $\eta_e = L_{ne}/L_{Te}$, ϵ_n, and electron collisionality, ν_{*e}. When $\eta_i > \eta_i^{\rm crit}$ (or $L_{ti}/R < L_{ti}^{\rm crit}/R$ in the flat density gradient limit), the toroidal ITG mode dominates, but can be further destabilized by the trapped electron precession resonance. Below the ITG threshold, the TEM can still exist if ν_{*e} is sufficiently small. Because electron temperature gradients can destabilize the trapped electron mode, whether or not the TEM will be unstable below $\eta_i^{\rm crit}$ depends on η_e and ϵ_n. If the electron collisionality is large enough, the TEM drive is removed, and the plasma can be completely stable for $\eta_i \lesssim 1$.

The nonlinear saturation of these instabilities and the resulting transport is of great interest and has been considered by many authors. Because of the difficulty of nonlinear analysis, much of this work has been based on simplified fluid models and sheared slab geometry, and has focused on the ITG mode, beginning with the early fluid simulations by [HORTON *et al.*, 1980]. In an analytic fluid theory, [LEE and DIAMOND, 1986] calculated the transport expected from ITG turbulence in a sheared slab, at a much greater level of detail than mixing length estimates. Later, [TERRY *et al.*, 1988] argued that higher radial eigenmodes strongly increase the predicted slab ITG ion heat transport, suggesting that ion temperature profiles would remain close to marginality. These analytic theories required a number of uncertain assumptions and approximations. The three dimensional direct simulations of [HAMAGUCHI and HORTON, 1990] resolved a number of these uncertainties and lead to a more reasonable scaling with shear and $(\eta_i - \eta_i^{\rm crit})$. However, as a fluid model, it still neglected some important kinetic effects. The importance of kinetic effects on microinstabilities stimulated the development of gyrokinetic particle simulations [LEE, 1983; DUBIN *et al.*, 1983; LEE, 1987], used to investigate

the sheared slab ITG mode in [LEE and TANG, 1988]. The sheared slab gyrokinetic particle simulations by [KOTSCHENREUTHER *et al.*, 1991] showed that fluid simulations without kinetic effects overestimate the ITG driven transport by a factor of ten. Recent work has focused on including kinetic effects in improved fluid equations by using closure approximations which model Landau damping [HAMMETT and PERKINS, 1990] and FLR effects. These slab gyrofluid simulations [DORLAND, 1993] find reduced transport compared to previous fluid simulations, bringing them into agreement with gyrokinetic particle simulations [PARKER *et al.*, 1994].

These improved slab ITG gyrofluid simulations [DORLAND *et al.*, 1992; DORLAND, 1993] also revealed that turbulence-generated sheared flows play an important role in the development and saturation of ITG turbulence, an effect which had previously been investigated as a mechanism for the H-mode transition [DIAMOND and KIM, 1991; BIGLARI *et al.*, 1990]. This effect had also been seen in simulations of resistive drift waves [HASEGAWA and WAKATANI, 1987] and resistive pressure gradient driven turbulence [CARRERAS *et al.*, 1991], which tended to emphasize the edge. Both slab and toroidal [BEER *et al.*, 1992; HAMMETT *et al.*, 1993] gyrofluid simulations showed that this is also an important effect in the plasma core, and for all modes with near-adiabatic electron response. This effect had been missed in most previous ITG simulations because of limitations in the adiabatic response or in the treatment of the ($k_\theta = 0$, $k_\parallel = 0$) mode and boundary conditions. Recent gyrokinetic particle simulations have also seen this effect [COHEN *et al.*, 1993]. The importance of the generation and damping of sheared flows is even more pronounced in the toroidal ITG simulations [BEER *et al.*, 1992; HAMMETT *et al.*, 1993; WALTZ *et al.*, 1994a] than in a sheared slab.

The obvious need to consider toroidal ITG turbulence was addressed with Braginskii-based fluid simulations first in a local 2D approximation (with $k_\parallel = 1/qR$ fixed) [WALTZ, 1986], and then in full 3D toroidal geometry [WALTZ, 1988]. The latter work used a rough model of Landau damping, rather than collisional based dissipation, and was one of the first in this regard. Analytic estimates of toroidal ITG transport were presented in [BIGLARI *et al.*, 1989]. Increasing computational power allowed full torus [PARKER *et al.*, 1993] and toroidal annulus [DIMITS *et al.*, 1994] gyrokinetic particle simulations. Meanwhile, the slab gyrofluid equations were extended to include the kinetic effects of toroidal drifts [WALTZ *et al.*, 1992], and

later improved to include more accurate models of toroidal drifts and the effects of trapped ions [Beer *et al.*, 1993]. These toroidal gyrofluid equations are simulated using a reduced flux-tube simulation geometry described in this thesis, allowing high resolution toroidal ITG simulations with kinetic effects. These simulations predict much larger transport than gyrofluid and gyrokinetic sheared slab simulations, reviving the notion that profiles may be forced to remain near marginality [Dorland *et al.*, 1994b; Kotschenreuther *et al.*, 1994a]. Recently, the trapped electron fluid equations presented in this thesis have been implemented in fully nonlinear simulations including both the trapped electron drive and the toroidal ITG drive.

A personal and readable perspective on the progress and challenges in understanding plasma turbulence through 1986 can be found in [Waltz, 1989]. A broader review through 1990 can be found in the U. S. DoE Transport Task Force Reviews on Anomalous Transport in Tokamaks in the December 1990 issue of Physics of Fluids B.

1.3 Simple Physics of the Toroidal ITG Driven Instability

Because the toroidal ITG instability is a likely cause of the observed density and temperature fluctuations in experiments, in this section the basic mechanism of the toroidal ITG instability is presented in the spirit of Cowley's picture of the slab ITG mechanism [Cowley *et al.*, 1991]. This rough picture will be based on a simple fluid model, and later chapters will introduce more physics to make our description of this instability more complete. Since later chapters will get quite complicated, it is useful to have in mind a rough picture of the structure and dynamics of these modes, and of the turbulence which ensues.

Before developing our model equations, we begin with a brief outline of the dynamics. The toroidal ITG mode is primarily driven by bad curvature effects, while the slab ITG mode is driven by parallel dynamics. Thus the toroidal version of this instability (the one most relevant to actual tokamak experiments) can be roughly described by ignoring the parallel dynamics altogether. This simplification will lead to reasonable estimates for growth rates, but cannot give the correct mode structure or the nonlinear evolution of the mode, since parallel Landau damping

is the dominant damping mechanism nonlinearly. The essential difference between the slab and toroidal ITG modes is the inclusion of the toroidal ∇B and curvature drifts. For low-β equilibria, the toroidal ∇B and curvature drifts can be combined into:

$$\mathbf{v}_d = \frac{v_\parallel^2 + v_\perp^2/2}{\Omega B^2}\mathbf{B} \times \nabla B. \tag{1.1}$$

Consider a pressure perturbation with $k_r \ll k_\theta$ on the outer midplane of the tokamak as shown in Fig. 1.1. The toroidal ∇B and curvature drifts, $\mathbf{v}_d$, are down. Because of the velocity dependence of $\mathbf{v}_d$, hot particles will drift down faster than the cold particles, increasing the density below the hot spots and above the cold spots. The ion density perturbation produced by $\mathbf{v}_d$ in turn causes a potential perturbation via quasineutrality, producing the electric field as shown. This electric field induces a radial $\mathbf{E}\times\mathbf{B}$ drift, which convects hotter plasma into the hot spots and colder plasma into the cold spots, causing the perturbation to grow. On the inner midplane, where ∇p_0 is reversed but ∇B points in the same direction, this feedback mechanism is shut off. In this case the toroidal drifts produce the same density perturbation and electric field, but now $\mathbf{E} \times \mathbf{B}$ convection brings hotter plasma into the cold spots and colder plasma into the hot spots, so the perturbations are damped.

Our derivation of this instability is based on a simplified limit of the gyrokinetic equation. Setting $k_\parallel = 0$, and ignoring finite Larmor radius effects, the drift kinetic equation is (the full toroidal gyrokinetic equation is given in Eq. (2.2)):

$$\frac{\partial}{\partial t}(FB) + \nabla \cdot [FB(\mathbf{v}_E + \mathbf{v}_d)] + \frac{\partial}{\partial v_\parallel}[FBv_\parallel(\hat{\mathbf{b}} \cdot \nabla\hat{\mathbf{b}}) \cdot \mathbf{v}_E] = 0. \tag{1.2}$$

Here $\mathbf{v}_E = (c/B^2)\mathbf{B} \times \nabla\tilde{\Phi}$ is the $\mathbf{E} \times \mathbf{B}$ drift velocity, and $\tilde{\Phi}$ is the perturbed electrostatic potential. The gyrokinetic equation is written here in conservative form, and the combination FB appears because B is the Jacobian of the transformation from $(v_\parallel, v_\perp)$ to the $(v_\parallel, \mu)$ variables used here, where $\mu = v_\perp^2/2B$ is the magnetic moment adiabatic invariant. The $\partial/\partial v_\parallel$ term conserves toroidal angular momentum: an $\mathbf{E} \times \mathbf{B}$ drift which moves a particle in major radius ($\hat{\mathbf{b}} \cdot \nabla\hat{\mathbf{b}}$ is in the ∇B direction) causes a parallel acceleration.

Simplified fluid equations can be derived by taking moments of Eq. (1.2) over velocity space. For example, the particle density is:

$$n = \int d^3v F = 2\pi \int_{-\infty}^{\infty} dv_\parallel \int_0^\infty d\mu BF \tag{1.3}$$

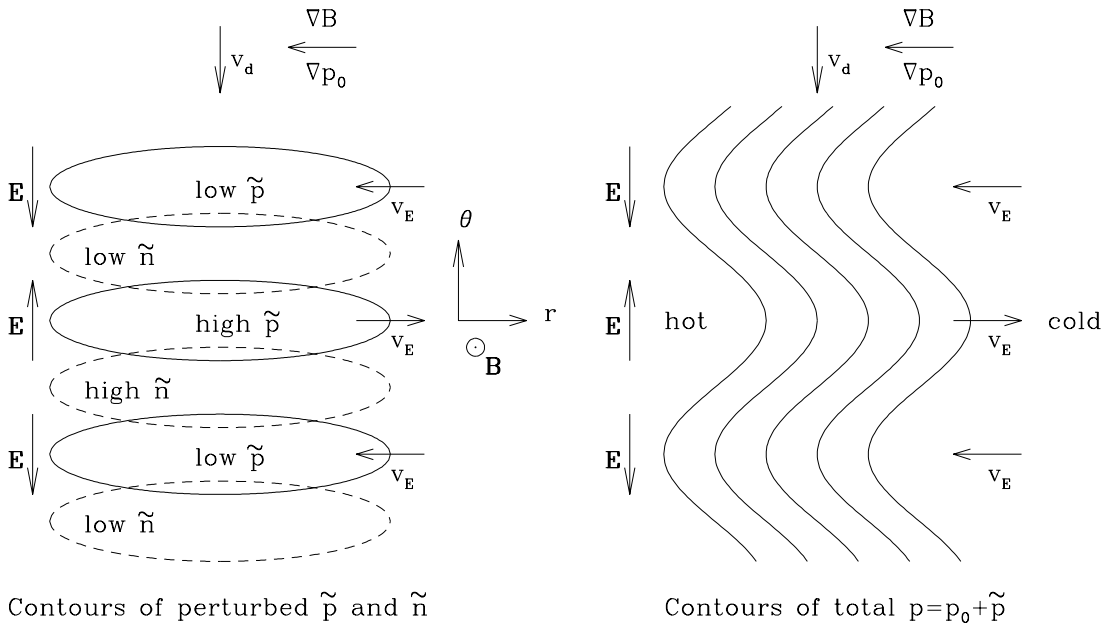

Figure 1.1: Simple picture of the toroidal ITG instability mechanism on the outer midplane of a tokamak. The velocity dependence of the downward ∇B and curvature drifts cause ion density build-up below the hot spots and above the cold spots. This produces the electric field, which $\mathbf{E} \times \mathbf{B}$ convects hotter plasma into the hot spots, and colder plasma into the cold spots. On the inner midplane where ∇p_0 is reversed with respect to ∇B, colder plasma is convected into the hot spots, and this feedback mechanism is shut off.

When taking moments of Eq. (1.2), the $v_\parallel^2$ and $v_\perp^2/2$ in $\mathbf{v}_d$ introduce the parallel and perpendicular pressures into the density equation, $p_\parallel = \int d^3v\, m v_\parallel^2 F$ and $p_\perp = \int d^3v (m v_\perp^2/2) F$. To avoid the complexity of evolving $p_\parallel$ and $p_\perp$ separately (as in Chapter 2), for the present simple model, assume that $v_\parallel^2 = v_\perp^2/2$ when taking moments of this term, i.e., the curvature drift is replaced by the ∇B drift. This is commonly called the ∇B approximation [Terry *et al.*, 1982]. The differences between the ∇B model and the constant energy resonance model, $v_\parallel^2 + v_\perp^2/2 = 2(v_\parallel^2 + v_\perp^2)/3$ [Romanelli and Briguglio, 1990], will not appear within the context of this simple fluid model. Integrating Eq. (1.2) over velocity space gives the evolution of the perturbed density:

$$\frac{\partial n}{\partial t} + \nabla \cdot \left[n \mathbf{v}_E + \frac{2p}{m\Omega B^2} \mathbf{B} \times \nabla B \right] = 0, \tag{1.4}$$

where the pressure $p = \int d^3v (mv^2)/3 = \int dv_\parallel \int d\mu B F m (v_\parallel^2 + 2\mu B)/3 \approx \int dv_\parallel \int d\mu\, BFm\mu B$ in the ∇B approximation. Breaking the density into equilibrium and perturbed parts, $n = n_0 + \tilde{n}$:

$$\frac{\partial \tilde{n}}{\partial t} + \mathbf{v}_E \cdot \nabla n_0 + \mathbf{v}_E \cdot \nabla \tilde{n} + n_0 \nabla \cdot \mathbf{v}_E + \frac{2}{m\Omega B^2} \mathbf{B} \times \nabla B \cdot \nabla \tilde{p} = 0. \tag{1.5}$$

The second term is the $\mathbf{E} \times \mathbf{B}$ convection of the equilibrium density gradient, and the third term is the nonlinear convection of the perturbed density. In the fourth term, as shown in Chapter 2, $\nabla \cdot \mathbf{v}_E = (2c/B^3) \mathbf{B} \times \nabla B \cdot \nabla \tilde{\Phi}$. This term arises from the variation of B with major radius in a tokamak; $\nabla \cdot \mathbf{v}_E = 0$ if B is constant, as in a sheared slab model. Also discussed in Chapter 2, $\nabla \cdot [(1/\Omega B^2) \mathbf{B} \times \nabla B] \approx 0$, so it comes out of the divergence, leaving the $\mathbf{v}_d$ term above. The divergence of the $\mathbf{v}_d$ drift comes from the fact that hot particles ∇B drift faster than cold particles, as shown by Eq. (1.1), so pressure perturbations cause density perturbations. The toroidal angular momentum conserving term vanishes upon integrating over $v_\parallel$.

The notation can be simplified by normalizing perturbed quantities to their equilibrium values, $n = \tilde{n}/n_0$, $p = \tilde{p}/p_0$, $\Phi = e\tilde{\Phi}/T_{i0}$, where $p_0 = n_0 T_0$, and introducing the diamagnetic drift and toroidal drift frequencies:

$$i\omega_* = \frac{cT_{i0}}{eB^2 n_0} \mathbf{B} \times \nabla n_0 \cdot \nabla, \tag{1.6}$$

$$i\omega_d = \frac{cT_{i0}}{eB^3} \mathbf{B} \times \nabla B \cdot \nabla. \tag{1.7}$$

In the usual low aspect ratio tokamak geometry, with $B = (B_0 R_0/R)(\mathbf{e}_\phi + r/qR_0\mathbf{e}_\theta)$, these frequencies become: $\omega_* = -k_\theta \rho_i v_{ti}/L_{ni}$ and $\omega_d = -(\rho_i v_{ti}/R)(k_r \sin\theta + k_\theta \cos\theta)$. In this discussion we will only consider non-inverted profiles, so $L_{ni}^{-1} = -d\ln n_{i0}/dr$ and $L_{Ti}^{-1} = -d\ln T_{i0}/dr$ are positive. The linearized density equation is then:

$$\frac{\partial n}{\partial t} - i\omega_* \Phi + 2i\omega_d \Phi + 2i\omega_d p = 0. \tag{1.8}$$

To find the evolution equation for the pressure, multiply Eq. (1.2) by $m\mu = mv_\perp^2/2B$ and integrate over velocity to get:

$$\frac{\partial}{\partial t}\frac{p}{B} + \nabla \cdot \left[\frac{p}{B}\mathbf{v}_E + \int d^3v F \frac{mv_\perp^2}{2B}\mathbf{v}_d \right] = 0. \tag{1.9}$$

The toroidal drift terms now introduce the $v_\parallel^2 v_\perp^2$ and $v_\perp^4$ moments. The simplest way to evaluate these terms is to assume that F is Maxwellian:

$$F = \frac{n}{(2\pi/m)^{3/2} T_\perp \sqrt{T_\parallel}} e^{-mv_\parallel^2/2T_\parallel - m\mu B/T_\perp}, \tag{1.10}$$

but with total (equilibrium plus perturbed) n, $T_\parallel$, and $T_\perp$. Then

$$\int d^3v F \frac{mv_\perp^2}{2B} \frac{v_\parallel^2 + v_\perp^2/2}{\Omega B^2} \mathbf{B} \times \nabla B = \frac{p_\parallel p_\perp + 2p_\perp^2}{nm\Omega B^3} \mathbf{B} \times \nabla B. \tag{1.11}$$

This is effectively a closure approximation for the $v_\parallel^2 v_\perp^2$ and $v_\perp^4$ moments in terms of the lower known moments (n and p). Better closure approximations will be introduced in Chapter 2 which model the phase mixing associated with toroidal drifts and its related resonances.

Again separating the equilibrium and perturbed parts, and approximating $p_\parallel = p_\perp$ in Eq. (1.11), the pressure equation Eq. (1.9) becomes:

$$\frac{\partial \tilde{p}}{\partial t} + \mathbf{v}_E \cdot \nabla p_0 + \mathbf{v}_E \cdot \nabla \tilde{p} + p_0 \nabla \cdot \mathbf{v}_E + p_0 B \mathbf{v}_E \cdot \nabla \frac{1}{B} + \frac{p_0}{n_0 m \Omega B^2} \mathbf{B} \times \nabla B \cdot \nabla (6\tilde{p} - 3\tilde{n}T_0) = 0. \tag{1.12}$$

Upon normalizing and linearizing, the $\nabla \cdot \mathbf{v}_E$ and $B\mathbf{v}_E \cdot \nabla(1/B)$ terms combine to give $3i\omega_d\Phi$, and the $\mathbf{v}_E \cdot \nabla p_0$ term becomes $-i(1+\eta_i)\omega_*\Phi$ using $\eta_i = L_{ni}/L_{Ti}$. The pressure equation is then:

$$\frac{\partial p}{\partial t} - i(1+\eta_i)\omega_* \Phi + 3i\omega_d \Phi + i\omega_d(6p - 3n) = 0. \tag{1.13}$$

For normal modes, the pressure and density are given by:

$$n = -\frac{\omega_*}{\omega}\Phi + 2\frac{\omega_d}{\omega}\Phi + 2\frac{\omega_d}{\omega}p, \tag{1.14}$$

$$p = \frac{-\omega_*(1+\eta_i)\Phi + 3\omega_d\Phi - 3\omega_d n}{\omega - 6\omega_d}. \tag{1.15}$$

Although $k_\parallel$ has been ignored so far, in reality these modes have $k_\parallel \sim 1/qR$. Because of their fast parallel motion, the electrons are nearly adiabatic ($k_\parallel v_{te} \sim v_{te}/qR \gg \omega \sim \omega_*$), and the perturbed electron density is given by $\tilde{n}_e/n_{e0} = e\tilde{\Phi}/T_{e0}$. Nonadiabatic electron response, which primarily comes from trapped electrons, can significantly affect these modes in some regimes, and will be considered in Chapter 3. The perturbed densities are quasineutral, since $k\lambda_D \ll 1$. Keeping the small $b = k_\perp^2\rho_i^2$ limit of the polarization density, Eq. (2.9), the perturbed electron and ion densities are related by:

$$\tilde{n}_e = \tilde{n}_i - b\frac{e\tilde{\Phi}}{T_{i0}}n_{i0},$$

Substituting $\tilde{n}_e = n_{e0}e\tilde{\Phi}/T_{e0}$ and again normalizing to $n_{e0} = n_{i0}$, and $\Phi = e\tilde{\Phi}/T_{i0}$,

$$\frac{T_{i0}}{T_{e0}}\Phi = n - b\Phi,$$

or

$$(\tau + b)\Phi = n, \tag{1.16}$$

where $\tau = T_{i0}/T_{e0}$.

The dispersion relation for this simple model is quadratic, and is obtained by combining Eqs. (1.14), (1.15), and (1.16):

$$(\tau+b)\omega^2 + \omega[-6\omega_d(\tau+b) + \omega_* - 2\omega_d] + 6\omega_d^2(1+\tau+b) + 2\omega_*\omega_d(\eta_i - 2) = 0. \tag{1.17}$$

with roots:

$$\omega = \frac{6\omega_d(\tau+b) + 2\omega_d - \omega_*}{2(\tau+b)} \tag{1.18}$$

$$\pm\frac{\sqrt{[6\omega_d(\tau+b) + 2\omega_d - \omega_*]^2 - 4(\tau+b)[6\omega_d^2(1+\tau+b) + 2\omega_d\omega_*(\eta_i - 2)]}}{2(\tau+b)}$$

The growth rate from this simple model is shown in Fig. 1.2 for $\eta_i = 2$, $\tau = 1$, $b = 0$, and varying $\epsilon_n = L_n/R$. Also shown are the fully kinetic and gyrofluid growth rates

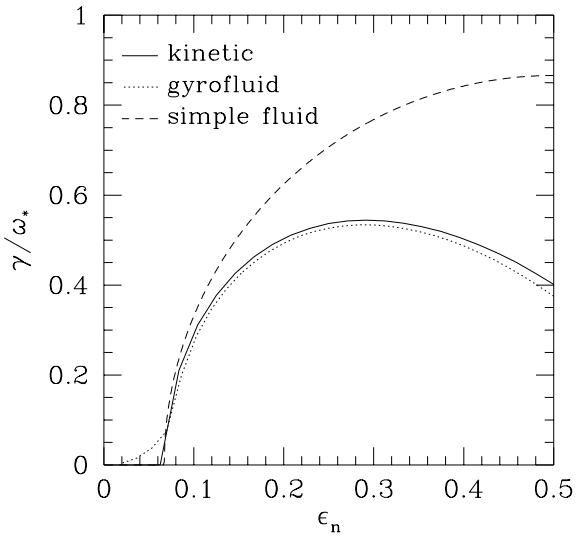

Figure 1.2: Comparison of kinetic, gyrofluid, and simple fluid growth rates of the purely toroidal ITG mode, for $\eta_i = 2$. Including models of kinetic effects significantly improves the accuracy of the gyrofluid results.

corresponding to this purely toroidal limit, as found in Chapter 2. Including kinetic effects brings the gyrofluid results into much better agreement with kinetic theory than the simple model discussed here, but this simple model captures the gross features of the instability.

In is instructive to first look at the flat density gradient limit, where $L_{ni} \to \infty$, so ϵ_n and $\eta_i \to \infty$. In this limit Eq. (1.18) reduces to:

$$\omega = \frac{3\omega_d(\tau+b)+\omega_d}{(\tau+b)} \pm \frac{\sqrt{3\omega_d^2(\tau+b)^2+\omega_d^2-2\omega_d\omega_*\eta_i(\tau+b)}}{(\tau+b)} \tag{1.19}$$

To get instability, we need $2\omega_d\omega_*\eta_i(\tau+b) > 3\omega_d^2(\tau+b)^2+\omega_d^2$. Clearly, $\omega_d\omega_*\eta_i > 0$ is necessary (but not sufficient) for instability, since the other terms inside the square root in Eq. (1.19) are positive. From this condition, it can be ascertained from the definitions of ω_* and ω_d in Eqs. (1.6) and (1.7) that ∇p_0 and ∇B must point in the same direction for instability ("bad" curvature), and if ∇p_0 and ∇B are antiparallel ("good" curvature) the mode is stable. Because $\omega_* = -k_\theta \rho_i v_{ti}/L_{ni}$ and $\omega_d = -(\rho_i v_{ti}/R)(k_r \sin\theta + k_\theta \cos\theta)$, perturbations on the outer midplane of the torus ($\theta = 0$) are unstable, while perturbations on the inner midplane ($\theta = \pi$) are stable.

The dispersion relation Eq. (1.19) shows the stabilizing effect of $T_{i0} > T_{e0}$, ($\tau > 1$), both in the threshold for instability, because the stabilizing $3\omega_d^2(\tau + b)^2$ term increases more rapidly with τ than the destabilizing $-2\omega_d\omega_*\eta_i(\tau + b)$ term, and in the growth rate, because the $(\tau + b)$ in the denominator beats the $\sqrt{\tau + b}$ coming from the drive. This stabilization of the toroidal ITG mode from $T_{i0} > T_{e0}$ is a likely mechanism for improved transport in supershots and hot-ion modes (in combination with relatively weak electron temperature gradients to keep TEM driven transport small). The stabilizing effect of $T_i > T_e$ occurs by reducing the ion density perturbation produced by Φ, weakening the feedback mechanism that causes instability, as discussed below. In addition, Eq. (1.19) shows some of the stabilizing influence of finite Larmor radius (FLR) effects through b, though the FLR corrections in the density and pressure equations have been neglected. Physically, FLR stabilization occurs because the ions feel the averaged potential around their gyro-orbits, and this gyroaveraging reduces the response to high $k_\perp\rho_i$ components of the potential. In the large η_i (strongly unstable) limit, Eq. (1.19) gives a purely growing root:

$$\omega \approx \pm i\sqrt{\frac{2\omega_d\omega_*\eta_i}{\tau + b}}. \tag{1.20}$$

Since $\omega_*, \omega_d \propto k_\perp$, the growth rate stops increasing with b near $b = k_\perp^2\rho_i^2 = 1$. With the more complete FLR terms in Chapter 2, the growth rates peak around $k_\perp\rho_i \sim 1/2$, and then drop. Though ignored in this simple model, the perturbed impurity and beam densities can also affect stability, as discussed in the previous section.

In the slab limit, where $\epsilon_n \to 0$ so the toroidal terms vanish, the two roots of Eq. (1.18) are neutrally stable, $\omega = 0$ (the ion acoustic wave) and $-\omega_*/(\tau + b)$ (the electron drift wave). Parallel dynamics are necessary for instability in the slab limit.

To see the physical mechanism of this instability, consider a perturbation on the outer midplane in the large η_i limit, where the mode is purely growing ($\gamma \gg \omega_r$). Assuming $\tau = 1$ and neglecting FLR corrections ($b = 0$), from Eq. (1.20) we find $\gamma = \sqrt{\eta_i\omega_d\omega_*} = \sqrt{2\omega_d\omega_{*T}}$. Eqs. (1.14) and (1.15) become: $\Phi = -2\omega_d p/\omega$ and $p = -\omega_*\eta_i\Phi/\omega$. Using $\Phi = \bar{\Phi}\exp[ik_\theta r_0\theta - i\omega t]$ and $p = \bar{p}\exp[ik_\theta r_0\theta - i\omega t + i\alpha]$,

where $\bar{\Phi}$ and $\bar{p}$ are real,

$$\Phi(\theta,t) = \Re[\Phi + \Phi^*]/2 = \bar{\Phi}\cos(k_\theta r_0\theta)\exp(\gamma t),$$

$$p(\theta,t) = \Re[p + p^*]/2 = \bar{p}\cos(k_\theta r_0\theta + \alpha)\exp(\gamma t).$$

From Eq. (1.15), taking $k_\theta > 0$, so $\omega_* < 0$:

$$\bar{p}e^{i\alpha} = \frac{-\eta\omega_*}{i\gamma}\bar{\Phi} \Rightarrow \alpha = -\pi/2,$$

thus the perturbed pressure will be $\pi/2$ out of phase with the potential, leading to the density perturbations as shown in Fig. 1.1, and the instability mechanism from $\mathbf{E}\times\mathbf{B}$ convection of the equilibrium pressure.

Now going back to the general dispersion relation, Eq. (1.17), but assuming $\tau = 1$ and $b = 0$, the roots are:

$$\omega = 4\omega_d - \frac{\omega_*}{2} \pm \frac{1}{2}\sqrt{16\omega_d^2 + \omega_*^2 - 8\omega_d\omega_*\eta_i}. \tag{1.21}$$

In this more general case, the $\mathbf{E}\times\mathbf{B}$ convection of n_0, and $\nabla\cdot\mathbf{v}_E$ (the first two terms on the RHS of Eq. (1.14) are not negligible (as they were in the large η_i limit), so the phase shift between the density and pressure perturbations will not be $\pi/2$. This makes the mode propagate; it propagates in the ion direction for $\epsilon_n > 1/8$ and in the electron direction for $\epsilon_n < 1/8$. For $b = 0$ and $\tau = 1$, the quasineutrality constraint, Eq. (1.16), gives $n = \Phi$, so Eq. (1.15) becomes:

$$p = \frac{-\omega_*(1+\eta_i)}{\omega - 6\omega_d}\Phi. \tag{1.22}$$

When the phase shift between p and Φ is large enough ($\alpha = 0$ or π for $\gamma = 0$), the feedback mechanism is shut off and the mode is stabilized. For this simple model, this occurs at:

$$\eta_i^{\rm crit} = \frac{1 + 16\epsilon_n^2}{8\epsilon_n},$$

and the mode is unstable for $\eta_i > \eta_i^{\rm crit}$. This is a reasonable approximation to the kinetic $\eta_i^{\rm crit}$, which is a also function of ϵ_n, but is always greater than 2/3. In the flat density limit, $\epsilon_n \to \infty$, $\eta_i^{\rm crit} \to 2\epsilon_n$, so the critical η_i becomes a critical temperature gradient, $L_{Tc}^{\rm sf}/R = 0.5$ from this simple fluid model, and instability requires $L_T < L_{Tc}$. The toroidal gyrofluid equations in Chapter 2 give $L_{Tc}^{\rm gf}/R = 0.33$, which is a better approximation to the kinetic $L_{Tc}^{\rm kin}/R = 0.36$.

Now consider a mode with $k_r \neq 0$, so the perturbations pictured in Fig. 1.1 are tilted in the poloidal plane. At the outer midplane, since $\sin\theta = 0$, ω_d is unchanged; also, ω_* is unchanged. The toroidal drifts still produce density perturbations aligned with the pressure perturbations, and $\mathbf{E} \times \mathbf{B}$ convection is along these tilted perturbations, leading to the same instability. Thus the only effect of k_r is to increase $b = k_\perp^2 \rho_i^2$, which is stabilizing, so $k_r = 0$ perturbations are the most unstable.

In a real tokamak these perturbations are aligned with the magnetic field lines, since parallel Landau damping or phase mixing quickly damps any high $k_\parallel$ components. As a field line rotates around the magnetic axis (from B_p), it samples both good and bad curvature regions. Minimizing $k_\parallel$ while simultaneously localizing the modes in the bad curvature region leads to mode structures with $k_\parallel \approx 1/qR$, with large amplitude at the outer midplane and smaller amplitude at the inner midplane ("ballooning" mode structure). In addition, magnetic shear causes the field lines on neighboring flux surfaces to rotate at different rates. The perturbations try to follow this twisting, which increases k_r moving along the field line. This increases FLR stabilization away from the point where $k_r = 0$. Thus the parallel mode structure is determined by the competition between minimizing $k_\parallel$, localizing the mode in the bad curvature region, and magnetic shear localization through FLR effects.

These instabilities grow until the nonlinear $\mathbf{E} \times \mathbf{B}$ terms in Eqs. (1.5) and (1.12) become comparable to the linear terms. For radially elongated modes as pictured in Fig. 1.1, $\nabla\tilde{n}$ and $\nabla\tilde{p}$ are nearly perpendicular to $\mathbf{v}_E$, so the nonlinearity is weak, allowing these modes to grow to large amplitude. However, these elongated modes may be susceptible to "secondary instabilities" [Cowley *et al.*, 1991], and are strongly affected by radially sheared perpendicular flows, which stretch and twist the perturbations, enhancing decorrelation and reducing the fluctuation amplitudes [Biglari *et al.*, 1990]. From this simple picture, we expect these modes to evolve into turbulent blobs with short perpendicular scales, $k_\perp \rho_i \lesssim 1/2$, and long parallel scales, $k_\parallel \sim 1/qR$ (i.e. very elongated along the field line), with ballooning mode structures. These gross features are in fact observed in the more complete nonlinear simulations discussed in Chapter 5.

1.4 Outline

1.4.1 Improved Toroidal Gyrofluid Equations

The inclusion of ∇B and curvature drift effects is an important destabilization mechanism for tokamak microinstabilities. The growth rates for the toroidal ITG mode are typically three to four times higher than the growth rates of the slab ITG mode. Using models similar to [Waltz *et al.*, 1992], toroidal gyrofluid equations with more accurate closure approximations to model toroidal phase mixing are derived in Chapter 2. These toroidal gyrofluid equations also incorporate models of parallel phase mixing [Hammett and Perkins, 1990] and linear and nonlinear FLR effects [Dorland and Hammett, 1993], although the linear FLR terms are slightly modified by toroidicity. The derivation presented in Chapter 2 is valid for finite $k_\parallel$, while [Waltz *et al.*, 1992] focused on the purely toroidal ($k_\parallel = 0$) limit and a term to remove a singularity for finite $k_\parallel$ was added *a posteriori*.

Slab [Dorland *et al.*, 1992; Dorland, 1993] and toroidal [Beer *et al.*, 1992; Hammett *et al.*, 1993] simulations revealed that an important nonlinear saturation process for tokamak turbulence is the nonlinear generation and damping of radially sheared "zonal" $\mathbf{E} \times \mathbf{B}$ flows (flows which cause flux surfaces to rotate). These sheared flows are very weakly damped in a sheared slab (via classical viscosity); the dominant damping mechanisms arise from toroidal effects. The mirroring $\mu \hat{\mathbf{b}} \cdot \nabla B$ term is included in these toroidal gyrofluid equations to provide accurate models of poloidal flow damping from magnetic pumping, and also to model the effects of trapped ions, which extend the validity of these equations into the trapped ion regime at low $k_\theta \rho_i$. Finally, a Krook collision operator has been incorporated, important for poloidal flow damping in the Pfirsch-Schlüter regime, and for collisional effects on very low frequency modes.

1.4.2 Fluid Models for Trapped Electrons

Trapped electron models developed in this thesis have provided the first high resolution three dimensional toroidal simulations which simultaneously include trapped-electron effects as well as the ITG drive, which we presented in [Hammett *et al.*, 1994]. This enables realistic nonlinear calculations of the full transport matrix

(electron and ion heat fluxes and particle fluxes). Previous ITG simulations using adiabatic electrons had no electron heat flux or particle flux. A sophisticated trapped electron fluid model is derived in Chapter 3 which retains the pitch angle dependence throughout, as opposed to more simplified trapped electron models which assume that the electrons are deeply trapped [KADOMTSEV and POGUTSE, 1970]. Retaining this pitch angle dependence is potentially important for advanced tokamak configurations in the second stability regime or with reversed magnetic shear [KESSEL *et al.*, 1994], where a major fraction of the trapped electrons have favorable toroidal precession drift, stabilizing trapped electron modes. Because these electron equations are bounce averaged, the fast parallel electron time scale is removed, and nonlinear simulations with trapped electrons are only about two times slower than simulations assuming adiabatic electrons. We can now study regimes where the collisionless or dissipative trapped electron mode (TEM) dominates over the ITG mode, or in mixed regimes where the TEM drive may double the growth rate of the ITG mode. These simulations can also investigate why the core of supershots are convection dominated, or search for "off-diagonal" pinch effects.

1.4.3 Flux Tube Simulation Geometry

Simulation of turbulence in a full tokamak is very challenging since one must simultaneously resolve the machine size and the scales of the turbulence. The scale of the turbulence is on the order of the ion gyroradius, ρ_i, while the size of present day tokamaks is much larger, $a/\rho_i \sim 500 - 1000$, where a is the minor radius. This requires a very fine computational grid, and is slightly beyond today's computational capabilities for realistic a/ρ_i. In Chapter 4 a reduced simulation geometry is presented which resolves only a thin flux tube rather than the full torus, exploiting the elongated nature of the turbulence, which has short perpendicular scales but long parallel scales. This method allows high resolution simulations in realistic tokamak geometry, retaining the important toroidal effects of good and bad curvature. It is also applicable to non-tokamak magnetic configurations, and the formulation in Chapter 4 is presented in a form applicable to general magnetic geometry. The material in Chapter 4 is available as a PPPL report [BEER *et al.*, 1994].

1.4.4 Nonlinear Simulation Results

The toroidal gyrofluid equations and bounce averaged trapped electron fluid equations derived in Chapters 2 and 3 are solved via direct numerical simulation using the efficient flux tube geometry in Chapter 4. The most interesting physics results from these simulations are presented in Chapter 5. The importance of small scale, turbulence-generated, sheared poloidal rotation, and the damping of this rotation, is demonstrated. The damping rates of this rotation from magnetic pumping from the gyrofluid model are calculated and compared with neoclassical theory. The nonlinear fluctuation spectra are peaked at long wavelengths compared to the fastest growing linear modes, and are anisotropic in k_r and k_θ, similar to BES measurements [FONCK *et al.*, 1993]. The fluctuation energy balance in the simulations shows that the dominant dissipation mechanism is parallel Landau damping, and that the dominant drive comes from equilibrium density and temperature gradients. Finally, nonlinear simulation results with trapped electrons are presented, where it is found that in moderate or low collisionality regimes, both ion and electron heat transport are strongly dependent on the electron collisionality and electron temperature and density gradients.

1.4.5 Comparison with Experiment

In Chapter 6, results from these nonlinear simulations are compared against a TFTR L-mode discharge, using measured plasma parameters. The predicted transport levels are in reasonable agreement with those calculated from power balance (SNAP). The central transport is small because the linear drive is weak, and increases toward the edge as the linear drive increases. Near $r/a \sim 0.8$, the predicted transport falls off. Possible mechanisms which could increase the predicted transport in the edge are discussed. This behavior is very similar to that found in [DORLAND *et al.*, 1994b; KOTSCHENREUTHER *et al.*, 1994a], where a transport model based on our toroidal gyrofluid simulations and linear kinetic theory was used to predict temperature profiles. The comparison with experiment is presented here to roughly demonstrate where we stand, and should be considered qualitative. Only one shot is compared here (though [DORLAND *et al.*, 1994b; KOTSCHENREUTHER *et al.*, 1994a] looked at many shots), and more detailed investigations are necessary.

Chapter 2

Derivation of the Toroidal Gyrofluid Equations

THE TOROIDAL GYROFLUID EQUATIONS describe the time evolution of a few moments of the gyrokinetic equation. We will concentrate on a set of six guiding center moments: the guiding center density, n, parallel velocity, $u_\parallel$, parallel pressure, $p_\parallel$, perpendicular pressure, $p_\perp$, and the parallel fluxes of parallel and perpendicular heat, $q_\parallel$ and $q_\perp$. The toroidal gyrofluid equations presented here incorporate reliable models of most of the physics considered important for ion dynamics in tokamak turbulence. The moment hierarchy is closed by approximations which model the kinetic effects of collisionless phase mixing from parallel free streaming and toroidal ∇B and curvature drifts, and linear and nonlinear FLR effects. The $\mu\hat{\mathbf{b}} \cdot \nabla B$ force is included, which recovers some trapped particle effects and magnetic pumping. Ion-ion collisions are modeled with a simple Krook collision operator. Since the effects of ion collisions are usually weak, this should be sufficient. Probably the most significant limitation of these equations is the electrostatic approximation. This reduced set of nonlinear fluid equations is simple, yet accurate enough to be used in 3D high resolution direct numerical simulations of tokamak turbulence.

2.1 The Toroidal Gyrokinetic Equation

The starting point of the derivation of the toroidal ion gyrofluid equations is the nonlinear electrostatic gyrokinetic equation in toroidal geometry [HAHM, 1988; FRIEMAN and CHEN, 1982], see also [LEE, 1983; DUBIN *et al.*, 1983; LEE, 1987]. The usual gyrokinetic ordering is used:

$$\frac{\omega}{\Omega} \sim \frac{k_\parallel v_t}{\Omega} \sim \frac{e\Phi}{T} \sim \frac{F_1}{F_0} \sim \frac{\rho}{L} \sim \varepsilon \ll 1, \qquad k_\perp \rho \sim 1, \tag{2.1}$$

where ω is a typical frequency, $\Omega = eB/mc$ is the cyclotron frequency, $k_\parallel$ is a typical parallel wavenumber, $k_\perp$ is a typical perpendicular wavenumber, $\rho = v_t/\Omega$ is the gyroradius, $v_t^2 = T/m$ is the thermal velocity, and L is a macroscopic (equilibrium) scale length, e.g. the density scale length $L_n^{-1} = -(1/n_0)\nabla n_0$. The equations derived in this chapter will apply to ion species, for which $k_\perp \rho \sim 1$ and $\omega \sim \omega_t = v_t/qR$: main ions, impurities, or a Maxwellian energetic component (e.g., beam ions). The ordering $k_\perp \rho \sim 1$ is a "maximal ordering" and allows for a subsidiary expansion $k_\perp \rho \ll 1$ at a later time, although we will assume that $k_\perp$ isn't too small, i.e., we will assume $k_\perp L \gg 1$. The gyrokinetic equations (at least the version we are presently using) may need a generalization to be able to handle the plasma edge where equilibrium gradients may be short enough that $k_\perp L \sim 1$ and $e\Phi/T \sim 1$. In Chapter 3 we will derive equations for the electrons by a very different approach, since they satisfy a different ordering: $k_\perp \rho_e \ll 1$ and $\omega \ll \omega_{te}$. The gyrokinetic ordering removes the fast cyclotron time scale, which allows averaging over the gyroangle, reducing the velocity space dimensions from three to two. It also retains the physics of strong turbulence even though the fluctuating quantities $e\Phi/T$ and F_1/F_0 are ordered small, since $\nabla F_1/\nabla F_0 \sim 1$. Thus the dominant $\mathbf{E} \times \mathbf{B}$ nonlinearity is retained, and other nonlinearities are $\mathcal{O}(\varepsilon)$ smaller. In conservative form, the resulting equation is:

$$\frac{\partial}{\partial t} FB + \nabla \cdot \Big[FB(v_\parallel \hat{\mathbf{b}} + \mathbf{v}_E + \mathbf{v}_d) \Big]$$

$$+ \frac{\partial}{\partial v_\parallel} \left[FB(-\frac{e}{m} \hat{\mathbf{b}} \cdot \nabla J_0 \Phi - \mu \hat{\mathbf{b}} \cdot \nabla B + v_\parallel (\hat{\mathbf{b}} \cdot \nabla \hat{\mathbf{b}}) \cdot \mathbf{v}_E) \right] = B\, C(F), \tag{2.2}$$

which is valid up to $\mathcal{O}(\varepsilon)$. This equation describes the evolution of the gyrophase independent part of the guiding center distribution function $F = F(\mathbf{R}, v_\parallel, \mu, t)$,

where $\mu = v_\perp^2/2B$, $v_\parallel$ is the parallel guiding center velocity, and $\mathbf{R}$ is the guiding center position. This form is valid for a general magnetic field, and $\hat{\mathbf{b}}$ is the unit vector in the direction of the magnetic field, $\mathbf{B} = B\hat{\mathbf{b}}$. The combination FB enters because B is the Jacobian of the transformation from $(v_\parallel, v_\perp)$ variables to $(v_\parallel, \mu)$. Because finite Larmor radius effects are retained ($k_\perp \rho \sim 1$), the particles feel the gyroaveraged $\mathbf{E} \times \mathbf{B}$ drift, $\mathbf{v}_E = (c/B)\hat{\mathbf{b}} \times \nabla J_0 \Phi$, where J_0 is the linear operator that carries out the gyroaveraging of the electrostatic potential. In Fourier space, this operator is the Bessel function $J_0(k_\perp v_\perp/\Omega)$, where $k_\perp$ is the perpendicular wavenumber of Φ, not of F.

The ∇B and curvature drifts have been combined in

$$\mathbf{v}_d = \frac{v_\parallel^2}{\Omega}\hat{\mathbf{b}} \times (\hat{\mathbf{b}} \cdot \nabla \hat{\mathbf{b}}) + \frac{\mu}{\Omega}\hat{\mathbf{b}} \times \nabla B. \tag{2.3}$$

Using the equilibrium relations $\nabla p = (1/c)\mathbf{J} \times \mathbf{B}$ and $(4\pi/c)\mathbf{J} = \nabla \times \mathbf{B}$, and the identity $\hat{\mathbf{b}} \cdot \nabla \hat{\mathbf{b}} = (\nabla \times \hat{\mathbf{b}}) \times \hat{\mathbf{b}}$, this can be written:

$$\mathbf{v}_d = \frac{v_\parallel^2 + \mu B}{\Omega B^2}\mathbf{B} \times \nabla B + \frac{4\pi v_\parallel^2}{\Omega B^2}\hat{\mathbf{b}} \times \nabla p, \tag{2.4}$$

where the ∇p term is negligible for $\beta = 8\pi p/B^2 \ll 1$, i.e. $\hat{\mathbf{b}} \cdot \nabla \hat{\mathbf{b}} \approx \nabla B$. (For larger β, or stongly rotating plasmas where $nm_i \mathbf{v} \cdot \nabla \mathbf{v}$ is not ignorable in the equilibrium pressure equation, one simply needs to keep the curvature and ∇B drifts separately. Thus instead of ω_d in Eq. (2.10), one would use two operators: $\omega_{\nabla B}$ and ω_κ.) Toroidicity enters in Eq. (2.2) through the ∇B and curvature drifts, the $v_\parallel(\hat{\mathbf{b}} \cdot \nabla \hat{\mathbf{b}}) \cdot \mathbf{v}_E$ toroidal angular momentum conserving term, through the non-zero divergence of $\mathbf{v}_E$ in toroidal geometry, toroidal FLR effects, and the $\mu \hat{\mathbf{b}} \cdot \nabla B$ mirroring force. All these terms arise because B is not constant in general, in contrast to a sheared slab model.

For ion species, collisional effects will be modeled with a particle, momentum, and energy conserving BGK operator [Gross and Krook, 1956] (ion-electron collisions are negligible):

$$C(F_j) = -\sum_k \nu_{jk}(F_j - F_{Mjk}), \tag{2.5}$$

where ν_{jk} is the collision rate of species j with species k. Collisions between species j and k cause F_j to relax to a shifted Maxwellian, F_{Mjk}, with the appropriate density,

velocity, and temperature to conserve particles, momentum, and energy. Because F_1 is small, F_{Mjk} can be linearized. For a single ion species plasma, this leads to:

$$C(F) = -\nu_{ii}\left\{F_1 - \left[\frac{n_1}{n_0} + \frac{u_\parallel v_\parallel}{v_t^2} + \frac{T_1}{T_0}\left(\frac{v^2}{2v_t^2} - \frac{3}{2}\right)\right]F_0\right\}, \tag{2.6}$$

where $v^2 = v_\parallel^2 + v_\perp^2$ and $T_1 = (T_{\parallel 1} + 2T_{\perp 1})/3$. The generalization for multiple ion species can be found in [Gross and Krook, 1956; Stringer and Connor, 1971].

Since the perturbations of interest satisfy $k\lambda_D \ll 1$ ($\lambda_D \ll \rho_i$ for typical tokamak parameters), we will assume quasineutrality, $n_e = \sum Z_j n_j$, where n_e is the electron density, n_j is the ion particle density (not the guiding center density) of the j'th species, and $Z_j e$ is the species charge. The ion particle density is related to the guiding center density by [Lee, 1983; Dubin *et al.*, 1983; Lee, 1987]:

$$n_j = \bar{n}_j - n_{j0}(1-\Gamma_0)\frac{Z_j e\Phi}{T_j}, \tag{2.7}$$

where $\Gamma_0(b_j) = \exp(-b_j)I_0(b_j)$, I_0 is a modified Bessel function, $b_j = k_\perp^2 v_{t\perp j}^2/\Omega_j^2 = k_\perp^2\rho_j$, and $v_{t\perp j}^2 = T_{\perp j}/m_j$. The second term on the right hand side of Eq. (2.7) comes from the gyrophase *dependent* part of the distribution function, and is usually called the polarization density. The $k_\perp$ in the polarization density term comes from Φ. The contribution to the particle density from the gyrophase *independent* part of the distribution function, $\bar{n}_j$, is

$$\bar{n}_j = \int d^3v\, J_0 F = \int d^3v\, (F_0 + J_0 F_1). \tag{2.8}$$

Here J_0 operates on F_1, i.e. $k_\perp$ comes from F_1. For a pure ion-electron plasma, with hydrogenic ions ($Z = 1$), the quasineutrality constraint then becomes:

$$n_e = \bar{n}_i - n_{i0}(1-\Gamma_0)\frac{e\Phi}{T_i}, \tag{2.9}$$

The equations derived in the remainder of this chapter are applicable for each ion species, but for simpler notation, we will drop the species index j and set $Z_j = 1$. To incorporate multiple ion species, one simply evolves the moments for each species independently. Different species are coupled together through the quasineutrality constraint and through inter-species collision terms.

We will now manipulate Eq. (2.2) into a form convenient for deriving fluid equations. All of the toroidal effects except the $\mu\hat{\mathbf{b}}\cdot\nabla B$ terms can be written

compactly using the notation:

$$i\omega_d \equiv (v_t^2/\Omega B^2)\mathbf{B}\times\nabla B\cdot\nabla. \tag{2.10}$$

Let us first look at the ∇B and curvature drift terms. For example, pulling $(\Omega B^2)^{-1}\mathbf{B}\times\nabla B$ out of the divergence:

$$\nabla\cdot[FB\mathbf{v}_d] = \frac{1}{\Omega B^2}\mathbf{B}\times\nabla B\cdot\nabla[FB(v_\parallel^2+\mu B)] + FB(v_\parallel^2+\mu B)\nabla\cdot\left[\frac{1}{\Omega B^2}\mathbf{B}\times\nabla B\right]$$

the second term becomes:

$$\nabla\cdot\left[\frac{1}{\Omega B^2}\mathbf{B}\times\nabla B\right] = \frac{1}{\Omega B^2}\nabla B\cdot\nabla\times\mathbf{B}\simeq 0$$

which is small for low β since the toroidal component of ∇B is zero and the current, $\mathbf{J}$, is mostly toroidal. Thus, for low β:

$$\nabla\cdot(FB\mathbf{v}_d) = \frac{1}{\Omega B^2}\mathbf{B}\times\nabla B\cdot\nabla[FB(v_\parallel^2+\mu B)] = (1/v_t^2)i\omega_d[FB(v_\parallel^2+\mu B)]. \tag{2.11}$$

In toroidal geometry, FLR effects are complicated by the fact that the argument of J_0 depends on B. When deriving fluid equations by taking moments of Eq. (2.2), it is easiest if F and J_0 appear together, i.e. on the same side of spatial gradient operators. We now manipulate the terms in Eq. (2.2) involving $J_0\Phi$ so gradients only act on the combination FJ_0 or FJ_1. Defining $\alpha = k_\perp v_\perp/\Omega$, and recalling that the spatial gradients are taken holding $v_\parallel$ and μ fixed, we can write:

$$\nabla J_0\Phi = J_0\nabla\Phi + \Phi\nabla J_0,$$

$$\nabla J_0(k_\perp v_\perp/\Omega) = \nabla J_0(\alpha) = \frac{\partial J_0}{\partial\alpha}\nabla\alpha = J_1(\alpha)\frac{\alpha}{2B}\nabla B.$$

The $\mathbf{E}\times\mathbf{B}$ term becomes:

$$\nabla\cdot[FB\mathbf{v}_E] = \nabla\cdot[FBJ_0\frac{c}{B^2}\mathbf{B}\times\nabla\Phi + FB\Phi J_1\frac{\alpha}{2B}\frac{c}{B^2}\mathbf{B}\times\nabla B].$$

The divergence of the $\mathbf{E}\times\mathbf{B}$ drift can be written in the same form as the ∇B and curvature drift terms:

$$\nabla\cdot[\frac{c}{B^2}\mathbf{B}\times\nabla\Phi] = \frac{c}{B^2}\nabla\Phi\times(\nabla\times\mathbf{B}) - \frac{2c}{B^3}(\mathbf{B}\times\nabla\Phi)\cdot\nabla B\simeq 2(e/T)i\omega_d\Phi,$$

since again, $\nabla\Phi$ is mostly perpendicular, and $\mathbf{J}$ is mostly toroidal. Writing $\mathbf{v}_\Phi = (c/B)\hat{\mathbf{b}} \times \nabla\Phi$, we have:

$$\nabla \cdot [FB\mathbf{v}_E] = \mathbf{v}_\Phi \cdot \nabla(FBJ_0) + 2FBJ_0(e/T)i\omega_d\Phi + (e/T)i\omega_d(FBJ_1\Phi\frac{k_\perp v_\perp}{2\Omega}).$$

The first term on the RHS includes the usual linear ω_* terms (from F_0) and the $\mathbf{E} \times \mathbf{B}$ nonlinearity (from F_1), with FLR corrections as discussed in [DORLAND and HAMMETT, 1993]. The linear pieces of the second and third (toroidal) terms ($\propto F_0$) are of the same order as the slab $\mathbf{E} \times \mathbf{B}$ nonlinearity in the gyrokinetic ordering (we keep $B^{-1}\nabla B \sim F_0^{-1}\nabla F_0$). The nonlinear pieces in the toroidal terms ($\propto F_1$) are higher order in the gyrokinetic ordering, and can be ignored.

Performing similar manipulations on the toroidal angular momentum conserving term, using the identity $(\hat{\mathbf{b}} \cdot \nabla\hat{\mathbf{b}}) \cdot \mathbf{v}_E = -(c/B^3)(\mathbf{B} \times \nabla B) \cdot \nabla J_0\Phi$, leads to:

$$\begin{aligned}\frac{\partial}{\partial v_\parallel}[FBv_\parallel(\hat{\mathbf{b}} \cdot \nabla\hat{\mathbf{b}}) \cdot \mathbf{v}_E] &= -\frac{\partial}{\partial v_\parallel}(Fv_\parallel)\frac{c}{B^2}\mathbf{B} \times \nabla B \cdot \nabla J_0\Phi \\ &= -\frac{\partial}{\partial v_\parallel}(Fv_\parallel)\frac{c}{B^2}\mathbf{B} \times \nabla B \cdot (J_0\nabla\Phi + J_1\frac{\alpha}{2B}\nabla B).\end{aligned}$$

The J_0 term again has the ω_d form, and the J_1 term vanishes leaving:

$$\frac{\partial}{\partial v_\parallel}[FBv_\parallel(\hat{\mathbf{b}} \cdot \nabla\hat{\mathbf{b}}) \cdot \mathbf{v}_E] = -\frac{\partial}{\partial v_\parallel}(FBJ_0v_\parallel)(e/T)i\omega_d\Phi.$$

Since $k_\parallel\rho \sim \varepsilon$, the only contribution from the $E_\parallel$ term is linear, so in this term we only need F_0. Using the notation $\nabla_\parallel = \hat{\mathbf{b}} \cdot \nabla$, and a Maxwellian F_0:

$$F_0 = \frac{n_0}{(2\pi v_t^2)^{3/2}}e^{-v_\parallel^2/2v_t^2 - \mu B/v_t^2}, \tag{2.12}$$

we have $\nabla_\parallel|_{v_\parallel,\mu} B(\partial F_0/\partial v_\parallel) = (\partial F_0/\partial v_\parallel)B(1 - \mu B/v_t^2)\nabla_\parallel \ln B$, so this term becomes:

$$-\frac{e}{m}(\hat{\mathbf{b}} \cdot \nabla J_0\Phi)\frac{\partial F_0}{\partial v_\parallel}B = -\frac{e}{m}\nabla_\parallel(J_0\Phi B\frac{\partial F_0}{\partial v_\parallel}) + \frac{e}{m}J_0\Phi B\frac{\partial F_0}{\partial v_\parallel}(\mu B/v_t^2 - 1)\nabla_\parallel \ln B.$$

Combining all these terms, Eq. (2.2) can be written:

$$\frac{\partial}{\partial t}FB + B\nabla_\parallel\frac{FBv_\parallel}{B} + \mathbf{v}_\Phi \cdot \nabla(FBJ_0) + 2FBJ_0(e/T)i\omega_d\Phi \tag{2.13}$$

$$+ \quad (e/T)i\omega_d(FBJ_1\Phi k_\perp v_\perp/2\Omega) + \frac{i\omega_d}{v_t^2}[FB(v_\parallel^2+\mu B)] - \frac{e}{m}\nabla_\parallel(J_0\Phi B\frac{\partial F_0}{\partial v_\parallel})$$
$$+ \quad \frac{e}{m}J_0\Phi B\frac{\partial F_0}{\partial v_\parallel}\left(\frac{\mu B}{v_t^2}-1\right)\nabla_\parallel \ln B - \mu B\frac{\partial}{\partial v_\parallel}(FB)\nabla_\parallel \ln B$$
$$- \quad \frac{\partial}{\partial v_\parallel}(FBJ_0 v_\parallel)(e/T)i\omega_d\Phi = 0.$$

This form is messy, but most suited for taking moments, because velocity dependent terms (such as F, J_0, μ, etc.) are grouped together on the same side of spatial gradient operators.

2.2 General Toroidal Gyrofluid Equations

We are interested in deriving evolution equations for velocity space moments of Eq. (2.13), defined by:

$$n = \int F\, d^3v \qquad nu_\parallel = \int F v_\parallel\, d^3v$$
$$p_\parallel = m\int F(v_\parallel-u_\parallel)^2\, d^3v \qquad p_\perp = (m/2)\int F v_\perp^2\, d^3v$$
$$q_\parallel = m\int F(v_\parallel-u_\parallel)^3\, d^3v \qquad q_\perp = (m/2)\int F v_\perp^2(v_\parallel-u_\parallel)\, d^3v$$
$$r_{\parallel,\parallel} = m\int F(v_\parallel-u_\parallel)^4\, d^3v \qquad r_{\parallel,\perp} = (m/2)\int F v_\perp^2(v_\parallel-u_\parallel)^2\, d^3v$$
$$r_{\perp,\perp} = (m/4)\int F v_\perp^4\, d^3v \qquad s_{\perp,\perp} = (m/4)\int F(v_\parallel-u_\parallel)v_\perp^4 d^3v$$
$$s_{\parallel,\parallel} = m\int F(v_\parallel-u_\parallel)^5 d^3v \qquad s_{\parallel,\perp} = (m/2)\int F(v_\parallel-u_\parallel)^3 v_\perp^2 d^3v$$

It will often be convenient to use temperature instead of pressure, where the parallel temperature is defined by $p_\parallel \equiv nT_\parallel$ and perpendicular temperature by $p_\perp \equiv nT_\perp$

We now proceed to derive moment equations by integrating Eq. (2.13) over velocity space. These equations express exact conservation laws of the gyrokinetic equation, e.g., conservation of particles, momentum, etc., in the collisionless limit. However, because of the velocity dependence in the parallel free streaming term, $k_\parallel v_\parallel$, the toroidal drift terms, $\omega_d(v_\parallel^2+v_\perp^2/2)$, the mirroring terms $v_\perp^2\nabla \ln B$, the FLR terms, $J_0(k_\perp v_\perp/\Omega)$, etc., higher moments are introduced into each of these equations, leading to the usual problem of the coupled moments hierarchy. These equations are not useful until closure approximations are made for the highest moments (which are not evolved), as discussed in following sections. Taking integrals of the form $\int dv_\parallel\, d\mu\, v_\parallel^j \mu^k \ldots$ of Eq. (2.13) leads to the following exact moment equations, using the notation: $n\langle A\rangle = \int d^3v\, FA = 2\pi\int dv_\parallel d\mu\, FBA$:

$$\frac{\partial n}{\partial t} \quad + \quad B\nabla_\parallel(nu_\parallel/B) + \mathbf{v}_\Phi\cdot\nabla(n\langle J_0\rangle) + 2n\langle J_0\rangle(e/T)i\omega_d\Phi \tag{2.14}$$

$$+ \quad (e/T)i\omega_d(\Phi n\langle J_1\alpha\rangle/2) + (1/T)i\omega_d(p_\parallel + p_\perp + nmu_\parallel^2) = 0,$$

$$\begin{aligned}\frac{\partial}{\partial t}nu_\parallel &+ B\nabla_\parallel(p_\parallel/m + nu_\parallel^2)/B + \mathbf{v}_\Phi\cdot\nabla(n\langle J_0 v_\parallel\rangle) + 2n\langle J_0 v_\parallel\rangle(e/T)i\omega_d\Phi \\ &+ (e/T)i\omega_d(\Phi n\langle J_1 v_\parallel\alpha\rangle/2) + (1/T)i\omega_d(q_\parallel + q_\perp + 3p_\parallel u_\parallel + p_\perp u_\parallel + nmu_\parallel^3) \\ &+ \frac{e}{m}\nabla_\parallel n\langle J_0\rangle\Phi + \frac{e}{m}n\langle J_0(v_\perp^2/2v_t^2 - 1)\rangle\Phi\nabla_\parallel\ln B + \frac{p_\perp}{m}\nabla_\parallel\ln B \\ &+ n\langle J_0 v_\parallel\rangle(e/T)i\omega_d\Phi = 0,\end{aligned} \tag{2.15}$$

$$\begin{aligned}\frac{\partial}{\partial t}(p_\parallel + nmu_\parallel^2) &+ B\nabla_\parallel(q_\parallel + 3p_\parallel u_\parallel + nmu_\parallel^2)/B + \mathbf{v}_\Phi\cdot\nabla(n\langle J_0 v_\parallel^2\rangle) \\ &+ 2n\langle J_0 v_\parallel^2\rangle(e/T)i\omega_d\Phi + (e/T)i\omega_d(\Phi n\langle J_1 v_\parallel^2\alpha\rangle/2) \\ &+ (1/T)i\omega_d(r_{\parallel,\parallel} + r_{\parallel,\perp} + 4q_\parallel u_\parallel + q_\perp u_\parallel + 6p_\parallel u_\parallel^2 + p_\perp u_\parallel^2 + nmu_\parallel^4) \\ &+ 2\frac{e}{m}\nabla_\parallel n\langle J_0 v_\parallel\rangle\Phi + 2\frac{e}{m}n\langle J_0 v_\parallel(v_\perp^2/2v_t^2 - 1)\rangle\Phi\nabla_\parallel\ln B \\ &+ 2(q_\perp + p_\perp u_\parallel)\nabla_\parallel\ln B + 2n\langle J_0 v_\parallel^2\rangle(e/T)i\omega_d\Phi = 0,\end{aligned} \tag{2.16}$$

$$\begin{aligned}\frac{\partial}{\partial t}\frac{p_\perp}{B} &+ B\nabla_\parallel(q_\perp + p_\perp u_\parallel)/B^2 + \mathbf{v}_\Phi\cdot\nabla\frac{n\langle J_0 v_\perp^2\rangle}{2B} + 2\frac{n\langle J_0 v_\perp^2\rangle}{2B}(e/T)i\omega_d\Phi \\ &+ (e/T)i\omega_d(\Phi n\langle J_1 v_\perp^2\alpha\rangle/4B) + (1/T)i\omega_d(r_{\parallel,\perp} + r_{\perp,\perp} + q_\perp u_\parallel + p_\perp u_\parallel^2)/B = 0,\end{aligned} \tag{2.17}$$

$$\begin{aligned}&\frac{\partial}{\partial t}(q_\parallel + 3p_\parallel u_\parallel + nmu_\parallel^2) + B\nabla_\parallel(r_{\parallel,\parallel} + 4q_\parallel u_\parallel + 6p_\parallel u_\parallel^2 + nmu_\parallel^4)/B \\ &+ \mathbf{v}_\Phi\cdot\nabla(n\langle J_0 v_\parallel^3\rangle) + 2n\langle J_0 v_\parallel^3\rangle(e/T)i\omega_d\Phi + (e/T)i\omega_d(\Phi n\langle J_1 v_\parallel^3\alpha\rangle/2) \\ &+ (1/T)i\omega_d(s_{\parallel,\parallel} + s_{\parallel,\perp} + 5r_{\parallel,\parallel}u_\parallel + 3r_{\parallel,\perp}u_\parallel + 10q_\parallel u_\parallel^2 + 10p_\parallel u_\parallel^3 + p_\perp u_\parallel^3 + nmu_\parallel^5) \\ &+ 3\frac{e}{m}\nabla_\parallel n\langle J_0 v_\parallel^2\rangle\Phi + 3\frac{e}{m}n\langle J_0 v_\parallel^2(v_\perp^2/2v_t^2 - 1)\rangle\Phi\nabla_\parallel\ln B \\ &+ 3(r_{\parallel,\perp} + q_\parallel u_\parallel + p_\perp u_\parallel^2)\nabla_\parallel\ln B + 3n\langle J_0 v_\parallel^3\rangle(e/T)i\omega_d\Phi = 0,\end{aligned} \tag{2.18}$$

$$\begin{aligned}&\frac{\partial}{\partial t}\frac{q_\perp + p_\perp u_\parallel}{B} + B\nabla_\parallel(r_{\parallel,\perp} + q_\perp u_\parallel + p_\perp u_\parallel^2)/B^2 + \mathbf{v}_\Phi\cdot\nabla\frac{n\langle J_0 v_\parallel v_\perp^2\rangle}{2B} \\ &+ 2\frac{n\langle J_0 m v_\parallel v_\perp^2\rangle}{2B}(e/T)i\omega_d\Phi + (e/T)i\omega_d(\Phi n\langle J_1 v_\parallel v_\perp^2\alpha\rangle/4B) \\ &+ (1/T)i\omega_d(s_{\parallel,\perp} + s_{\perp,\perp} + 3r_{\parallel,\perp}u_\parallel + r_{\perp,\perp}u_\parallel + p_\perp u_\parallel^3)/B + \frac{e}{m}\nabla_\parallel\frac{n\langle J_0 v_\perp^2\rangle\Phi}{2B} \\ &+ \frac{e}{m}n\langle J_0(v_\perp^2/2B)(v_\perp^2/2v_t^2 - 1)\rangle\Phi\nabla_\parallel\ln B \\ &+ \frac{r_{\perp,\perp}}{B}\nabla_\parallel\ln B + n\langle J_0 v_\parallel v_\perp^2/B\rangle(e/T)i\omega_d\Phi = 0.\end{aligned} \tag{2.19}$$

Before proceeding to discuss closure approximations, it is useful to note that many of these terms are higher order in the gyrokinetic ordering, and can be neglected. By separating the moments into equilibrium and fluctuating parts, e.g., $n = n_0 + n_1$, where $n_1/n_0 \sim \mathcal{O}(\varepsilon)$, the parallel nonlinearities drop out, since they are higher order in ε. In addition, we assume F_0 is an unshifted Maxwellian, so the equilibrium parts of odd moments are zero, and terms like $u_\parallel^2$ are higher order. We retain the $\mathbf{E} \times \mathbf{B}$ nonlinearities (the $\mathbf{v}_\Phi \cdot \nabla$ terms), which are leading order.

2.3 Finite Larmor Radius Effects

In [Dorland and Hammett, 1993], accurate models of FLR effects were developed by carefully approximating velocity space averages of J_0 which appear in the dynamical equations and in the quasineutrality constraint, Eq. (2.9). As they did, we choose to evolve moments of the guiding center distribution function, not real space moments, to provide a better description of linear FLR effects (including the "Bakshi-Linsker" effect [Bakshi *et al.*, 1977; Linsker, 1981]) and additional FLR nonlinearities. For simplicity, we will not incorporate the nonlinear FLR phase mixing model in [Dorland and Hammett, 1993], specifically because we do not see large fluctuation levels at high $k_\perp \rho_i$ in our toroidal nonlinear simulations, where these terms become important. In addition to approximating $\langle J_0 \rangle$, $\langle J_0 v_\parallel \rangle$, $\langle J_0 v_\parallel^2 \rangle$, $\langle J_0 v_\perp^2 \rangle$, $\langle J_0 v_\parallel^3 \rangle$, and $\langle J_0 v_\parallel v_\perp^2 \rangle$, which appear in the slab limit, we also need to approximate $\langle J_0 v_\perp^4 \rangle$, $\langle J_1 \alpha \rangle$, $\langle J_1 v_\parallel^2 \alpha \rangle$, and $\langle J_1 v_\perp^2 \alpha \rangle$, which arise from toroidal terms. Linearly, these terms involve only F_0, and could be evaluated exactly. However, in the quasineutrality constraint we have to approximate $\bar{n}_i$, which comes from F_1, see Eq. (2.8). F_1 is not Maxwellian, so the $\langle J_0 F_1 \rangle$ term in $\bar{n}_i$ needs to be approximated. As discussed in [Dorland and Hammett, 1993], the best agreement with linear kinetic theory is obtained by approximating both the $\langle J_0 \rangle$ terms and $\bar{n}_i$. In the linear kinetic equation, the J_0 in Eq. (2.8) combines with the J_0 in the $\mathbf{E} \times \mathbf{B}$ drifts in the gyrokinetic equation, Eq. (2.2), so the average of J_0^2 over a Maxwellian enters the dispersion relation (in the slab limit), not the average of J_0. These are quite different, since $\langle J_0^2 \rangle = \Gamma_0(b)$ and $\langle J_0 \rangle^2 = \exp(-b)$ behave quite differently for large b. This motivated the $\langle J_0^2 \rangle \approx \Gamma_0^{1/2}$ approximation introduced by [Dorland and Hammett, 1993], which is more robust and more accurate for linear dispersion relations. With the inclusion of toroidal effects, the $v_\perp$ in $J_0(k_\perp v_\perp/\Omega)$ couples with

the $v_\perp^2$ in the toroidal drifts, so it is no longer simply $\Gamma_0(b)$ that enters the linear kinetic equation, see Eq. (2.56) and Eq. (2.62). We have not found a completely satisfying replacement to $\langle J_0 \rangle \approx \Gamma_0^{1/2}$ for the general toroidal case, but $\langle J_0 \rangle \approx \Gamma_0^{1/2}$ continues to work reasonably well. Therefore, we will use the results of [Dorland and Hammett, 1993] to approximate:

$$\langle J_0 \rangle = \Gamma_0^{1/2}, \tag{2.20}$$

$$\langle J_0 v_\parallel \rangle = v_t \Gamma_0^{1/2}, \tag{2.21}$$

$$\langle J_0 v_\parallel^2 \rangle = v_t^2 \Gamma_0^{1/2}, \tag{2.22}$$

$$\langle J_0 v_\perp^2 \rangle = 2 v_t^2 \frac{\partial}{\partial b}(b \Gamma_0^{1/2}) = v_t^2 (2\Gamma_0^{1/2} + \hat{\nabla}_\perp^2) \tag{2.23}$$

$$\langle J_0 v_\parallel^3 \rangle = v_t^3 \Gamma_0^{1/2}, \tag{2.24}$$

$$\langle J_0 v_\parallel v_\perp^2 \rangle = 2 v_t^3 \frac{\partial}{\partial b}(b \Gamma_0^{1/2}) = v_t^3 (2\Gamma_0^{1/2} + \hat{\nabla}_\perp^2). \tag{2.25}$$

The modified Laplacian operators $\hat{\nabla}_\perp^2$ and $\hat{\hat{\nabla}}_\perp^2$ are defined by:

$$\frac{1}{2} \hat{\nabla}_\perp^2 \Psi = b \frac{\partial \Gamma_0^{1/2}}{\partial b} \Phi, \tag{2.26}$$

$$\hat{\hat{\nabla}}_\perp^2 \Psi = b \frac{\partial^2}{\partial b^2}(b \Gamma_0^{1/2}) \Phi, \tag{2.27}$$

where $\Psi = \Gamma_0^{1/2} \Phi$ is the approximation to the gyroaveraged potential.

There are four new terms due to toroidicity that need approximating: $\langle J_0 v_\perp^4 \rangle$, $\langle J_1 \alpha \rangle$, $\langle J_1 v_\parallel^2 \alpha \rangle$, and $\langle J_1 v_\perp^2 \alpha \rangle$. Several techniques could be used to approximate these terms; one is to follow the approach and rationale in [Dorland and Hammett, 1993]. For example, the $\langle J_1 \alpha \rangle$ term can be rewritten using the following trick:

$$\langle J_1 \alpha \rangle \approx - \left. \frac{\partial}{\partial \beta} \right|_{\beta=1} \langle J_0(\beta \alpha) \rangle \,. \tag{2.28}$$

Thus the approximation for $\langle J_0 \rangle$ is the fundamental one, and all other FLR terms can be derived from it. Using $\langle J_0 \rangle \approx \Gamma_0^{1/2}$ leads to:

$$\langle J_1 \alpha \rangle \approx - \left. \frac{\partial}{\partial \beta} \right|_{\beta=1} \Gamma_0^{1/2}(\beta^2 b) = -2b \frac{\partial \Gamma_0^{1/2}}{\partial b} = -\hat{\nabla}_\perp^2, \tag{2.29}$$

and

$$\left\langle J_1 v_\parallel^2 \alpha \right\rangle \approx -2 v_t^2 b \frac{\partial \Gamma_0^{1/2}}{\partial b} = -v_t^2 \hat{\nabla}_\perp^2. \tag{2.30}$$

For the $\langle J_1 v_\perp^2 \alpha \rangle$ term, we will assume that F is approximately Maxwellian, so that $v_\perp^2 F \approx 2 v_t^2 \partial (T_\perp F)/\partial T_\perp$, and:

$$\left\langle J_1 v_\perp^2 \alpha \right\rangle \approx -\left.\frac{\partial}{\partial \beta}\right|_{\beta=1} 2 v_t^2 \frac{\partial}{\partial T_\perp} \left(T_\perp \left\langle J_0(\beta\alpha) \right\rangle \right) = -4 v_t^2 \frac{\partial}{\partial b} \left(b^2 \frac{\partial \Gamma_0^{1/2}}{\partial b} \right) = -4 v_t^2 \hat{\hat{\nabla}}_\perp^2. \tag{2.31}$$

The final toroidal FLR term is:

$$\langle J_0 v_\perp^4 \rangle \approx 4 v_t^4 \left[b \frac{\partial^2}{\partial b^2} (b \Gamma_0^{1/2}) + 2b \frac{\partial}{\partial b} (b \Gamma_0^{1/2}) \right] = 4 v_t^4 \left(2\Gamma_0^{1/2} + \hat{\nabla}_\perp^2 + \hat{\hat{\nabla}}_\perp^2 \right). \tag{2.32}$$

These approximations remain first order accurate in b to those obtained using the Taylor series expansion $J_0 \approx 1 - k_\perp^2 v_\perp^2 / 4\Omega^2$.

While the above represents one consistent way to approximate all of the toroidal FLR terms, we empirically find that the agreement with kinetic theory near marginal stability for some parameters can be slightly improved by using the following FLR approximations for the toroidal terms:

$$\langle J_1 \alpha \rangle = (\hat{\nabla}_\perp^2 - 2\hat{\hat{\nabla}}_\perp^2), \tag{2.33}$$

$$\langle J_1 v_\parallel^2 \alpha \rangle = v_t^2 (\hat{\nabla}_\perp^2 - 2\hat{\hat{\nabla}}_\perp^2), \tag{2.34}$$

$$\langle J_1 v_\perp^2 \alpha \rangle = v_t^2 (2\hat{\nabla}_\perp^2 + 4\hat{\hat{\nabla}}_\perp^2). \tag{2.35}$$

$$\langle J_0 v_\perp^4 \rangle = 8 v_t^4 (\Gamma_0^{1/2} + \hat{\nabla}_\perp^2). \tag{2.36}$$

The third of these, Eq. (2.35), is not first order accurate in b. This appears to compensate for errors in the linear response of $T_\perp$ in the toroidal case, whereas the linear response of $T_\perp$ in the slab limit is quite good. The FLR closures in Eqs. (2.33)-(2.36) were used in the nonlinear runs in Chapter 5 and 6, and in the trapped electron mode comparisons in Chapter 3. Far from marginality, these terms give very similar results to Eqs. (2.29)-(2.32) (for example, in Fig. 3.4, the difference in the linear growth rates is less than 5%). The approximations Eqs. (2.29)-(2.32) are more consistent and rigorous (they are $\mathcal{O}(b)$ accurate), so in the derivation that follows we will use Eqs. (2.29)-(2.32) instead of Eqs. (2.33)-(2.36). We do

not recommend using Eqs. (2.33)-(2.36), since they may actually do worse than Eqs. (2.29)-(2.32) in some regimes, but include them here for completeness. With these closures, the toroidal FLR terms in Eqs. (2.91), (2.93), (2.94), and (2.96) are modified as follows:

$$\begin{aligned}
\left(2+\frac{1}{2}\hat{\nabla}_\perp^2\right) i\omega_d\Psi &\longrightarrow \left(2+\frac{3}{2}\hat{\nabla}_\perp^2-\hat{\hat{\nabla}}_\perp^2\right) i\omega_d\Psi,\\
\left(4+\frac{1}{2}\hat{\nabla}_\perp^2\right) i\omega_d\Psi &\longrightarrow \left(4+\frac{3}{2}\hat{\nabla}_\perp^2-\hat{\hat{\nabla}}_\perp^2\right) i\omega_d\Psi,\\
\left(3+\frac{3}{2}\hat{\nabla}_\perp^2+\hat{\hat{\nabla}}_\perp^2\right) i\omega_d\Psi &\longrightarrow \left(3+2\hat{\nabla}_\perp^2+3\hat{\hat{\nabla}}_\perp^2\right) i\omega_d\Psi,\\
\left(\hat{\hat{\nabla}}_\perp^2\Psi-\frac{1}{2}\hat{\nabla}_\perp^2\Psi\right)\nabla_\parallel \ln B &\longrightarrow \left(\frac{1}{2}\hat{\nabla}_\perp^2\Psi\right)\nabla_\parallel \ln B.
\end{aligned}$$

Now we look at linear FLR effects in the $\mathbf{E}\times\mathbf{B}$ terms. For example, in the density equation, following [Dorland and Hammett, 1993]:

$$\mathbf{v}_\Phi\cdot\nabla n\langle J_0\rangle \simeq \mathbf{v}_\Phi\cdot\nabla(n_0\Gamma_0^{1/2}) + \text{nonlinear terms} \tag{2.37}$$

Since $b=k_\perp^2 v_{t\perp}^2/\Omega^2$ depends on both B and $T_\perp$ (through $v_{t\perp}^2=T_{\perp 0}/m$), gradients acting on functions of b (FLR modified terms), introduce pieces proportional to ∇B and $\nabla T_{\perp 0}$:

$$\nabla b = \frac{b}{T_{\perp 0}}\nabla T_{\perp 0} - \frac{2b}{B}\nabla B,$$

$$\nabla n_0\Gamma_0^{1/2} = \Gamma_0^{1/2}\nabla n_0 + n_0\frac{\partial\Gamma_0^{1/2}}{\partial b}\nabla b.$$

We now introduce the diamagnetic frequency $i\omega_* \equiv -(cT/eBn_0)\nabla n_0\cdot\hat{\mathbf{b}}\times\nabla$, $\eta_\parallel = L_n/L_{T_\parallel}$, and $\eta_\perp = L_n/L_{T_\perp}$, where $L_{T_\parallel}$ and $L_{T_\perp}$ are the equilibrium scale lengths of parallel and perpendicular temperature, which can be different in general. When they are assumed to be the same, we drop the subscripts, and write η. With these definitions, Eq. (2.37) becomes:

$$\mathbf{v}_\Phi\cdot\nabla n\langle J_0\rangle = -n_0 i\omega_*\Gamma_0^{1/2}\frac{e\Phi}{T_0} - n_0\eta_\perp b\frac{\partial\Gamma_0^{1/2}}{\partial b}i\omega_*\frac{e\Phi}{T_0} + 2n_0 b\frac{\partial\Gamma_0^{1/2}}{\partial b}i\omega_d\frac{e\Phi}{T_0},$$

since $\mathbf{v}_\Phi\cdot(1/B)\nabla B = -i\omega_d(e\Phi/T)$. For a general function of b,

$$\mathbf{v}_\Phi\cdot\nabla n_0 f(b) = -n_0 f(b) i\omega_*\frac{e\Phi}{T_0} - n_0\eta_\perp b\frac{\partial f}{\partial b}i\omega_*\frac{e\Phi}{T_0} + 2n_0 b\frac{\partial f}{\partial b}i\omega_d\frac{e\Phi}{T_0}.$$

This form will be used to evaluate terms like $\mathbf{v}_\Phi \cdot \nabla \langle n J_0 v_\perp^2 \rangle$.

In the linear part of the $(e/2T) i\omega_d(\Phi n \langle J_1 \alpha \rangle)$ terms, we need to evaluate

$$\omega_d(\Phi n \langle J_1 \alpha \rangle) = n_0 \langle J_1 \alpha \rangle \omega_d \Phi + \Phi n_0 \frac{\partial \langle J_1 \alpha \rangle}{\partial b} \omega_d b + \Phi \langle J_1 \alpha \rangle \omega_d n_0,$$

The last two terms are higher order in ε, so the $\langle J_1 \alpha \rangle$ terms only contribute:

$$(e/2T) i\omega_d(\Phi n \langle J_1 \alpha \rangle) = i n_0 \left\langle J_1 \frac{\alpha}{2} \right\rangle \omega_d \frac{e\Phi}{T_0}.$$

Because the final equations will get rather complicated, for the moment, we will treat the linear and nonlinear terms separately. We normalize time, parallel lengths, and perpendicular lengths as

$$(t, k_\parallel, k_\perp) = (\frac{t v_t}{L_n}, k_\parallel L_n, k_\perp \rho), \tag{2.38}$$

and fluctuating quantities as

$$(\Phi, n, u, p, q, r, s) = \frac{\rho}{L_n}(\frac{e\Phi}{T_0}, \frac{n_1}{n_0}, \frac{u_1}{v_t}, \frac{p_1}{n_0 m v_t^2}, \frac{q_1}{n_0 m v_t^3}, \frac{r_1}{n_0 m v_t^4}, \frac{s_1}{n_0 m v_t^5}), \tag{2.39}$$

where normalized quantities are on the left hand side and dimensional quantities are on the right. With these normalizations, the characteristic drift wave time and space scales are $\mathcal{O}(1)$, and the perturbed quantities will be $\mathcal{O}(1)$ at the gyro-Bohm saturation level. In this chapter, all equilibrium quantities are ion parameters, i.e. $T_0 = T_{i0}$, $v_t = v_{ti}$. For the equilibrium F_0 we use a Maxwellian, so the normalized equilibrium values of the moments are $p_{\parallel 0} = 1$, $p_{\perp 0} = 1$, $r_{\parallel,\parallel 0} = 3$, $r_{\parallel,\perp 0} = 1$, and $r_{\perp,\perp 0} = 2$. With the linear FLR approximations discussed above, the moment equations are:

$$\frac{\partial n}{\partial t} + B\nabla_\parallel \frac{u_\parallel}{B} - \left(1 + \frac{\eta_\perp}{2}\hat{\nabla}_\perp^2\right) i\omega_* \Psi + \left(2 + \frac{1}{2}\hat{\nabla}_\perp^2\right) i\omega_d \Psi + i\omega_d(p_\parallel + p_\perp) = 0, \tag{2.40}$$

$$\frac{\partial u_\parallel}{\partial t} + B\nabla_\parallel \frac{p_\parallel}{B} + \nabla_\parallel \Psi + \left(p_\perp + \frac{1}{2}\hat{\nabla}_\perp^2 \Psi\right) \nabla_\parallel \ln B + i\omega_d(q_\parallel + q_\perp + 4u_\parallel) = 0, \tag{2.41}$$

$$\frac{\partial p_\parallel}{\partial t} + B\nabla_\parallel \frac{q_\parallel + 3u_\parallel}{B} + 2(q_\perp + u_\parallel)\nabla_\parallel \ln B - \left(1 + \eta_\parallel + \frac{\eta_\perp}{2}\hat{\nabla}_\perp^2\right) i\omega_* \Psi \tag{2.42}$$

$$+ \left(4 + \frac{1}{2}\hat{\nabla}_\perp^2\right) i\omega_d \Psi + i\omega_d(r_{\parallel,\parallel} + r_{\parallel,\perp}) = 0,$$

$$\frac{\partial p_\perp}{\partial t} + B^2\nabla_\parallel\frac{q_\perp + u_\parallel}{B^2} - \left[1 + \frac{1}{2}\hat{\nabla}_\perp^2 + \eta_\perp\left(1 + \frac{1}{2}\hat{\nabla}_\perp^2 + \hat{\hat{\nabla}}_\perp^{\,2}\right)\right] i\omega_* \Psi \tag{2.43}$$
$$+ \left(3 + \frac{3}{2}\hat{\nabla}_\perp^2 + \hat{\hat{\nabla}}_\perp^{\,2}\right) i\omega_d \Psi + i\omega_d(r_{\parallel,\perp} + r_{\perp,\perp}) = 0,$$

$$\frac{\partial q_\parallel}{\partial t} + \nabla_\parallel(r_{\parallel,\parallel} - 3p_\parallel) + (-r_{\parallel,\parallel} + 3p_\parallel + 3r_{\parallel,\perp} - 3p_\perp)\nabla_\parallel \ln B \tag{2.44}$$
$$+ i\omega_d(s_{\parallel,\parallel} + s_{\parallel,\perp} - 3q_\parallel - 3q_\perp + 6u_\parallel) = 0,$$

$$\frac{\partial q_\perp}{\partial t} + \nabla_\parallel\left(r_{\parallel,\perp} - p_\parallel + \frac{1}{2}\hat{\nabla}_\perp^2\Psi\right) + (-2r_{\parallel,\perp} + r_{\perp,\perp} + p_\parallel - p_\perp)\nabla_\parallel \ln B \tag{2.45}$$
$$+ \left(\hat{\hat{\nabla}}_\perp^{\,2}\Psi - \frac{1}{2}\hat{\nabla}_\perp^2\Psi\right)\nabla_\parallel \ln B + i\omega_d(s_{\parallel,\perp} + s_{\perp,\perp} - q_\parallel - q_\perp + u_\parallel) = 0.$$

If we had evaluated the velocity space averages using a Maxwellian F, giving $\langle J_0\rangle = \exp(-b)$, the n, $u_\parallel$, $p_\parallel$ and $p_\perp$ equations above would be equivalent to those derived in [Brizard, 1992] (in the electrostatic limit of his equations). The q equations would also be equivalent if [Brizard, 1992] had proceeded to higher moment equations, but he stopped at p. This equivalence can be verified by replacing $\Gamma_0^{1/2} \to \exp(-b/2)$ and evaluating the derivatives with respect to b in Eqs. (2.26) and (2.27). These equations require closure approximations for $r_{\parallel,\parallel}$, $r_{\parallel,\perp}$, $r_{\perp,\perp}$, $s_{\parallel,\parallel}$, $s_{\parallel,\perp}$, and $s_{\perp,\perp}$, which [Brizard, 1992] did not address, and will be discussed in following sections.

For the nonlinear terms, we follow [Dorland and Hammett, 1993]. Thus, to each of the equations above we add the usual $\mathbf{E}\times\mathbf{B}$ nonlinearities plus additional FLR nonlinearities, as follows:

$$\frac{\partial n}{\partial t} + \mathbf{v}_\Psi\cdot\nabla n + [\frac{1}{2}\hat{\nabla}_\perp^2\mathbf{v}_\Psi]\cdot\nabla T_\perp + \cdots \tag{2.46}$$

$$\frac{\partial u_\parallel}{\partial t} + \mathbf{v}_\Psi\cdot\nabla u_\parallel + [\frac{1}{2}\hat{\nabla}_\perp^2\mathbf{v}_\Psi]\cdot\nabla q_\perp + \cdots \tag{2.47}$$

$$\frac{\partial p_\parallel}{\partial t} + \mathbf{v}_\Psi\cdot\nabla p_\parallel + [\frac{1}{2}\hat{\nabla}_\perp^2\mathbf{v}_\Psi]\cdot\nabla T_\perp + \cdots \tag{2.48}$$

$$\frac{\partial p_\perp}{\partial t} + \mathbf{v}_\Psi\cdot\nabla p_\perp + [\frac{1}{2}\hat{\nabla}_\perp^2\mathbf{v}_\Psi]\cdot\nabla p_\perp + [\hat{\hat{\nabla}}_\perp^{\,2}\mathbf{v}_\Psi]\cdot\nabla T_\perp + \cdots \tag{2.49}$$

$$\frac{\partial q_\parallel}{\partial t} + \mathbf{v}_\Psi\cdot\nabla q_\parallel + \cdots \tag{2.50}$$

$$\frac{\partial q_\perp}{\partial t} + \mathbf{v}_\Psi\cdot\nabla q_\perp + [\frac{1}{2}\hat{\nabla}_\perp^2\mathbf{v}_\Psi]\cdot\nabla u_\parallel + [\hat{\hat{\nabla}}_\perp^{\,2}\mathbf{v}_\Psi]\cdot\nabla q_\perp + \cdots \tag{2.51}$$

In these terms, $\mathbf{v}_\Psi$ is the approximation to the $\mathbf{E} \times \mathbf{B}$ drift in the gyroaveraged potential, $\mathbf{v}_\Psi = (c/B)\hat{\mathbf{b}} \times \Psi$, where $\Psi = \Gamma_0^{1/2}\Phi$. There is a typological error in Eq. (59) of [DORLAND and HAMMETT, 1993], where the nonlinear term involving $q_\perp$ should be dropped.

Now let us return to the quasineutrality constraint, Eq. (2.9). Here we have to approximate the real space density. Because of the J_0 which acts on F_1, $\bar{n}_i$ will involve the guiding center density and all higher perpendicular moments, but we only evolve up to $T_\perp$. Thus we need another closure approximation which relates $\bar{n}_i$ to n and $T_\perp$. The approximation for $\bar{n}_i$ in [DORLAND and HAMMETT, 1993] was tailored to fit the local kinetic dispersion relation in the slab limit. In the toroidal case, because of the $v_\perp$ dependence of the toroidal drifts in the resonant denominator of the toroidal response function, Eq. (2.56), following such a procedure is more complicated, so we simply use

$$\bar{n}_i = \frac{1}{1+b/2} n - \frac{2b}{(2+b)^2} T_\perp. \tag{2.52}$$

This is first order accurate in b for both the n and $T_\perp$ terms, and behaves appropriately ($\bar{n}_i \to 0$) in the $b \to \infty$ limit. The FLR approximations used here and above provide a reasonably accurate fit to the kinetic FLR behavior in the local kinetic dispersion relation, and continue to perform well nonlocally, as demonstrated in Section 2.8 of this chapter. Note that the FLR models described in this section can also be used with a simpler Padé approximation, by substituting $\Gamma_0^{1/2} \to (1+b/2)^{-1}$ in Eqs. (2.26) and (2.27), as discussed in [DORLAND and HAMMETT, 1993].

2.4 Local Linear Toroidal Response Function

Our closure approximations for $r_{\parallel,\parallel}$, $r_{\parallel,\perp}$, $r_{\perp,\perp}$, $s_{\parallel,\parallel}$, $s_{\parallel,\perp}$, and $s_{\perp,\perp}$, will be chosen to provide accurate models of the kinetic effects of parallel and toroidal drift phase mixing. Ultimately, we choose the closure coefficients to provide an accurate fit to the local linear toroidal response function, which is derived in this section.

We begin by transforming the linearized gyrokinetic equation to (E, μ) variables, so $F = F(\mathbf{R}, E, \mu)$, where $E = v_\parallel^2/2 + \mu B$. Then breaking F into adiabatic and nonadiabatic pieces, $F = g - F_0 J_0 e\Phi/T_0$, the equation for the nonadiabatic

piece is found to be:

$$g = F_0 \frac{\omega - \omega_*^T}{\omega - k_\parallel v_\parallel - \omega_{dv}} J_0 \frac{e\Phi}{T_0}, \tag{2.53}$$

where $\omega_{dv} = \omega_d(v_\parallel^2 + \mu B)/v_t^2$ and $\omega_*^T = \omega_*[1 + \eta(v_\parallel^2/2v_t^2 + \mu B/v_t^2 - 3/2)]$. In the local approximation, we treat ω_d, ω_*, and $k_\parallel$ as constants, using $\omega_d = -k_\theta \rho v_t/R$ and $\omega_* = -k_\theta \rho v_t/L_n$, so $\omega_d/\omega_* = L_n/R \equiv \epsilon_n$. The total distribution function in guiding center coordinates, $f = f(\mathbf{R}, E, \mu)$ is:

$$f(\mathbf{R}) = F + \tilde{f} = F(\mathbf{R}) - \frac{e\Phi(\mathbf{x})}{T_0} F_0 + F_0 J_0 \frac{e\Phi(\mathbf{R})}{T_0}. \tag{2.54}$$

where F is gyrophase independent, and $\tilde{f}$ is the gyrophase dependent part. The first piece of $\tilde{f}$ is in real space, $\mathbf{x}$. To obtain the real space ion density (not the density of gyrocenters), only the parts in guiding center space need to be gyroaveraged (acted on by J_0):

$$\begin{aligned} n(\mathbf{x}) = \int d^3v f(\mathbf{x}) &= \int d^3v \left[J_0 F(\mathbf{R}) - \frac{e\Phi(\mathbf{x})}{T_0} F_0 + F_0 J_0^2 \frac{e\Phi(\mathbf{R})}{T_0} \right] \\ &= -n_0 \frac{e\Phi}{T_0} + \int d^3v J_0 g, \end{aligned} \tag{2.55}$$

since the $J_0 F$ and $F_0 J_0^2\, e\Phi/T_0$ pieces combine to give $J_0 g$. Inserting the solution for g, Eq. (2.53), the ion density response function is:

$$R_i = \frac{n}{-n_0 e\Phi/T_0} = 1 - \frac{1}{n_0} \int d^3v F_0 \frac{\omega - \omega_*^T}{\omega - k_\parallel v_\parallel - \omega_{dv}} J_0^2(k_\perp v_\perp/\Omega), \tag{2.56}$$

which is the usual linear form. Trapped particle effects appear in the variation of $v_\parallel$ along a particle's orbit. We will neglect trapped particle effects in this section, and treat $v_\parallel$ as a constant.

For $\mathrm{Im}(\omega) > 0$, the resonant denominator can be written:

$$\frac{1}{\omega - k_\parallel v_\parallel - \omega_{dv}} = -\frac{i}{\omega_d} \int_0^\infty d\tau\, e^{i\tau(\omega - k_\parallel v_\parallel - \omega_{dv})/\omega_d}, \tag{2.57}$$

and now the $v_\parallel$ and $v_\perp$ integrals can be evaluated. Normalizing ω and $k_\parallel v_t$ to the toroidal drift frequency by introducing $x = \omega/\omega_d$ and $z_\parallel = k_\parallel v_t/\omega_d$, and using a Maxwellian F_0, Eq. (2.12), the response function becomes:

$$R_i = 1 + \frac{i}{\sqrt{2\pi}} \int_0^\infty d\tau \int_0^\infty dv_\perp v_\perp \int_{-\infty}^\infty dv_\parallel \left\{ x - \frac{1}{\epsilon_n} \left[1 + \eta \left(\frac{v_\parallel^2 + v_\perp^2}{2v_t^2} - \frac{3}{2} \right) \right] \right\}$$

$$\times e^{i\tau[x-z_\parallel v_\parallel/v_t - v_\parallel^2/v_t^2 - v_\perp^2/2v_t^2]} e^{-(v_\parallel^2+v_\perp^2)/2v_t^2} J_0^2(k_\perp v_\perp/\Omega)$$

The $v_\perp$ integrals are:

$$\int_0^\infty dv_\perp v_\perp e^{-(1+i\tau)v_\perp^2/2v_t^2} J_0^2(\sqrt{b}v_\perp/v_t) = v_t^2 \frac{e^{-b/(1+i\tau)}}{1+i\tau} I_0\left(\frac{b}{1+i\tau}\right), \tag{2.58}$$

and

$$\int_0^\infty dv_\perp v_\perp^3 e^{-(1+i\tau)v_\perp^2/2v_t^2} J_0^2(\sqrt{b}v_\perp/v_t) = \tag{2.59}$$
$$2v_t^2 \frac{e^{-b/(1+i\tau)}}{(1+i\tau)^2} I_0\left(\frac{b}{1+i\tau}\right)\left[1 - \frac{b}{1+i\tau} + \frac{b}{1+i\tau}\frac{I_1(b/1+i\tau)}{I_0(b/1+i\tau)}\right],$$

where I_0 and I_1 are modified Bessel functions. The $v_\perp$ dependence in the resonant denominator was neglected in the numerical evaluation of the $v_\perp$ integrals of J_0 in [Waltz *et al.*, 1992] (although it was retained everywhere else), and thus I_0 and I_1 had real arguments, instead of the complex arguments in the expressions above. This produces differences in the local dispersion relations at large b. The response function in [Kim *et al.*, 1994] correctly retains the $v_\perp$ dependence of the resonant denominator while integrating over $v_\perp$. The local kinetic response function described here, and the local kinetic eigenvalues calculated using this response function in Section 2.8, were carefully checked against the results of [Kim *et al.*, 1994].

The $v_\parallel$ integrals are:

$$\int_0^\infty dv_\parallel e^{-(1+2i\tau)v_\parallel^2/2v_t^2 - i\tau z_\parallel v_\parallel/v_t} = \sqrt{2\pi} v_t \frac{e^{-\tau^2 z_\parallel^2/2(1+2i\tau)}}{\sqrt{1+2i\tau}}, \tag{2.60}$$

and

$$\int_0^\infty dv_\parallel v_\parallel^2 e^{-(1+2i\tau)v_\parallel^2/2v_t^2 - i\tau z_\parallel v_\parallel/v_t} = \sqrt{2\pi} v_t^3 \frac{e^{-\tau^2 z_\parallel^2/2(1+2i\tau)}}{(1+2i\tau)^{5/2}}(1+2i\tau-\tau^2 z_\parallel^2). \tag{2.61}$$

Putting it all together:

$$R_i = 1 + i\int_0^\infty d\tau\, e^{i\tau x} e^{-\tau^2 z_\parallel^2/2(1+2i\tau)} e^{-b/(1+i\tau)} I_0\left(\frac{b}{1+i\tau}\right)\left\{\frac{x - (1-\frac{3}{2}\eta_i)/\epsilon_n}{(1+i\tau)\sqrt{1+2i\tau}}\right. \tag{2.62}$$
$$\left. - \frac{\eta_i}{\epsilon_n}\left[\frac{1 - \frac{b}{1+i\tau} + \frac{b}{1+i\tau} I_1(\frac{b}{1+i\tau})/I_0\left(\frac{b}{1+i\tau}\right)}{(1+i\tau)^2\sqrt{1+2i\tau}}\right] - \frac{\eta_i}{\epsilon_n}\left[\frac{1+2i\tau-\tau^2 z_\parallel^2}{2(1+i\tau)(1+2i\tau)^{5/2}}\right]\right\},$$

Thus, the local toroidal response function is a rather complicated function, $R_i = R_i(x, z_\parallel, b, \epsilon_n, \eta)$. We are looking for closure approximations so the fluid equations

will closely match this response function. In this form (a one dimensional integral) the response function is easy to evaluate numerically, which we will be forced to do to find the optimal closure coefficients and to solve the local dispersion relation. The response function can be factored into three pieces, the first independent of ω_*, the second proportional to $1/\epsilon_n$, and the third proportional to η/ϵ_n. Since we will be interested in matching this kinetic response for all η and ϵ_n, we need to fit each of these pieces independently:

$$R_i = R_0 + R_1/\epsilon_n + R_2\eta/\epsilon_n, \tag{2.63}$$

where R_0, R_1, and R_2 are independent of η and ϵ_n:

$$R_0 = 1 + i\int_0^\infty d\tau\, e^{i\tau x} e^{-\tau^2 z_\parallel^2/2(1+2i\tau)} e^{-b/(1+i\tau)} I_0\left(\frac{b}{1+i\tau}\right)\left\{\frac{x}{(1+i\tau)\sqrt{1+2i\tau}}\right\}, \tag{2.64}$$

$$R_1 = -i\int_0^\infty d\tau\, e^{i\tau x} e^{-\tau^2 z_\parallel^2/2(1+2i\tau)} e^{-b/(1+i\tau)} I_0\left(\frac{b}{1+i\tau}\right)\left\{\frac{1}{(1+i\tau)\sqrt{1+2i\tau}}\right\} \tag{2.65}$$

$$R_2 = i\int_0^\infty d\tau\, e^{i\tau x} e^{-\tau^2 z_\parallel^2/2(1+2i\tau)} e^{-b/(1+i\tau)} I_0\left(\frac{b}{1+i\tau}\right)\left\{\frac{3/2}{(1+i\tau)\sqrt{1+2i\tau}}\right. \tag{2.66}$$

$$\left. -\frac{1-\frac{b}{1+i\tau}+\frac{b}{1+i\tau}I_1(\frac{b}{1+i\tau})/I_0(\frac{b}{1+i\tau})}{(1+i\tau)^2\sqrt{1+2i\tau}} - \frac{1+2i\tau-\tau^2 z_\parallel^2}{2(1+i\tau)(1+2i\tau)^{5/2}}\right\},$$

The response function of the fluid equations will also naturally factor into these three parts. In the purely toroidal limit ($k_\parallel = 0$), neglecting FLR ($b = 0$), these expressions simplify considerably, and can be written in terms of the usual plasma dispersion function [Biglari *et al.*, 1989]:

$$R_0 = 1 - \frac{x}{2} Z^2\left(\sqrt{\frac{x}{2}}\right) \tag{2.67}$$

$$R_1 = \frac{1}{2} Z^2\left(\sqrt{\frac{x}{2}}\right) \tag{2.68}$$

$$R_2 = \left(\frac{x}{2} - \frac{1}{2}\right) Z^2\left(\sqrt{\frac{x}{2}}\right) + \sqrt{\frac{x}{2}} Z\left(\sqrt{\frac{x}{2}}\right) \tag{2.69}$$

The resonant denominator in Eq. (2.56),

$$\omega - k_\parallel v_\parallel - \omega_d(v_\parallel^2 + v_\perp^2/2)/v_t^2 = 0,$$

can be written, by completing the square:

$$\frac{\omega}{\omega_d} + \frac{k_\parallel^2 v_t^2}{4\omega_d^2} = \left(\frac{k_\parallel v_t}{2\omega_d} + \frac{v_\parallel}{v_t}\right)^2 + \frac{v_\perp^2}{2v_t^2}. \tag{2.70}$$

The left hand side of Eq. (2.70) is negative, but the right hand side is positive for all v. Thus along the real ω axis, no particles are in resonance for $\omega < -k_\parallel^2 v_t^2/4\omega_d$, and R_i is purely real, as shown in Figs. 2.1 and 2.2. As $k_\parallel \to \infty$, this cutoff frequency moves to $-\infty$, and R_i approaches the slab limit response function.

We will also use the kinetic response function of other moments (not just density), which can be written in the following compact form in the $b = 0$ limit:

$$M_{j,k} = \int d^3v f v_\parallel^j (v_\perp^2/2)^k = -n_0 v_t^{2k+j} \frac{e\Phi}{T_0} \tilde{M}_{j,k} \tag{2.71}$$

$$\tilde{M}_{j,k} = \tilde{M}_{j,k}^{(0)} + \tilde{M}_{j,k}^{(1)}/\epsilon_n + \tilde{M}_{j,k}^{(2)}\eta/\epsilon_n \tag{2.72}$$

$$\tilde{M}_{j,k} = \frac{2^{j/2}}{\sqrt{\pi}} \frac{1+(-1)^j}{2} \Gamma(k+1)\Gamma(\frac{j+1}{2}) + i2^{-j/2} \int d\tau\, e^{i\tau x} \times \tag{2.73}$$

$$\left\{ \left[x - \frac{1}{\epsilon_n} + \frac{3}{2}\frac{\eta}{\epsilon_n} - \frac{\eta}{\epsilon_n}\frac{k+1}{1+i\tau} \right] \tilde{K}_j - \frac{\eta}{\epsilon_n} \tilde{K}_{j+2} \right\} \frac{\Gamma(k+1) e^{-\tau^2 z_\parallel^2/2(1+2i\tau)}}{(1+i\tau)^{k+1}(1+2i\tau)^{j+1/2}}$$

$$\tilde{K}_j = \frac{2^{j/2}(1+2i\tau)^{j+1/2}}{\sqrt{2\pi} v_t^{j+1}} e^{\tau^2 z_\parallel^2/2(1+2i\tau)} \int_{-\infty}^{\infty} dv_\parallel v_\parallel^j e^{-(1+2i\tau)v_\parallel^2/2v_t^2 - i\tau z_\parallel v_\parallel/v_t} \tag{2.74}$$

For the lowest few j's, we have:

$$\begin{aligned}
\tilde{K}_0 &= 1, \\
\tilde{K}_1 &= -i\tau z_\parallel, \\
\tilde{K}_2 &= 2(1+2i\tau) - \tau^2 z_\parallel^2, \\
\tilde{K}_3 &= \tau z_\parallel [-6i(1+2i\tau) + i\tau^2 z_\parallel^2)], \\
\tilde{K}_4 &= 12(1+2i\tau)^2 - 12\tau^2 z_\parallel^2 (1+2i\tau) + \tau^4 z_\parallel^4.
\end{aligned}$$

The odd $\tilde{K}_j$'s are proportional to odd powers of $z_\parallel$ (or $k_\parallel$), while the even $\tilde{K}_j$'s are proportional to even powers of $z_\parallel$. This will guide our choice of closure approximations in the next section.

2.5 General Closure

There are three places in the moment equations Eqs. (2.42)-(2.45) where closure approximations are needed (in addition to the FLR closures in Section 2.3): in the parallel terms $\nabla_\parallel r_{\parallel,\parallel}$ and $\nabla_\parallel r_{\parallel,\perp}$; in the toroidal terms $\omega_d(r_{\parallel,\parallel} + r_{\parallel,\perp})$, $\omega_d(r_{\parallel,\perp} + r_{\perp,\perp})$,

$\omega_d(s_{\parallel,\parallel}+s_{\parallel,\perp})$, and $\omega_d(s_{\parallel,\perp}+s_{\perp,\perp})$; and in the mirroring terms $r_{\parallel,\parallel}\nabla_\parallel \ln B$, $r_{\parallel,\perp}\nabla_\parallel \ln B$, and $r_{\perp,\perp}\nabla_\parallel \ln B$. For each, we make closure approximations designed to model the physical processes these terms represent.

The velocity dependence in the $k_\parallel v_\parallel$ parallel term introduces parallel phase mixing, leading to linear Landau damping. Consider a simple 1D kinetic equation with no $\mathbf{E}$ field:

$$\frac{\partial f}{\partial t} + v_\parallel \frac{\partial f}{\partial z} = 0. \tag{2.75}$$

The solution is simply $f(z, v_\parallel, t) = f(z - v_\parallel t, v_\parallel, t = 0)$. If we start with a Maxwellian perturbation in f,

$$f_0 = e^{ik_\parallel z} f_M = e^{ik_\parallel z} \frac{n_0}{\sqrt{2\pi v_t^2}} e^{-v_\parallel^2/2v_t^2}, \tag{2.76}$$

free streaming will cause moments of f to phase mix away. For example, the density is:

$$n = \int d^3v\, f = \frac{n_0}{\sqrt{2\pi v_t^2}} \int dv_\parallel\, e^{ik_\parallel(z - v_\parallel t)} e^{-v_\parallel^2/2v_t^2} = n_0 e^{ik_\parallel z} e^{-k_\parallel^2 v_t^2 t^2/2}. \tag{2.77}$$

To model this process, we need to introduce damping proportional to $|k_\parallel| v_t$ into our fluid equations. Thus, for the parallel closures, we choose [Hammett and Perkins, 1990; Dorland and Hammett, 1993]:

$$r_{\parallel,\parallel} = 3(2p_\parallel - n) + \beta_\parallel T_\parallel - i\sqrt{2} D_\parallel \frac{|k_\parallel|}{k_\parallel} q_\parallel, \tag{2.78}$$

$$r_{\parallel,\perp} = p_\parallel + p_\perp - n - i\sqrt{2} D_\perp \frac{|k_\parallel|}{k_\parallel} q_\perp, \tag{2.79}$$

where $\beta_\parallel = (32 - 9\pi)/(3\pi - 8)$, $D_\parallel = 2\sqrt{\pi}/(3\pi - 8)$, and $D_\perp = \sqrt{\pi}/2$. With this closure, the fluid equations reproduce the linear kinetic behavior quite well in the slab limit, as shown in [Hammett and Perkins, 1990; Dorland and Hammett, 1993].

Similarly, the velocity dependence of the ∇B and curvature drifts introduces phase mixing. In this case the damping rate is different, since the toroidal drifts depend on $v_\parallel^2$ and $v_\perp^2/2$. Now consider only the phase mixing due to the toroidal drifts:

$$\frac{\partial f}{\partial t} + v_d \frac{\partial f}{\partial y} = 0, \tag{2.80}$$

$$v_d = v_{d0}\frac{v_\parallel^2 + v_\perp^2/2}{v_t^2}, \qquad\qquad v_{d0} = \frac{\rho v_t}{R}.$$

The solution is $f(y, v_\parallel, v_\perp, t) = f(y - v_d t, v_\parallel, v_\perp, t = 0)$. Starting with a Maxwellian perturbation in f,

$$f_0 = e^{ik_y y} f_M = e^{ik_y y}\frac{n_0}{(2\pi v_t^2)^{3/2}} e^{-(v_\parallel^2+v_\perp^2)/2v_t^2}, \tag{2.81}$$

free streaming will again cause moments of f to phase mix away. For example, the density is:

$$n = \int d^3v\, f = \frac{n_0}{(2\pi v_t^2)^{3/2}} 2\pi \int dv_\parallel dv_\perp v_\perp e^{ik_y y - v_{d0}[v_\parallel^2/v_t^2 - v_\perp^2/2v_t^2)t]} e^{-(v_\parallel^2+v_\perp^2)/2v_t^2}$$

$$= \frac{n_0 e^{ik_y y}}{\sqrt{1 + ik_y v_{d0} t}(1 + ik_y v_{d0} t/2)}. \tag{2.82}$$

To capture this toroidal phase mixing, damping proportional to $|k_y| v_{d0} = |\omega_d|$ must be introduced into the fluid equations, but with complex closure coefficients to get the phase shift in Eq. (2.82).

The toroidal closure terms enter in the combinations $r_{\parallel,\parallel} + r_{\parallel,\perp}$, $r_{\parallel,\perp} + r_{\perp,\perp}$, $s_{\parallel,\parallel} + s_{\parallel,\perp}$, and $s_{\parallel,\perp} + s_{\perp,\perp}$. Expanding the general moment response functions Eq. (2.73) for small $k_\parallel$, all the odd j moments have $\mathcal{O}(k_\parallel)$ corrections, while the even j moments have $\mathcal{O}(k_\parallel^2)$ corrections. Thus in our closure approximations for the toroidal terms, we close the even moments $r_{\parallel,\parallel} + r_{\parallel,\perp}$ and $r_{\parallel,\perp} + r_{\perp,\perp}$ in terms of the lower even moments (n, $p_\parallel$, and $p_\perp$), and the odd moments $s_{\parallel,\parallel} + s_{\parallel,\perp}$ and $s_{\parallel,\perp} + s_{\perp,\perp}$ in terms of the lower odd moments ($u_\parallel$, $q_\parallel$, and $q_\perp$), to preserve this small $k_\parallel$ behavior. At large $k_\parallel$ (the slab limit) the response function is primarily determined by the parallel closures, and the toroidal closure approximations are subdominant. In addition, we break the r and s closures into dissipative and Maxwellian pieces (the terms that would arise if F was exactly Maxwellian). The Maxwellian parts are $r_{\parallel,\parallel} = 3p_\parallel^2/n$, $r_{\parallel,\perp} = p_\parallel p_\perp/n$, $r_{\perp,\perp} = 2p_\perp^2/n$, and $s_{\parallel,\parallel} = s_{\parallel,\perp} = s_{\perp,\perp} = 0$. Linearizing and normalizing, these become $r_{\parallel,\parallel} = 6p_\parallel - 3n$, $r_{\parallel,\perp} = p_\parallel + p_\perp - n$, and $r_{\perp,\perp} = 4p_\perp - 2n$. Guided by the discussion above, we choose dissipative pieces proportional to $|\omega_d|/\omega_d$. Thus in the toroidal terms, combining the Maxwellian and dissipative pieces, we choose:

$$r_{\parallel,\parallel} + r_{\parallel,\perp} \;=\; 7p_\parallel + p_\perp - 4n - 2i\frac{|\omega_d|}{\omega_d}(\nu_1 T_\parallel + \nu_2 T_\perp) \tag{2.83}$$

$$r_{\parallel,\perp} + r_{\perp,\perp} = p_\parallel + 5p_\perp - 3n - 2i\frac{|\omega_d|}{\omega_d}(\nu_3 T_\parallel + \nu_4 T_\perp) \quad (2.84)$$

$$s_{\parallel,\parallel} + s_{\parallel,\perp} = -i\frac{|\omega_d|}{\omega_d}(\nu_5 u_\parallel + \nu_6 q_\parallel + \nu_7 q_\perp) \quad (2.85)$$

$$s_{\parallel,\perp} + s_{\perp,\perp} = -i\frac{|\omega_d|}{\omega_d}(\nu_8 u_\parallel + \nu_9 q_\parallel + \nu_{10} q_\perp) \quad (2.86)$$

Each closure coefficient has both a dissipative and non-dissipative piece, $\nu = \nu_r + i\nu_i|\omega_d|/\omega_d$. This choice is motivated by [Waltz *et al.*, 1992]. Making the dissipative parts of the r closures only depend on $T_\parallel$ and $T_\perp$ ensures that the fluid response will match the kinetic response at $\omega/\omega_d = 0$ in the $k_\parallel = 0$ limit.

The toroidal closure coefficients $\nu_1 - \nu_{10}$ are chosen so the response function of the fluid equations closely approximates kinetic response function, Eq. (2.62). In the local limit with $b = 0$ and $\nabla_\parallel B = 0$, and inserting the closure approximations above, the fluid equations Eqs. (2.40-2.45) can be written in matrix form, using $g \equiv \omega_d/\omega = 1/x$ and $k = k_\parallel/\omega$, and assuming $\omega_d > 0$ to simplify notation:

$$M = \begin{bmatrix} 1 & -k & -g & -g & \cdots & 0 & 0 \\ 0 & 1-4g & -k & 0 & & -g & -g \\ g(4-2i\nu_1-2i\nu_2) & -3k & 1-g(7-2i\nu_1) & -g(1-2i\nu_2) & & -k & 0 \\ g(3-2i\nu_3-2i\nu_4) & -k & -g(1-2i\nu_3) & 1-g(5-2i\nu_4) & & 0 & -k \\ (3+\beta)k & -g(6-i\nu_5) & -(3+\beta)k & 0 & & 1+i\sqrt{2}D_\parallel k+g(3+i\nu_6) & g(3+i\nu_7) \\ k & -g(1-i\nu_8) & 0 & -k & & g(1+i\nu_9) & 1+i\sqrt{2}D_\perp k+g(1+i\nu_{10}) \end{bmatrix}$$

$$M\begin{bmatrix} n \\ u_\parallel \\ p_\parallel \\ p_\perp \\ q_\parallel \\ q_\perp \end{bmatrix} = \begin{bmatrix} 2 \\ k/g \\ 4 \\ 3 \\ 0 \\ 0 \end{bmatrix} g\Phi + \begin{bmatrix} -1 \\ 0 \\ -1 \\ -1 \\ 0 \\ 0 \end{bmatrix} \frac{g}{\epsilon_n}\Phi + \begin{bmatrix} 0 \\ 0 \\ -1 \\ -1 \\ 0 \\ 0 \end{bmatrix} \frac{g\eta}{\epsilon_n}\Phi \quad (2.87)$$

Thus, the response functions of the fluid equations also naturally factor into the form Eq. (2.63). Because this set of equations is rather complicated, to determine the toroidal fluid response functions we solve for n and $p_\perp$ by numerically

row reducing the matrix M. In [WALTZ *et al.*, 1992], the fluid and kinetic response functions were compared only in the $\omega_* = 0$ and $\eta = 0$ limit. In the slab limit, determining the closure coefficients in the $\omega_* = 0$ and $\eta = 0$ limit (R_0) also gave an equally good fit for the ω_* and η pieces (R_1 and R_2), but in the toroidal case this is not automatic. In addition, in [WALTZ *et al.*, 1992] the toroidal closure coefficients were matched at $k_\parallel = 0$, and good agreement for $k_\parallel \neq 0$ is not guaranteed (although as $k_\parallel \to \infty$ the slab limit is recovered and the agreement will again be good). In fact, if the toroidal terms are closed in the purely toroidal limit ($k_\parallel = 0$), the toroidal closure terms in the odd moment equations drop out. This led to singular behavior of the response function for the closure in [WALTZ *et al.*, 1992] at some non-zero $k_\parallel$, since the $\omega_d(q_\parallel + q_\perp)$ term in the parallel velocity equation was dropped. This was corrected in the addendum to that paper.

Therefore, special care must be taken find toroidal closure coefficients which simultaneously provide a good fit to the kinetic response function for all three parts of the response function, for all $k_\parallel$. Because both fluid and kinetic response functions are complicated with finite $k_\parallel$, we choose the closure coefficients numerically, by minimizing the difference between the kinetic and fluid response functions over a range of $k_\parallel$'s simultaneously, but in the $b = 0$ limit. We use Powell's method (an efficient multidimensional minimization method) [PRESS *et al.*, 1986] to adjust the coefficients $\nu_1 - \nu_{10}$ until the error between the kinetic and fluid response functions along the real x axis is minimized. If R has no poles in the upper-half x plane, matching along the real axis guarantees that the fluid R will also match the kinetic R in the upper-half x plane. Since we are primarily interested in accurately modeling the growth rates of unstable modes, the errors in the lower half plane are probably not important, as long as we do have damped modes in the system. The best fit between the kinetic and fluid R's was found using 12 $k_\parallel$'s evenly spaced from $z_\parallel = 0$ to 4.2, over the range of x where the kinetic response function is changing most rapidly, $-8 < x < 16$ at $z_\parallel = 0$ and $-14 < x < 22$ at $z_\parallel = 4.2$, with 100 grid points in x. To the error in the density response function, we also add 1/100 the error between the kinetic and fluid $p_\perp$ responses, since n is most important for the local dispersion relation, but $p_\perp$ enters the linear dispersion relation from FLR effects. While an excellent fit to n is obtained, it is difficult to simultaneously match the $p_\perp$ response for intermediate $k_\parallel$'s. We find $\nu_1 = (2.019, -1.620)$, $\nu_2 = (0.433, 1.018)$, $\nu_3 = (-0.256, 1.487)$, $\nu_4 =$

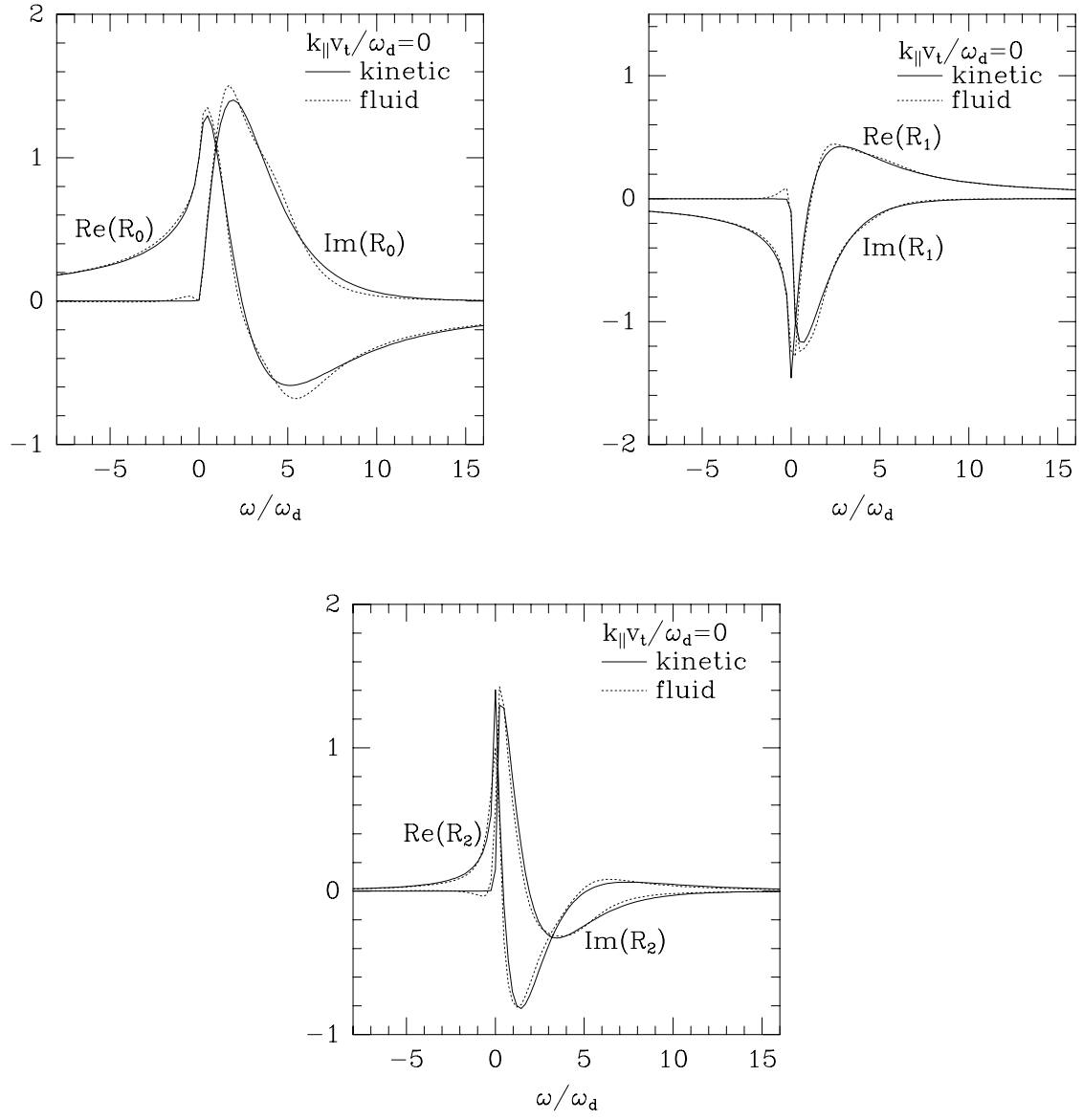

Figure 2.1: Kinetic and fluid toroidal response functions in the purely toroidal limit, R_0, R_1, and R_2, with $b = 0$ and $k_\parallel = 0$.

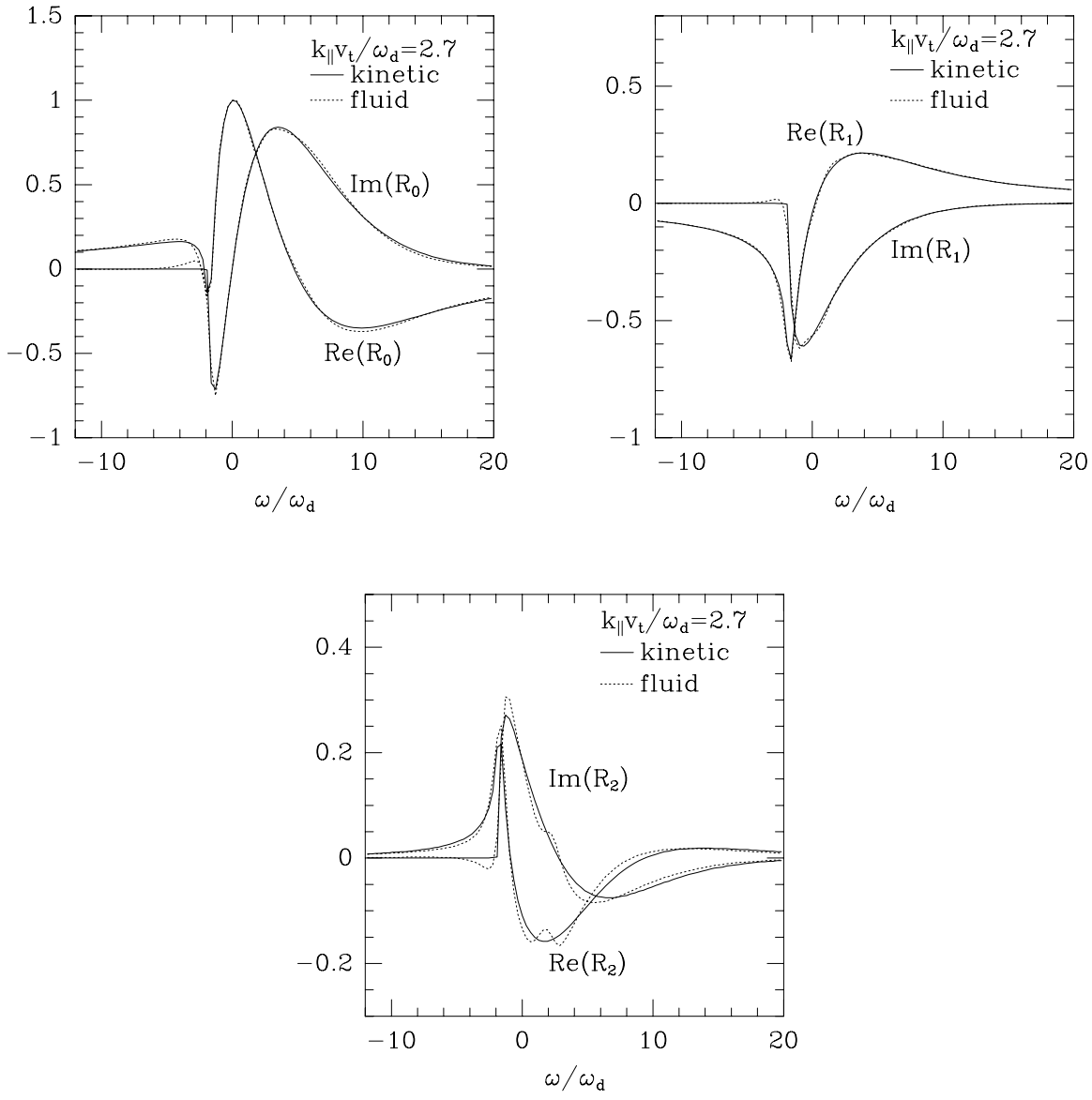

Figure 2.2: Kinetic and fluid toroidal response functions in the mixed toroidal/slab limit, R_0, R_1, and R_2, with $b = 0$ and $k_\parallel v_t/\omega_d = 2.7$.

$(-0.070, -1.382)$, $\nu_5 = (-8.927, 12.649)$, $\nu_6 = (8.094, 12.638)$, $\nu_7 = (13.720, 5.139)$, $\nu_8 = (3.368, -8.110)$, $\nu_9 = (1.974, -1.984)$, and $\nu_{10} = (8.269, 2.060)$. These are an improvement over the closure coefficients in [HAMMETT *et al.*, 1993]. The fit between the kinetic and fluid response functions is excellent, as shown in Figs. 2.1 and 2.2. The fluid equations give a rational function approximation (a ratio of polynomials) to the kinetic response function, and cannot capture the branch cut at $\omega/\omega_d = -k_\parallel^2 v_t^2/4\omega_d^2$ exactly (see Eq. (2.70)), but this set of closure approximations provides a reasonable fit to this sharp transition.

Finally, we have to close the mirroring terms, introduced by the $\mu\hat{\mathbf{b}} \cdot \nabla B$ terms in the gyrokinetic equation. These terms incorporate trapped particle effects, reproducing the CGL [CHEW *et al.*, 1956] pressure balance equation. They are also important to model the damping of poloidal flows by magnetic pumping. Since these terms introduce no new dissipative processes, we take Maxwellian closures:

$$r_{\parallel,\parallel} = 6p_\parallel - 3n, \tag{2.88}$$

$$r_{\parallel,\perp} = p_\parallel + p_\perp - n, \tag{2.89}$$

$$r_{\perp,\perp} = 4p_\perp - 2n. \tag{2.90}$$

While this is not the ultimate set of closure approximations, the resulting fluid equations provide a very accurate model of the physics underlying ion dynamics in toroidal plasmas. More complicated closure approximations could certainly be developed which are more accurate, but the relative simplicity of the closures used here afford a tractable and sufficiently accurate model.

2.6 Final Equations

We arrive at the six moment toroidal gyrofluid equations by inserting the closures discussed in the previous section into the moment equations, Eqs. (2.40)-(2.45), with the nonlinear terms given by Eqs. (2.46)-(2.51). Specifically, we use the parallel phase mixing closures in Eqs. (2.78)-(2.79), the toroidal phase mixing closures in Eqs. (2.83)-(2.86), and Maxwellian closures for the mirroring terms, Eqs. (2.88)-(2.90). In addition, we add the collision terms obtained by integrating Eq. (2.6) over velocity space. We will also refer to this set of equations as the "4+2" model,

since it evolves 4 parallel moments and 2 perpendicular moments.

$$\begin{aligned}
\frac{dn}{dt} &+ [\frac{1}{2}\hat{\nabla}_\perp^2 \mathbf{v}_\Psi]\cdot\nabla T_\perp + B\nabla_\parallel \frac{u_\parallel}{B} - \left(1+\frac{\eta_\perp}{2}\hat{\nabla}_\perp^2\right) i\omega_* \Psi \qquad (2.91)\\
&+ \left(2+\frac{1}{2}\hat{\nabla}_\perp^2\right) i\omega_d \Psi + i\omega_d(p_\parallel + p_\perp) = 0,\\
\frac{du_\parallel}{dt} &+ [\frac{1}{2}\hat{\nabla}_\perp^2 \mathbf{v}_\Psi]\cdot\nabla q_\perp + B\nabla_\parallel \frac{p_\parallel}{B} + \nabla_\parallel \Psi + \left(p_\perp + \frac{1}{2}\hat{\nabla}_\perp^2 \Psi\right)\nabla_\parallel \ln B \qquad (2.92)\\
&+ i\omega_d(q_\parallel + q_\perp + 4u_\parallel) = 0,\\
\frac{dp_\parallel}{dt} &+ [\frac{1}{2}\hat{\nabla}_\perp^2 \mathbf{v}_\Psi]\cdot\nabla T_\perp + B\nabla_\parallel \frac{q_\parallel + 3u_\parallel}{B} + 2(q_\perp + u_\parallel)\nabla_\parallel \ln B \qquad (2.93)\\
&- \left(1+\eta_\parallel + \frac{\eta_\perp}{2}\hat{\nabla}_\perp^2\right) i\omega_* \Psi + \left(4+\frac{1}{2}\hat{\nabla}_\perp^2\right) i\omega_d \Psi + i\omega_d(7p_\parallel + p_\perp - 4n)\\
&+ 2|\omega_d|(\nu_1 T_\parallel + \nu_2 T_\perp) = -\frac{2}{3}\nu_{ii}(p_\parallel - p_\perp),\\
\frac{dp_\perp}{dt} &+ [\frac{1}{2}\hat{\nabla}_\perp^2 \mathbf{v}_\Psi]\cdot\nabla p_\perp + [\hat{\hat{\nabla}}_\perp^2 \mathbf{v}_\Psi]\cdot\nabla T_\perp + B^2\nabla_\parallel \frac{q_\perp + u_\parallel}{B^2} \qquad (2.94)\\
&- \left[1+\frac{1}{2}\hat{\nabla}_\perp^2 + \eta_\perp\left(1+\frac{1}{2}\hat{\nabla}_\perp^2 + \hat{\hat{\nabla}}_\perp^2\right)\right] i\omega_* \Psi + \left(3+\frac{3}{2}\hat{\nabla}_\perp^2 + \hat{\hat{\nabla}}_\perp^2\right) i\omega_d \Psi\\
&+ i\omega_d(5p_\perp + p_\parallel - 3n) + 2|\omega_d|(\nu_3 T_\parallel + \nu_4 T_\perp) = \frac{1}{3}\nu_{ii}(p_\parallel - p_\perp),\\
\frac{dq_\parallel}{dt} &+ (3+\beta_\parallel)\nabla_\parallel T_\parallel + \sqrt{2}D_\parallel |k_\parallel| q_\parallel + i\omega_d(-3q_\parallel - 3q_\perp + 6u_\parallel) \qquad (2.95)\\
&+ |\omega_d|(\nu_5 u_\parallel + \nu_6 q_\parallel + \nu_7 q_\perp) = -\nu_{ii} q_\parallel,\\
\frac{dq_\perp}{dt} &+ [\frac{1}{2}\hat{\nabla}_\perp^2 \mathbf{v}_\Psi]\cdot\nabla u_\parallel + [\hat{\hat{\nabla}}_\perp^2 \mathbf{v}_\Psi]\cdot\nabla q_\perp + \nabla_\parallel\left(T_\perp + \frac{1}{2}\hat{\nabla}_\perp^2 \Psi\right) \qquad (2.96)\\
&+ \sqrt{2}D_\perp |k_\parallel| q_\perp + \left(p_\perp - p_\parallel + \hat{\hat{\nabla}}_\perp^2 \Psi - \frac{1}{2}\hat{\nabla}_\perp^2 \Psi\right)\nabla_\parallel \ln B\\
&+ i\omega_d(-q_\parallel - q_\perp + u_\parallel) + |\omega_d|(\nu_8 u_\parallel + \nu_9 q_\parallel + \nu_{10} q_\perp) = -\nu_{ii} q_\perp.
\end{aligned}$$

The main $\mathbf{E}\times\mathbf{B}$ nonlinearities have been absorbed in the total time derivative $d/dt = \partial/\partial t + \mathbf{v}_\Psi\cdot\nabla$. In the slab limit ($\omega_d = \nabla_\parallel \ln B = 0$) these equations reduce to Eqs. (56)-(61) of [Dorland and Hammett, 1993]. The quasineutrality constraint is:

$$n_e = \frac{n}{1+b/2} - \frac{bT_\perp}{2(1+b/2)^2} + (\Gamma_0 - 1)\Phi. \qquad (2.97)$$

When the electrons are assumed to be adiabatic,

$$n_e = \tau(\Phi - \langle\Phi\rangle), \qquad (2.98)$$

where $\tau = T_{i0}/T_{e0}$ and $\langle\Phi\rangle$ is a flux surface average. This will be discussed in Section 5.3.

This constitutes a fairly complicated set of fluid equations compared to those usually used in plasma physics. A somewhat simpler four moment model is described below, and it is worth justifying the complication of the six moment model. In principle, the six moment model is more appealing because as more moments are retained, more details of the distribution function are accurately described. On more pragmatic grounds, the six moment model provides a significantly improved fit to the kinetic response function, and is necessary for quantitative accuracy in linear growth rates and mode structures, especially near marginal stability. The six moment model is also required to capture the destabilization from trapped ion effects, which become important in the long wavelength regime. Finally, six moments may be required to obtain accurate damping rates of poloidal flows from magnetic pumping. Magnetic pumping arises from parallel flow damping, and since no closure approximations appear in Eq. (2.92), the $u_\parallel$ equation is an exact moment of the gyrokinetic equation to $\mathcal{O}(b)$. This is not the case for the simpler four moment model discussed below. Magnetic pumping rates from this six moment model are calculated in Section 5.3.

A variation of these equations was used in [HAMMETT *et al.*, 1993] where $|k_\parallel|q_\parallel$ in Eq. (2.95) was replaced by $B|k_\parallel|(q_\parallel/B)$ and where $|k_\parallel|q_\perp$ in Eq. (2.96) was replaced by $B^2|k_\parallel|(q_\perp/B^2)$, i.e. $|k_\parallel|$ acted on $q_\perp/B^2$, not just $q_\perp$. However, it was found that this leads to a weakly growing mode even in the $\omega_d = \omega_* = \eta = 0$ limit which should be stable (a bumpy cylinder limit). Switching to the present form of the parallel closures removed this spurious instability.

2.7 Four Moment Model

We present here a simpler and slightly less accurate gyrofluid model which only evolves four moments: n, $u_\parallel$, $p_\parallel$, and $p_\perp$. We will also refer to this set of equations as the "3+1" model, since it evolves three parallel moments and one perpendicular moment. In this case, since we are not evolving $q_\parallel$ and $q_\perp$, instead of closing the toroidal s terms with Eqs. (2.85) and (2.86), we need to close the $\omega_d(q_\parallel + q_\perp)$ term

in the parallel velocity equation:

$$q_\parallel + q_\perp = -2i\frac{|\omega_d|}{\omega_d}\nu_5 u_\parallel. \tag{2.99}$$

We still use the toroidal r closures in Eqs. (2.83) and (2.84), but with new closure coefficients. In addition, we use the parallel closures of [HAMMETT and PERKINS, 1990; DORLAND and HAMMETT, 1993], extended to include collisions as well as collisionless phase mixing:

$$q_\parallel = -\frac{3+\beta_\parallel}{\sqrt{2}D_\parallel|k_\parallel|+\nu_{ii}}ik_\parallel T_\parallel \tag{2.100}$$

$$q_\perp = -\frac{1}{\sqrt{2}D_\perp|k_\parallel|+\nu_{ii}}ik_\parallel\left(T_\perp+\frac{1}{2}\hat{\nabla}_\perp^2\Psi\right) \tag{2.101}$$

These are essentially the high $k_\parallel$ and/or high ν_{ii} limit Eqs. (2.95) and (2.96), keeping only the slab terms.

We again use the method described in Section 2.5 to minimize the error between the fluid and kinetic local response functions to determine the toroidal closure coefficients $\nu_1-\nu_5$. The best fit is $\nu_1=(1.232,0.437)$, $\nu_2=(-0.912,0.362)$, $\nu_3=(-1.164,0.294)$, $\nu_4=(0.478,-1.926)$, and $\nu_5=(0.515,-0.958)$.

Inserting these q closures into Eqs. (2.40)-(2.43), using the nonlinear FLR terms in Eqs. (2.46)-(2.49) without the $q_\perp$ part of Eq. (2.47), and dropping the $q_\parallel$ and $q_\perp$ mirroring terms ($q_\parallel=q_\perp=0$ for a Maxwellian), the dynamical equations are:

$$\begin{aligned}\frac{dn}{dt} &+ [\frac{1}{2}\hat{\nabla}_\perp^2\mathbf{v}_\Psi]\cdot\nabla T_\perp + B\nabla_\parallel\frac{u_\parallel}{B} - \left(1+\frac{\eta_\perp}{2}\hat{\nabla}_\perp^2\right)i\omega_*\Psi \\ &+ \left(2+\frac{1}{2}\hat{\nabla}_\perp^2\right)i\omega_d\Psi + i\omega_d(p_\parallel+p_\perp)=0,\end{aligned} \tag{2.102}$$

$$\begin{aligned}\frac{du_\parallel}{dt} &+ B\nabla_\parallel\frac{p_\parallel}{B} + \nabla_\parallel\Psi + \left(p_\perp+\frac{1}{2}\hat{\nabla}_\perp^2\Psi\right)\nabla_\parallel\ln B + 4i\omega_d u_\parallel \\ &+ 2|\omega_d|\nu_5 u_\parallel = 0,\end{aligned} \tag{2.103}$$

$$\begin{aligned}\frac{dp_\parallel}{dt} &+ [\frac{1}{2}\hat{\nabla}_\perp^2\mathbf{v}_\Psi]\cdot\nabla T_\perp + \frac{(3+\beta_\parallel)k_\parallel^2 T_\parallel}{\sqrt{2}D_\parallel|k_\parallel|+\nu_{ii}} + 3\nabla_\parallel u_\parallel - u_\parallel\nabla_\parallel\ln B \\ &- \left(1+\eta_\parallel+\frac{\eta_\perp}{2}\hat{\nabla}_\perp^2\right)i\omega_*\Psi + \left(4+\frac{1}{2}\hat{\nabla}_\perp^2\right)i\omega_d\Psi + i\omega_d(7p_\parallel+p_\perp-4n) \\ &+ 2|\omega_d|(\nu_1 T_\parallel+\nu_2 T_\perp) = -\frac{2}{3}\nu_{ii}(p_\parallel-p_\perp),\end{aligned} \tag{2.104}$$

$$\begin{aligned}
\frac{dp_\perp}{dt} &+ [\frac{1}{2}\hat{\nabla}_\perp^2 \mathbf{v}_\Psi] \cdot \nabla p_\perp + [\hat{\hat{\nabla}}_\perp^{\,2} \mathbf{v}_\Psi] \cdot \nabla T_\perp + \frac{k_\parallel^2}{\sqrt{2} D_\perp |k_\parallel| + \nu_{ii}} (T_\perp + \frac{1}{2}\hat{\nabla}_\perp^2 \Psi) \\
&+ B^2 \nabla_\parallel \frac{u_\parallel}{B^2} - \left[1 + \frac{1}{2}\hat{\nabla}_\perp^2 + \eta_\perp \left(1 + \frac{1}{2}\hat{\nabla}_\perp^2 + \hat{\hat{\nabla}}_\perp^{\,2} \right) \right] i\omega_* \Psi \qquad (2.105) \\
&+ \left(3 + \frac{3}{2}\hat{\nabla}_\perp^2 + \hat{\hat{\nabla}}_\perp^{\,2} \right) i\omega_d \Psi + i\omega_d (5p_\perp + p_\parallel - 3n) + 2|\omega_d| (\nu_3 T_\parallel + \nu_4 T_\perp) \\
&= \frac{1}{3}\nu_{ii}(p_\parallel - p_\perp).
\end{aligned}$$

The quasineutrality constraint, Eq. (2.97), is unchanged for this model.

2.8 Linear Benchmarks

In this section the accuracy of the toroidal gyrofluid equations is demonstrated by comparing with linear kinetic theory, using adiabatic electrons. We first test the toroidal gyrofluid equations against kinetic theory in the local limit, where $k_\parallel$ and ω_d are treated as constants. The eigenfrequencies are determined by finding roots of the local dispersion relation with adiabatic electrons, $R_i = -\tau$, where the kinetic R_i is calculated by numerically evaluating the integrals Eq. (2.63) and the fluid R_i is calculated by numerically row reducing the matrix equation in Eq. (2.87), with additional FLR terms on the right hand side if b is non-zero. In the local limit, we ignore the $\nabla_\parallel \ln B$ terms in the gyrofluid equations and ignore the modulation of $v_\parallel$ along a particle's orbit in the kinetic response.

Fig. 2.3 shows the kinetic and gyrofluid growth rates in the purely toroidal limit ($k_\parallel = 0$), with $b = 0$, for the parameters of Fig. 5a of [Waltz *et al.*, 1992], where $\tau = 1$, $\eta_i = 1$, 1.5, 2, and 3, varying ϵ_n. The four moment model in Section 2.7 reproduces the stable low ϵ_n regime better than the four moment model presented in [Waltz *et al.*, 1992] (which used different closure coefficients). The six moment equations provide much better agreement with kinetic theory, but are slightly off for low η_i, near marginal stability.

Fig. 2.4 shows a comparison in the local limit for $k_\parallel \neq 0$, the the mixed toroidal/slab limit. We use the parameters of [Dong *et al.*, 1992] Fig. 3, where $\eta_i = 1.5, 2, 3$, $\epsilon_n = 0.2$, and we choose $k_\parallel L_n = L_n/qR = 0.1$, using the normal connection length for the mode width $L_\parallel \sim qR$, and $q = 2$. The linear growth rates

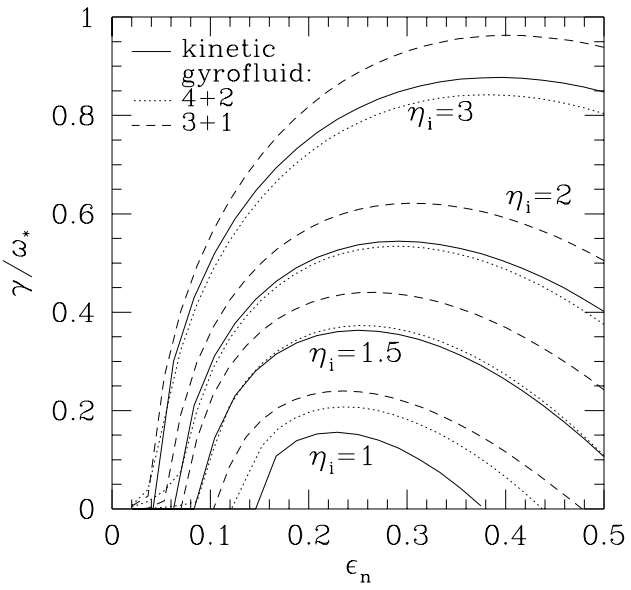

Figure 2.3: Comparison of local linear growth rates from the (4+2) and (3+1) toroidal gyrofluid equations vs. kinetic theory in the toroidal limit, with $k_\parallel = 0$ and $b = 0$. The four moment equations in Section 2.7 reproduce the stable low ϵ_n regime better than the four moment model in [Waltz *et al.*, 1992] but is slightly less accurate at large ϵ_n. The six moment equations are much more accurate, and are quite good for $\eta_i > 1$, away from marginal stability.

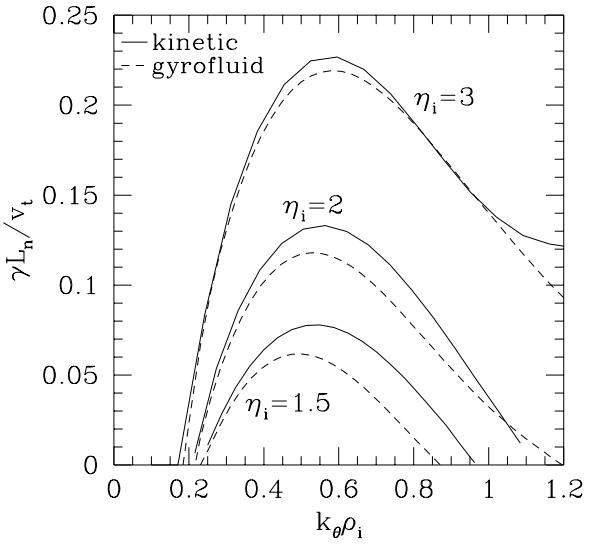

Figure 2.4: Local growth rates from the six moment toroidal gyrofluid equations compared with kinetic theory, now in the mixed toroidal/slab limit with $k_\parallel = 0.1$ and $\epsilon_n = 0.2$. The toroidal gyrofluid equations again provide a very accurate model of the fully kinetic results.

from the six moment toroidal gyrofluid model and kinetic theory are shown vs. $k_\theta \rho_i$. The six moment toroidal gyrofluid equations provide an accurate description of the full kinetic behavior. Both the growth rate and real frequency of the toroidal ITG mode vary roughly as $\gamma, \omega_r \propto k_\theta \rho_i$ at long wavelengths. As $k_\theta \rho_i$ decreases, $|\omega| = \sqrt{\gamma^2 + \omega_r^2}$ decreases, and the stabilizing effect of parallel Landau damping becomes more important. When $|\omega| \sim k_\parallel v_{ti}$, the mode is stabilized, producing the long wavelength cutoff at $k_\theta \rho_i \propto k_\parallel L_n \propto L_n / qR$.

Now we move on to nonlocal comparisons with kinetic theory. We will compare with fully kinetic calculations in the circular flux surface equilibrium, as described in Section 4.6. Linearly, the coordinate system in Chapter 4 is equivalent to the ballooning representation, so we compare with the ballooning calculations of [Dong *et al.*, 1992] and [Xu and Rosenbluth, 1991]. Nonlocally, we evolve the eigenmode structure along the field line coordinate θ, so a range of $k_\parallel$'s are coupled for each eigenmode. The θ coordinate described in Chapter 4 is the "extended ballooning angle" in the ballooning representation. In these nonlocal calculations,

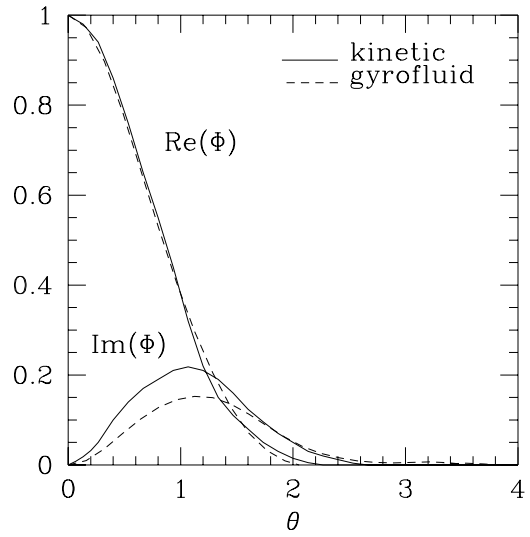

Figure 2.5: Linear nonlocal eigenfunction comparison with the fully kinetic calculations of [Dong *et al.*, 1992]. The coordinate along the field line, θ, is equivalent to the "extended ballooning angle."

both ω_d and $k_\perp$ vary along the field line, as given by Eqs. (4.44) and (4.42). The θ dependence of ω_d describes the effects of the good and bad curvature regions, and the θ dependence of $k_\perp$ comes from the fact that as one moves along the field line, the mode twists, and $k_\perp$ increases. For the comparison with [DONG *et al.*, 1992], we neglect trapped particle effects by turning off the $\nabla_\parallel \ln B$ terms. In circular flux surface geometry, $B = B_0 R_0/R = B_0/(1+\epsilon\cos\theta)$, so setting $\epsilon = 0$ removes the $\nabla_\parallel \ln B$ mirroring terms. As in [DONG *et al.*, 1992], we also neglect collisions and assume adiabatic electrons. All of the results compared in this section will only look at modes with $\theta_0 = 0$, i.e. those centered in the bad curvature region, since they are typically the most unstable and most kinetic calculations only focus on these modes. The growth rate spectrum for $\theta_0 \neq 0$ is discussed in Chapter 5, and has important implications for the anisotropic fluctuation spectra seen in our nonlinear simulations and in experimental fluctuation measurements in tokamaks. Fig. 2.5 shows the eigenfunction from the fully kinetic integral calculation of [DONG *et al.*, 1992] and from the 4+2 toroidal gyrofluid equations for the parameters in Fig. 2(c) of [DONG *et al.*, 1992], $\eta_i = 3$, $\epsilon_n = 0.2$, $q = 2$, $\hat{s} = 1$, $k_\theta \rho_i = 0.53$, and $\tau = 1$. The

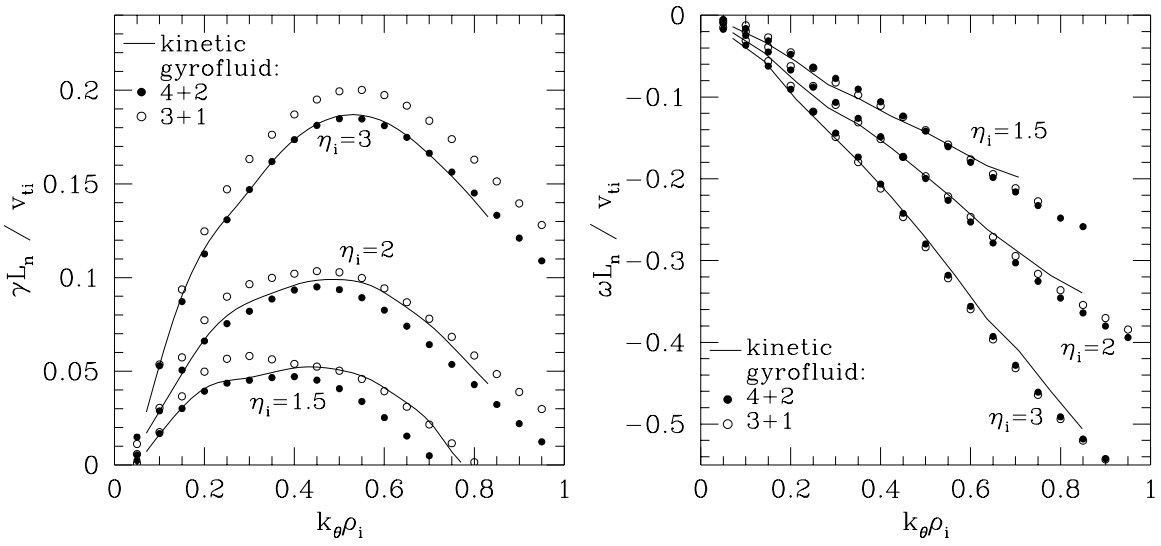

Figure 2.6: Nonlocal linear growth rate and real frequency comparison between the toroidal gyrofluid equations and kinetic theory, for the four moment and six moment models. The six moment model provides excellent agreement with fully kinetic theory, especially for $k_\theta \rho_i < 1/2$.

"ballooning" mode structure along the field line shown in Fig. 2.5 is determined by the θ dependence of both ω_d and $k_\perp$. The mode is primarily localized near $\theta = 0$ in the bad curvature region. Landau damping is strongly stabilizing for high $k_\parallel$, so the the most unstable modes have broad mode structures along the field line. Minimizing $k_\parallel$ while simultaneously localizing the modes in the bad curvature region leads to mode structures with $k_\parallel \approx 1/qR$, with large amplitude at the outer midplane and smaller amplitude at the inner midplane. Further along the field line (i.e. away from $\theta = 0$), magnetic shear causes $k_\perp$ to increase, which leads to FLR stabilization at large $\theta - \theta_0$. This magnetic shear stabilization through FLR effects keeps the mode amplitude small in bad curvature regions further along the field line, e.g. at $\theta = 2\pi$. When $\hat{s}$ or $k_\theta \rho_i$ are small, this magnetic shear effect is weaker, and the eigenfunctions get broader.

Fig. 2.6 compares the kinetic and fluid growth rates and real frequencies for the parameters of Fig. 3 in [DONG *et al.*, 1992]: $\eta_i = 1.5$, 2, and 3, $\epsilon_n = 0.2$, $q = 2$, $\hat{s} = 1$, and $\tau = 1$. The agreement between the 4+2 gyrofluid equations and

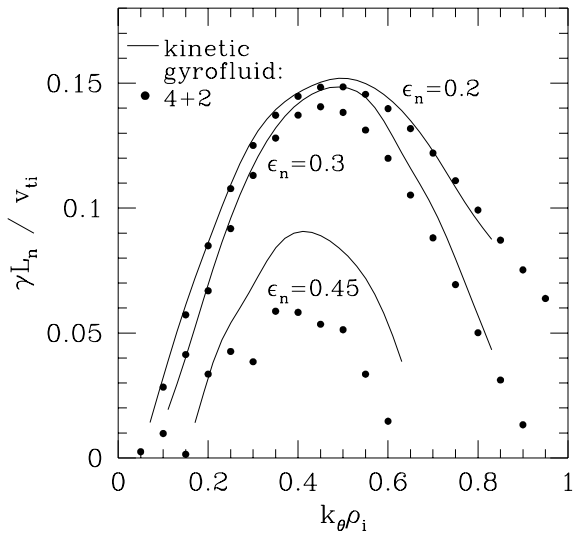

Figure 2.7: Comparison of linear growth rates from kinetic theory and the six moment model. Again, the agreement is quite good except for $\epsilon_n = 0.45$, where $\hat{s} = 1/3$.

kinetic theory is quite satisfactory, especially for $k_\theta \rho_i < 0.5$ where our models of FLR effects are very accurate. This level of agreement is a substantial improvement over previous fluid theories, and is more accurate than the four moment gyrofluid model of [Waltz *et al.*, 1992]. As $k_\theta \rho_i$ decreases, the mode width increases and $k_\parallel$ becomes smaller, which shifts the long wavelength cutoff to lower $k_\theta \rho_i$ than in the local limit, where $k_\parallel$ is held fixed. In other respects the fully nonlocal results seem to follow the local trends fairly closely.

Fig. 2.7 shows a comparison with [Dong *et al.*, 1992] Fig. 4 parameters: $\eta_i = 2.5$, $\epsilon_n = 0.2$, 0.3, 0.45, $q = 1.5$, and $\hat{s} = 0.1 \times q/\epsilon_n$. The toroidal gyrofluid and kinetic results are not in terribly good agreement for low $\hat{s}$. At low $\hat{s}$, shear localization is weak, and the eigenfunction becomes more extended along the field line. For the $\epsilon_n = 0.45$, $\hat{s} = 1/3$ case, the eigenfuction extends out to $\theta \approx 8$, roughly twice as broad as for $\epsilon_n = 0.2$ and $\hat{s} = 0.75$. It may be that the kinetic calculations were not resolving this broad eigenfunction.

To test of our models of trapped ion effects, we compare with the linear gyrokinetic particle simulations of [Xu and Rosenbluth, 1991], and the gyroki-

netic "Vlasov" simulations of [Liu and Cheng, 1993] which both include trapped ion effects. Fig. 2.8 shows a comparison of nonlocal linear eigenfrequencies from all three approaches, in the flat density limit, $\eta_i \to \infty$. The other parameters are: $L_T/R = 0.1$, $q = 2$, $\hat{s} = 1$, $\tau = 1$, and $\epsilon = 0.3$, in the collisionless limit, as in Fig. 6 of [Xu and Rosenbluth, 1991]. All three calculations assumed adiabatic electrons. The gyrofluid and Vlasov results are shown with ($\epsilon = 0.3$) and without ($\epsilon = 0$) trapped ion effects, to show the destabilizing effect of the trapped ions for very long wavelengths. Since the $\nabla_\parallel \ln B$ mirroring terms are proportional to ϵ, setting $\epsilon = 0$ turns off these terms. Without the mirroring terms, all modes are stable below $k_\theta \rho_i \approx 0.04$. With the mirroring terms, the toroidal ITG mode gradually evolves into a trapped ion mode. Trapped ion effects become important when the mode time scales are comparable to or less than the ion bounce frequency, $|\omega| \lesssim \omega_{bi} = \sqrt{\epsilon} v_{ti}/qR$. For these parameters $\omega_{bi} L_T/v_{ti} = \sqrt{\epsilon} L_T/qR = 0.03$, so trapped ion effects become significant for $k_\theta \rho_i \lesssim 0.1$. The six moment toroidal gyrofluid equations model this effect with reasonable accuracy. In particular, the gyrofluid model shows that trapped ions can remove the long wavelength cutoff which exists when trapped ions are ignored, in agreement with fully kinetic theory.

In Fig. 2.9 we show the same results as in Fig. 2.8, but now normalized to v_{ti}/L_T, which is independent of k_θ, and is thus proportional to the growth rate in physical units. This demonstrates more clearly than in Fig. 2.8 that the growth rates of the trapped ion modes are much less than those of the fastest growing modes near $k_\theta \rho_i \sim 1/2$, and suggests that our models of trapped ion effects are probably adequate.

For the measured parameters used in [Xu and Rosenbluth, 1991], $\rho_i \approx$ 0.13cm and $r_0 = 50$cm; so $k_\theta \rho_i = 0.01 = nq/r_0$ implies $n \approx 2$, where n is the toroidal mode number. Thus, the ballooning approximation (and in the representation in Chapter 4, the neglect of radial variations in the equilibrium) is definitely breaking down at these very long wavelengths. This issue is discussed in Section 4.8.

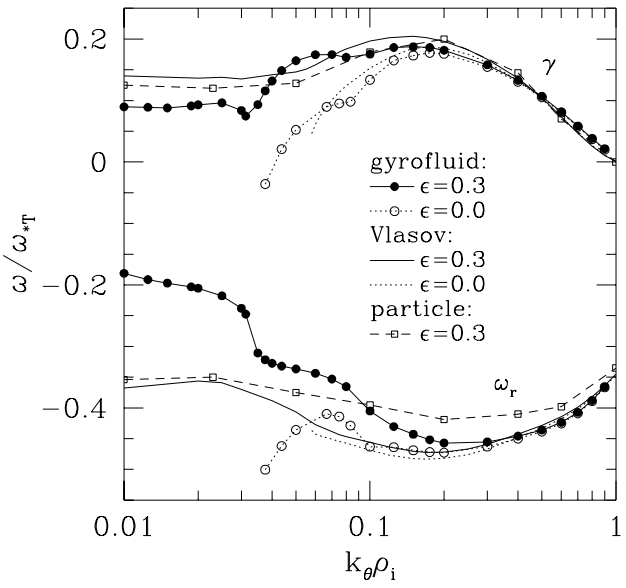

Figure 2.8: Comparison of linear growth rates and real frequencies normalized to $\omega_* T$ from fully kinetic calculations and the six moment toroidal gyrofluid equations with trapped ion effects. Including trapped ions ($\epsilon = 0.3$) further destabilizes the toroidal ITG mode at long wavelengths, which gradually evolves into a trapped ion mode for $k_\theta \rho_i \lesssim 0.1$.

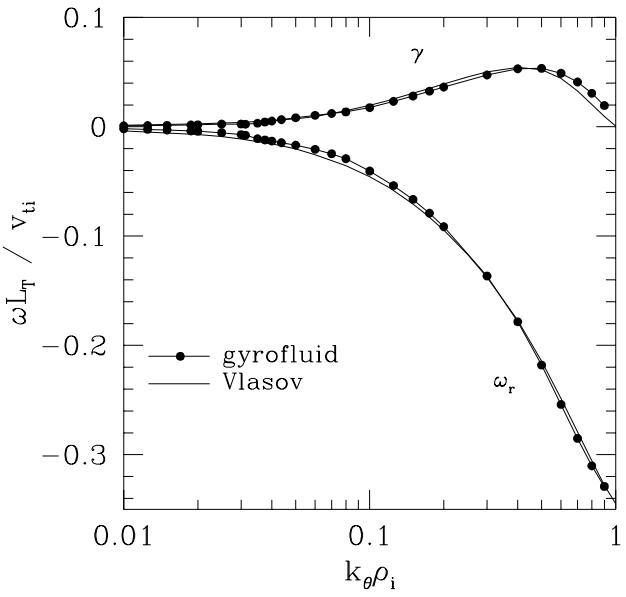

Figure 2.9: Linear growth rates and real frequencies normalized to v_t/L_T. In physical units, the growth rates of the trapped ion modes are much less than those of the fastest growing modes near $k_\theta \rho_i \sim 1/2$, which suggests that our models of trapped ion effects are probably adequate.

Chapter 3

Bounce Averaged Electron Fluid Equations

NEW FLUID EQUATIONS FOR TRAPPED ELECTRONS are developed in this chapter. The fluid equations for the ions derived in Chapter 2 can accurately describe the dynamics of the toroidal ITG and (somewhat less accurately) trapped ion modes when the electrons are adiabatic, but for realistic tokamak parameters, the nonadiabatic electron response, which primarily comes from trapped electrons, is often important. Proper treatment of the nonadiabatic electron response is essential to describe electron heat transport and particle transport. When the electrons are purely adiabatic, there is no net particle transport, since the $\mathbf{E} \times \mathbf{B}$ convection of the perturbed electron density is zero ($\mathbf{E} \times \mathbf{B} \cdot \nabla \tilde{n}_e \propto \nabla \tilde{\Phi} \times \mathbf{B} \cdot \nabla \tilde{\Phi} = 0$). Quasineutrality then implies no net ion transport. In addition, in the adiabatic limit there are no electron temperature fluctuations, so there is no electron heat transport. Trapped electrons are a well known important destabilization mechanism; the drive from the trapped electron toroidal precession resonance can double the growth rate of the ITG mode in some regimes, and can also destabilize the trapped electron mode (TEM). In this chapter, a sophisticated bounce averaged trapped electron fluid model is derived which retains the pitch angle dependence of the trapped electron response, as opposed to more simplified trapped electron models which assume the electrons are deeply trapped [KADOMTSEV and POGUTSE, 1970]. Retaining this pitch angle dependence is potentially important for advanced tokamak configurations in the second stability regime or with reversed magnetic shear [KESSEL *et al.*, 1994], where a major

fraction of the trapped electrons have favorable toroidal precession drift. It also allows use of a full pitch angle scattering collision operator for electron collisions (and not a Krook-type algebraic approximation), so these equations are continuously valid from the collisionless regime, where the trapped electron response is driven by the toroidal precession resonance, to the dissipative regime, to the very collisional regime where the trapped electrons become adiabatic.

Since their fast parallel motion allows bounce averaging of the electrons, the fast parallel time scale is removed, and these trapped electron fluid equations are not numerically stiff. Coupled with the ion equations derived in Chapter 2, these equations can be used efficiently in high resolution 3D toroidal simulations which simultaneously include trapped electron effects as well as the ITG drive, and enable calculation of the full transport matrix: electron and ion heat fluxes and particle fluxes.

3.1 Nonlinear Bounce Averaged Kinetic Equation

The electron dynamics are actually simpler than the ion dynamics in two respects, because $m_e \ll m_i$. Firstly, since the turbulent scales are on the order of the ion gyroradius, $k_\perp \rho_e \ll 1$, so we can neglect FLR effects for the electrons and use the drift kinetic equation instead of the gyrokinetic equation. Secondly, the turbulent time scales (on the order of the ion transit frequency, $\omega_{ti} = v_{ti}/qR$, or the diamagnetic frequency, $\omega_* = k_\perp \rho_i v_{ti}/L_n$) are long compared to the electron bounce frequency, $\omega \ll \omega_{be} = v_{te}/qR$. (This ordering breaks down for barely trapped particles, where $\omega_{be} \to 0$, but only over a very small region of velocity space.) Thus we can average over the fast electron bounce motion, so the trapped electron dynamics are described by the nonlinear bounce averaged drift kinetic equation [Gang and Diamond, 1990]:

$$(\frac{\partial}{\partial t} + i\omega_{de} - C)\tilde{h}^e_n = -\frac{e}{T_e}F_e(\frac{\partial}{\partial t} + i\omega^T_{*e})\left\langle e^{-inq\theta}\Phi_n\right\rangle_b + N_n. \tag{3.1}$$

This equation is four dimensional (two velocity space and two configuration space dimensions), since the variation along the field line has been removed by bounce averaging. Before deriving the trapped electron fluid equations, it is useful to rewrite this equation in a form more suitable for taking moments.

In Eq. (3.1), $\tilde{h}^e_n$ is the nonadiabatic part of the electron distribution function, $f_e = F_e e\Phi/T_e + h_e$. This equation was derived for axisymmetric circular concentric flux surfaces, and the perturbed distribution function and potential were written using:

$$h_e(r,\theta,\zeta) = \sum_n h^e_n(r,\theta) e^{-in\zeta}, \tag{3.2}$$

$$\Phi(r,\theta,\zeta) = \sum_n \Phi_n(r,\theta) e^{-in\zeta}. \tag{3.3}$$

To lowest order in ω/ω_{be}, the fast parallel motion causes h_e to be constant along the field line, so

$$h^{e(0)}_n = \tilde{h}^e_n(r) e^{inq\theta}, \tag{3.4}$$

and h_e is zero to lowest order in ω/ω_{be} for passing electrons. Thus Eq. (3.1) describes the evolution of the bounce averaged part of the nonadiabatic electron distribution function. The bounce average is defined by:

$$\langle A(r,\theta,\zeta)\rangle_b = \frac{\oint dl/|v_\parallel| A(r,\theta,\zeta)}{\oint dl/|v_\parallel|}, \tag{3.5}$$

where the integration is along a field line, and l is the distance along the field line. The nonlinear term N_n describes convection by the bounce averaged $\mathbf{E}\times\mathbf{B}$ drift:

$$N_n = -i\frac{c}{B}\sum_{n_1+n_2=n}\left(\frac{n_2 q}{r}\tilde{h}^e_{n_2}\frac{\partial}{\partial r}\left\langle e^{-in_1 q\theta}\Phi_{n1}\right\rangle_b - \frac{n_1 q}{r}\left\langle e^{-in_2 q\theta}\Phi_{n2}\right\rangle_b \frac{\partial}{\partial r}\tilde{h}^e_{n_2}\right). \tag{3.6}$$

Using a field-aligned coordinate system, as described in Chapter 4, this equation can be cast in a simpler form. Specifically, if we use the transformation Eq. (4.36), where x is the radial variable, y is perpendicular and mostly poloidal, and $z = \theta$ is the coordinate along the field line, we can rewrite Eqs. (3.2) and (3.4):

$$h_e(r,\theta,\zeta) = h_e(x,y,z) = \sum_n \tilde{h}^e_n(r) e^{-in(\zeta - q\theta)} = \sum_{k_y} h_e(x,k_y) e^{ik_y y}, \tag{3.7}$$

so to lowest order in ω/ω_{be}, h_e is independent of the coordinate along the field line, z. At fixed z, the y variable is simply the toroidal angle, so h_e can be thought of as the distribution function of banana centers at minor radius x and toroidal angle y. It will be most convenient to use the velocity space variables v and κ, where v is the total velocity ($E = v^2/2$) and κ is a pitch angle variable defined by:

$$\kappa^2 = \frac{1 - \mu B_{\min}/E}{2\epsilon_B}, \tag{3.8}$$

where $\epsilon_B = (B_{\max} - B_{\min})/2B_{\max}$. This is the pitch angle at the outer midplane normalized to unity at the trapped-passing boundary, and is a constant of the electron bounce motion. For deeply trapped electrons (with $E = \mu B_{\min}$), $\kappa = 0$; and the maximum κ for passing particles (where $\mu = 0$) is $1/\sqrt{2\epsilon_B}$. At the trapped-passing boundary (where $E = \mu B_{\max}$), $\kappa = 1$. For trapped particles ($\kappa < 1$), the poloidal angle of the banana tip or turning point, θ_t, is related to κ by:

$$\kappa = \sin(\theta_t/2). \tag{3.9}$$

This can be seen by using $E = \mu B_t$ where B at the turning point is $B_t = B_0/(1 + \epsilon\cos\theta_t)$. If we expand for small $\epsilon = r/R_0$, the definition for κ, Eq. (3.8), becomes:

$$\kappa^2 = [v^2/2 - \mu B_0(1-\epsilon)]/\epsilon v^2. \tag{3.10}$$

This pitch angle variable differs slightly from the one used in [Gang and Diamond, 1990], $\kappa^2 = [v^2/2 - \mu B_0(1-\epsilon)]/2\epsilon\mu B_0$, but for trapped particles the difference is negligible since $v \approx v_\perp$. So to lowest order in ω/ω_{be}, the nonadiabatic distribution function is a function of two spatial coordinates (x and y) and two velocity space coordinates, (v and κ). The eikonal $e^{-inq\theta}$ appears inside the bounce average $\left\langle \Phi_n e^{-inq\theta} \right\rangle_b$ since Eq. (3.1) has been written as an evolution equation for $\tilde{h}^e_n$, and both sides of $(\partial h_e/\partial t + \cdots)$ have been multiplied by $e^{-inq\theta}$. Using Eq. (3.8) to write $|v_\parallel|$ in terms of v and κ: $|v_\parallel| = v\sqrt{1 - B/B_{\min}(1 - 2\epsilon_B\kappa^2)}$, the bounce time is

$$\tau_b(\kappa) = \oint dl/|v_\parallel| = \frac{qR}{v}\int_{-\theta_t}^{\theta_t} \frac{d\theta}{\sqrt{1 - B/B_{\min}(1 - 2\epsilon_B\kappa^2)}}, \tag{3.11}$$

and the bounce average becomes:

$$\langle\Phi\rangle_b(x,y,\kappa) = \frac{\oint dz\Phi(x,y,z)/|v_\parallel|}{\oint d\theta/|v_\parallel|} = \frac{qR}{v}\int_{-\theta_t}^{\theta_t} \frac{d\theta\,\Phi(x,y,\theta)}{\tau_b\sqrt{1 - B/B_{\min}(1 - 2\epsilon_B\kappa^2)}}, \tag{3.12}$$

Bounce averaging turns functions of θ into functions of pitch angle, because of the κ dependence of the turning point, $|v_\parallel|$, and τ_b. Our derivation is correct for general magnetic geometry, but from time to time it is instructive to look at the large aspect ratio (small ϵ) limit to relate to previous work. Using $B = B_0/(1 + \epsilon\cos\theta)$ and expanding for small ϵ leads to the more standard form:

$$\langle\Phi\rangle_b = \int_{-\theta_t}^{\theta_t} \frac{d\theta\,\Phi(x,y,\theta)}{\sqrt{\kappa^2 - \sin^2(\theta/2)}\,4K(\kappa^2)}, \tag{3.13}$$

where $K(\kappa^2)$ is the complete elliptic integral of the first kind,

$$K(\kappa^2) = \int_0^1 \frac{dt}{\sqrt{(1-t^2)(1-\kappa^2 t^2)}} = \int_0^{\pi/2} \frac{dt}{\sqrt{1-\kappa^2 \sin^2 t}}. \tag{3.14}$$

The bounce averaged ∇B and curvature drift frequency, ω_{de}, is the toroidal precession frequency. For small ϵ, this is [KADOMTSEV and POGUTSE, 1966]:

$$\omega_{de} = \frac{cT_e}{eB}\frac{k_y}{R}\frac{v^2}{2v_{te}^2} G(\hat{s},\kappa), \tag{3.15}$$

$$G(\hat{s},\kappa) = \left(2\frac{E(\kappa^2)}{K(\kappa^2)} - 1\right) + 4\hat{s}\left(\frac{E(\kappa^2)}{K(\kappa^2)} - 1 + \kappa^2\right),$$

where $E(\kappa^2)$ is the complete elliptic integral of the second kind,

$$E(\kappa^2) = \int_0^1 dt \frac{\sqrt{1-\kappa^2 t^2}}{\sqrt{1-t^2}} = \int_0^{\pi/2} dt \sqrt{1-\kappa^2 \sin^2 t}. \tag{3.16}$$

It is important to keep the pitch angle dependence of ω_{de} to describe the stabilization of trapped electron modes in reversed shear configurations ($\hat{s} < 0$). The limiting values $G(\hat{s}, \kappa = 0) = 1$ and $G(\hat{s}, \kappa = 1) = -1$ are independent of shear, but as $\hat{s}$ decreases, more trapped particles precess in the favorable direction, $G < 0$, as shown in Fig. 3.1.

Finally, ω_{*e}^T is the bounce averaged diamagnetic frequency:

$$\omega_{*e}^T = \frac{cT_e}{eB}\frac{k_y}{L_n}\left[1 + \eta_e\left(\frac{v^2}{v_{te}^2} - \frac{3}{2}\right)\right].$$

To derive electron fluid equations, it is more convenient to write Eq. (3.1) in terms of $\langle f_e \rangle_b$ instead of $\tilde{h}_n^e$. Writing Eq. (3.1) in terms of h_e instead of $\tilde{h}_n^e$ removes the eikonal from inside the bounce average. Then the $\partial/\partial t$ term can be removed from the right hand side of Eq. (3.1) by evolving $\langle f_e \rangle_b$ instead of h_e, using:

$$\langle f_e \rangle_b = \langle h_e \rangle_b (x, y, v, \kappa) + F_e \left\langle \frac{e\Phi}{T_e} \right\rangle_b (x, y, \kappa). \tag{3.17}$$

Since h_e is independent of z to this order in ω/ω_{be}, $\langle h_e \rangle_b = h_e$:

$$f_e = h_e + F_e\frac{e\Phi}{T_e} = \langle h_e \rangle_b + F_e\frac{e\Phi}{T_e} = \langle f_e \rangle_b - F_e\left\langle \frac{e\Phi}{T_e} \right\rangle_b + F_e\frac{e\Phi}{T_e}. \tag{3.18}$$

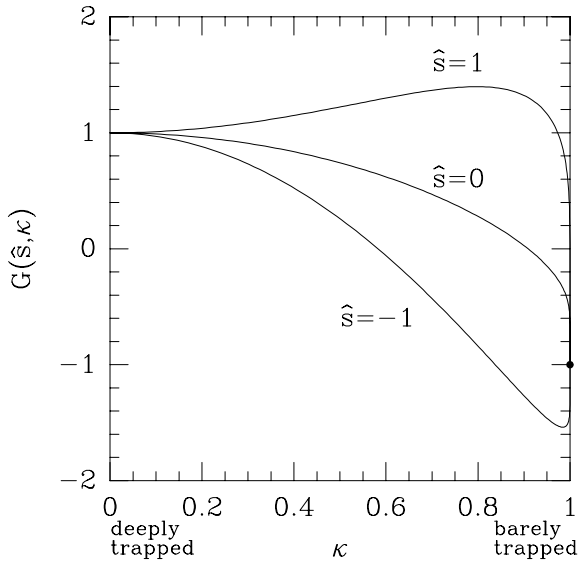

Figure 3.1: Pitch angle dependence of the toroidal precession frequency in the function $G(\hat{s},\kappa)$.

Then Eq. (3.1) becomes:

$$\left(\frac{d}{dt}+i\omega_{de}\right)\langle f_e\rangle_b = \langle C\rangle_b\left(\langle f_e\rangle_b - \langle\Phi\rangle_b\right) + iF_e(\omega_{de}-\omega_{*e}^T)\langle\Phi\rangle_b\,. \tag{3.19}$$

The nonlinear term has been absorbed in the total time derivative $d/dt = \partial/\partial t + \hat{\mathbf{b}}\times\langle\Phi\rangle_b\cdot\nabla$, and Φ has been normalized to e/T_e.

Before taking moments of this equation, let us calculate the total electron density, which we break into separate integrals over passing and trapped particles. Since the passing particles are adiabatic:

$$\begin{aligned} n_e(x,y,z) &= \int_p d^3v\,\Phi F_e + \int_t d^3v\, f_e \\ &= \int_p d^3v\,\Phi F_e + \int_t d^3v\left(\langle f_e\rangle_b - \langle\Phi\rangle_b F_e + \Phi F_e\right) \end{aligned}$$

The last line made use of Eq. (3.18). The adiabatic pieces for trapped and passing particles can now be combined:

$$n_e(x,y,z) = n_0\Phi + \int_t d^3v\left(\langle f_e\rangle_b - \langle\Phi\rangle_b F_e\right). \tag{3.20}$$

As in the purely adiabatic limit, special treatment is required for components which are constant on flux surfaces, i.e. with $k_y = 0$. Treatment of this subtlety is postponed until Section 3.5. The velocity space integral over trapped particles in v and κ variables is

$$\int_t d^3v \, \langle f_e \rangle_b = \int_0^\infty 4\pi dv \, v^2 \int_{\sin(\theta/2)}^1 \frac{2B\epsilon_B \kappa \, \langle f_e \rangle_b \, d\kappa}{B_{\min}\sqrt{1-(B/B_{\min})(1-2\epsilon_B\kappa^2)}}, \tag{3.21}$$

where the κ integral is limited to the range $\sin(\theta/2)$ to 1, since at a given θ, only particles with turning points beyond θ will contribute to the local density, and $\kappa = \sin(\theta_t/2)$. Expanding for small ϵ, this takes the more familiar form:

$$\int_t d^3v \, \langle f_e \rangle_b = \sqrt{2\epsilon} \int_0^\infty 4\pi dv \, v^2 \int_{\sin(\theta/2)}^1 \frac{d\kappa \, \kappa \, \langle f_e \rangle_b}{\sqrt{\kappa^2 - \sin^2(\theta/2)}}.$$

We introduce the following shorthand notation for the pitch angle integration:

$$\langle A(\kappa) \rangle_\kappa = \int_{\sin(\theta/2)}^1 \frac{2B\epsilon_B \kappa A(\kappa) d\kappa}{B_{\min}\sqrt{1-(B/B_{\min})(1-2\epsilon_B\kappa^2)}}. \tag{3.22}$$

Averaging in pitch angle turns functions of κ into functions of θ, because of the θ dependence of the Jacobian and the turning points. The electron density in real space is just the κ average of the v-averaged $\langle f_e \rangle_b$. Defining a pitch angle dependent trapped electron "density" by integrating only over v:

$$n_t(x,y,\kappa) = \int_0^\infty 4\pi dv \, v^2 \, \langle f_e \rangle_b \, ,$$

the total electron density in real space is:

$$n_e(x,y,z) = n_0\Phi + \langle n_t(x,y,\kappa) \rangle_\kappa - n_0 \langle \langle \Phi \rangle_b (x,y,\kappa) \rangle_\kappa. \tag{3.23}$$

The κ average of $\langle \Phi \rangle_b$ which appears here is analogous to the polarization density in the ion real space density, Eq. (2.9), and comes from the z-dependent part of the total electron distribution function.

3.2 Bounce Averaged Fluid Equations

As seen in the previous section, the pitch angle dependence of the electron distribution function enters the kinetic equation in a fundamentally different way than

the v dependence. Firstly, the κ dependence of the toroidal precession drift is separable from the v dependence, and secondly, the bounce averaged potential which enters the kinetic equation is pitch angle dependent, since deeply trapped particles only respond to the potential on the outer midplane, while barely trapped particles respond to the potential averaged over the entire poloidal angle. This suggests a significantly different approach for deriving trapped electron fluid equations. For the ions, we take moments over $v_\parallel$ and $v_\perp$ of the five dimensional $f_i(x, y, z, v_\parallel, v_\perp)$ to obtain three dimensional ion fluid equations. For the electrons, we start with the five dimensional $f_e(x, y, z, v, \kappa)$ and bounce average, which removes the parallel coordinate. Then we only need to take moments over v of $\langle f_e \rangle_b (x, y, v, \kappa)$ to obtain three dimensional pitch angle dependent "fluid" equations for the electrons, which are functions of x, y, and κ. These moments can be thought of as the electron density, pressure, etc., of banana tips, since κ is directly related to the turning point by $\kappa = \sin(\theta_t/2)$. The resulting trapped electron fluid equations look similar to the 3D fluid equations derived in Chapter 2, with the parallel coordinate replaced by the pitch angle variable, κ. Retaining the pitch angle dependence of the electron moments allows us to keep the full pitch angle pitch angle dependence of the toroidal precession frequency and the bounce averaged potential. It also allows the use of a full pitch angle scattering Lorentz collision operator for electron collisions. When the real space electron density is needed in the quasineutrality constraint, we perform the κ average in Eq. (3.22).

We derive trapped electron moment equations by averaging in v over the bounce averaged electron distribution function, $\langle f_e \rangle_b$. Since only even powers of v appear in Eq. (3.19), we will only need even moments:

$$\begin{aligned}
n_t(x, y, \kappa) &= \frac{4\pi}{n_0} \int_0^\infty dv\, v^2 \langle f_e \rangle_b \,, \\
p_t(x, y, \kappa) &= \frac{4\pi}{3 n_0 v_{te}^2} \int_0^\infty dv\, v^4 \langle f_e \rangle_b \,, \\
r_t(x, y, \kappa) &= \frac{4\pi}{15 n_0 v_{te}^4} \int_0^\infty dv\, v^6 \langle f_e \rangle_b \,, \\
t_t(x, y, \kappa) &= \frac{4\pi}{105 n_0 v_{te}^6} \int_0^\infty dv\, v^8 \langle f_e \rangle_b \,, \\
v_t(x, y, \kappa) &= \frac{4\pi}{945 n_0 v_{te}^8} \int_0^\infty dv\, v^{10} \langle f_e \rangle_b \,,
\end{aligned}$$

where the electron moments have been normalized to their Maxwellian values. The

v^2 dependence of the bounce averaged precession frequency, Eq. (3.15), brings the next higher even moment into each dynamical equation, introducing the usual closure problem of the coupled moments hierarchy. Performing the v integration, we have:

$$\frac{dn_t}{dt} + \frac{3}{2}i\omega_{de}p_t - \frac{3}{2}i\omega_{de}\langle\Phi\rangle_b + i\omega_{*e}\langle\Phi\rangle_b = \langle C\rangle_b (n_t - \langle\Phi\rangle_b) \quad (3.24)$$

$$\frac{dp_t}{dt} + \frac{5}{2}i\omega_{de}r_t - \frac{5}{2}i\omega_{de}\langle\Phi\rangle_b + i(1+\eta_e)\omega_{*e}\langle\Phi\rangle_b = \langle C\rangle_b (p_t - \langle\Phi\rangle_b) \quad (3.25)$$

$$\frac{dr_t}{dt} + \frac{7}{2}i\omega_{de}t_t - \frac{7}{2}i\omega_{de}\langle\Phi\rangle_b + i(1+2\eta_e)\omega_{*e}\langle\Phi\rangle_b = \langle C\rangle_b (r_t - \langle\Phi\rangle_b) \quad (3.26)$$

$$\frac{dt_t}{dt} + \frac{9}{2}i\omega_{de}v_t - \frac{9}{2}i\omega_{de}\langle\Phi\rangle_b + i(1+3\eta_e)\omega_{*e}\langle\Phi\rangle_b = \langle C\rangle_b (r_t - \langle\Phi\rangle_b) \quad (3.27)$$

The collision terms will be discussed in Section 3.4. We require a closure approximation for the highest moment which models toroidal precession drift phase mixing. By analogy with Chapter 2, we use an extension of the method of [Hammett and Perkins, 1990]. For a 3-moment electron model (evolving n_t, p_t, and r_t) we choose:

$$t_t = -i\frac{|\omega_{de}|}{\omega_{de}}(\nu_a n_t + \nu_b p_t + \nu_c r_t), \quad (3.28)$$

and in the 4-moment electron model (also evolving t_t), we choose:

$$v_t = -i\frac{|\omega_{de}|}{\omega_{de}}(\nu_a n_t + \nu_b p_t + \nu_c r_t + \nu_d t_t). \quad (3.29)$$

As in Chapter 2, each closure coefficient has both a dissipative and non-dissipative piece, $\nu = \nu_r + i\nu_i|\omega_{de}|/\omega_{de}$, but now ω_{de} is pitch angle dependent. We choose these closure coefficients to closely approximate the bounce averaged kinetic response function, derived in the next section.

3.3 Electron Closures

From the linearized bounce kinetic equation, we can derive the response function for the pitch angle dependent electron density:

$$R_e = \frac{n_t(\kappa)}{n_0\, e\langle\Phi\rangle_b(\kappa)/T_e} = 4\pi\int dv\, v^2 F_e \frac{-\omega_{de} + \omega_{*e}^T}{\omega - \omega_{de}}, \quad (3.30)$$

which can again be factored into the form:

$$R_e = R_{e0} + \frac{\omega_{*e}}{\omega_{de}} R_{e1} + \frac{\omega_{*e}\eta_e}{\omega_{de}} R_{e2}. \tag{3.31}$$

These integrals can be performed analytically, and are functions of $x_e = \omega/\omega_{de}$ and κ (through $\omega_{de}(\kappa)$) [TANG, 1974].

$$R_{e0} = 1 + 2x_e + 2x_e^{3/2} Z(\sqrt{x_e}), \tag{3.32}$$

$$R_{e1} = -2[1 + \sqrt{x_e} Z(\sqrt{x_e})], \tag{3.33}$$

$$R_{e2} = -[1 + 2x_e + 2x_e^{3/2} Z(\sqrt{x_e})] + 3[1 + \sqrt{x_e} Z(\sqrt{x_e})], \tag{3.34}$$

where Z is the usual plasma dispersion function.

Choosing $\omega_{de} > 0$ to simplify the notation in the following expressions, the response functions from the 3-moment electron equations are:

$$R_{e0} = -\frac{12\,x_e^2 - 42\,\nu_c x_e - 105\,\nu_b + 30\,x_e - 105\,\nu_c + 105}{8\,x_e^3 - 28\,\nu_c x_e^2 - 70\,\nu_b x_e - 105\,\nu_a}, \tag{3.35}$$

$$R_{e1} = \frac{8x_e^2 - 28\nu_c x_e - 70\nu_b + 12x_e - 42\nu_c + 30}{8x_e^3 - 28\nu_c x_e^2 - 70\nu_b x_e - 105\nu_a}, \tag{3.36}$$

$$R_{e2} = \frac{12x_e - 42\nu_c + 60}{8x_e^3 - 28\nu_c x_e^2 - 70\nu_b x_e - 105\nu_a}, \tag{3.37}$$

and for the 4-moment electron equations:

$$R_{e0} = \frac{24x_e^3 - 108\nu_d x_e^2 - 378\nu_c x_e - 945(\nu_b + \nu_c + \nu_d - 1) + 60x_e^2 - 270\nu_d x_e + 210x_e}{-16x_e^4 + 72\nu_d x_e^3 + 252\nu_c x_e^2 + 630\nu_b x_e + 945\nu_a}, \tag{3.38}$$

$$R_{e1} = \frac{16x_e^3 - 72\nu_d x_e^2 - 252\nu_c x_e - 630\nu_b + 24x_e^2 - 108\nu_d x_e - 378\nu_c + 60x_e - 270\nu_d + 210}{16x_e^4 - 72\nu_d x_e^3 - 252\nu_c x_e^2 - 630\nu_b x_e - 945\nu_a}, \tag{3.39}$$

$$R_{e2} = \frac{-24x_e^2 + 108\nu_d x_e + 378\nu_c - 120x_e + 540\nu_d - 630}{-16x_e^4 + 72\nu_d x_e^3 + 252\nu_c x_e^2 + 630\nu_b x_e + 945\nu_a}. \tag{3.40}$$

Powell's method [PRESS *et al.*, 1986] is again used to determine the closure coefficients by minimizing the error between the fluid and kinetic response functions, R_{e0}, R_{e1}, and R_{e2}, along the real x_e axis for $-3 < x_e < 8$. The best fits are $\nu_a = (-.071, -.290)$, $\nu_b = (-.689, 1.102)$, and $\nu_c = (1.774, -.817)$ for the 3-moment model, and $\nu_a = (.073, .038)$, $\nu_b = (-.060, -.657)$, $\nu_c = (-1.085, 1.522)$, and $\nu_d = (2.073, -.905)$ for the 4-moment model. The response functions for the 4-moment model are shown in Fig. 3.2.

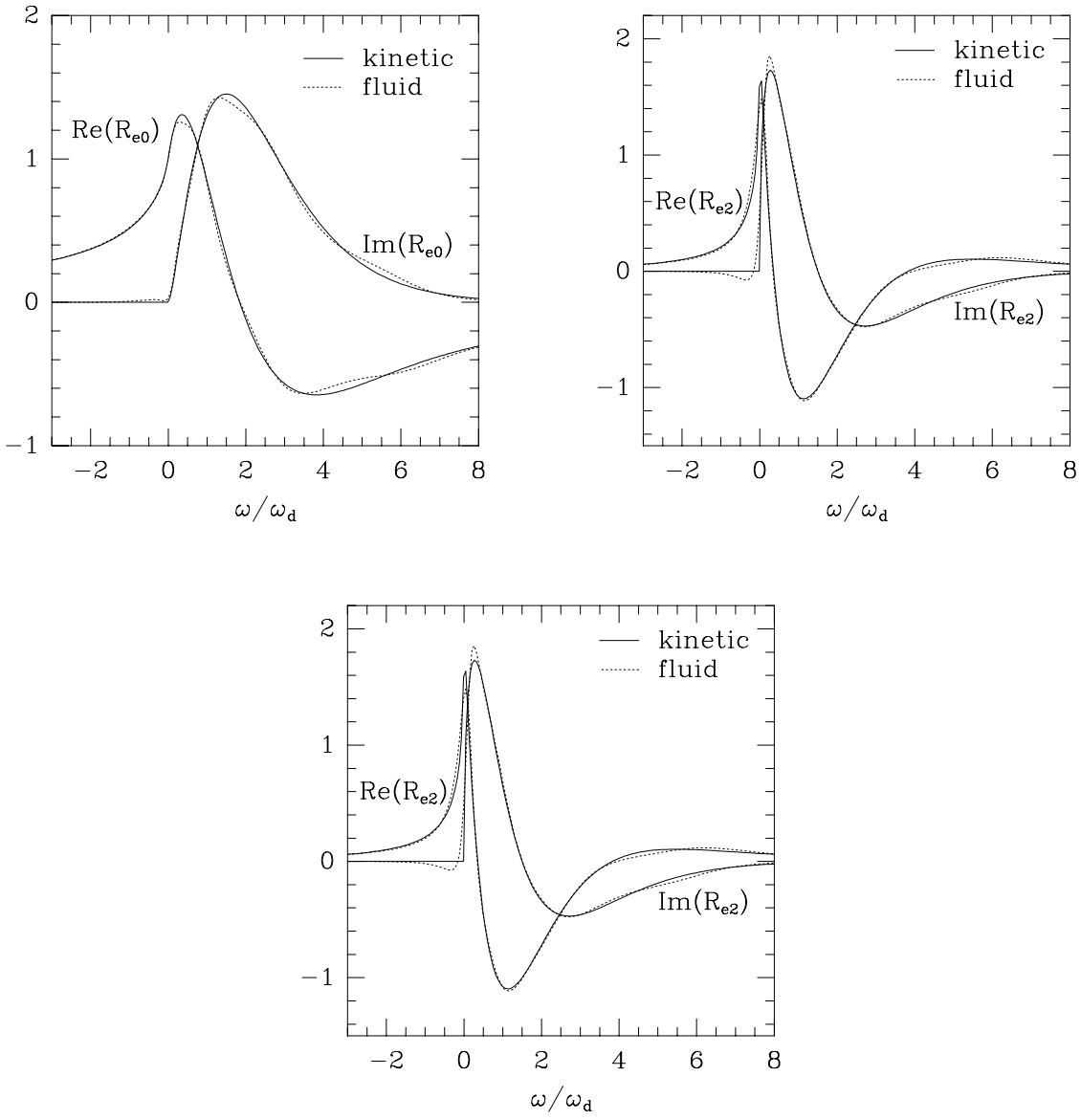

Figure 3.2: Kinetic and fluid bounce averaged response functions, R_{e0}, R_{e1}, and R_{e2}, for the 4-moment electron model.

3.4 Bounce Averaged Lorentz Collision Operator

Since the pitch angle dependence is retained in the trapped electron fluid moments, it is possible to use a Lorentz collision operator (a differential operator rather than a Krook algebraic model) for pitch angle scattering by electron-electron and electron-ion collisions:

$$C = \frac{\nu_e(v)}{2}\frac{\partial}{\partial\xi}(1-\xi^2)\frac{\partial f_e}{\partial\xi}, \tag{3.41}$$

where the pitch angle, $\xi = v_\parallel/v$. The energy dependent collision frequency is:

$$\nu_e(v) = \frac{4\pi n_e e^4 \ln\Lambda}{m_e^2 v^3}(Z_{\text{eff}} + H_{ee}(v/v_{te})), \tag{3.42}$$

where the Z_{eff} part accounts for electron-ion collisions (assuming $v \gg v_{ti}$) summed over ion species ($Z_{\text{eff}} = \sum_j Z_j^2 n_j/n_e$), and the $H_{ee}(x)$ part is from electron-electron collisions, where $H_{ee}(x) = \sqrt{2/\pi}\exp(-x^2/2)/x + [1-1/(x^2)]\text{erf}(x/\sqrt{2})$. This collision operator conserves particles and energy, but not momentum. Electron-ion collisions do cause a loss of electron momentum, which is transferred to ion momentum, but is usually ignorable since $m_e \ll m_i$.

The bounce average of this collision operator enters Eq. (3.19), and is calculated in [Cordey, 1976; Hammett, 1986]:

$$\langle C\rangle_b = \frac{\nu_e}{2|\xi_0|\tau_b}\frac{\partial}{\partial\xi_0}\left[(1-\xi_0^2)\frac{\tau_b}{|\xi_0|}\left\{\left\langle\frac{B_{\min}}{B}\right\rangle_b - (1-\xi_0^2)\right\}\frac{\partial f}{\partial\xi_0}\right], \tag{3.43}$$

where ξ_0 is $v_\parallel/v$ at the midplane, $\xi_0 = \sqrt{1-\mu B_{\min}/E}$. Transforming to κ using $\xi_0 = \sqrt{2\epsilon_B}\kappa$, using Eq. (3.18) for f_e, and the fact that the adiabatic piece $F_e e\Phi/T_e$ is independent of pitch angle, we have:

$$\langle C\rangle_b = \frac{\nu_e}{8\epsilon_B^2|\kappa|\tau_b}\frac{\partial}{\partial\kappa}\left[(1-2\epsilon_B\kappa^2)\frac{\tau_b}{|\kappa|}\left\{\left\langle\frac{B_{\min}}{B}\right\rangle_b - 1 + 2\epsilon_B\kappa^2\right\}\times\right. \tag{3.44}$$

$$\left.\frac{\partial}{\partial\kappa}\left(\langle f_e\rangle_b - \langle\Phi\rangle_b\right)\right],$$

This collision operator must be integrated over velocity, v, to find the collision terms in the trapped electron fluid equations. This leads to two complications: the $1/v^3$ dependence of the electron-ion term is singular in the electron density equation, and the other integrals do not lead to simple combinations of the electron moments we

evolve. For example, the collision term in the trapped electron pressure equation couples different moments together:

$$\frac{\partial p_t}{\partial t} = -\frac{4\pi}{3n_0 v_{te}^2}\int_0^\infty dv\, v^4 \langle C\rangle_b \propto -\nu_{e0}\int dv\, v \langle f_e\rangle_b \tag{3.45}$$

$$\propto -\nu_{e0}(\alpha n_t + \beta p_t + \cdots),$$

where in the last step, $\langle f_e\rangle_b$ has been expanded using the electron moments as a basis set, with as yet undetermined coefficients. To avoid solving the closure problem again, at this point we assume ν_e = constant, using:

$$\nu_e \approx \nu_{e0} = \frac{4\sqrt{2\pi}n_e e^4 \ln\Lambda}{3m_e^{1/2}T_e^{3/2}}(Z_{\text{eff}}+1). \tag{3.46}$$

Integration over v then leads to the collision terms in Eqs. (3.24-3.27). A better approximation, which we leave to future work, would lead to weaker coefficients in the higher moment equations to model the velocity dependence of ν_e, but the present approximation captures the essential feature of the collision operator, which is primarily the pitch angle scattering process.

3.5 Evolution of Trapped Electron Moments

This section describes how these electron moment equations are solved. The emphasis is on numerical solution, but analytic solution would follow conceptually similar procedures.

In the numerical simulations described in later chapters, the ion gyrofluid moments are stored and evolved in (x, y, z) space. The parallel grid points are evenly spaced in $z = \theta$ from $-N\pi$ to $N\pi$, where $N \geq 1$, as discussed in Chapter 4. This parallel coordinate is linearly equivalent to the extended poloidal angle in the ballooning representation. The electron moments are stored and evolved in (x, y, κ) space. The pitch angle grid points are at $\kappa = \sin(\theta)/2$ to provide more resolution near the trapped-passing boundary where ω_{de} is varying rapidly. Separate electron moments are independently evolved in each magnetic well along the parallel coordinate, i.e., the moments for $-\pi < \theta < \pi$ are separate from the moments for $\pi < \theta < 3\pi$. The bounce averaged $\langle\Phi\rangle_b(x, y, \kappa)$ is calculated from $\Phi(x, y, z)$ by numerically integrating Eq. (3.12), and then used to advance the electron moments

in time. Special care must be taken at the turning points, where Eq. (3.12) has integrable singularities. Choosing the κ spacing $\kappa = \sin(\theta/2)$ so that the turning points lie exactly on a θ grid point simplifies this integration. The electron nonlinearities are evaluated in a manner completely analogous to the ion nonlinearities, but in κ rather than in z. The electron collision terms are evaluated implicitly. The κ dependence in Eq. (3.44) and the boundary condition that $\langle f_e \rangle_b = \langle \Phi \rangle_b$ at the trapped-passing boundary automatically incorporates the strong effects of pitch angle scattering near the trapped-passing boundary.

Only the electron density moment ever needs to be evaluated in real space. To solve the quasineutrality equation, Eq. (2.9), the real space electron density, $n_e(x,y,z)$, is calculated by performing the κ averages of $n_t(x,y,\kappa)$ and $\langle \Phi \rangle_b$ as given by Eqs. (3.22) and (3.23). Again, special care must be taken at the turning points where Eq. (3.22) contains integrable singularities. Then the quasineutrality equation is solved for Φ, and this entire process is repeated for the next time step.

As in the adiabatic limit, special treatment is required for perturbations with $k_y = 0$, which are constant on flux surfaces. When $k_y \neq 0$, trapped electrons scattered onto passing orbits quickly become adiabatic, but this is not true if $k_y = 0$. When $k_y = 0$, $\omega_{de} = \omega_{*e} = 0$, so the bounce averaged kinetic equation reduces to:

$$\frac{d}{dt} \langle f_e \rangle_b = \langle C \rangle_b \left(\langle f_e \rangle_b - \langle \Phi \rangle_b \right). \tag{3.47}$$

The $k_y = 0$ electron moments for passing particles are separately evolved, and interact with the trapped electron $k_y = 0$ moments through collisions. We need to extend the κ variable to include passing particles, which occupy the range $1 < \kappa < 1/\sqrt{2\epsilon_B}$, and extend the definition of the bounce average for $\kappa > 1$:

$$\langle \Phi \rangle_b = \frac{\int_{-\pi}^{\pi} dz \Phi(x,z)/|v_\parallel|}{\int_{-\pi}^{\pi} dz/|v_\parallel|}, \tag{3.48}$$

for modes which are independent of y. For modes with $k_y \neq 0$, $\langle \Phi \rangle_b = 0$ for passing particles. Including nonadiabatic passing particles for $k_y = 0$, the generalization of Eq. (3.23) is:

$$n_e(x,y,z) = \int_p d^3v f_e + \int_t d^3v f_e = \int d^3v \left(\langle f_e \rangle_b - \langle \Phi \rangle_b F_e + \Phi F_e \right), \tag{3.49}$$

which can be written in the same form as Eq. (3.23),

$$n_e(x,y,z) = n_0 \Phi + \langle n_t \rangle_\kappa - n_0 \langle \langle \Phi \rangle_b \rangle_\kappa, \tag{3.50}$$

if we extend the κ average to include passing particles:

$$\langle A(\kappa)\rangle_\kappa = \int_{\sin(\theta/2)}^{1/\sqrt{2\epsilon_B}} \frac{2B\epsilon_B\kappa A(\kappa)d\kappa}{B_{\min}\sqrt{1-(B/B_{\min})(1-2\epsilon_B\kappa^2)}}. \tag{3.51}$$

When $n_t = 0$, Eq. (3.50) becomes $n_e = n_0(\Phi - \langle\langle\Phi\rangle_b\rangle_\kappa)$. That this is the proper adiabatic density response, Eq. (2.98), can be seen by using the identity $\langle\langle\Phi\rangle_b\rangle_\kappa = \int dz\, \Phi(x,y,z)/B$.

3.6 Comparison with Linear Kinetic Theory

We first test these trapped electron fluid equations by comparing the local linear growth rates and frequencies with kinetic theory. In the local limit, we choose $k_\parallel = 1/qR$, and ignore the bounce averages, i.e. we approximate $\Phi = \langle\Phi\rangle_b$. We also evaluate ω_{de} in the deeply trapped limit, at $\kappa = 0$. The local dispersion relation with trapped electrons is $R_i = -\tau R_e$, where the fluid and kinetic R_i's are given in Chapter 2 and the fluid and kinetic R_e's are given by Eq. (3.31) and Eq. (3.35)-(3.40). Fig. 3.3 shows the growth rates and real frequencies vs. $k_\theta\rho_i$ for the parameters $\eta_i = \eta_e = 3$, $q = 1.5$, $\epsilon_n = 1/3$, $\epsilon = 1/6$, and $T_i = T_e$, in the collisionless limit. The gyrofluid and trapped electron fluid results are in very good agreement with fully kinetic theory. The eigenfrequencies with adiabatic electrons are also shown. These are the same parameters as in Fig. 1 of [Kotschenreuther *et al.*, 1994b], and comparison with Fig. 3.4 shows that the destabilization by trapped electrons is strongly over-emphasized by the local and deeply trapped approximations, which neglect the bounce averaging of the potential and the variation of the toroidal precession frequency with pitch angle. Both of these effects will reduce the trapped electron density response. The three and four moment electron equations yield virtually identical results.

We next compare fully nonlocal results with kinetic theory in the collisionless limit. The eigenfrequencies from the six moment toroidal gyrofluid equations and the three moment trapped electron fluid equations are compared with fully kinetic calculations [Kotschenreuther *et al.*, 1994b] in Fig. 3.4. These results are for a pure deuterium plasma in the collisionless limit for the parameters $\eta_i = \eta_e = 3$, $\hat{s} = 1$, $q = 1.5$, $\epsilon_n = 1/3$, and $\epsilon = 1/6$, as in Fig. 1 of [Kotschenreuther *et al.*, 1994b]. The gyrofluid results with purely adiabatic electrons are also shown.

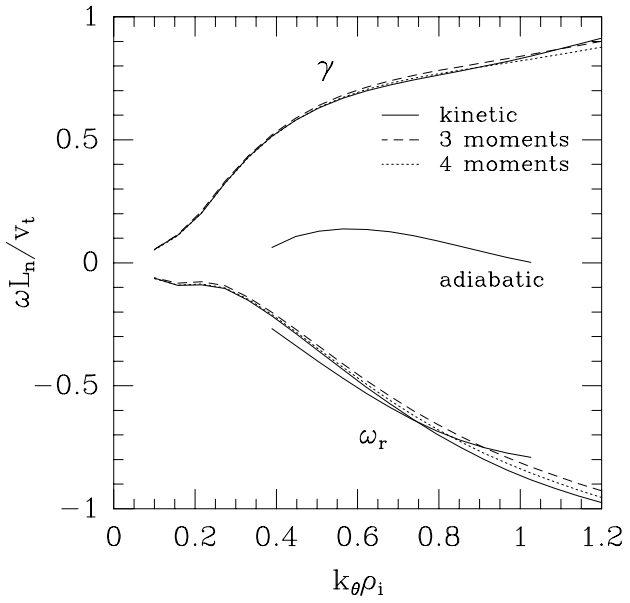

Figure 3.3: Comparison of local linear eigenfrequencies from gyrofluid and trapped electron fluid equations and fully kinetic results. The six moment toroidal gyrofluid equations are used, coupled with either the 3 moment or 4 moment electron equations. The fluid results are in very good agreement with kinetic theory. The results with adiabatic electrons are also shown. Comparison with Fig. 3.4 shows that the destabilization by trapped electrons is strongly over-emphasized by the local and deeply trapped approximations.

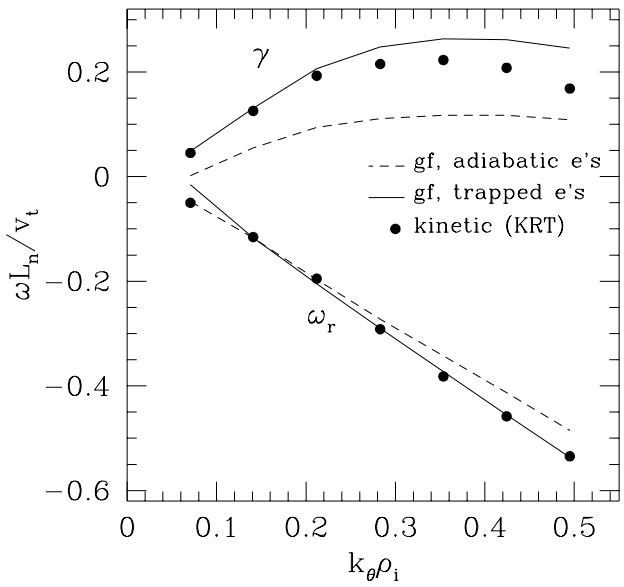

Figure 3.4: Comparison of linear eigenfrequencies from gyrofluid trapped electron fluid equations and fully kinetic results. The agreement is quite favorable. Also shown are the gyrofluid results with adiabatic electrons, showing that the trapped electron response doubles the growth rates for these parameters, even though this is an ITG mode.

The trapped electron response doubles the growth rates for these parameters, even though this is an ITG mode. Overall the agreement between gyrofluid and kinetic results is quite favorable.

Now we test our model of electron collisions by comparing with fully kinetic results. In Fig. 3.5, the variation of linear eigenfrequencies with collisionality is shown, for $k_\theta \rho_i = 0.35$, as in Fig. 2 of [KOTSCHENREUTHER *et al.*, 1994b]. The other parameters are as above. Again, there is very good agreement. The gyrofluid equations give a somewhat sharper transition from the collisionless regime to the strongly collisional regime where the electrons become adiabatic. Better agreement should be possible by modeling some of the velocity dependence of $\nu_e(v)$.

While trapped electrons have a strong effect on the ITG mode for low collisionality, the most interesting effect of the nonadiabatic electron dynamics is the destabilization of the trapped electron mode (TEM). For large collisionality the elec-

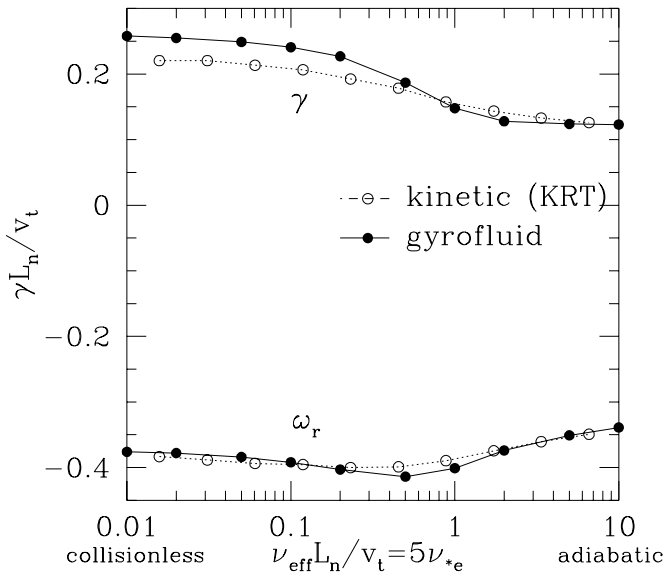

Figure 3.5: Variation of linear eigenfrequencies with ν_e, from kinetic theory and the gyrofluid trapped electron model. There is good agreement from the collisionless regime where the electron destabilization comes from the toroidal precession resonance, to the strongly collisional regime where the electrons become adiabatic.

trons are nearly adiabatic, and when η_i falls below a critical value, $\eta_i^{\rm crit}$, the ITG mode is stabilized and the plasma is completely stable. At low collisionality, when η_i falls below the adiabatic $\eta_i^{\rm crit}$, the trapped electron mode can still be unstable [Rewoldt and Tang, 1990]. Fig. 3.6 shows this behavior using the gyrofluid trapped electron model, for the parameters above, holding $\eta_i = \eta_e$. The solid squares are the linear growth rates for $k_\theta \rho_i = 0.3$ at large ν_{*e}. At this large collisionality, below $\eta_i \approx 1.5$, the ITG mode is stabilized. The open circles are the linear growth rates for $\nu_{*e} = 0.02$. For $\eta_i \gtrsim 1.5$, the ITG mode is unstable, and is further destabilized by trapped electrons (compared to its growth rate with adiabatic electrons). Below $\eta_i \approx 1.5$, it evolves into a trapped electron mode. When this transition occurs is a function of $k_\theta \rho_i$, so the trapped electron mode growth rates are also shown for $k_\theta \rho_i = 0.4$. Near $\eta_i = 1.5$, it is difficult to determine the eigenfrequency, since there are two unstable modes with nearly the same growth rates.

Thus, at low collisionality, the most striking effect of trapped electrons is to soften the ITG threshold. The TEM has quasilinear $Q_e > Q_i$, while the ITG mode has $Q_e < Q_i$, as in [Rewoldt and Tang, 1990], so the TEM can be expected to cause less ion heat transport. In this respect, there is still a threshold for the ion heat transport, but it is not a sharp threshold at low collisionality. Below the adiabatic ITG threshold, the growth rates become strong functions of electron collisionality and electron temperature and density gradients, which suggests that the turbulence levels and both ion and electron heat transport will be strongly dependent on these parameters in this regime.

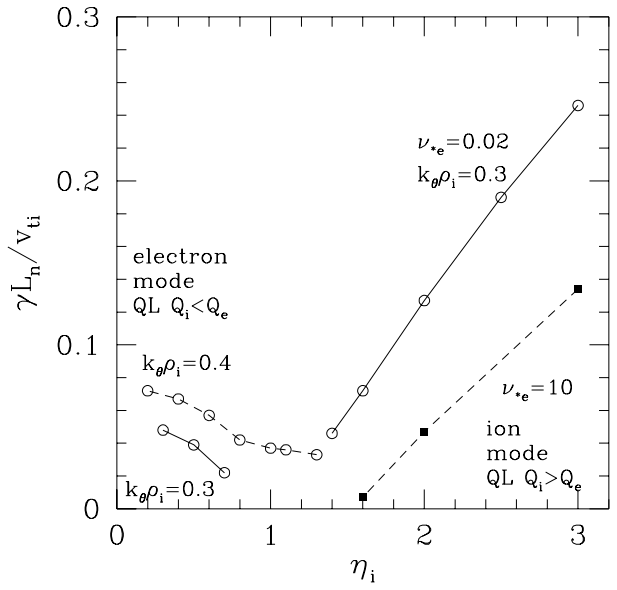

Figure 3.6: Linear growth rates from the gyrofluid trapped electron model varying η_i and holding $\eta_i = \eta_e$, showing the transition from an ITG mode to a trapped electron mode at $k_\theta\rho_i = 0.3$. At high collisionality (solid squares), $\nu_{*e} = 10$, the electrons are nearly adiabatic, and when $\eta_i \lesssim 1.5$ the plasma is completely stable. At low collisionality (open circles), $\nu_{*e} = 0.02$, for $\eta_i \lesssim 1.5$ the TEM is unstable. The TEM growth rate for $k_\theta\rho_i = 0.4$ is also shown, since the transition from ITG to TEM depends on $k_\theta\rho_i$.

Chapter 4

Field-aligned Coordinate System

TURBULENCE IN TOKAMAKS is characterized by long parallel wavelengths and short perpendicular wavelengths. This chapter describes a coordinate system for nonlinear fluid, gyrokinetic "Vlasov", or particle simulations that exploits the elongated nature of the turbulence by resolving the minimum necessary simulation volume: a long thin twisting flux tube. It is very similar to the ballooning representation, although periodicity constraints can be incorporated in a manner that allows $\mathbf{E} \times \mathbf{B}$ nonlinearities to be evaluated efficiently with FFTs. If the parallel correlation length is very long, however, enforcing periodicity can introduce artificial correlations, so periodicity should not necessarily be enforced in poloidal angle at $\theta = \pm\pi$. The advantages and limitations of this approach are discussed, and some of the inherent assumptions are tested numerically with 3D simulations of toroidal ITG driven turbulence.

4.1 Motivation

The turbulence that evolves from fine-scale instabilities (e.g. η_i, trapped electron, or resistive ballooning modes) is thought to be responsible for the anomalously large particle, momentum, and heat transport levels in tokamaks. It is therefore of great interest to simulate numerically the nonlinear evolution of these instabilities to determine the resulting fluctuation and transport levels. These instabilities are characterized by long wavelengths parallel to the magnetic field and short perpendicular wavelengths, on the order of the ion gyroradius, ρ_i. This is, of course, a

consequence of the rapid communication along field lines (at the sound speed for electrostatic instabilities) and slow communication across the field lines (typically velocities across the field do not exceed the diamagnetic speed). In addition, fluctuation measurements [FONCK *et al.*, 1993; MAZZUCATO and NAZIKIAN, 1993] in tokamaks indicate a relatively short perpendicular correlation length ($\sim 10\rho_i$), but a long parallel correlation length [ZWEBEN and MEDLEY, 1989]. Simulation of a full tokamak with adequate resolution of these fine perpendicular scales is somewhat beyond the presently available computational resources, since $\rho_i/a \sim 10^{-3}$ for present day large tokamaks, where a is the minor radius. (The latest full torus gyrokinetic particle simulations can now be run down to $\rho_i/a = 1/128$ [HAMMETT *et al.*, 1994].) However, it may be unnecessary to simulate a whole torus to reproduce small-scale, locally-driven turbulence. This chapter describes a coordinate system for nonlinear simulations that resolves a much smaller volume and is therefore computationally more efficient, while still resolving the relevant small scales. The smallest possible simulation volume is a long thin flux tube that is several correlation lengths wide in both perpendicular directions (radial and poloidal), and extended along the field line, exploiting the elongated nature of the turbulence ($k_\perp \gg k_\parallel$). This approach is advantageous for fluid, gyrokinetic "Vlasov", and particle simulations, and could eventually be compared with full torus simulations.

The fundamental idea is to use coordinates that follow field lines. With such coordinates a flux tube (a tube with a surface parallel to $\mathbf{B}$) which is bent by magnetic curvature and twisted by magnetic shear, is mapped into a rectangular domain. Such twisting coordinates were originally proposed by [ROBERTS and TAYLOR, 1965], and [COWLEY *et al.*, 1991] emphasized their utility for nonlinear calculations. In [HAMMETT *et al.*, 1993], we described the essential features of this approach, with an emphasis on slab geometry. Here we focus more on the toroidal aspects and actual details of implementation. The major problem of these field line coordinates is enforcing the periodicity constraint since the coordinates are multivalued in a torus (except at low order rational surfaces). In [COWLEY *et al.*, 1991] it was emphasized that it is unlikely that the correlated volume wraps around the torus and overlaps itself. When this is true, the physical periodicity of the full torus is irrelevant, and the simplest approach is to simulate a flux tube subdomain that is several parallel correlation lengths long (just as it should be several perpendicular correlation lengths wide). As will be described in Section 4.3, this can be

different from imposing periodicity at $\theta = \pm\pi$ as is usually suggested for the ballooning representation (and which could lead to artificial correlations which modify the results).

Another advantage of the field-line coordinates, in addition to the efficiency of a minimum simulation volume, is that it can easily implement radial periodicity (which in regular coordinates is complicated by the shear of the magnetic field), thus avoiding the problems of "quasilinear flattening" and allowing self-consistent turbulence-generated "zonal" flows (flows which cause flux surfaces to rotate). The field-line coordinates are also particularly convenient for gyrofluid simulations where partially Fourier transformed quantities (in 2 of the 3 dimensions) need to be evaluated, such as $|\omega_d(\theta)| \propto |k_\theta \cos(\theta) + k_r \sin(\theta)|$.

We have carried out simulations with various sizes for the flux-tube "box", and verified that the results are independent of the box size once it is larger than the correlation lengths in each direction, thus justifying some of the assumptions implicit in simulating a flux tube subdomain rather than the full torus. This leads to interesting questions regarding Bohm vs. gyro-Bohm scaling for the turbulence, which we will consider in the Section 4.8.

4.2 Flux Tube Simulations in General

If one wants to describe turbulence which is highly elongated along field lines and narrowly localized across field lines it is natural to introduce coordinates which are constant on field lines. A natural way to do this for any general magnetic field is to use the Clebsch representation of the magnetic field [Kruskal and Kulsrud, 1958] (since $\nabla \cdot \mathbf{B} = 0$):

$$\mathbf{B} = \nabla\alpha \times \nabla\psi. \tag{4.1}$$

Clearly $\mathbf{B} \cdot \nabla\alpha = \mathbf{B} \cdot \nabla\psi = 0$ so that α and ψ are constant on field lines. Thus α and ψ are natural coordinates for the flux tube. A third coordinate, z, must be defined that represents distance along the flux tube. One obvious choice of the third coordinate is the physical length along the field line, though this is not always the most convenient choice. A complication of using α and ψ as coordinates is that they are not unique, for instance if $\alpha' = \alpha + g(\psi)$ then $\mathbf{B} = \nabla\alpha' \times \nabla\psi$. In many applications toroidal flux surfaces are defined and it is natural to take ψ to be the

poloidal flux. The choice of α is less obvious and may be optimized for a particular calculation. A further complication is that α and ψ are typically not naturally single valued and a cut must be introduced to enforce single values [KRUSKAL and KULSRUD, 1958]. This issue will be discussed extensively below. Let us imagine that a choice of α, ψ, and z has been made and that $\alpha = \alpha(\mathbf{r})$, $\psi = \psi(\mathbf{r})$, and $z = z(\mathbf{r})$ are known functions. This information can be obtained for instance from the output of an equilibrium code. Thus, in what follows, the metric coefficients for the transformation to the α, ψ, z coordinates are taken to be known. The Jacobian of this transformation is $J = (\nabla\alpha \times \nabla\psi \cdot \nabla z)^{-1}$.

Three spatial operators appear many times in the equations for the perturbations, they are: $\mathbf{B} \cdot \nabla$, $\nabla_\perp^2$, and $\mathbf{B} \times \nabla\Phi \cdot \nabla$. In the α, ψ, z coordinates we have:

$$\mathbf{B} \cdot \nabla A = (\nabla\alpha \times \nabla\psi \cdot \nabla z)\left(\frac{\partial A}{\partial z}\right)_{\alpha,\psi} = \frac{1}{J}\frac{\partial A}{\partial z}, \tag{4.2}$$

$$\begin{aligned}
\nabla^2 A &= \frac{1}{J}\frac{\partial}{\partial\alpha}\left[J\frac{\partial A}{\partial\alpha}|\nabla\alpha|^2 + J\frac{\partial A}{\partial\psi}\nabla\alpha\cdot\nabla\psi + J\frac{\partial A}{\partial z}\nabla\alpha\cdot\nabla z\right] \\
&+ \frac{1}{J}\frac{\partial}{\partial\psi}\left[J\frac{\partial A}{\partial\alpha}\nabla\alpha\cdot\nabla\psi + J\frac{\partial A}{\partial\psi}|\nabla\psi|^2 + J\frac{\partial A}{\partial z}\nabla\psi\cdot\nabla z\right] \\
&+ \frac{1}{J}\frac{\partial}{\partial z}\left[J\frac{\partial A}{\partial\alpha}\nabla\alpha\cdot\nabla z + J\frac{\partial A}{\partial\psi}\nabla\psi\cdot\nabla z + J\frac{\partial A}{\partial z}|\nabla z|^2\right],
\end{aligned} \tag{4.3}$$

$$\begin{aligned}
\mathbf{B}\times\nabla\Phi\cdot\nabla A &= \left(\frac{\partial A}{\partial\psi}\frac{\partial\Phi}{\partial\alpha} - \frac{\partial A}{\partial\alpha}\frac{\partial\Phi}{\partial\psi}\right)B^2 \\
&+ \left(\frac{\partial A}{\partial z}\frac{\partial\Phi}{\partial\alpha} - \frac{\partial A}{\partial\alpha}\frac{\partial\Phi}{\partial z}\right)(\nabla\alpha\times\nabla\psi)\cdot(\nabla\alpha\times\nabla z) \\
&+ \left(\frac{\partial A}{\partial z}\frac{\partial\Phi}{\partial\psi} - \frac{\partial A}{\partial\psi}\frac{\partial\Phi}{\partial z}\right)(\nabla\alpha\times\nabla\psi)\cdot(\nabla\psi\times\nabla z),
\end{aligned} \tag{4.4}$$

where A and Φ are any scalars. Eqs. (4.2)-(4.4) are completely general.

We shall assume that the turbulence we wish to simulate has perpendicular correlation lengths that are short compared to equilibrium scale lengths but a parallel correlation length of the same order as the equilibrium scale lengths. Let us consider a simulation domain that is a flux tube volume defined by $\alpha_0 - \Delta\alpha < \alpha < \alpha_0 + \Delta\alpha$, $\psi_0 - \Delta\psi < \psi < \psi_0 + \Delta\psi$, and $-z_0 < z < z_0$. This volume is chosen to

be several correlation lengths in all three directions. Of course one wants to make this volume as small as possible to save computer time. Once the box volume is larger than several correlation lengths the turbulence should be insensitive to the size of the box. One tests whether the box size is adequate (in the usual way) by increasing the box size and comparing the turbulence in the different size boxes, or by measuring the correlation functions in a given box and verifying that they go to zero at the edges of the box. In this way we arrive at a minimum simulation volume.

Since the simulation volume is narrow in α and ψ (compared to equilibrium variations) all equilibrium quantities (or gradients of equilibrium quantities when they appear in the equations) are to lowest order functions of z alone. In other words, the perpendicular scale of the equilibrium is much greater than the perpendicular scale of the perturbations, and the box is chosen to be only slightly larger than the largest scale perturbations, so across the box (i.e. in α and ψ) one can ignore the variation of these equilibrium quantities. For example, the Jacobian $J = (\nabla\alpha \times \nabla\psi \cdot \nabla z)^{-1}$ is to a good approximation constant across the box but not along the box, thus $J = J(\alpha_0, \psi_0, z)$.

When A is a perturbed scalar (e.g. n, T, etc.), and Φ is the potential, we can neglect the $\partial/\partial z$ terms in Eqs. (4.3) and (4.4) since they are smaller by $k_\parallel/k_\perp$. The coefficients in Eqs. (4.2), (4.3), and (4.4) (various elements of the metric tensor) are again roughly constant across the box and therefore may be taken as functions of z alone with $\alpha = \alpha_0$ and $\psi = \psi_0$. Then Eqs. (4.3) and (4.4) reduce to:

$$\nabla_\perp^2 A = |\nabla\alpha|^2 \frac{\partial^2 A}{\partial\alpha^2} + 2\nabla\alpha \cdot \nabla\psi \frac{\partial^2 A}{\partial\alpha\partial\psi} + |\nabla\psi|^2 \frac{\partial^2 A}{\partial\psi^2}, \tag{4.5}$$

$$\mathbf{B} \times \nabla\Phi \cdot \nabla A = \left(\frac{\partial A}{\partial\psi}\frac{\partial\Phi}{\partial\alpha} - \frac{\partial A}{\partial\alpha}\frac{\partial\Phi}{\partial\psi} \right) B^2. \tag{4.6}$$

Therefore, the equations to be solved in this (minimum simulation) volume have no explicit dependence on α or ψ, which leads to great computational simplification. The $\mathbf{E} \times \mathbf{B}$ nonlinearity takes the simple form Eq. (4.6), and all other coefficients in the equations are only functions of z.

The perpendicular boundary conditions on the perturbations at $\alpha = \alpha_0 \pm \Delta\alpha$ and $\psi = \psi_0 \pm \Delta\psi$ are taken to be periodic. If the box is more than a correlation length wide the turbulence should be insensitive to the boundary conditions,

although one set of boundary conditions that is not advisable is fixed boundary conditions which prohibit energy and particle fluxes through the boundary. If fixed radial boundary conditions without sources or sinks are used, then the $m = 0, n = 0$ component of the perturbations (where m is the poloidal mode number and n is the toroidal mode number) will grow to eventually cancel the driving equilibrium gradients ("quasilinear flattening"), thus turning off the turbulence. In principle, this problem can be overcome with a sufficiently large box so that the time scale to flatten the driving gradients becomes much longer than the simulation time. But periodic radial boundary conditions avoid flattening altogether and allow the use of a more efficient, smaller box. Past simulations have sometimes zeroed out the $m = 0, n = 0$ components of perturbations to avoid this flattening, but that prevents the turbulence from being able to generate sheared zonal flows (resulting from the $m = 0, n = 0$ component of the electrostatic potential, $\Phi(\psi)$, which varies only with minor radius), which can be an important nonlinear saturation process [Hammett *et al.*, 1993; Dorland *et al.*, 1993; Cohen *et al.*, 1993; Hasegawa and Wakatani, 1987; Carreras *et al.*, 1991; Diamond and Kim, 1991]. Periodic radial boundary conditions allow the self-consistent evolution of $m = 0, n = 0$ perturbations such as the zonal flows.

The assumption of radial periodicity in the small flux-tube is not based on actual physical constraints (that would require simulating the full tokamak to include losses to the limiter, auxiliary heating of the tokamak core, and including a vacuum region and a conducting shell). Instead, we are assuming that the statistical properties of the fluctuations at $\psi + 2\Delta\psi$ are the same as at ψ, and that if the simulation box width $2\Delta\psi$ is larger than the radial correlation length we can assume that they are actually identical at every instant. This statistical radial periodicity also serves as a model of the effect of turbulence in neighboring regions on the simulated subdomain. This is illustrated by the contours in Fig. 4.9, which show eddies that stick out of one side of the box and reenter on the other side of the box. Periodic boundary conditions are often used in 2-D plasma simulations (such as Hasegawa-Mima) or in simulations of homogeneous Navier-Stokes Turbulence, but are complicated somewhat in 3-D plasma simulations by the shear in the magnetic field. Because the parallel dynamics are so much faster than the perpendicular dynamics (so $k_\parallel \ll k_\perp$), the fluctuations tend to be elongated along the direction of the magnetic field, which points in different directions at different radii. In

regular coordinates this requires the use of something like the "twist-and-shift" radial boundary conditions suggested by [KOTSCHENREUTHER and WONG, 1991]; also discussed in [DORLAND *et al.*, 1993; DIMITS, 1993]. The field-line coordinates, however, are already aligned with the magnetic field, so radial periodicity becomes simply $A(\psi + 2\Delta\psi, \alpha, z, t) = A(\psi, \alpha, z, t)$. Some of the issues involved in radial periodicity are discussed in more detail in [DORLAND *et al.*, 1993; DORLAND, 1993; COHEN *et al.*, 1993].

For the same reasons, we can also assume statistical periodicity in the α direction, $A(\psi, \alpha + 2\Delta\alpha, z, t) = A(\psi, \alpha, z, t)$. There is no explicit dependence of the operators in Eqs. (4.5,4.6) on α or ψ, so it is useful to expand in a Fourier series in ψ and α (which also provides periodicity in those directions):

$$A(\psi, \alpha, z, t) = \sum_{j=-\infty}^{\infty} \sum_{k=-\infty}^{\infty} \hat{A}_{j,k}(z, t) e^{ij\pi(\psi-\psi_0)/\Delta\psi + ik\pi(\alpha-\alpha_0)/\Delta\alpha}. \tag{4.7}$$

The boundary conditions in the z direction will be discussed in the next section. Note that while each term in the Fourier series is a plane wave in α, ψ coordinates, the wavefronts in real space can be very distorted. Perhaps the most pronounced distortion arises from magnetic shear. To understand this we first define the angle, λ, between constant α and ψ surfaces:

$$\cos\lambda = \frac{\nabla\alpha \cdot \nabla\psi}{|\nabla\alpha||\nabla\psi|}. \tag{4.8}$$

Magnetic shear makes λ change as z changes—in real space the flux tube is then sheared and its cross-section goes from being rectangular where $\lambda = \pi/2$ to being a parallelogram where $\lambda \neq \pi/2$, as shown in Fig. 4.1. The wavefronts of each term in the Fourier series, Eq. (4.7), also get sheared. For example the $j = 0$, $k \neq 0$ term has wavefronts corresponding to the constant α lines. The individual terms in the series Eq. (4.7) are therefore "twisted eddies" [ROBERTS and TAYLOR, 1965; COWLEY *et al.*, 1991] whose wavefronts twist as one moves along z.

Now let us discuss the choice of the coordinates α and ψ. A useful discussion of this procedure can be found in [WHITE, 1989]. As shown in [GREENE and JOHNSON, 1962], it is possible to choose α, ψ, and generalized "toroidal" and "poloidal" angle variables ζ and θ such that the field lines are straight in the (ζ,θ) plane and physical quantities are periodic over 2π in both variables. This choice of coordinates

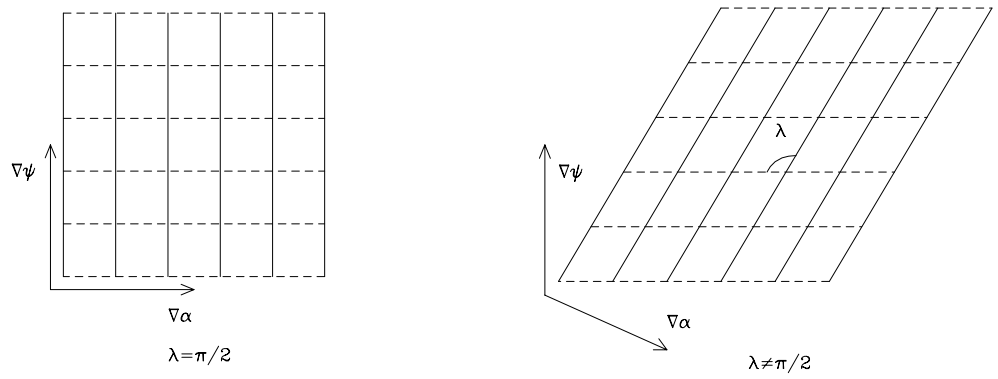

Figure 4.1: Shearing of flux tube cross section at different positions along the tube. Lines represent constant ψ (dashed) and constant α (solid) lines.

will simplify our discussion of periodicity in section 4.3. For the general magnetic field Eq. (4.1), we have [KRUSKAL and KULSRUD, 1958]:

$$\alpha = \phi - q(\psi)\theta - \nu(\psi, \theta, \phi), \tag{4.9}$$

where $\psi = (2\pi)^{-2} \int_V d\tau \mathbf{B} \cdot \nabla\theta$ is the poloidal flux, $q(\psi) = d\psi_T/d\psi$, $\psi_T = (2\pi)^{-2}$ $\int_V d\tau \mathbf{B} \cdot \nabla\phi$ is the toroidal flux, $d\tau$ is the volume element, and ϕ and θ are the physical toroidal and poloidal angles, so physical quantities are periodic over 2π in ϕ and θ. The function ν is also periodic in ϕ and θ. We now introduce a new toroidal coordinate,

$$\zeta = \phi - \nu(\psi, \theta, \phi). \tag{4.10}$$

With this choice

$$\alpha = \zeta - q(\psi)\theta, \tag{4.11}$$

and the magnetic field lines are straight in the (ζ,θ) plane. Further, periodicity is preserved in ζ and θ. Often, θ is also redefined to choose a specific form of the Jacobian. An alternative to Eq. (4.10) would be to use $\zeta = \phi$ and introduce a new poloidal coordinate $\theta' = \theta + \nu/q$. In any case, we will make use of the fact that a coordinate system can be chosen such that magnetic fields lines are straight

in the (θ, ζ) plane, and are given by $\alpha = \zeta - q(\psi)\theta = \text{constant}$. For our parallel coordinate z we will use $z = \theta$, since this makes our description very close to the usual ballooning mode formalism. Note that z is not restricted to $-\pi < z < \pi$, as we may choose to simulate a flux tube which follows a field line wrapping around the torus several times in the poloidal direction, not just once. This will be discussed further in the next section.

In summary, our field-line following coordinate system is given by (ψ, α, z), where field lines are labeled by constant ψ and α. One can think of ψ as a radial coordinate, $\alpha = \zeta - q(\psi)\theta$ as a perpendicular-to-the-field coordinate, and $z = \theta$ as a parallel-to-the-field coordinate. Our notation simplifies if we introduce the following new variables:

$$x = \frac{q_0}{B_0 r_0}(\psi - \psi_0), \qquad y = -\frac{r_0}{q_0}(\alpha - \alpha_0), \qquad z = \theta, \tag{4.12}$$

where $q_0 = q(\psi_0)$, B_0 is the field at the magnetic axis, and r_0 is the distance from the magnetic axis to the center of the box. Then Eq. (4.7) becomes:

$$A(x, y, z, t) = \sum_{k_x=-\infty}^{\infty} \sum_{k_y=-\infty}^{\infty} e^{ik_x x + ik_y y}\, \hat{A}_{k_x,k_y}(z, t), \tag{4.13}$$

with $k_x = j\pi/\Delta x$, $k_y = -k\pi/\Delta y$, $\Delta x = q_0 \Delta\psi / B_0 r_0$, and $\Delta y = r_0 \Delta\alpha / q_0$. The rectangular computational box of "radial" width $2\Delta x$, and "poloidal" width $2\Delta y$, and extended along the field line, θ, is mapped onto a flux tube, as shown in Fig. 4.2, for example.

These coordinates are similar to those used in [Waltz and Boozer, 1993]. Our α, ψ, and z are analogous to $-q\theta'$, ρ', and ϕ' in [Waltz and Boozer, 1993], respectively, since they have chosen to measure the distance along the field line with ϕ', a "toroidal" angle, while we use θ. A more significant difference between our representation and [Waltz and Boozer, 1993] is the treatment of periodicity, though their more recent work [Waltz *et al.*, 1994a] has adopted a similar treatment to ours, described in the next section.

4.3 Periodicity and Parallel Boundary Conditions

The choice of parallel boundary conditions involves a number of subtle, yet important issues. The main concept is that of a statistically-motivated periodicity,

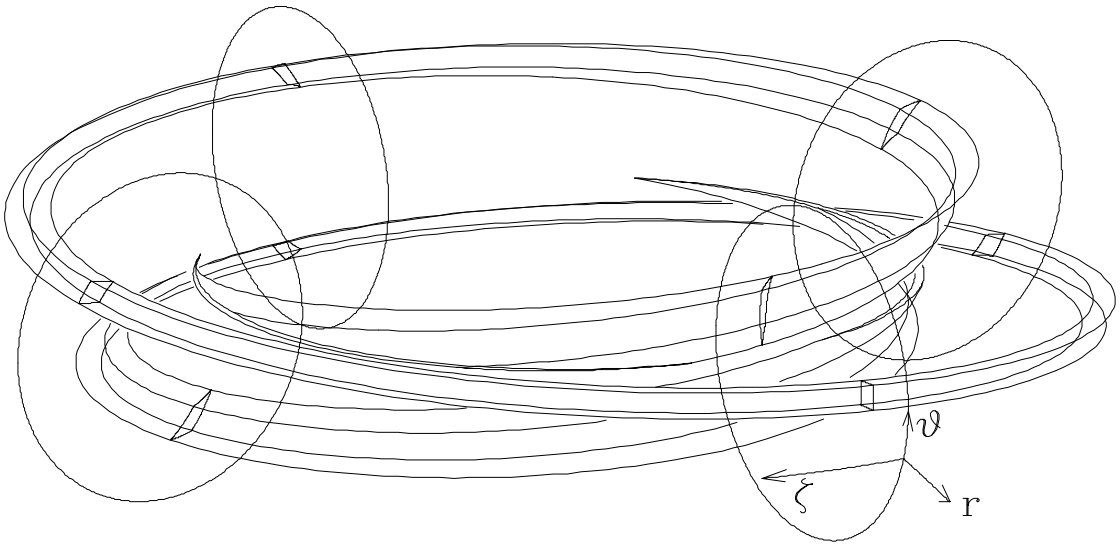

Figure 4.2: The rectangular computational domain mapped onto a flux tube in a torus, with $q_0 = 2.4$ and shear, $\hat{s} = 1.5$. The ends of this flux tube are cut off at poloidal angle $-\pi$ and π, and the sheared cross-sections of the flux tube in the poloidal plane are indicated.

as described in Section 4.2 for the ψ and α boundary conditions. For moderately "ballooning" turbulence we might expect parallel correlation lengths $\theta_c \sim (1-2)\pi$ (though it might be longer than this). The simulation box should have a length $2z_0 = 2\pi N$ in the parallel direction which is several times the parallel correlation length. In some cases a box length of 2π might be sufficient. But an even longer box may be necessary in many cases to ensure that one end of the box is sufficiently decorrelated from the other end of the box to avoid artificially constraining correlation effects, just as the box must be at least a few correlation lengths wide in the ψ and α directions. For the cases simulated in Section 4.7, parallel box lengths of at least 4π were needed for good convergence.

One must be careful about which other coordinates are held fixed while applying parallel periodicity, just as one must be careful to impose radial periodicity in field-line coordinates (ψ, α, z) (i.e., impose periodicity in ψ while holding α and z fixed). As discussed in Section 4.2, trying to impose radial periodicity in the usual (ψ, θ, ζ) coordinates would miss the fact that fluctuations tend to be extended along the magnetic field, which changes direction in the the (θ, ζ) plane as ψ is varied. Similarly, though the flux-tube is rectangular in (ψ, α) coordinates, it twists into a parallelogram in physical space as one follows the flux-tube along z (Figs. 4.1 and 4.2). The fluctuations in the physical plane perpendicular to a magnetic field line should be statistically identical at all places along that field-line with the same poloidal angle ($z = 0, 2\pi, 4\pi, \ldots$), irrespective of the twisting of the flux-tube which increases without bound as $z \to \infty$. Because of this, we will assume that the fluctuations are periodic in z while holding (ψ, ζ) fixed, rather than holding the field-line coordinates (ψ, α) fixed. The reader may find it easier to visualize this in sheared slab geometry, as carried out in [HAMMETT *et al.*, 1993].

A related problem is that if we were to impose parallel periodicity as $A(\psi, \alpha, +z_0) = A(\psi, \alpha, -z_0)$, then *every* field line would effectively be a rational field line that connected to itself. Field lines are labeled by constant (ψ, α), and such a boundary condition causes any particles flowing out one end of the field line to flow back in the other end of the box on the same field line. This is unlike a real sheared magnetic field where the set of irrational field-lines is dense, i.e., most of the field-lines are irrational and never connect to themselves.

So, we will impose periodicity in z while holding ψ and ζ fixed (rather than

holding ψ and α fixed). Specifically,

$$A(\psi, \alpha(\theta, \zeta), z(\theta))\Big|_{\theta=N\pi} = A(\psi, \alpha(\theta, \zeta), z(\theta))\Big|_{\theta=-N\pi}$$

Rather than the form of a boundary condition in z, this can be stated as a more general periodicity relation with period $2\pi N$:

$$A(\psi, \alpha(\theta + 2\pi N, \zeta), z(\theta + 2\pi N)) = A(\psi, \alpha(\theta, \zeta), z(\theta)) \tag{4.14}$$

Physically, this is equivalent to considering two (ψ, ζ) planes cutting through the flux tube, at $z = \theta$ and at $z = \theta + 2\pi N$, and assuming that the turbulence is (statistically) identical in those two planes. To evaluate this periodicity constraint, first substitute $\alpha = \zeta - q(\psi)\theta$, $z = \theta$ into Eq. (4.7), and take $\alpha_0 = 0$ for simplicity (it drops out), to get

$$A = \sum_{j=-\infty}^{\infty} \sum_{k=-\infty}^{\infty} \hat{A}_{j,k}(\theta, t) e^{ij\pi(\psi-\psi_0)/\Delta\psi + ik\pi\zeta/\Delta\alpha - ik\pi q(\psi)\theta/\Delta\alpha}. \tag{4.15}$$

For a thin flux-tube, we can approximate $q(\psi) \approx q_0 + (\psi - \psi_0)q'$, where $q' \equiv (\partial q/\partial\psi)_{\psi=\psi_0}$, to get

$$A = \sum_{j=-\infty}^{\infty} \sum_{k=-\infty}^{\infty} \hat{A}_{j,k}(\theta, t) e^{i\pi(\psi-\psi_0)(j/\Delta\psi - kq'\theta/\Delta\alpha) + ik\pi\zeta/\Delta\alpha - ik\pi q_0\theta/\Delta\alpha}. \tag{4.16}$$

Substituting this into Eq. (4.14) yields

$$\sum_{j=-\infty}^{\infty} \sum_{k=-\infty}^{\infty} \hat{A}_{j,k}(\theta + 2\pi N, t) e^{i\pi(\psi-\psi_0)(j/\Delta\psi - kq'(\theta+2\pi N)/\Delta\alpha) + ik\pi\zeta/\Delta\alpha - ik\pi q_0(\theta+2\pi N)/\Delta\alpha}$$

$$= \sum_{j=-\infty}^{\infty} \sum_{k=-\infty}^{\infty} \hat{A}_{j,k}(\theta, t) e^{i\pi(\psi-\psi_0)(j/\Delta\psi - kq'\theta/\Delta\alpha) + ik\pi\zeta/\Delta\alpha - ik\pi q_0\theta/\Delta\alpha}. \tag{4.17}$$

In order for this to be valid at any arbitrary value of ζ, the coefficient of each $\exp(ik\pi\zeta/\Delta\alpha)$ term must be identical:

$$\sum_{j=-\infty}^{\infty} \hat{A}_{j,k}(\theta + 2\pi N, t) e^{i\pi(\psi-\psi_0)(j/\Delta\psi - kq'(\theta+2\pi N)/\Delta\alpha) - ik\pi q_0(\theta+2\pi N)/\Delta\alpha}$$

$$= \sum_{j=-\infty}^{\infty} \hat{A}_{j,k}(\theta, t) e^{i\pi(\psi-\psi_0)(j/\Delta\psi - kq'\theta/\Delta\alpha) - ik\pi q_0\theta/\Delta\alpha}. \tag{4.18}$$

We can make the coefficients of $(\psi - \psi_0)$ identical by shifting the j index with the substitution $j = j' + \delta j$ into the left-hand side, where

$$\delta j = 2\pi N k q' \Delta\psi / \Delta\alpha = 2\pi N k \Delta q / \Delta\alpha, \tag{4.19}$$

and where $2\Delta q = 2q'\Delta\psi$ is the change in q from one edge of the box to the other. Note that δj must be an integer, which quantizes the ratio $\Delta q/\Delta\alpha$, as discussed below. We now have

$$\sum_{j'=-\infty}^{\infty} \hat{A}_{j'+\delta j,k}(\theta + 2\pi N, t) e^{i\pi(\psi-\psi_0)(j'/\Delta\psi - kq'\theta/\Delta\alpha) - ik\pi q_0(\theta+2\pi N)/\Delta\alpha}$$

$$= \sum_{j=-\infty}^{\infty} \hat{A}_{j,k}(\theta, t) e^{i\pi(\psi-\psi_0)(j/\Delta\psi - kq'\theta/\Delta\alpha) - ik\pi q_0\theta/\Delta\alpha}. \tag{4.20}$$

For convenience, we can take the width of the simulation volume $2\Delta\alpha$ to be $1/n_0$ of the circumference in the toroidal direction,

$$\Delta\alpha = \pi/n_0, \tag{4.21}$$

where n_0 is a positive integer. Dropping the primes on j in Eq. (4.20), the parallel periodicity condition now becomes

$$\hat{A}_{j+\delta j,k}(\theta + 2\pi N, t) C_k = \hat{A}_{j,k}(\theta, t), \tag{4.22}$$

$$\delta j = kJ, \qquad\qquad J = 2n_0 N \Delta q, \tag{4.23}$$

where the phase-factor $C_k = \exp(-i2\pi N k q_0 n_0)$. Note that the requirement that j be an integer quantizes the range of q spanned by the flux tube $2\Delta q$ to be $J/n_0 N$, where J is an integer. For $q' \neq 0$, this then quantizes the radial box size since $\Delta q = q'\Delta\psi$. One can treat shearless $q' = 0$ cases as well, then $\delta j = J = 0$, and the radial box size $2\Delta\psi$ is no longer quantized and just needs to be at least a few radial correlation lengths wide. In the usual $q' \neq 0$ case, the radial position of the simulation box can always be adjusted slightly (less than one radial box width) so that $q_0 = q(\psi_0)$ is rational such that the phase-factor $C_k = 1$.

Eq. (4.22) thus expresses a modified periodicity condition on the mode amplitudes: the value of a coefficient at one end of the box is specified by the value of another coefficient (with the same k but a different j, i.e., a different θ_0, as we will describe below) at the other end of a box. This is represented graphically in

Fig. 4.3 (which uses notation introduced below). Of course computer simulations can not retain an infinite set of j's and k's. Instead, enough j and k modes are kept to be able to resolve up to a desired value of $k_\perp \rho_i$, above which the coefficients $\hat{A}_{j,k}$ are assumed to vanish. Note that $\delta j = 0$ for $k = 0$ modes, so the periodicity condition for $k = 0$ modes simplifies to $\hat{A}_{j,0}(\theta + 2\pi N, t) = \hat{A}_{j,0}(\theta, t)$.

This completes the formal specification of the boundary conditions, but we go on to express it in terms of notation often used in the ballooning transformation. It is common to introduce the "ballooning angle" $\theta_0(j,k)$, such that the radial derivative of an individual (j,k) mode of Eq. (4.16),

$$\left.\frac{\partial}{\partial\psi}\right|_{\theta,\zeta} \propto i\pi(j/\Delta\psi - kq'\theta/\Delta\alpha), \tag{4.24}$$

vanishes at $\theta = \theta_0$. Note that this definition of θ_0 employs a derivative with respect to ψ while holding θ and ζ fixed, *not* α and θ. Clearly at $\theta = \theta_0(j,k)$ the wavefronts of the j,k'th term in Eq. (4.7) are perpendicular to the ψ surfaces. Eqs. (4.21-4.24) yield

$$k\theta_0(j,k) = \frac{j\Delta\alpha}{\Delta\psi q'} = \frac{j\pi}{n_0\Delta q}. \tag{4.25}$$

θ_0 is discrete with spacing $\delta\theta_0 = j\pi/kn_0\Delta q$ that is dependent on k. Only the combination $k\theta_0$ ever appears and the limit $k = 0$ must be interpreted in terms of the discrete j sum. In particular, the turbulence can generate $k = 0$ ($\theta_0 = \infty$) modes corresponding to zonal flows which can be important in the nonlinear dynamics, so the $k = 0$ modes must be allowed to evolve self-consistently. (Likewise, one must be careful about the shearless limit $q' = 0$, where $\theta_0 \to \infty$. The field-line coordinates are still useful, but it is then better to think about the j (or k_x) label of the mode, which remains finite, rather than the θ_0 label.) Using the definition of θ_0 in Eq. (4.25), we can express the shift δj in Eq. (4.19) as a shift in θ_0 instead:

$$\Delta\theta_0 = \frac{\delta j\pi}{kn_0\Delta q} = 2\pi N. \tag{4.26}$$

Using the definition of θ_0 to denote $\hat{A}_{j,k}$ by a corresponding $\hat{A}_{\theta_0,k}$, and absorbing a phase factor which is independent of the coordinates (ψ,θ,ζ) by using $\bar{A}_{j,k} = \hat{A}_{j,k}\exp[-ikn_0(q_0\theta_0(j,k) + \alpha_0)]$, the parallel periodicity condition of Eq.(4.22) can be written in a form related to the familiar ballooning representation,

$$\bar{A}_{\theta_0+2\pi N,k}(\theta,t) = \bar{A}_{\theta_0,k}(\theta - 2\pi N, t). \tag{4.27}$$

This form of the periodicity relation is illustrated graphically in Fig. 4.3.

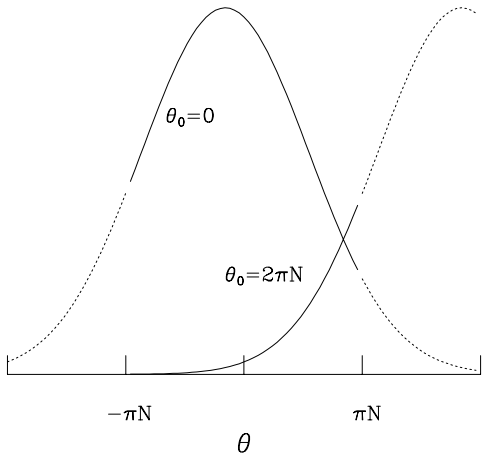

Figure 4.3: Boundary condition for $\bar{A}$ along the field line coordinate, Eq. (4.27). Different k_x modes (i.e. θ_0's) with the same k_y are connected at $\pm\pi N$, i.e. $\bar{A}_{\theta_0,k}(-\pi N)$ is connected to $\bar{A}_{\theta_0+2\pi N,k}(\pi N)$.

Using Eqs. (4.21) and (4.25) and $q(\psi) \approx q_0 + (\psi - \psi_0)q'$ (or going back to Eq. (4.7) and using q itself for the radial-like coordinate ψ), we can rewrite Eq. (4.16) as

$$A(\psi,\theta,\zeta,t) = \sum_{j=-\infty}^{\infty} \sum_{k=-\infty}^{\infty} \bar{A}_{j,k}(\theta,t) e^{ikn_0[\zeta - q(\psi)(\theta-\theta_0(j,k))]}, \tag{4.28}$$

It should be emphasized that Eqs. (4.16) and (4.28) are merely the same equations in different notation. Eq. (4.28) bears a strong resemblance to the standard ballooning representation. There are however important differences which we will discuss more fully in Section 4.5.

Eq. (4.28), when used with the periodicity relation in Eq. (4.27), is periodic in θ with period $2\pi N$. By setting $N = 1$, this can satisfy physical periodicity in θ, achieving the same result as the "sum over p" in the standard ballooning representation (see Eq. (4.32)). Thus, we are able to recover physical periodicity as does the quasiballooning approach [Dimits, 1993]. However, one should not necessarily use $N = 1$. Rather, one should use a large enough N so that the parallel box length $2z_0 = 2\pi N$ is at least several times the parallel correlation length, as

argued in the beginning of this section. This point may be confusing to those who think that $N = 1$ regular periodicity in θ should always be enforced because θ is a physical variable. This would be true if we were simulating the full torus with $n_0 = 1$. Indeed, Eq. (4.28) or (4.16) provides an expansion in a complete basis set if $n_0 = 1$ and $N = 1$. However, we are not trying to simulate the full torus, but a thin flux-tube whose width is only $1/n_0$ of the full toroidal circumference (motivated by the short wavelengths and short perpendicular correlation lengths of the turbulence). Then Eq. (4.28) represents n_0 identical copies of the simulation volume if one considers the full range of ζ, $0 \to 2\pi$. The distance along the field line in this simulation volume is parameterized by $z = \theta$. Following the flux tube along the field lines (at fixed $\alpha = \zeta - q(\psi)\theta$) from $\theta = 0$ to $\theta = 2\pi$ will not lead to the same physical location (unless q is very close to an integer) but to one of the $n_0 - 1$ identical copies of itself. Forcing periodicity at this point is undesirable (unless the parallel correlation length is indeed significantly shorter than 2π) because it is a fiction of simulating only $1/n_0$ of the toroidal direction with n_0 identical copies.

This is illustrated by Fig. 4.4, which shows a correlated volume with a parallel correlation length $\theta_c \approx 3\pi$, and a perpendicular correlation length equal to half the simulation box width, $\alpha_c = \Delta\alpha = \pi/6$. If the simulation flux tube has a parallel length of only 2π, then this correlated volume would be forced to overlap with one of the n_0 images of itself, causing artificial interference effects. By extending the simulated flux tube to a length of 4π, we allow the whole region to evolve self-consistently.

Of course, at an integer q flux surface, a simulation volume really does overlap itself within a distance $\theta = 2\pi$ and experience these interference effects. More generally, a correlated volume will overlap itself when θ increases by $2\pi N$ if $q2\pi N$ modulo 2π is less than the perpendicular correlation length α_c. This can be used to define a maximum parallel length θ_{max} which the flux-tube can be without physically overlapping itself. θ_{max} is also the maximum correlation length a correlated perturbation can have without "biting it's tail" and experiencing coherent interference effects. θ_{max} is plotted vs. $q(\psi)$ in Fig. 4.5. Note that if one simulates only $1/n_0$ of the toroidal direction, then a correlated perturbation is n_0 times as likely to run into itself or one of its images. In this case we may need to extend the parallel length of the simulated flux-tube to avoid these artificial correlations. For most

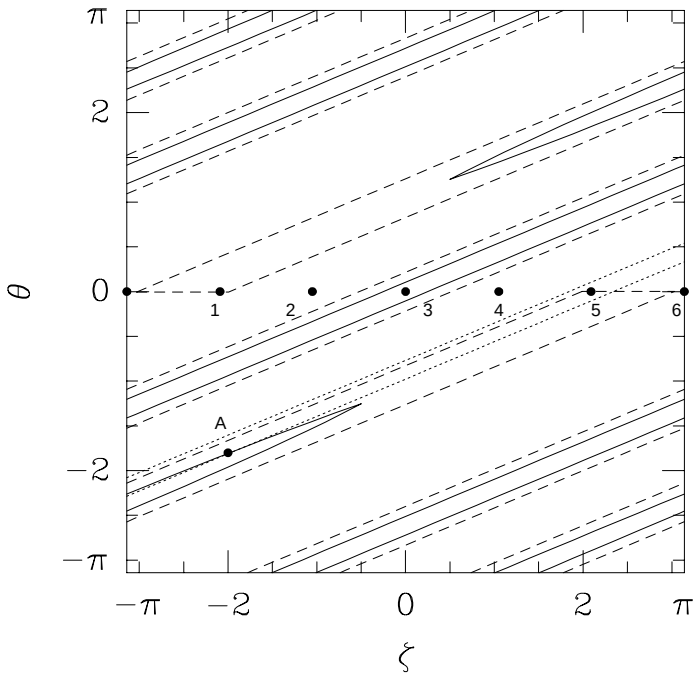

Figure 4.4: Illustration on a flux surface of a possible correlated volume of the point 3 (enclosed by the solid line, with parallel correlation length $\theta_c \approx 3\pi$), and a minimum simulation volume enclosed by the dashed line. The diagonal lines are parallel to the field lines (here $q = 2.4$). In this case the simulation volume has a toroidal width of one sixth the total toroidal circumference, i.e. n_0 in Eq. (4.21) is 6. If the potential is represented by Eq. (4.28) and Φ is made periodic in θ, there are six identical copies of the correlated volume centered at the points 1-6. The correlated volume of point 5 (dotted line) partially overlaps the correlated volume of point 3, at the point marked A. This is unphysical and can be avoided in this case by making the system periodic over 4π, $-2\pi < \theta < 2\pi$. The minimum simulation volume illustrated is for $-2\pi < \theta < 2\pi$.

of the plasma, there is no difficulty in extending the simulated flux-tube to be 2-3 times longer than 2π, without having the flux-tube physically run in to itself. Even for a simulation flux tube which spans a range of q values, for example $2\Delta q \sim 1/2$, at worst the flux tube might overlap itself briefly near an integer or half-integer q surface. As pointed out in [COWLEY *et al.*, 1991], these low-order rational surfaces occupy a small fraction of a minor radius of a tokamak and so it is very infrequent that a correlated perturbation will "bite it's tail". Furthermore, experimental evidence [ZARNSTORFF *et al.*, 1993] on tokamaks indicates that there are no unusual features near low-order rational surfaces (except when there are macroscopic MHD instabilities).

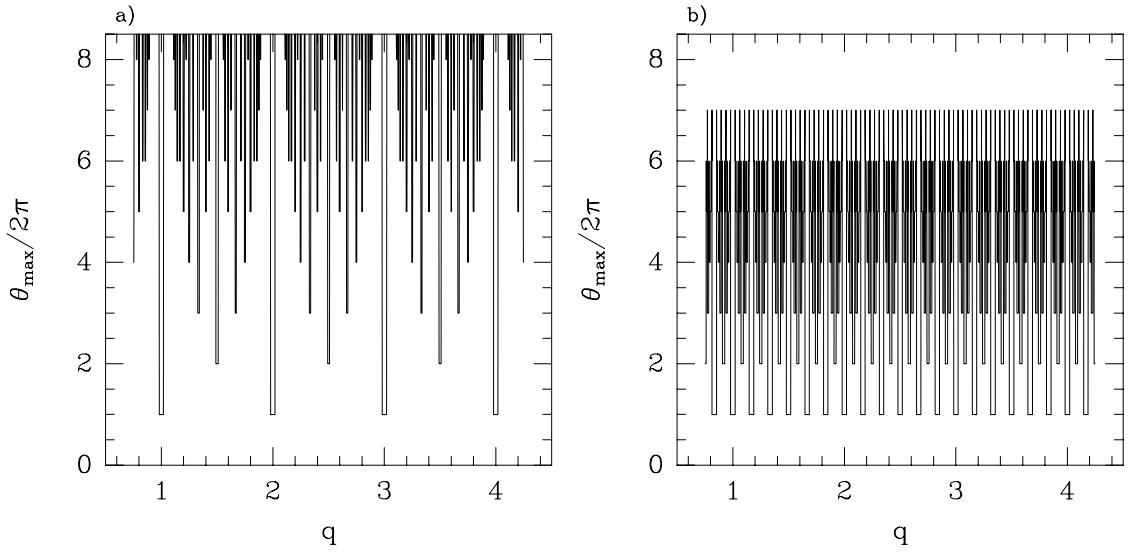

Figure 4.5: Distance along the field line, θ_{max}, at which a correlated volume (with perpendicular width $2\Delta\alpha = \pi/25$) overlaps itself, for varying q. a) For $n_0 = 1$, θ_{max} is small only near low order q surfaces. b) For $n_0 = 6$, the maximum correlation length is reduced, since the correlated volume can hit copies of itself. In this case, if the physical correlation length is longer than θ_{max}, the box must be extended and the periodicity condition relaxed.

In practice we find that the flux-tube length $2\pi N$ doesn't need to be extremely large, and $N = 2$ may usually be sufficient. For the particular cases used in Section 4.7, (Figs. 4.12 and 4.13), we find that $N = 1$ simulations produce a χ_i which is about 30% low, while $N = 2 - 4$ are virtually indistinguishable. However,

there may be other cases where an even larger N is required. In each case, one should justify the value of N *a posteriori*, by verifying that the parallel correlation functions from the simulations indeed fall off significantly in a distance $2\pi N$, and/or by carrying out convergence studies with different values of N (just as convergence with the size of the box in the other 2 directions should also be studied). Again, the fundamental assumption in all of this is that it is probably sufficient (and most efficient) to use a simulation volume which is just a few correlation lengths in all 3 directions.

4.4 Boundary Conditions for Particle Simulations

Particle simulations can also take advantage of an optimum flux-tube simulation volume using the field-line coordinates (ψ, α, z) described in Section 4.2. Field quantities such as the electrostatic potential can be represented by the Fourier series Eq. (4.7), with the parallel boundary conditions given by Eq. (4.22), or equivalently, Eq. (4.27).

For the particles, we must specify the location where a particle will reenter the box after passing through an edge of the box. The particle's velocity should not be changed. In the perpendicular directions ψ and α, standard periodicity is used. In the parallel direction, z, periodicity is applied while holding ψ and ζ fixed (rather than holding the field-line coordinates ψ and α fixed), for the reasons described at the beginning of Section 4.3. To quantify this, first recall the definitions $\alpha = \zeta - q(\psi)\theta$, and $z = \theta$. If a particle exits the box at the position $(\psi_1, \alpha_1, z = +\pi N)$, where $\alpha_1 = \zeta_1 - q(\psi_1)\pi N$, then it will reenter the opposite side of the box at $(\psi_2, \alpha_2, z = -\pi N)$, where $\psi_2 = \psi_1$, and $\alpha_2 = \zeta_1 + q(\psi_1)\pi N$. Thus the particle will be shifted in α by the amount

$$\delta\alpha = \alpha_2 - \alpha_1 = q(\psi_1)2\pi N \text{ modulo } 2\Delta\alpha \tag{4.29}$$

Where the modulo operation accounts for the fact that if this shift in α causes α_2 to fall outside the range of the box, $-\Delta\alpha < \alpha < \Delta\alpha$, then the particle has fallen into a periodic copy of the original box, and is simply shifted by a multiple of $2\Delta\alpha$ back into the simulation domain. Expanding $q(\psi) = q_0 + (\psi - \psi_0)q'$, using Eqs.(4.21) and (4.23), and introducing an integer K to reproduce the $2K\Delta\alpha$ shift of the modulo

function, we find that

$$\frac{\delta\alpha(\psi)}{2\Delta\alpha} = q_0 N n_0 + K + J\frac{(\psi-\psi_0)}{2\Delta\psi}. \tag{4.30}$$

As discussed after Eq. (4.23), $q_0 N n_0$ can usually be assumed to be an integer. At the outer edge of the box, $\psi = \psi_0 + \Delta\psi$, the box has twisted by $J/2$ box lengths in the α direction, and by $-J/2$ box lengths at the inner edge of the box, $\psi = \psi_0 - \Delta\psi$. Thus J represents the integer number of box widths in α that the box has twisted from one end in z to the other end. This is illustrated for $J = 2$ in Fig. 4.6. In this figure, $q_0 N n_0$ is assumed to be an integer for simplicity, so the center of the box is at the same physical point at $\theta = \pm\pi N$. In general, the ends of the box will overlap with periodic copies of the original box. (It may be easier to visualize this in a box which spans $\psi_0 < \psi < \psi_0 + 2\Delta\psi$, rather then being centered around ψ_0. Then the inner edge of the box at ψ_0 is stationary, and the outer edge at $\psi_0 + 2\Delta\psi$ will be twisted by J box widths.)

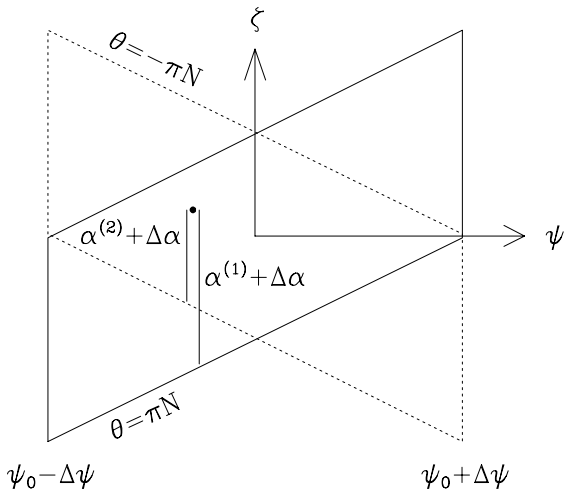

Figure 4.6: Boundary conditions in the parallel direction. At $\theta = 0$, the simulation box is rectangular in ζ and ψ. The twisted ends of the box at $\theta = \pi N$ (solid) and $\theta = -\pi N$ (dashed) are shown. If a particle leaves the $\theta = \pi N$ end of the box at $\alpha^{(1)}$, it reenters the $\theta = -\pi N$ end of the box at $\alpha^{(2)}$, given by Eq. (4.29).

To summarize, if a particle:

leaves the box from	then it reenters at
$(\psi_0 + \Delta\psi, \alpha, z)$	$(\psi_0 - \Delta\psi, \alpha, z)$
$(\psi, +\Delta\alpha, z)$	$(\psi, -\Delta\alpha, z)$
$(\psi, \alpha, +\pi N)$	$(\psi, \alpha + \delta\alpha, -\pi N)$

The equivalent particle boundary conditions can also be stated for the (x,y,z) coordinates of Eq. (4.12). If a particle leaves the end of the box at $(x_1, y_1, z = +\pi N)$, it reenters at $(x_1, y_2, z = -\pi N)$, where

$$\delta y = y_2 - y_1 = -(q_0 N n_0 2\Delta y + J\Delta y\, x/\Delta x) \,\text{modulo}\, 2\Delta y, \tag{4.31}$$

the analogue of Eq. (4.29). The integer $J = 2\pi N \hat{s} \Delta x/\Delta y$, (where $\hat{s} \equiv (r_0/q_0)(\partial q/\partial r)_{r=r_0}$) measures the number of twists of the box in the y direction from one end in z to the other. Thus, if a particle:

leaves the box from	then it reenters at
$(\Delta x, y, z)$	$(-\Delta x, y, z)$
$(x, \Delta y, z)$	$(x, \Delta y, z)$
$(x, y, +\pi N)$	$(x, y + \delta y, -\pi N)$

Of course all of the above boundary conditions are reversible, i.e., if a particle leaves at $(-\Delta x, y, z)$, it will reenter at $(\Delta x, y, z)$, etc.

4.5 The Ballooning Transformation and its Relation to Flux Tube Simulation

The linear theory of short perpendicular wavelength instabilities in tokamaks has been developed largely in terms of the so called "Ballooning Transformation" [Connor *et al.*, 1979; Glasser, 1977; Lee and Van Dam, 1977]. In this section we will discuss the relationship of the "Ballooning Transformation" to our flux tube simulation scheme. In Ballooning theory a single eigenmode is represented as:

$$\Phi_n(\psi, \theta, \zeta, t) = \sum_{p=-\infty}^{\infty} e^{-i\omega t + in\zeta - inq(\psi)(\theta - \theta_0 + 2\pi p)} \hat{\Phi}_{n,\theta_0}(\theta + 2\pi p, \psi), \tag{4.32}$$

where $\theta_0 = \theta_0(\psi)$ and $\hat{\Phi}_{n,\theta_0}(\theta, \psi)$ depend on ψ. The toroidal mode number n is any large integer. The variation in θ and ψ of the exponential is large whereas the variation of θ_0 and $\hat{\Phi}$ is finite. In lowest order in an expansion in $1/nq$ one obtains a differential equation in θ for $\hat{\Phi}_{n,\theta_0}(\theta, \psi)$. This equation is solved with θ_0

a parameter and with the boundary conditions $\hat{\Phi} \to 0$ as $|\theta| \to \infty$, so the sum over p can converge. Periodicity in θ is recovered by the p summation in Eq. (4.32). A lowest order approximation to the eigenvalue $\omega_n(\theta_0, \psi)$ is obtained on each surface. In higher order the eigenvalue is quantized by solving radial differential equations. Much has been written about this higher order procedure to find the radial behavior and we cannot do justice to the subtleties here [CONNOR *et al.*, 1993; TAYLOR *et al.*, 1993]. Let us consider instead a narrow radial annulus $\psi_0 - \Delta\psi < \psi < \psi_0 + \Delta\psi$. Let Φ be periodic in ψ over $2\Delta\psi$ at constant $\alpha = \zeta - q(\psi)\theta$ and θ; then we can represent the radial variation of Φ in a Fourier series in ψ, with $n\theta_0 = l\pi/\Delta q$, i.e. the ψ variation of $\theta_0(\psi)$ and $\hat{\Phi}_{n,\theta_0}(\theta, \psi)$ are combined into a discrete series in θ_0. Thus one could write for an arbitrary perturbation in this annulus:

$$\Phi(\psi, \theta, \zeta, t) = \sum_{n=-\infty}^{\infty} \sum_{l=-l_0+1}^{l_0} \sum_{p=-\infty}^{\infty} e^{in\zeta - inq(\psi)(\theta+2\pi p) + il\pi(\psi-\psi_0)/\Delta\psi} \bar{\Phi}_{n,l}(\theta + 2\pi p, t), \tag{4.33}$$

where we have rescaled $e^{ilq_0\pi/q'\Delta\psi}\hat{\Phi}_{n,l} = \bar{\Phi}_{n,l}$. The p summation makes this expression manifestly periodic in θ. Expanding $q(\psi)$, so $\exp[-inq2\pi p + il\pi(\psi-\psi_0)/\Delta\psi] = \exp[-inq_0 2\pi p + i\pi(l - 2pn\Delta q)(\psi - \psi_0)/\Delta\psi]$, it is clear that in this summation we need only take $|l| \le l_0 = n\Delta q$ since otherwise the p and l sums duplicate terms. This restricts the bandwidth in ψ of the perturbations in ballooning space, and makes the ballooning transformation unique [HAZELTINE and NEWCOMB, 1990].

If we set $n_0 = 1$ in Eq. (4.28) and $N = 1$ in Eqs. (4.22) and (4.23) we obtain an exactly equivalent representation to Eq. (4.33). To see this we note that the j in Eq. (4.28) and p and l in Eq. (4.33) are related by $j = l - 2pl_0$ and $\delta j = 2l_0$, and we set $k = n$. Thus the $-\pi < \theta < \pi$ range of the $\bar{\Phi}_{n,l}$ modes with $|l| < l_0$ correspond to the $\bar{A}_{j,k}$ modes with $|j| < \delta j/2$ (defined only from $-\pi < \theta < \pi$ for $N = 1$). The $\bar{A}_{j,k}$ modes with $|j| > \delta j/2$ correspond to the $-\pi - 2\pi p < \theta < \pi - 2\pi p$ range of the $\bar{\Phi}_{n,l}$ modes with $p = (j - l)/\delta j$. The boundary condition Eq. (4.22) makes this series of $\bar{A}_{j,k}$ modes (for all j) identical to $\bar{\Phi}_{n,l}$ (for $|l| < l_0$) defined on the extended domain $-\infty < \theta < \infty$ (when $n_0 = N = 1$).

The boundary condition Eq. (4.22) simplifies the evaluation of the $\mathbf{E} \times \mathbf{B}$ nonlinearities compared to the usual ballooning representation. The simple form Eq. (4.6) is easy to evaluate using a pseudospectral method. A fully spectral method remains in $\mathbf{k}$ space at all times, so the nonlinear terms become convo-

lutions in $\mathbf{k}$ space and require of order $N_x^2 N_y^2 N_z \sim N^5$ operations. By using Fast Fourier Transforms (FFTs), the pseudospectral method reduces the operations to $N_x N_y N_z (\log_2 N_x + \log_2 N_y) \sim N^3$ resulting in a very significant savings for large N.

In the ballooning representation (i.e. using Eq. (4.33) to represent the perturbations) the nonlinear terms involve sums over p [FRIEMAN and CHEN, 1982]:

$$(\mathbf{v}_E \cdot \nabla A)_{n,l}(\theta) = \frac{c}{2} \sum_{n'+n''=n} \sum_{l'} \sum_{p',p''} e^{-2\pi i q_0 (n'p'+n''p'')} n' n'' q' [2\pi(p''-p') + \theta_0' - \theta_0''] \times \tag{4.34}$$
$$\left[\bar{\Phi}_{n',l'}(\theta + 2\pi p') \, \bar{A}_{n'',l''}(\theta + 2\pi p'') - \bar{A}_{n',l'}(\theta + 2\pi p') \, \bar{\Phi}_{n'',l''}(\theta + 2\pi p'') \right],$$

where $l'' = l - l' + 2\Delta q(n'p' + n''p'')$ and $\theta_0(n,l) = l\pi/n\Delta q$. Again $|l'| \le |n'|\Delta q$ and $|l''| \le |n''|\Delta q$, and $\bar{A}$ and $\bar{\Phi}$ are defined on an infinitely extended θ domain, without the boundary condition Eq. (4.22). This expression differs slightly from earlier literature since we are using a discrete representation in ψ, and have implicitly used the inverse ballooning transformation [HAZELTINE and NEWCOMB, 1990]. If the mode width in θ is less than π, the sums over p appear to be a small effect, and are usually neglected in nonlinear calculations using the ballooning representation. This conclusion may be misleading. Noting that in Eq. (4.33) $k_x = j\pi/\Delta x = (l - 2pl_0)\pi/\Delta x$ and $k_y = -n\pi/\Delta y = -nq_0/r_0$, we see that in the standard ballooning representation, only a wedge of $\bar{\Phi}_{n,l}$'s in (k_x, k_y) space are evolved, $-n\Delta q < l < n\Delta q$ (for $n \neq 0$), and the rest of $\mathbf{k}$ space is filled by the sum over p. For small n the range of k_x's evolved is small, so it may take many terms in the p sum to reach moderate k_x's. The wedge of modes evolved in the ballooning representation are the open circles in Fig. 4.7, while our approach evolves a rectangle of modes in k_x and k_y, up to $k_y\rho_i \approx 1$ and at least $k_x\rho_i \approx 1$ (both the circles and the dots in Fig. 4.7). This figure corresponds to the mode arrangement of the runs in Fig. 4.13, where the shear is very weak ($\hat{s} = 0.1$), $\Delta x \approx 1.4\,\Delta y$, $k_y^{\max}\rho_i \approx 1$, and $k_x^{\max}\rho_i \approx 1.2$, so $J = N$. The nonlinear interaction between a mode (k_x, k_y) within the $p = 0$ wedge and a mode outside the wedge (the square box in Fig. 4.7, for example) could be strong, even if its linearly most unstable mode structure (of many eigenmodes in θ) is centered a long distance down the field line. For low k_y and large k_x one would have to include many p's to capture this interaction (in this case, nine). In our nonlinear simulations, we do see modes outside the $p = 0$ wedge excited to significant amplitudes.

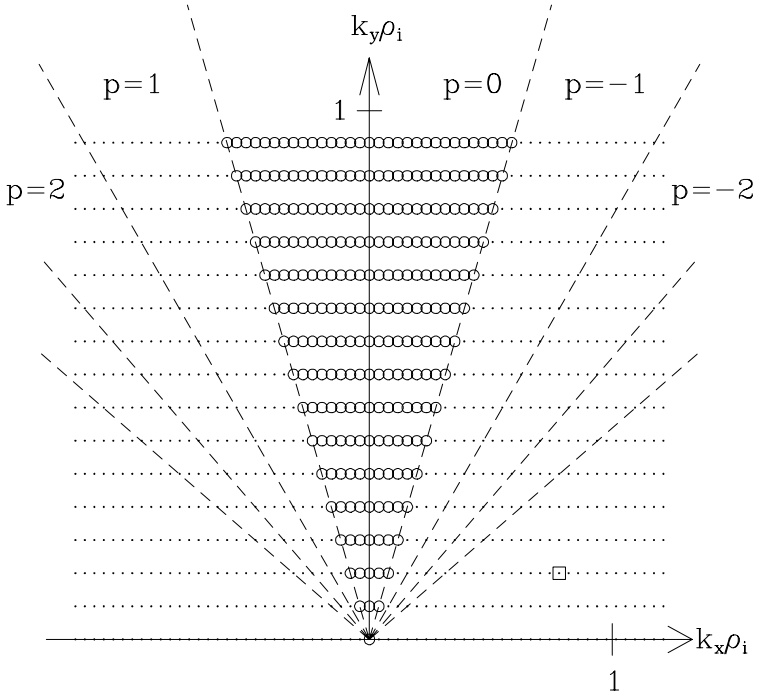

Figure 4.7: The wedge of k_x, k_y modes evolved in the ballooning representation (open circles), and the rectangle of modes evolved in our approach (circles and dots). To recover the nonlinear interaction between the $p = 0$ modes and the mode marked by the square box, nine terms in the p sum of Eq. (4.34) are needed, even though $k_x \rho_i \approx 0.8$ for this mode.

While the usual $\mathbf{k}_\perp{}' \times \mathbf{k}_\perp{}'' \cdot \hat{\mathbf{b}}$ nonlinearity can be efficiently evaluated pseudospectrally, it is not obvious that the ballooning nonlinearity, with its sums over p, can be. However, since our representation is equivalent to the ballooning representation (if $n_0 = N = 1$), it automatically includes the sums over p in the nonlinearity. Thus the most efficient way to numerically evaluate the nonlinear terms using the ballooning representation, if one were forced to, is probably to break the θ domain into segments of 2π, fill a rectangle in (k_x, k_y) space with the sum over p, and apply the pseudospectral method to Eq. (4.6). Our representation automatically accomplishes all of this. Our representation should also be more convenient for analytic calculations, since the nonlinearity takes a simple form, and the choice of θ_0's, or k_x's, is well defined.

4.6 Axisymmetric Low-β Equilibrium

We now specialize to the case of a low-β, large aspect ratio, axisymmetric torus with circular concentric flux surfaces. In the usual r, θ, ϕ, coordinates (minor radius, poloidal angle, and toroidal angle), $\nu = -(qr/R_0)\sin\theta$ in Eq. (4.10), and

$$\mathbf{B} = B(\hat{\mathbf{e}}_\phi + \frac{r}{qR_0}\hat{\mathbf{e}}_\theta), \tag{4.35}$$

where $B = B_0R_0/R$, R is the distance from the axis of symmetry, and R_0 is the major radius. The ζ defined in Eq. (4.10) is the usual toroidal angle, ϕ, to lowest order in r/R_0; we will only keep terms to lowest order in r/R_0 here. Near ψ_0, we can expand $\psi - \psi_0 = \int_{r_0}^{r} dr B_0 r/q \simeq (r - r_0)B_0 r_0/q_0$. Then Eq. (4.12) becomes, choosing $\alpha_0 = 0$:

$$x = r - r_0, \qquad y = \frac{r_0}{q_0}\left[q(r)\theta - \phi\right], \qquad z = \theta. \tag{4.36}$$

In these variables, the parallel derivative becomes, using Eq. (4.2) with $J^{-1} \simeq q_0R_0/B_0$,

$$\hat{\mathbf{b}}\cdot\nabla A = \frac{1}{q_0R_0}\frac{\partial A}{\partial\theta}, \tag{4.37}$$

and the perpendicular gradient is:

$$\nabla_\perp A = \left(\frac{\partial A}{\partial x} + \hat{s}\theta\frac{\partial A}{\partial y}\right)\hat{\mathbf{e}}_r + \frac{\partial A}{\partial y}\hat{\mathbf{e}}_\theta. \tag{4.38}$$

The linear ω_* terms, arising from $\mathbf{E}\times\mathbf{B}$ convection of the equilibrium, using Eq. (4.6), are:

$$\mathbf{v}_E\cdot\nabla A_0 = \frac{c}{B^2}\mathbf{B}\times\nabla\Phi\cdot\nabla A_0 = c\frac{\partial A_0}{\partial\psi}\frac{\partial\Phi}{\partial\alpha} = -\frac{c}{B_0}\frac{\partial A_0}{\partial r}\frac{\partial\Phi}{\partial y}. \tag{4.39}$$

The nonlinear $\mathbf{E}\times\mathbf{B}$ terms are:

$$\mathbf{v}_E\cdot\nabla A = \frac{c}{B_0}\left(\frac{\partial\Phi}{\partial x}\frac{\partial A}{\partial y} - \frac{\partial\Phi}{\partial y}\frac{\partial A}{\partial x}\right). \tag{4.40}$$

Using Eq. (4.5), with $|\nabla\alpha|^2 \simeq q_0^2(1+\hat{s}^2\theta^2)/r_0^2$, $\nabla\alpha\cdot\nabla\psi \simeq -B_0\theta\hat{s}$, and $|\nabla\psi| \simeq B_0r_0/q_0$:

$$\nabla_\perp^2 A = \frac{\partial^2 A}{\partial y^2}(1+\hat{s}^2\theta^2) + 2\hat{s}\theta\frac{\partial^2 A}{\partial x\partial y} + \frac{\partial^2 A}{\partial x^2}. \tag{4.41}$$

Using the definition of θ_0 in Eq. (4.25), $k_x = -k_y \hat{s}\theta_0$,

$$\nabla_\perp^2 A = -k_y^2 A[1 + \hat{s}^2(\theta - \theta_0)^2]. \tag{4.42}$$

That this takes the usual ballooning form should come as no surprise, given the discussion in Section 4.5. The combined ∇B and curvature drifts can be written:

$$\mathbf{v}_d = \frac{v_\parallel^2 + v_\perp^2/2}{\Omega B^2}\mathbf{B} \times \nabla B + \frac{4\pi v_\parallel^2}{\Omega B^2}\hat{\mathbf{b}} \times \nabla p, \tag{4.43}$$

where the ∇p term is negligible in this low-β equilibrium. For an axisymmetric $\mathbf{B}$, $\partial B/\partial\alpha = 0$; for our low-$\beta$ equilibrium we also have $\partial B/\partial\psi \simeq -(q_0/r_0R_0)\cos\theta$, $\partial B/\partial z \simeq (B_0 r_0/R_0)\sin\theta$, $\mathbf{B}\cdot\nabla\alpha\times\nabla z \simeq -(B_0 q_0/r_0^2)\hat{s}\theta$, and $\mathbf{B}\cdot\nabla\psi\times\nabla z \simeq B_0^2/q_0$. Thus using Eq. (4.4),

$$\begin{aligned}\mathbf{v}_d\cdot\nabla A &= -\frac{v_\parallel^2 + v_\perp^2/2}{\Omega_0 R_0}\left[\frac{\partial A}{\partial y}\cos\theta + \frac{\partial A}{\partial y}\hat{s}\theta\sin\theta + \frac{\partial A}{\partial x}\sin\theta\right], \\ &= -ik_y A\frac{v_\parallel^2 + v_\perp^2/2}{\Omega_0 R_0}\left[\cos\theta + \hat{s}(\theta - \theta_0)\sin\theta\right],\end{aligned} \tag{4.44}$$

for $k_y \neq 0$ and $\mathbf{v}_d\cdot\nabla A = (-ik_x A/\Omega_0 R_0)(v_\parallel^2 + v_\perp^2/2)\sin\theta$, for $k_y = 0$. Other terms in the equations, such as $\nabla\cdot\mathbf{v}_E$ and $(\hat{\mathbf{b}}\cdot\nabla\hat{\mathbf{b}})\cdot\mathbf{v}_E$ can also be written in the form Eq. (4.44), as shown in Section 2.1.

4.7 Simulation Results

This coordinate system has been implemented in nonlinear toroidal gyrofluid simulations. Some simulation results are presented in this section to describe practical computational issues and to test some the assumptions implicit in flux tube simulations. These nonlinear results will be discussed more fully in Chapter 5. This chapter specifically focuses on testing the flux tube simulation method, so for computational expediency the less accurate four moment model is used (as opposed to six), and the electrons assumed to be adiabatic. For historical reasons, these simulations used an older version of the four moment toroidal gyrofluid equations, which are given in Appendix A for completeness.

There are two ways to implement the boundary condition Eq. (4.22). Because our equations involve $|k_\parallel|$ Landau damping terms (equivalent to a non-local integral

operator in real space [HAMMETT and PERKINS, 1990]), it is easiest to Fourier transform from θ to $k_\parallel$ to evaluate the parallel terms. However, over the θ domain, each mode is not periodic with itself, but with a different mode. This mode will in turn be connected to another mode, etc. The most accurate way to implement the boundary condition is then to line up all the j modes connected by the boundary condition onto an extended θ domain and Fourier transform in $k_\parallel$ over this domain. Because the computational grid is rectangular in k_x and k_y, the length in θ of this extended domain will be longer at lower k_y. Then we evaluate the $k_\parallel$ terms, transform back to θ, and extract each j mode from its position on the extended θ domain. An alternative method is to add equal length extensions in θ to each (k_x, k_y) mode, as shown in Fig. 4.3, and copy the part of $\hat{A}_{j+\delta j,k}(\theta)$ within $-\pi N < \theta < \pi N$ onto the extension ($|\theta| > \pi N$) of $\hat{A}_{j,k}$ before transforming to $k_\parallel$. Since we have a finite number of k_x's, not all modes will have a mode to connect to at $j + \delta j$. In this case $\hat{A}_{j,k}$ is zeroed in the extension, preserving periodicity. We have arranged the box so the mode amplitudes are small where this is necessary (at large k_y). The second approach ("the equal-length extension method") is easier to implement and to parallelize on computers, since all the FFTs in θ have the same length. But it may be linearly less accurate than the first method ("the multiply-connected method") if there are low k_y modes which extend much further along the field line than even the extension region. (This is related to the fact that the minimum non-zero $|k_\parallel|$ which can resolved for the Landau-damping operator is given by $2\pi/L_\parallel$, where $L_\parallel$ is the parallel box length including the extension region.) This difference is probably less important in nonlinear runs where the relevant parameter for determining the parallel box length is the parallel correlation length and not a linear mode width. In practice, we have observed no significant differences between these two methods in the nonlinear simulations done to date. The issues of an extension region (or the filtering described next) are ignorable for a particle or Vlasov simulation, since they do not require evaluation of $k_\parallel$ and can directly use the boundary conditions in Section 4.4.

There is another implementation detail involving the parallel FFTs. Note that the $\theta_0 = 2\pi N$ mode in Fig. 4.3 has a large amplitude at the right-hand side of the extended domain, and is not naturally periodic with itself at the left-hand end of the figure where it is zero. Fourier transforms assume periodicity, so there is effectively a sharp discontinuity for this mode across the endpoints in θ which

introduces high-$k_{||}$ components into the solution. These high $k_{||}$ components are Landau-damped, but a small amount of high $k_{||}$ oscillations can propagate from the ends of the extended domain into the physical region $-N\pi < \theta < N\pi$. This high $k_{||}$ noise is reduced as the extension region is made longer, but convergence can be greatly accelerated by smoothly filtering the modes to zero near end points of the extended box. We use a filtering window which is 1 in most of the domain, and goes to zero smoothly near ends of the full (extended) domain as $2x^2/(1+x^4)$, where $x = (\theta - \theta_{\rm end})/\theta_{\rm width}$ is a normalized distance from the end points. A filtering width $\theta_{\rm width}$ of 1/2 to 1/4 of the width of the extension regions appears sufficient. Thus a typical run with a physical θ domain from -2π to 2π might use a fully extended domain of $-3\pi < \theta < 3\pi$, and the filter begins to turn on within $\pi/2$ of the endpoints at $\theta_{\rm end} = \pm 3\pi$. In practice, though the filtering is useful for reducing the small amount of high $k_{||}$ errors sometimes seen linearly (particularly for low k_y modes at low shear which are extended along the field line), no statistically significant differences have been observed in the nonlinear runs with or without this filtering.

To test the small-scale assumption, we present two simulations, one with perpendicular dimensions ($L_x = 85\rho_i$, $L_y = 100\rho_i$), and one with double the box size ($L_x = 170\rho_i$, $L_y = 200\rho_i$). That these simulations give similar results indicates that the small flux tube may be capturing the essence of the turbulence. It is a necessary but not sufficient test, as discussed in Section 4.8. The physical parameters are taken from TFTR L-mode shot #41309: $\eta_i = 4$, $L_n/R = 0.4$, $\hat{s} = 1.5$, $q = 2.4$, $T_i = T_e$, $\rho_i = 0.14$cm, $L_n = 103$cm, and the computational box is centered at $r_0 = 53$cm. The box sizes then correspond to $n_0 = 10$ for the small box and $n_0 = 5$ for the large box. Both simulations use 64 grid points along the field line coordinate θ. Using 128 grid points along θ gives essentially the same results. For these runs, $N = 2$, so the physical θ domain extends from -2π to 2π. The equal length (π) extension method (for a total extended θ domain from -3π to 3π) was used to implement the parallel boundary condition.

We use a spectral representation in x and y, with $\pm$ 42 k_x modes and $\pm$ 15 k_y modes for the small simulation and $\pm$ 63 k_x modes and $\pm$ 21 k_y modes for the large simulation, not counting additional modes added at high k for dealiasing. The modes are evenly spaced such that $k_y^{\rm max}\rho_i \approx 1$ and $k_x^{\rm min} \approx k_y^{\rm min}$, making the

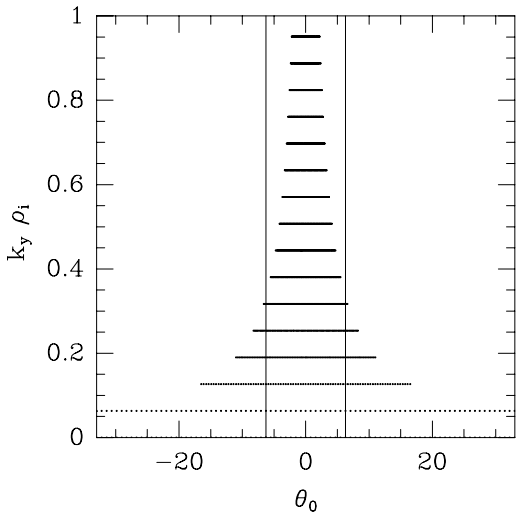

Figure 4.8: Distribution of θ_0's for the small run. The solid lines denote the ends of the computational domain in θ.

computational domain roughly square in x and y. For $N > 1$, it is necessary to include more k_x's to include unstable modes localized near $\theta = \pm 2\pi$, $\pm 4\pi$, etc., in the bad curvature regions (i.e. modes with θ_0's near $\pm 2\pi$, $\pm 4\pi$, etc.). The modes tend to be localized along the field line near θ_0, so ideally one would like to include enough k_x's to cover the range $-\pi N < \theta_0 < \pi N$ for all k_y's. This is very expensive at high k_y, where the spacing in θ_0 gets small, since $\theta_0 = -k_x/\hat{s}k_y$. We arrange our modes in k space so that the θ_0's cover the θ domain for low k_y's, but not high k_y's, as shown in Fig. 4.8 for the smaller simulation. This implies $k_x^{\max} \gg k_y^{\max}$ for $N > 1$ and $\hat{s} \approx 1$. Since most of the energy is at $k_y\rho_i < 1/2$, the missing θ_0's at high k_y have very little effect.

Fig. 4.9 shows contours of electrostatic potential in the (x,y) plane at $\theta = 0$ (the outer midplane of the torus), for both runs at saturation. It is apparent that although the box was doubled, the dominant scale didn't change. This is also evident from the spectra in Fig. 4.10, also at $\theta = 0$, where $|\Phi|^2(k_x) = \sum_{k_y} \Phi_{k_x,k_y}\Phi^*_{k_x,k_y}$, $|\Phi|^2(k_y) = \sum_{k_x} \Phi_{k_x,k_y}\Phi^*_{k_x,k_y}$, and the low resolution spectra are reduced by a factor of two to account for mode density. Although the resolution has increased, the shape and the location of the peak in the spectrum is roughly the same. These spectra are similar to BES measurements on TFTR [Fonck *et al.*, 1993]. The large $k_y = 0$

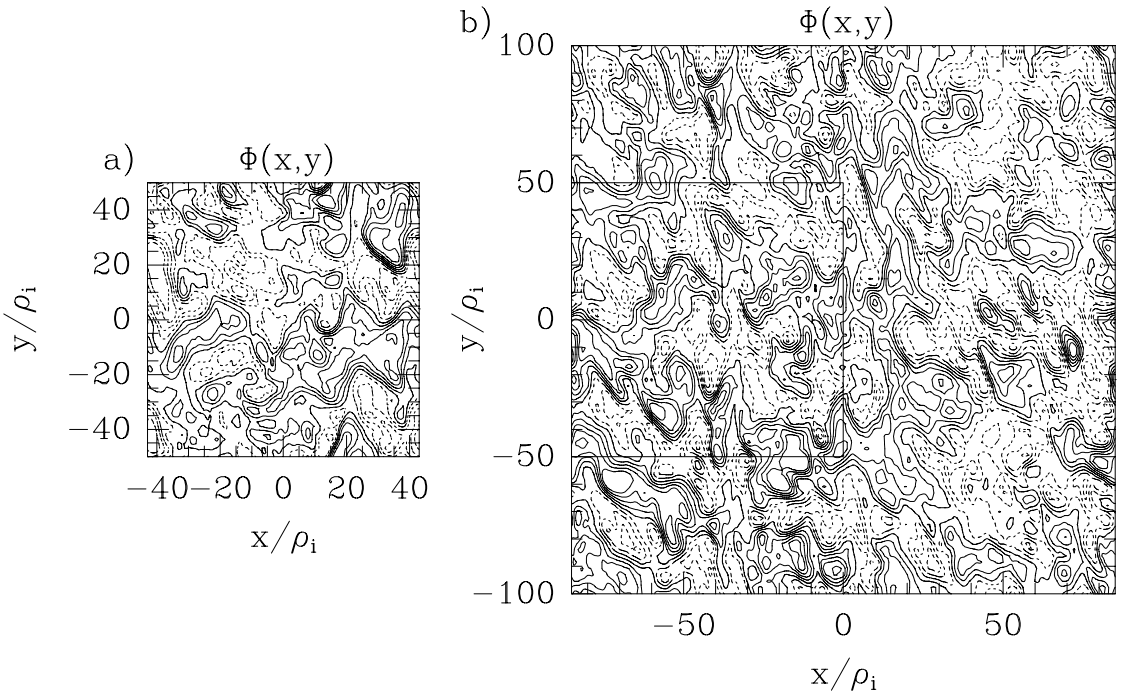

Figure 4.9: Contours of potential on the outer midplane for a) small run, and b) large run. Doubling the perpendicular simulation domain did not change the dominant scale of the fluctuations.

component is evidence of perpendicular $\mathbf{E} \times \mathbf{B}$ rotation, as discussed in [HAMMETT *et al.*, 1993]. Though there are some small differences in the spectra, the two runs agree within statistical fluctuations on global quantities such as the volume averaged RMS fluctuation levels and transport levels: $e\Phi/T_i = 15\rho_i/L_n \simeq 0.020$ and $\chi_i = 7.4\rho_i^2 v_{ti}/L_n$, averaged from $tv_{ti}/L_n = 150 - 300$. In these simulations, the electron density fluctuations on the outer midplane of the tokamak are roughly two times larger than those on the inner midplane. The evolution of χ_i for the two runs is shown in Fig. 4.11, where the statistical fluctuations are approximately 10%. This level of ion heat transport is near the experimentally measured $\chi_i = 8.8\rho_i^2 v_{ti}/L_n$, but these simulations ignore impurities and beams (usually a stabilizing effect), trapped electrons (destabilizing), and use our old four moment model (Appendix A) which gives lower transport than our more accurate six moment model. Nevertheless, this level of agreement is encouraging, and suggests that toroidal ITG turbulence is responsible for anomalous ion heat transport in tokamaks. More com-

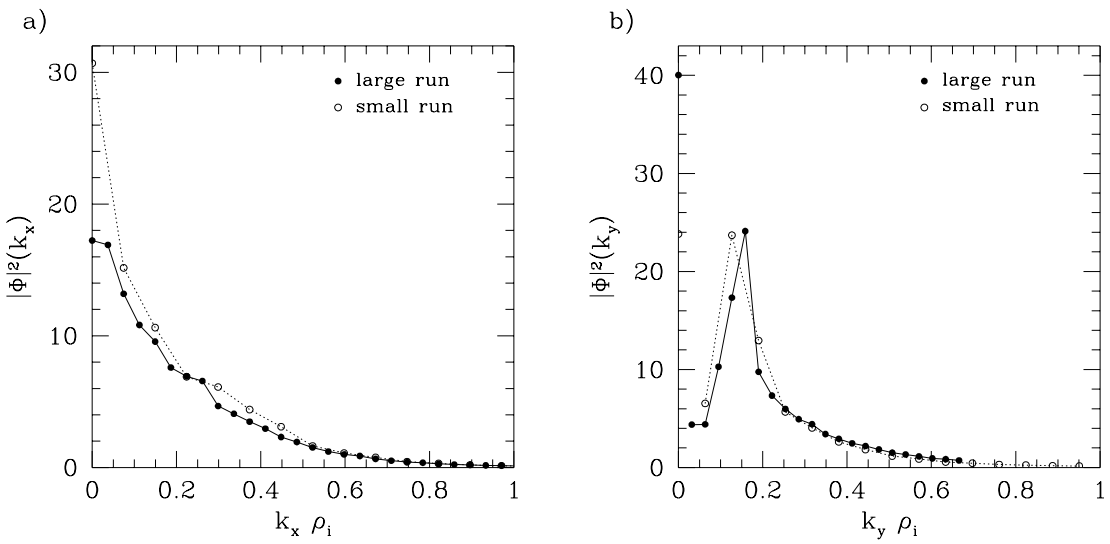

Figure 4.10: Time averaged potential spectra for both runs. a) Radial spectrum, $|\Phi(k_x)|^2$. b) Poloidal spectrum, $|\Phi(k_y)|^2$.

plete simulations are compared with experiment in Chapter 6. The transport from these toroidal simulations is about a factor of 25 larger than sheared slab simulations for the same parameters, demonstrating the importance of toroidicity. Our toroidal simulations can be run in the sheared slab limit by taking $L_n/R \to 0$ and $q/\hat{s} \to 0$ so that $L_n/L_s = L_n\hat{s}/qR$ remains finite. We should point out that our preliminary results, Fig. 4.4a of [HAMMETT *et al.*, 1993], were high by a factor of 16/3 due to a numerical error in calculating χ_i. The remaining change is due to increased resolution.

We have also performed tests varying the box length in the parallel direction. For these tests we have used the fully connected method to implement the parallel boundary conditions, for greatest accuracy, as described earlier in this section. Fig. 4.12a shows the time evolution of the volume averaged χ_i for two runs with box length $N = 1$ and 2, i.e. $\Delta\theta = 2\pi$ and 4π, with $n_0 = 10$, and other parameters as above. Fig. 4.12b shows the correlation function along the field line,

$$C(\theta, 0) = \frac{\langle \Phi(x, y, \theta)\Phi(x, y, \theta = 0)\rangle}{\langle \Phi(x, y, \theta = 0)^2\rangle}, \tag{4.45}$$

for the two runs. The averaging $\langle\ \rangle$ is over x, y, and time once the simulation has reached a quasi-steady state. If this correlation function were not averaged in x and

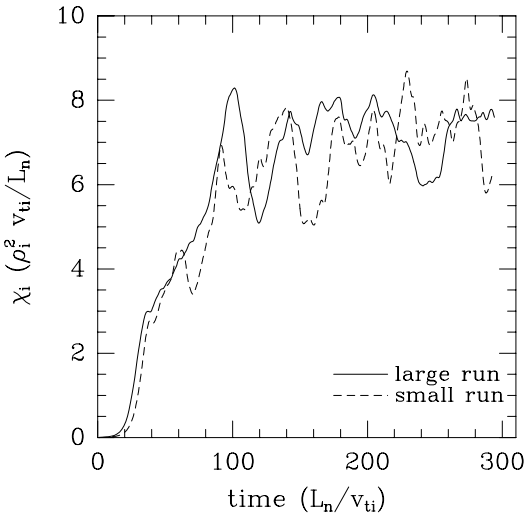

Figure 4.11: Evolution of χ_i for the large and small runs.

y (only taken along the field line passing through $x = y = 0$), it would return to one at $\theta = \pm 2\pi$ for the $N = 1$ run, because of periodicity. The Fourier transform of $C(\theta, 0)$ is the $k_\parallel$ spectrum. As discussed in Section 4.3, since $n_0 > 1$, using a box with $-\pi < \theta < \pi$, $(N = 1)$, can artificially constrain the parallel correlation length. There are significant correlations at $\theta \pm \pi$ for these parameters, indicating that this is the case, and that the box should be extended. These additional correlations in the 2π box are in some way constraining the nonlinear dynamics and reducing the flux.

It is easier to test the scaling with box length at low shear, since the turbulence at $\pm 2\pi$, $\pm 4\pi$, etc., is not at such high k_x, since $k_x = -k_y \hat{s} \theta_0$. This allows us to increase the box length and resolve the turbulence all along the box with fewer k_x modes than at high shear. Also, at low shear the linear mode structure is broader in θ, leading to slightly broader parallel correlation functions. Fig. 4.13a shows the time evolution of χ_i in four runs with box lengths $N = 1, 2, 3, 4$ or $\Delta\theta = 2\pi, 4\pi, 6\pi, 8\pi$. The physical parameters are the same as above, except $\hat{s} = 0.1$ and $q = 1.2$, and the perpendicular box size is $L_x = 160\rho_i$, $L_y = 100\rho_i$. Again, the $\Delta\theta = 2\pi$ box gives slightly lower flux, while the larger boxes all give the same flux, so the minimum box length is $\Delta\theta = 4\pi$. The correlation functions of electron density for these runs are shown in Fig. 4.13b, and are noticeably broader than in the

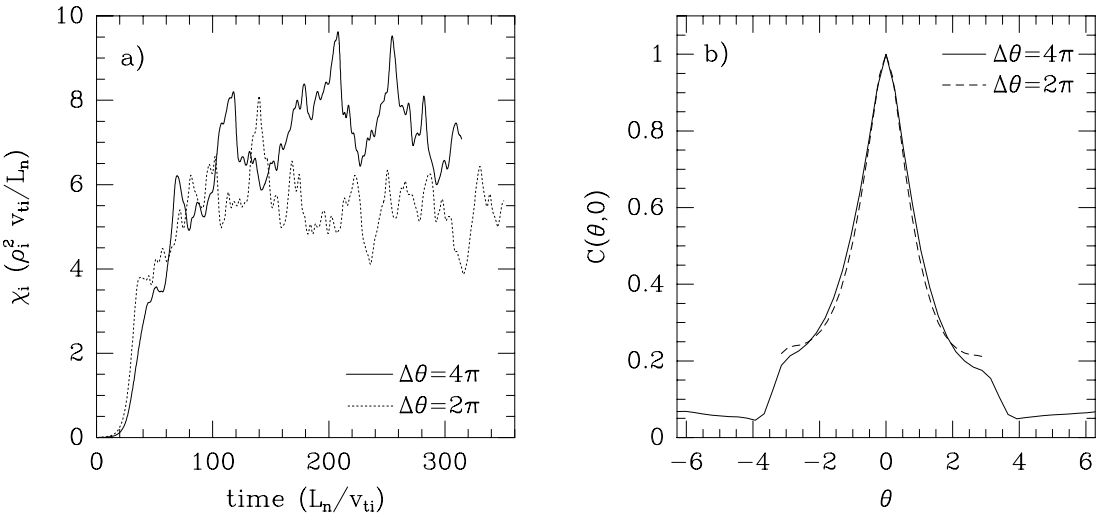

Figure 4.12: a) Evolution of χ_i for two runs with varying box length and $\hat{s} = 1.5$, $q = 2.4$ b) Correlation functions along the field line for the same two runs.

higher shear cases. Using n_e in the correlation functions removes the $k_\parallel = 0$ component present in the Φ correlation functions in Fig. 4.12b, since $n_e = \tau(\Phi - \langle\Phi\rangle)$ (see Section 5.3). For these low shear runs, the poloidal spectrum peaks at $k_y\rho_i = 0.35$, so the perpendicular correlation length is smaller than in the high shear cases. This may contribute to the slightly smaller change in flux in going from $\Delta\theta = 2\pi$ to $\Delta\theta = 4\pi$, even though the parallel correlation functions are broader. The low shear runs in Fig. 4.13 are better resolved and are easier to run longer than the high shear runs, so we expect that a 30% change in flux is typical for ITG turbulence, where $\theta_c \sim 2\pi$, when the artificial correlations are removed by using a longer box. We have also run with $\hat{s} = 0.1$ and $q = 2.4$, where $\chi_i = 7.5\rho_i^2 v_{ti}/L_n$ for $\Delta\theta = 4\pi$ and $\chi_i = 6.5\rho_i^2 v_{ti}/L_n$ for $\Delta\theta = 2\pi$. For $\hat{s} = 0.25$ and $q = 1.2$, both $\Delta\theta = 2\pi$ and $\Delta\theta = 4\pi$ give $\chi_i = 5\rho_i^2 v_{ti}/L_n$, any change is within the statistical fluctuations.

4.8 Discussion

To summarize, we are simulating a rectangular domain in (x, y, z), and using the transformation Eq. (4.12), this domain becomes a long, thin, twisting flux tube in a torus. The differential operators take the particularly useful forms Eq. (4.37-

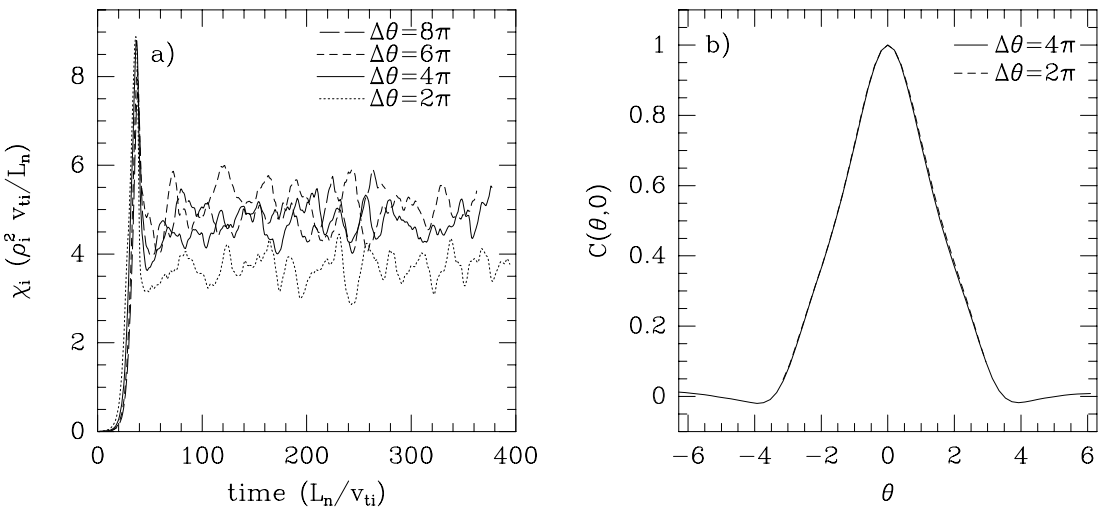

Figure 4.13: a) Evolution of χ_i for four runs with varying box length and $\hat{s} = 0.1$, $q = 1.2$. b) Correlation functions along the field line for $\Delta\theta = 2\pi$ and 4π.

4.44) in the traditional tokamak model of concentric circular flux surfaces. Our flux tube approach is also applicable to general magnetic geometry, using Eqs. (4.2,4.5-4.6) for the differential operators. (In this case the metric coefficients $\nabla\alpha$, $\nabla\psi$, and ∇z need to be specified.) The boundary condition Eq. (4.22) can make the perturbations periodic in θ, if $N = 1$, which makes this representation equivalent to the ballooning representation for a coarse grid in n, with spacing n_0. However, when $n_0 > 1$, the box must be extended in θ to avoid non-physical correlations if the parallel correlation length is longer than $2\pi qR$, i.e. $\theta_c > 2\pi$. The fundamental assumptions are that the correlation lengths (both parallel and perpendicular) are smaller than the box size, that the equilibrium gradients vary slowly across the small perpendicular extent of the box, and that the turbulence is local, i.e. driven only by the equilibrium gradients within the box.

The assumptions implicit in simulating a thin flux-tube subdomain should always be checked *a posteriori* by verifying that the simulation box is indeed at least a few correlation lengths long in each direction, so that the box is large enough for the type of turbulence under consideration. One should also verify that the results are independent of the size of the simulated flux tube (and independent of the particular choice of boundary conditions), as the flux tube is made larger than

the correlation lengths. This chapter has demonstrated that both conditions are met, at least for the particular cases considered in Section 4.7. Thus our results show the existence of a gyro-Bohm scaling regime, at least for sufficiently small $\rho_* = \rho_i/L_n$. (Our gyrofluid equations have been scaled to the gyroradius ρ_i, and the limit $\rho_i/L_n \to 0$ taken, using the usual small-scale turbulence ordering assumptions.)

While the turbulent heat conduction from our simulations is of the right order-of-magnitude to explain experimental results from the main core region of many tokamak experiments, they have a gyro-Bohm scaling while the actual experiments have a Bohm scaling [SCOTT *et al.*, 1993; PERKINS *et al.*, 1993]. (The experiments have a Bohm-like scaling with magnetic field, though the magnitude of the experimental χ_i is about two orders of magnitude smaller than Bohm's original formula $D = (1/16)cT/eB$.) Several possibilities for this discrepancy exist. One is that the experimental ρ_*, while small ($\sim 10^{-3} - 10^{-2}$), may be large enough that the radial variation of equilibrium gradients, i.e. $\omega_*(\psi)$, $\eta_i(\psi)$, etc., or equilibrium flows, may be affecting the turbulence. For very small ρ_* there is a scale separation between the turbulence, with scales of order ρ_i, and the equilibrium, with scale L_n, but if ρ_* is not small enough, the turbulence may begin to feel radial variations in the equilibrium. It is interesting to note that the BES measured [FONCK *et al.*, 1993] correlation length $\lambda_c \sim 2$ cm is of order the geometric mean between $\rho_i \sim 0.15$ cm and the minor radius $a \sim 90$ cm. Another possible explanation is that the instabilities driving the turbulence may be near marginal stability, which can mask gyro-Bohm scaling trends and, in some limits, tie the core transport scaling to edge parameters [TERRY *et al.*, 1988; BIGLARI *et al.*, 1989; KOTSCHENREUTHER *et al.*, 1993]. The experiments have gone to great pains to keep other parameters and profiles as fixed as possible while studying the ρ_* scaling, but a very sensitive dependence on some parameters (some of which are hard to measure) could also mask, at least partially, a gyro-Bohm scaling. Another possible explanation might involve non-local turbulence, where fluctuations radially propagate a significant distance from where they were generated by an instability, an effect which is currently under debate [GARBET *et al.*, 1993; MATTOR and DIAMOND, 1994].

Numerical studies of some of these effects do not necessarily require simulating the whole tokamak. Rather, one could consider a somewhat thicker flux-tube than usual, and include the radial variations of $\omega_*(\psi)$, $\eta_i(\psi)$, and other plasma

parameters over the simulated region in the governing gyrofluid (or gyrokinetic) equations. Even if simulating the full torus radially, field-line coordinates are useful to allow a coarser grid in the parallel direction, and a coarser grid in the toroidal mode number n. When the equilibrium profiles are assumed to be constant, so L_n, L_T, etc. do not vary radially (as assumed in our simulations), the linear eigenmodes are unbounded radially. In ballooning terminology, the solutions of the zeroth order eigenmode equation in $1/nq$ are independent of ψ. In a real tokamak, however, the radial profile variation determines the radial extent of the linear modes, and this radial structure is determined from a higher order equation in $1/nq$. Recently, there has been renewed interest in the solution for this radial envelope, and the modifications to the zeroth order eigenfrequencies [Connor *et al.*, 1993; Taylor *et al.*, 1993]. For longer wavelength global modes, the linear radial mode structure is also determined by the radial variation of equilibrium gradients [Tang and Rewoldt, 1993]. An alternative way to include these effects is to still use Eq. (4.7) to represent the perturbations, but to include the radial variation of equilibrium profiles. This ψ dependence will linearly couple different j modes in Eq. (4.7), which are uncoupled when the profiles have constant gradients. Then the superposition of different j (i.e. k_x) modes will determine the radial envelope of the true linear mode. However, since the nonlinear $\mathbf{E} \times \mathbf{B}$ coupling of the various $\hat{A}_{j,k}$ modes is usually much stronger than this linear coupling, it is likely that the precise radial linear mode shape is subdominant, and that the radial scale length of the turbulence is set by nonlinear processes, as suggested by [Cowley *et al.*, 1991] and [Mattor, 1991]. Comparing the order of magnitude of these effects in, for example, the density equation, we have:

$$\frac{1}{n_0}\mathbf{v}_E \cdot \nabla n_1 \sim \rho_i v_{ti} k_\perp^2 \frac{e\Phi}{T_i}\frac{n_1}{n_0},$$

$$\frac{1}{n_0}\mathbf{v}_E \cdot \nabla n_0(x) \sim \frac{\rho_i v_{ti} k_y}{L_n}\frac{e\Phi}{T_i}\left[1 + \mathcal{O}\left(\frac{x}{L_*}\right)\right],$$

Where L_* is the scale length for the radial *variation* in L_n, and is typically of order L_n. The nonlinear term is of the same order as the x independent linear term (i.e. the $\omega_*(\psi_0)$ term) in the standard gyrokinetic ordering, where $n_1/n_0 \sim \rho_i/L_n$ and $k_\perp \rho_i \sim 1$. As the linear mode widths get broader radially (in x), the x/L_* terms become more important. While the *linear* modes are broad, the typical turbulent eddy size is not much larger than $\Delta x \sim 10\rho_i$, so it would seem that the x-dependent term ($\propto \partial\omega_*/\partial\psi$) can safely be ignored, as long as $\Delta x \ll L_*$.

The effects of radial variations in the equilibrium may start becoming important if $\rho_* = \rho_i/L_*$ is large enough, and could lead to a transition from gryo-Bohm to Bohm behavior [HAMMETT *et al.*, 1994]. From the above arguments, it would seem that experiments should have small enough ρ_* to be in the gyro-Bohm regime, though TFTR seems to be in the Bohm regime [SCOTT *et al.*, 1993; PERKINS *et al.*, 1993].

Equilibrium sheared zonal flows ($k_y = 0, k_z = 0, k_x \neq 0$ flows which cause flux surfaces to rotate) can be included in our representation in several ways (one of which is presented in [WALTZ *et al.*, 1994a]), though we have not yet implemented them in our simulations. Such sheared flows can be important, particularly near the plasma edge where they appear to be responsible for the H-mode transition [BIGLARI *et al.*, 1990]. Though we are presently neglecting equilibrium-scale zonal flows, we do include the higher k_r components of the zonal flows which are generated by the turbulence itself.

For typical tokamak parameters, our reduced simulation volume can represent large computational savings. We compare rough scalings with some other methods; the results are only order of magnitude estimates. Perhaps the most straightforward way to simulate a tokamak is with the "m, n, r" representation:

$$\Phi(\psi, \theta, \zeta) = \sum_{m,n} e^{in\zeta - im\theta} \hat{\Phi}_{m,n}(\psi). \tag{4.46}$$

Since we are interested in simulating fine-scale turbulence, we need to resolve perpendicular scales of order ρ_i. If we are simulating a full torus, the range of m's must be $m \in (0, \pm 1, \ldots, \pm a/\rho_i)$. To resolve the long parallel structure, the range of n's must be $n \in (0, \pm 1, \ldots, \pm a/q\rho_i)$, where q is a representative value, around 2. The radial grid for $\hat{\Phi}_{m,n}(\psi)$ must resolve ρ_i and span the minor radius, so $r = l\Delta_r$, where $\Delta_r \sim \rho_i$ and $l \in (0, 1, \ldots, a/\rho_i)$. This gives the total number of grid points, for $a \sim 10^3 \rho_i$,

$$N_{m,n,r} \sim \frac{1}{q}\left(\frac{a}{\rho_i}\right)^3 \sim 10^9.$$

This is the same as expected from a computational grid in the physical r, θ, ζ space, where the ζ grid can be $1/q$ coarser than the r or θ directions.

By simulating a thin toroidal annulus in r, but still going all the way around in θ and ζ, the number of radial grid points is reduced by $\Delta r/a$, which for our simulations is typically $1/10$. Further, aligning the grid points with the field lines (or

nearly aligning with the field, as proposed by [DIMITS, 1993]) reduces the necessary resolution in this direction. We have found that 64 grid points along the field line is adequate, so the number of grid points for a thin annulus with a field-aligned coordinate is:

$$N_{m,n,r} \sim 64\left(\frac{a}{\rho_i}\right)^2 \frac{\Delta r}{a} \sim 10^7.$$

The next level of reduction is to also exploit the small perpendicular correlation length in the poloidal direction, which brings us to our twisting flux tube:

$$N_{\text{flux tube}} \sim 64\left(\frac{a}{\rho_i}\right)^2 \frac{\Delta r}{a}\frac{\Delta y}{a} \sim 10^6,$$

so for the simulation in Fig. 4.9a, counting modes included for dealiasing, we used:

$$N \sim 64 \times 128 \times 48 \sim 4 \times 10^5.$$

[KOTSCHENREUTHER and WONG, 1991] have proposed using the representation:

$$\Phi(r,\theta,\zeta) = \sum_{j,l} e^{il(m_0\theta - n_0\zeta)} e^{ij\theta} \hat{\Phi}_{j,l}(r - r_0), \tag{4.47}$$

which has many similarities to our representation. It is periodic in ζ with period $2\pi/n_0$ and in θ over 2π, and is therefore simulating a wedge of a toroidal annulus when the r domain is small. Thus Eq. (4.47) is numerically as efficient as the one described in this chapter, however, if $\theta_c > 2\pi$ false correlations along the parallel direction will be introduced, as discussed in Section 4.3. It is not obvious how to remedy this problem with Eq. (4.47), but with our approach one simply uses a longer box, i.e. $N > 1$.

The "quasiballooning" approach of [DIMITS, 1993] shares similar computational advantages to our method. Indeed, the quasiballooning (almost-field-line coordinates) method has many similarities to the field-line coordinates approach of [ROBERTS and TAYLOR, 1965], and [COWLEY *et al.*, 1991], upon which our representation is based, though the quasiballooning method emphasizes the perspective of a real-space radial grid while we use discrete Fourier transforms for the radial direction which illustrate its relation to the usual ballooning transformation. We have shown that physical periodicity in θ can be also be implemented with our approach, but that there are cases where one should forgo physical periodicity in

favor of a longer box (i.e., $N > 1$) to avoid false parallel correlations. As described in Section 4.3, simulating only $1/n_0$ of the toroidal direction is often justified by the short perpendicular correlation lengths of the turbulence, but that makes a perturbation extended along a field-line n_0 times as likely to "bite it's tail", which should be compensated for by making the box longer than a parallel correlation length. In principle, $N = 1$ simulations should eventually converge as the box is made large enough in the perpendicular directions (so that $n_0 \to 1$), but from the runs we have done it appears that faster convergence is obtained by allowing the box to be longer than a parallel correlation length as well, thus consistently following the principle that the simulation domain should be longer than the correlation lengths in all three directions.

Chapter 5

Nonlinear Results

THE EQUATIONS DEVELOPED in Chapters 2 and 3 provide a relatively simple yet accurate model of the dynamics underlying electrostatic tokamak turbulence. Using the flux-tube simulation geometry discussed in Chapter 4, we have developed high resolution nonlinear 3D toroidal simulations to investigate the nonlinear dynamics of tokamak turbulence via direct numerical simulations. Having demonstrated the efficacy of this flux-tube simulation geometry in Section 4.7, this Chapter investigates the nonlinear dynamics in more detail. These simulations have revealed several interesting features of toroidal microinstability driven turbulence, including the importance of nonlinear generation and damping of sheared $\mathbf{E} \times \mathbf{B}$ flows, a nonlinear peak in the fluctuation spectrum at much longer wavelengths than the fastest growing linear modes, similar to experimental measurements on TFTR [Fonck *et al.*, 1993] (also seen in full torus gyrokinetic particle simulations [Parker *et al.*, 1993]), and much larger heat fluxes and fluctuation levels than those observed in sheared slab simulations. Finally, using the bounce averaged trapped electron fluid equations, toroidal simulation results are presented which simultaneously retain the toroidal ITG drive and the TEM drive, allowing calculation of both ion and electron heat transport and particle transport.

5.1 Fluctuation Spectra

One of the most interesting features of these toroidal simulations is the long wavelength peak in the fluctuation spectra, consistent with BES measurements on TFTR

[FONCK *et al.*, 1993]. A contour plot of the linear growth rates vs. k_x and k_y is shown in Fig. 5.1 for the parameters: $\hat{s} = 1.5$, $q = 2$, $\eta_i = 4$, $\epsilon_n = 0.4$ and $T_i = T_e$, using the four moment toroidal gyrofluid equations with adiabatic electrons. These parameters are from TFTR L-mode shot #41309 at $r_0 = 53$cm, and are the same parameters used in the runs in Section 4.7. As described in Section 4.6, k_y corresponds to k_θ and k_x corresponds to θ_0 in the ballooning representation. There may be several eigenmodes for a given k_x and k_y corresponding to different mode structures along the field line. With the initial value toroidal gyrofluid code, the fastest growing of these eigenmodes eventually dominates, and it is this largest growth rate which is plotted in Fig. 5.1, in normalized units, $\gamma L_n / v_{ti}$. As discussed in Chapter 4, k_x corresponds to the radial wavevector (k_r) and k_y corresponds to the poloidal wavevector (k_θ). The anisotropy of the linear growth rate spectrum in k_x and k_y arises from "good" and "bad" curvature effects, as discussed in Section 1.3. At poloidal angle $\theta = \theta_0 = -k_x/k_y\hat{s}$, $k_\perp$ is minimized, and FLR stabilization tends to localize the mode near this poloidal angle through magnetic shear. If $\cos(\theta_0) > 0$, the modes are localized in the bad curvature region and are unstable, and modes with $\cos(\theta_0) < 0$ are localized in the good curvature region and are stable. The lines $k_x = \pm k_y \hat{s}\pi/2$, $k_x = \pm k_y \hat{s} 3\pi/2$, etc., determine the boundary between modes localized in the good and bad curvature regions. The wedge of unstable modes with $-k_y\hat{s}\pi/2 < k_x < k_y\hat{s}\pi/2$ are localized in the bad curvature region $-\pi/2 < \theta < \pi/2$. There are also unstable wedges of modes with $-k_y\hat{s}5\pi/2 < k_x < -k_y\hat{s}3\pi/2$ and $k_y\hat{s}3\pi/2 < k_x < k_y\hat{s}5\pi/2$ localized in the bad curvature regions farther along the field line, at $-5\pi/2 < \theta < -3\pi/2$ and $3\pi/2 < \theta < 5\pi/2$. The linear growth rate spectrum peaks near $k_y\rho_i = 0.35$.

In the nonlinear simulations, these modes grow linearly until the $\mathbf{E} \times \mathbf{B}$ nonlinearities are no longer negligible compared to the linear terms. At the beginning of the nonlinear stage, the spectrum is dominated by the fastest growing modes. The $\mathbf{E} \times \mathbf{B}$ nonlinearities transfer energy between different $\mathbf{k}_\perp$ modes until a statistically steady but turbulent steady state is reached. The nonlinear fluctuation spectrum is obtained by averaging in time over this saturated steady state. Averaging over several different realizations (runs with different initial conditions) is theoretically more sound, but should be equivalent if the turbulence is stationary and the time averaging is over many correlation times (by the ergodic theorem). Fig. 5.2 shows contours of the energy spectrum in $\mathbf{k}_\perp$ space, $E(k_x, k_y) = \left\langle n^2 + u_\parallel^2 + T_\parallel^2/2 + T_\perp^2 \right\rangle /2$

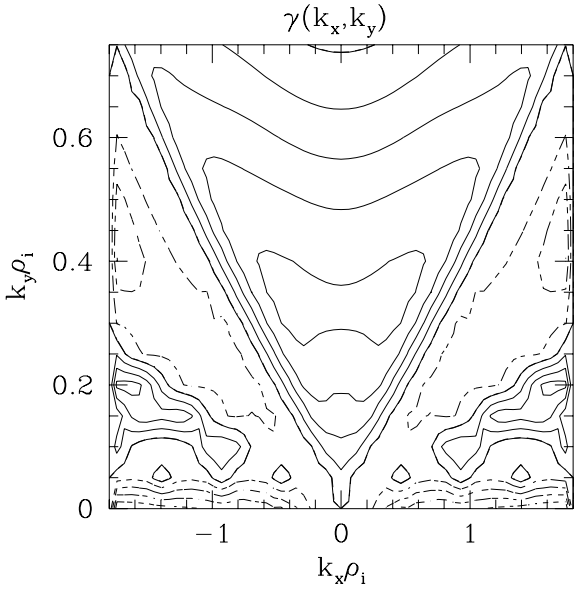

Figure 5.1: Linear growth rate spectrum for TFTR L-mode #41309 at $r_0 = 53$cm. The contours are at $\gamma = \pm 0,\ 0.05,\ 0.1,\ 0.15,\ 0.2\, v_{ti}/L_n$, with solid lines for $\gamma \geq 0$ and dashed for $\gamma < 0$. The peak growth rate is $\gamma \approx 0.2 v_{ti}/L_n$, at $k_\theta \rho_i \approx 0.35$.

(defined by Eq. (5.14) in the next section) averaged over the saturated state from $t = 75 - 170\, L_n/v_t$, for a run using the #41309 parameters above, using the four moment gyrofluid model and adiabatic electrons. The $\Phi^2(k_x, k_y)$ spectrum is very similar, as shown in Section 4.7. The nonlinear energy spectrum is concentrated at $k_\theta \rho_i \approx 0.15$. By comparison with Fig. 5.1, this is at significantly longer wavelength than the fastest growing linear modes. The nonlinear spectrum remains anisotropic in (k_x, k_y), but there is a tendency towards isotropy at high $\mathbf{k}_\perp$, compared to Fig. 5.1.

5.2 Nonlinear Energy Balance

To investigate the nonlinear dynamics, it is useful to construct a quadratic energy-like quantity for the fluctuations:

$$E = \frac{1}{2} \left\langle n^2 + u_\parallel^2 + T_\parallel^2/2 + T_\perp^2 \right\rangle , \tag{5.1}$$

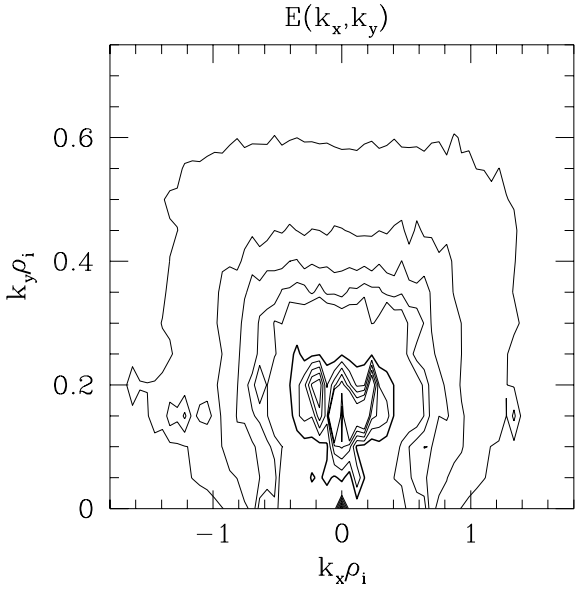

Figure 5.2: Time averaged nonlinear energy spectrum for #41309 parameters. Contours are at 0, 0.1, 0.2, 0.3, 0.4, 0.5, 1, 1.5, 2, 2.5, 3, and the $E = 1$ contour is bold for reference.

where $\langle\,\rangle$ is an average over the simulation volume:

$$\langle AB\rangle = \frac{1}{L_x L_y L_z}\int dxdydz AB.$$

for any fluctuating quantities A and B. For simplicity, we will use the 3+1 model in Section 2.7 to find the evolution of this energy, neglecting collisions and the mirroring terms ($\epsilon = 0$). Some terms in Eqs. (2.102-2.105) vanish upon volume averaging due to the periodicity of the simulation domain: $\langle A\mathbf{v}_\Psi\cdot\nabla A\rangle = \langle A\hat{\hat{\nabla}}_\perp^2\mathbf{v}_\Psi\cdot\nabla A\rangle = 0$, leaving:

$$\begin{aligned}\left\langle n\frac{\partial n}{\partial t}\right\rangle &= -\left\langle n[\frac{1}{2}\hat{\nabla}_\perp^2\mathbf{v}_\Psi]\cdot\nabla T_\perp\right\rangle - \langle n\nabla_\parallel u_\parallel\rangle + \left\langle n\left(1+\frac{\eta_\perp}{2}\hat{\nabla}_\perp^2\right)i\omega_*\Psi\right\rangle \qquad (5.2)\\ &\quad -\left\langle n\left(2+\frac{1}{2}\hat{\nabla}_\perp^2\right)i\omega_d\Psi\right\rangle - i\left\langle n\omega_d(p_\parallel+p_\perp)\right\rangle,\\ \left\langle u_\parallel\frac{\partial u_\parallel}{\partial t}\right\rangle &= -\langle u_\parallel\nabla_\parallel p_\parallel\rangle - \langle u_\parallel\nabla_\parallel\Psi\rangle - \langle u_\parallel 4i\omega_d u_\parallel\rangle - \langle u_\parallel 2|\omega_d|\nu_5 u_\parallel\rangle, \qquad (5.3)\\ \left\langle T_\parallel\frac{\partial T_\parallel}{\partial t}\right\rangle &= -\langle T_\parallel 2\nabla_\parallel u_\parallel\rangle - \left\langle T_\parallel\sqrt{2}\chi_\parallel|k_\parallel|T_\parallel\right\rangle + \langle T_\parallel\eta_\parallel i\omega_*\Psi\rangle - \langle T_\parallel 2i\omega_d\Psi\rangle \qquad (5.4)\end{aligned}$$

$$\begin{aligned}
& - \langle T_\parallel i\omega_d(6p_\parallel - 4n)\rangle - \langle T_\parallel 2|\omega_d|(\nu_1 T_\parallel + \nu_2 T_\perp)\rangle\,, \\
\left\langle T_\perp \frac{\partial T_\perp}{\partial t}\right\rangle &= - \left\langle T_\perp [\frac{1}{2}\hat{\nabla}_\perp^2 \mathbf{v}_\Psi]\cdot\nabla n\right\rangle - \left\langle T_\perp \sqrt{2}\chi_\perp |k_\parallel| \left(T_\perp + \frac{1}{2}\hat{\nabla}_\perp^2\Psi\right)\right\rangle \\
& + \left\langle T_\perp \left[\frac{1}{2}\hat{\nabla}_\perp^2 - \eta_\perp(1+\hat{\hat{\nabla}}_\perp^{\,2})\right] i\omega_*\Psi\right\rangle - \left\langle T_\perp \left(1 + \hat{\nabla}_\perp^2 + \hat{\hat{\nabla}}_\perp^{\,2}\right) i\omega_d\Psi\right\rangle \\
& - \langle T_\perp i\omega_d(4p_\perp - 3n)\rangle - \langle T_\perp 2|\omega_d|(\nu_3 T_\parallel + \nu_4 T_\perp)\rangle\,.
\end{aligned} \tag{5.5}$$

Adding these together as in Eq. (5.1), some more terms cancel from periodicity: $\langle A\nabla_\parallel B\rangle = -\langle B\nabla_\parallel A\rangle$, $\langle A\omega_d B\rangle = -\langle B\omega_d A\rangle$, $\langle A\omega_* B\rangle = -\langle B\omega_* A\rangle$, and $\left\langle n[\frac{1}{2}\hat{\nabla}_\perp^2\mathbf{v}_\Psi]\cdot\nabla T_\perp\right\rangle = -\left\langle T_\perp[\frac{1}{2}\hat{\nabla}_\perp^2\mathbf{v}_\Psi]\cdot\nabla n\right\rangle$. For this definition of the fluctuation energy, Eq. (5.1), all the nonlinear FLR terms (cubic in perturbed quantities) cancel, so the final energy evolution contains only quadratic quantities and is given by:

$$\frac{\partial E}{\partial t} = D_* + D_{dr} + D_\parallel + D_{di} + W_{u\Psi} = T. \tag{5.6}$$

The terms that affect the total energy evolution can be grouped into five classes: drive from the equilibrium gradients, D_*, reactive contributions from the real parts of the toroidal terms, D_{dr}, parallel Landau damping, $D_\parallel$, damping from toroidal phase mixing (from the imaginary parts of the toroidal terms), D_{di}, and parallel electric field work, $W_{u\Psi}$:

$$\begin{aligned}
D_* &= \langle n(1+\frac{\eta_\perp}{2}\hat{\nabla}_\perp^2) i\omega_*\Psi\rangle + \frac{\eta_\parallel}{2}\langle T_\parallel i\omega_*\Psi\rangle \\
&\quad + \langle T_\perp[\frac{1}{2}\hat{\nabla}_\perp^2 + \eta_\perp(1+\hat{\hat{\nabla}}_\perp^{\,2})] i\omega_*\Psi\rangle,
\end{aligned} \tag{5.7}$$

$$\begin{aligned}
D_{dr} &= -\langle n(2+\frac{1}{2}\hat{\nabla}_\perp^2) i\omega_d\Psi\rangle - \langle T_\parallel i\omega_d\Psi\rangle - \nu_{2i}\langle T_\parallel i\omega_d T_\perp\rangle \\
&\quad - \nu_{3i}\langle T_\perp i\omega_d T_\parallel\rangle - \langle T_\perp(1+\hat{\nabla}_\perp^2 + \hat{\hat{\nabla}}_\perp^{\,2}) i\omega_d\Psi\rangle,
\end{aligned} \tag{5.8}$$

$$D_\parallel = \frac{\sqrt{2}}{2}\chi_\parallel\langle T_\parallel|k_\parallel|T_\parallel\rangle + \sqrt{2}\chi_\perp\langle T_\perp|k_\parallel|(T_\perp + \frac{1}{2}\hat{\nabla}_\perp^2\Psi)\rangle, \tag{5.9}$$

$$\begin{aligned}
D_{di} &= -2\nu_{5r}\langle u_\parallel|\omega_d|u_\parallel\rangle - \nu_{1r}\langle T_\parallel|\omega_d|T_\parallel\rangle - \nu_{2r}\langle T_\parallel|\omega_d|T_\perp\rangle \\
&\quad - 2\nu_{3r}\langle T_\perp|\omega_d|T_\parallel\rangle - 2\nu_{4r}\langle T_\perp|\omega_d|T_\perp\rangle\,,
\end{aligned} \tag{5.10}$$

$$W_{u\Psi} = -\langle u_\parallel\nabla_\parallel\Psi\rangle. \tag{5.11}$$

As a test of the numerical accuracy of the nonlinear simulations, we evaluate these driving and damping terms and compare them to the actual time evolution of the energy. The degree to which the simulations reproduce these conservation

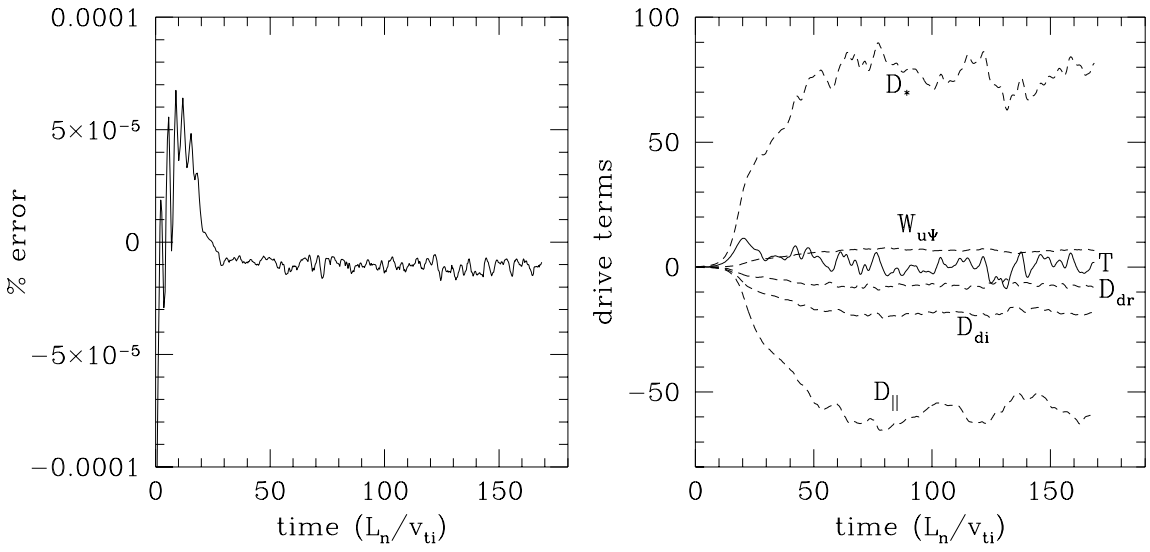

Figure 5.3: Energy conservation and time evolution of the various drive terms for a nonlinear run at the #41309 parameters.

properties of the equations is shown in Fig. 5.3 by plotting:

$$\% \text{ error} = \frac{\partial E/\partial t - T}{E}. \tag{5.12}$$

The energy balance Eq. (5.6) is preserved quite well.

At saturation, where $E \approx$ constant, it is interesting to look at the relative nonlinear magnitudes of the five driving and damping terms in Eq. (5.6). The time evolution of these terms for the #41309 run is shown in Fig. 5.3. For these parameters, the dominant drive is from equilibrium gradients, not from toroidal terms. This is to be expected because ω_d is not by itself a free energy source for instabilities. The local dispersion relation involves (see Eq. (2.56)):

$$g = F_0 \frac{\omega - \omega_*^T}{\omega - k_\parallel v_\parallel - \omega_{dv}} J_0 \frac{e\Phi}{T_0}, \tag{5.13}$$

where ω_*^T drives instabilities, but ω_d only appears in the resonant denominator. The dominant damping in the nonlinear simulations is from parallel Landau damping, not from toroidal phase mixing, although the amount by which parallel damping dominates can depend on the physical parameters of the run.

Because the toroidal gyrofluid equations constitute a multiple field system with many nonlinearities, constructing a simple nonlinear transfer function is more difficult than, for example, in the Hasegawa-Mima equation [HASEGAWA and MIMA, 1977]. Nevertheless, we can begin to investigate the nonlinear dynamics by looking at the energy spectrum in k_x and k_y, obtained by averaging only over the parallel direction:

$$E(k_x, k_y) = \frac{1}{L_z} \int dz \frac{1}{2} \left(n^2 + u_\parallel^2 + \frac{1}{2} T_\parallel^2 + T_\perp^2 \right). \tag{5.14}$$

Similarly, $\mathbf{k}_\perp$ dependent drive terms can be defined by integrating only over z:

$$T(k_x, k_y) = D_*(k_x, k_y) + D_{dr}(k_x, k_y) + \cdots, \tag{5.15}$$

where D_*, D_{dr}, etc., are as given in Eqs. (5.7-5.11), but with $\langle\,\rangle$ now representing only integration over z, with a few additional terms which are not cancelled by integration over y. The evolution of the $\mathbf{k}_\perp$ dependent energy is now given by:

$$\frac{\partial}{\partial t} E(k_x, k_y) = T(k_x, k_y) + N(k_x, k_y), \tag{5.16}$$

where $N(k_x, k_y)$ represents energy transfer from the nonlinear terms (triple correlation terms in the $E(\mathbf{k}_\perp)$ energy balance). Note that at saturation, $\int dxdy\, T(x,y) \propto \sum_{k_x,k_y} T(k_x, k_y) = 0$ and $\sum_{k_x,k_y} N(k_x, k_y) = 0$. The total drive, $T(k_x, k_y)$ shows where the energy is coming in linearly in $\mathbf{k}_\perp$ space. The nonlinear terms convect energy around in $\mathbf{k}_\perp$ space to provide the balance $\partial E(k_x, k_y)/\partial t = 0$ for each $\mathbf{k}_\perp$ at saturation. The total drive is plotted in Fig. 5.4 for the #41309 run. The most interesting feature of this plot is that the linear drive is coming in where the spectrum peaks, at long wavelengths, and not at the shorter wavelengths where the linear growth rate is larger. This implies that at saturation, there is not a strong nonlinear transfer of energy from modes with the largest linear growth rates to the energy containing modes. Most of the nonlinear energy transfer in $\mathbf{k}_\perp$-space is from the energy containing range to longer wavelengths which are damped. However, since $T(k_x, k_y)$ is averaged in z, it *only* diagnoses the energy transfer in $\mathbf{k}_\perp$-space. The dominant energy transfer could very well be from low $k_\parallel$ to high $k_\parallel$, since parallel Landau damping is dominant. More detailed diagnostics are required to isolate and identify these various possible cascade mechanisms. We can also construct a nonlinear growth rate, $T(k_x, k_y)/E(k_x, k_y)$ which is also plotted in Fig. 5.4.

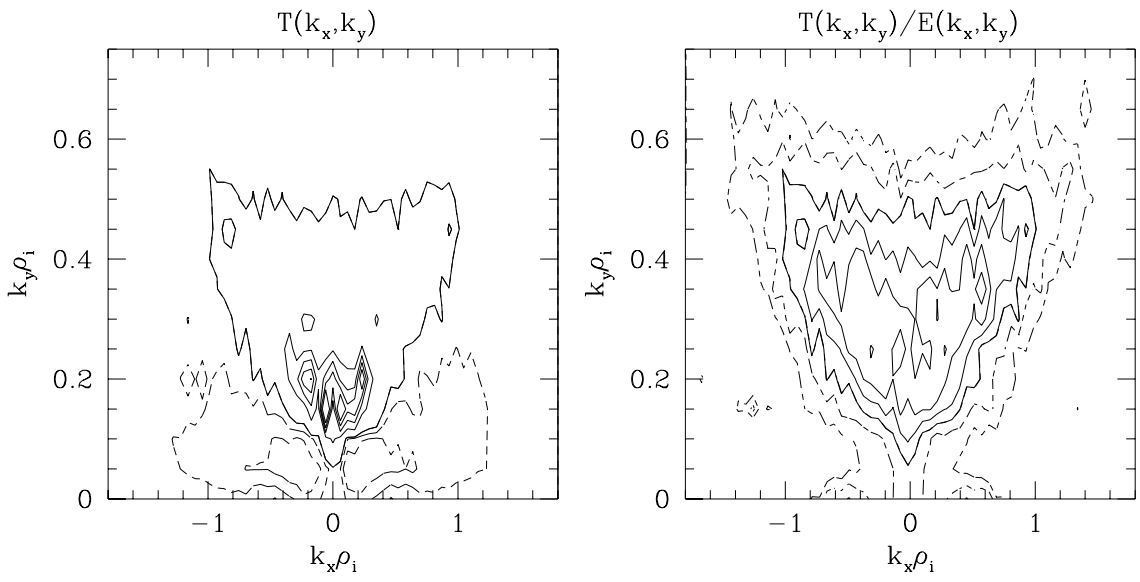

Figure 5.4: Time averaged total linear drive spectrum $T(k_x, k_y)$, and $T/E(k_x, k_y)$ spectrum, for the #41309 run. Contours for T are at -0.1, -0.05, 0, 0.25, 0.5, 0.75, 1, and contours for T/E are at -0.2, -0.1, 0, 0.1, 0.2.

Clearly, much more work is need to understand the nonlinear dynamics in more detail, beyond these cursory investigations. It is of great interest to understand the processes which set the dominant nonlinear scale.

5.3 Nonlinear Generation and Damping of Sheared E × B Flows

Both slab [Dorland *et al.*, 1992; Dorland, 1993] and toroidal [Beer *et al.*, 1992; Hammett *et al.*, 1993] simulations have revealed that an important nonlinear saturation process for core tokamak turbulence is the nonlinear generation and damping of sheared $\mathbf{E} \times \mathbf{B}$ flows. The amplitude of these flows is determined by the balance between the nonlinear generation and linear damping of the poloidal component of these flows. The amplitude of these flows is a sensitive control of the turbulence levels and transport. In this section the effects of these flows are discussed, and the gyrofluid models of the linear damping processes are carefully investigated.

It should be emphasized that in these simulations, the sheared $\mathbf{E} \times \mathbf{B}$ flows are small-scale flows generated by the turbulence, with $k_r \rho_i \sim 0.1$, and evolve on the turbulent time scales. This is in contrast to most theoretical and experimental studies of the shear flow stabilization, where the effects of large scale $\mathbf{E} \times \mathbf{B}$ flows are considered, with $k_r L_n \sim \mathcal{O}(1)$. The large scale flows evolve on the slower transport time scale, except right at the L-H transition, and are equilibrium flows within the gyrokinetic ordering. We have not considered the effects of *equilibrium* sheared $\mathbf{E} \times \mathbf{B}$ flows or sheared parallel flows on our simulations, although these effects can be incorporated.

5.3.1 Proper Treatment of Adiabatic Electron Response

When the electrons are assumed to be adiabatic (or are nearly adiabatic) it is important to use an expression for the perturbed electron density that allows consistent evolution of sheared $\mathbf{E} \times \mathbf{B}$ flows. A historical review of various assumptions about the adiabatic electron response is given in [Dorland, 1993]. Adiabatic electrons experience no net radial transport since the $\mathbf{E} \times \mathbf{B}$ convection of the perturbed electron density is zero ($\mathbf{E} \times \mathbf{B} \cdot \nabla \tilde{n}_e \propto \nabla \tilde{\Phi} \times \mathbf{B} \cdot \nabla \tilde{\Phi} = 0$). If the electrons are allowed to respond to a potential perturbation which is constant on a flux surface, this implies net radial transport of electrons, which is unphysical unless the magnetic field is stochastic. Thus for adiabatic electrons, it is essential to use [Dorland and Hammett, 1993]:

$$n_e = \tau \left(\Phi - \langle \Phi \rangle \right), \tag{5.17}$$

where $\tau = T_{i0}/T_{e0}$, Φ has been normalized to e/T_{i0}, and $\langle \Phi \rangle$ is a flux surface average.

The effect of this proper adiabatic response on our toroidal nonlinear simulations is shown in Fig. 5.5. These simulations used the six moment toroidal gyrofluid equations and assumed adiabatic electrons. The parameters correspond to TFTR L-mode shot #65018 at $r/a = 0.78$: $\epsilon = 0.25$, $\epsilon_n = 0.26$, $\eta_i = 2.31$, $\hat{s} = 1.7$, $q = 3.42$, and $T_i/T_e = 1.19$. Because this is near the edge, $\hat{s}$ is relatively large. When $n_e = e\Phi/T_e$ is used, radially elongated structures form and grow, showing no signs of saturating throughout the length of this run. When the $k_\theta = 0$, $k_\parallel = 0$ components of Φ are artificially suppressed, so $\langle \Phi \rangle = 0$, there is no $\mathbf{E} \times \mathbf{B}$ rotation. It is curious that the simulations with $n_e = \tau\Phi$ behave so differently from the those with $\langle \Phi \rangle = 0$. Using $n_e = \tau(\Phi - \langle \Phi \rangle)$ allows nonlinear generation of radially sheared

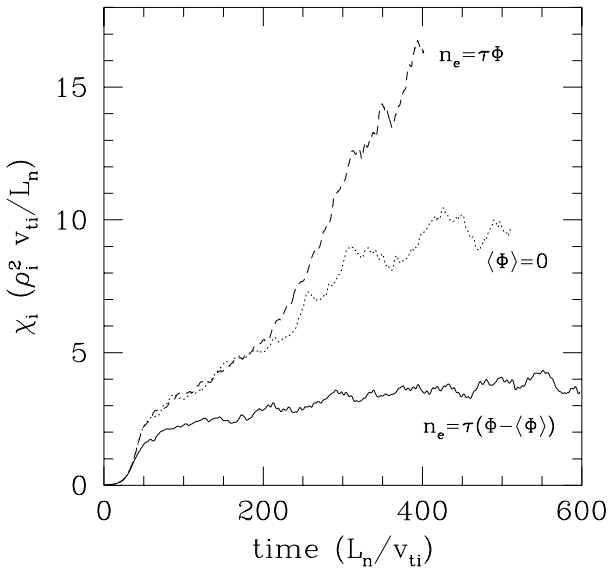

Figure 5.5: Effect of the proper adiabatic response in nonlinear simulations. When $n_e = e\Phi/T_e$ is used (dashed line), radially elongated structures form and grow throughout the run. Using $n_e = e(\Phi - \langle\Phi\rangle)/T_e$ allows nonlinear generation of radially sheared $\mathbf{E} \times \mathbf{B}$ flows, which rip apart these radially elongated structures (solid line). A saturated state is reached where the turbulence generated sheared $\mathbf{E} \times \mathbf{B}$ flows in turn regulate the turbulence. Also shown (dotted line) is a run forcing the flux surface averaged Φ to zero, disallowing sheared flows.

$\mathbf{E} \times \mathbf{B}$ flows, which rip apart these radially elongated structures. A saturated state is reached where the turbulence generated sheared $\mathbf{E} \times \mathbf{B}$ flows in turn regulate the turbulence. This interplay leads to lower fluctuation and turbulence levels than the case with no sheared $\mathbf{E} \times \mathbf{B}$ flows.

It is interesting to investigate why the adiabatic response $n_e = \tau\,(\Phi - \langle\Phi\rangle)$, as opposed to $n_e = \tau\Phi$, has such a dramatic effect on the nonlinear evolution. Consider a potential perturbation as shown in Fig. 5.6, which is constant on a flux surface, i.e. $k_\theta = k_\parallel = 0$, but is radially varying. In this figure, r is a small fraction of the minor radius of the tokamak. Since this perturbation has $k_\parallel = 0$, if $n_e = \tau\Phi$ were used for the adiabatic electron response, the flux surface averaged perturbed electron density, $n_e(r)$, would have radial variation, as shown below $\Phi(r)$. The perturbation on the left of Fig. 5.6 could evolve into the perturbation on the right, and this would

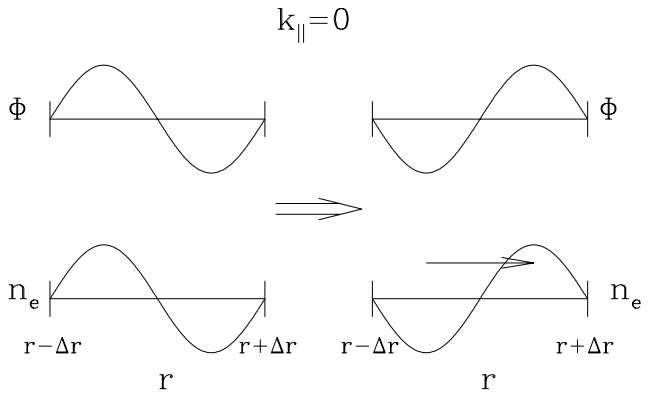

Figure 5.6: A possible evolution of the electrostatic potential, showing the necessity of the form Eq. (5.17) for the adiabatic response. The potential perturbation on the left could evolve into the perturbation on the right, implying nonphysical net radial transport of adiabatic electrons if $n_e/n_{e0} = e\Phi/T_e$. If $n_e/n_{e0} = e(\Phi - \langle\Phi\rangle)/T_e$, the electrons do not respond to the flux surface averaged component.

imply a net radial transport of electrons, which is unphysical if the electrons are adiabatic. Thus, the electrons should not respond to the $k_\theta = k_\parallel = 0$ component of the potential, leading to Eq. (5.17). The electrons *can* respond to potential perturbations with $k_\parallel \neq 0$, since in this case the flux surface averaged perturbed electron density is zero and there is no net radial electron transport. The form Eq. (5.17) is essential to properly describe the evolution of radially varying potential perturbations, which gives rise to sheared perpendicular $\mathbf{E} \times \mathbf{B}$ flow. Assuming $n_e = \tau\Phi$ essentially allows the electrons to move radially, so they effectively short out these components of the potential. Using Eq. (5.17) prohibits radial motion of adiabatic electrons, and allows the self-consistent generation of sheared $\mathbf{E} \times \mathbf{B}$ flows.

The turbulence level is very sensitive to the damping of these flux surface averaged $\mathbf{E} \times \mathbf{B}$ flows, as shown in Fig. 5.7 The damping of the $k_\theta = 0$ modes is dominantly due to the toroidal effects associated with magnetic pumping which damp the (large) poloidal component of this flow. These effects are independent of k_r for small $k_r\rho_i$, and dominate over viscous effects which are proportional to $\nu_{ii}\nabla_\perp^2$. The poloidal damping can be turned off in the simulations by artificially setting

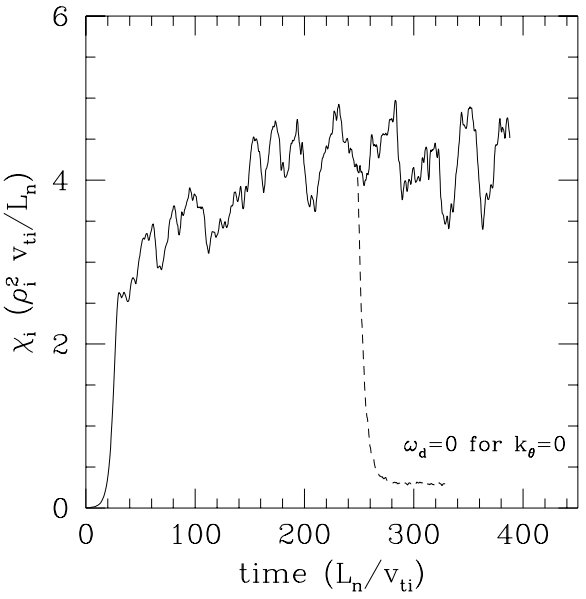

Figure 5.7: Effect of poloidal flow damping on the nonlinear saturation level. At $t = 250L_n/v_t$, the poloidal flow damping is artificially turned off by setting $\omega_d = 0$ for $k_\theta = 0$ modes (dashed line). Compared to the case *with* flow damping (solid line), the $\mathbf{E} \times \mathbf{B}$ flows grow to much larger amplitude and greatly reduce the fluctuation levels and transport.

$\omega_d = 0$ for these modes, which for $k_\theta = 0$ is normally $\omega_d = -k_r \epsilon_n \sin(\theta)$. Fig. 5.7 shows a simulation with the proper treatment which was restarted at $t = 250L_n/v_{ti}$ with $\omega_d = 0$ for the $k_\theta = 0$ rotation modes. This allows the sheared rotation to grow to much larger amplitude, and the turbulence level is greatly reduced.

The radial variation of the flux surface averaged potential $\langle \Phi \rangle$ and parallel flow $\langle u_\parallel \rangle$ are shown in Fig. 5.8, plotted at the end ($t = 170L_n/v_{ti}$) of the simulation discussed in Sections 5.1 and 5.2, i.e. for TFTR L-mode shot #41309 at $r/a =$ 53cm. Both radially sheared $\mathbf{E} \times \mathbf{B}$ flow and sheared parallel flow can enhance the radial decorrelation of the turbulence, reducing the fluctuation levels [Biglari *et al.*, 1990; Hahm, 1994]. (Large equilibrium sheared flows can also introduce a Kelvin-Helmholtz type instability, see for example [Waltz *et al.*, 1994a].) It is interesting to compare the relative strength of the radial decorrelation from the perpendicular $\mathbf{E} \times \mathbf{B}$ and the parallel flows. This is measured by the perpendicular

and parallel shearing rates: $\omega_s^\perp = \Delta r\, \partial(k_\theta v_{E\theta})/\partial r$ and $\omega_s^\parallel = \Delta r\, \partial(k_\parallel u_\parallel)/\partial r$, where Δr is the radial correlation length of the turbulence (a typical eddy or blob size). Using a perpendicular correlation length $r_0 \Delta\theta \approx 1/k_\theta$, the shearing rate from $v_E = ik_r \rho_i v_{ti}(e\Phi_1/T_{i0})$ is:

$$\omega_s^\perp \sim \Delta r \frac{\partial}{\partial r}\left(\frac{k_r \rho_i^2 \Phi}{r_0 \Delta\theta}\right)\frac{v_{ti}}{L_n}.$$

Recall that $e\Phi_1/T_{i0} = \Phi(\rho_i/L_n)$ and $u_1/v_{ti} = u_\parallel(\rho_i/L_n)$ in our normalization, Eq. 2.39. The shearing rate from parallel flow, since $k_\parallel \sim 1/qR$, see Figs. 4.12(b) and 4.13(b), is:

$$\omega_s^\parallel \sim \Delta r \frac{\partial}{\partial r}\left(\frac{\rho_i u_\parallel}{qR}\right)\frac{v_{ti}}{L_n}.$$

The shearing rate from perpendicular $\mathbf{E} \times \mathbf{B}$ flow is larger than that from parallel flow by

$$\frac{\omega_s^\perp}{\omega_s^\parallel} \sim \frac{k_r \rho_i^2 \Phi}{r_0 \Delta\theta}\frac{qR}{\rho_i u_\parallel} \sim (k_r \rho_i)(k_\theta \rho_i)\frac{qR}{\rho_i} \sim \frac{1}{\varepsilon},$$

in the gyrokinetic ordering. Using $\Phi \approx 5u_\parallel$ from Fig. 5.8, $k_r\rho_i \approx 0.15$ and $k_\theta \rho_i \approx \rho_i/(r_0\Delta\theta) \approx 0.15$ from the simulations, and the measured $q = 2.4$, $\rho_i = 0.14$cm, and $R = 258$cm yields $\omega_s^\perp \approx 500\,\omega_s^\parallel$, indicating that perpendicular flow shearing dominates over parallel flow shearing for the elongated turbulence ($k_\parallel \ll k_\perp$) in these toroidal simulations. Note that this is true for the flows generated by the turbulence, but does not preclude the importance of large scale equilibrium toroidal (mostly parallel) flows. In addition, since the radial scale of the flows and the turbulence are comparable, the parameters above lead to an estimate of the perpendicular shearing rate, $\omega_s^\perp \approx 0.2 v_t/L_n$. The measured turbulent decorrelation time from the simulation is $\tau_c \sim 5L_n/v_{ti}$ (which can also be roughly estimated from the time scale of the fluctuations in the time history plots in Figs. 4.12(a) and 5.3). This leads to an estimate for the turbulent scattering rate of $\omega_T \sim 0.2 v_{ti}/L_n$. The sheared flows should strongly influence the turbulence if $\omega_s \gtrsim \omega_T$, which is satisfied here. While these are rough estimates, it is clear that the levels of sheared $\mathbf{E} \times \mathbf{B}$ flow in the simulations is large enough to have a significant impact on the turbulence. Thus the conventional theoretical picture of the stabilizing influence of sheared $\mathbf{E} \times \mathbf{B}$ flow [Biglari *et al.*, 1990] on the turbulence seems consistent with the large effects observed in these simulations.

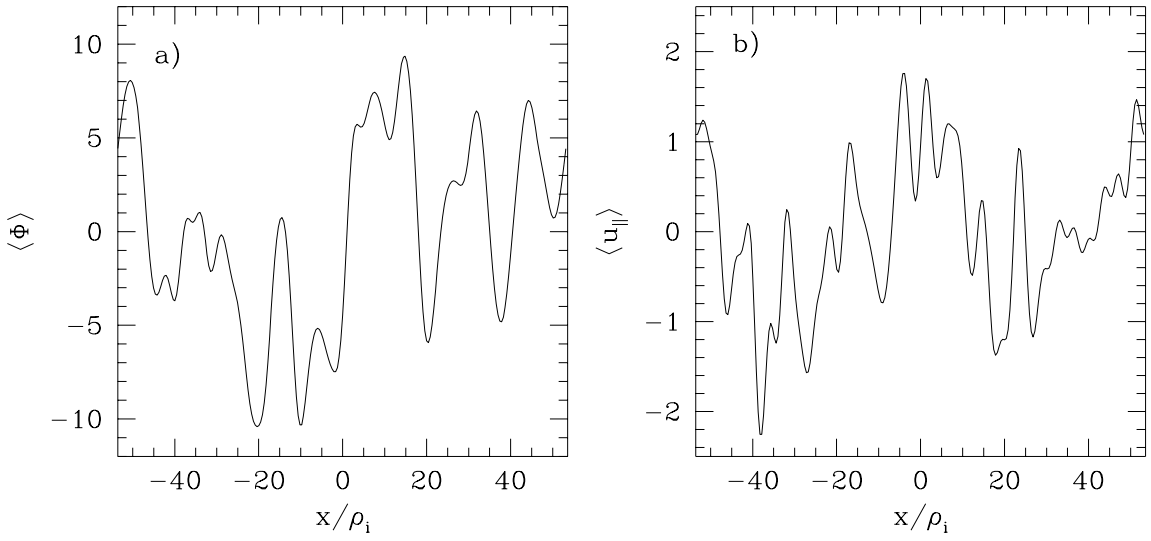

Figure 5.8: Flux surface averaged potential and parallel flow at the end of the simulation at the #41309 parameters. The radial variation (first derivative) of the potential leads to a perpendicular (mostly poloidal) $\mathbf{E} \times \mathbf{B}$ flow, which is radially sheared (second derivative of Φ).

5.3.2 Neoclassical Damping of Poloidal Flows

These sheared $\mathbf{E} \times \mathbf{B}$ flows are damped primarily by toroidal effects. While (classical) collisional damping would damp these flows in sheared slab geometry, in a toroidal system the strongest damping mechanism is neoclassical magnetic pumping. Magnetic pumping damps the (large) poloidal component of the $\mathbf{E} \times \mathbf{B}$ flow until the total flow (parallel flow plus $\mathbf{E} \times \mathbf{B}$ flow) is purely toroidal. Because this process arises from the variation of B with major radius, we have termed these effects "neoclassical," even though for turbulent time scales collisionless "transit-time magnetic pumping" [STIX, 1973] dominates over collisional effects. This damping arises from collisionless phase mixing (Landau damping), which dominates for short time scales, $t < \omega_{bi}^{-1}$, and damps the flows at a rate proportional to ω_{ti}. For these short times, $t < \omega_{bi}^{-1}$, trapped particles do not know that they are trapped, so the plateau regime damping rates are applicable. After a bounce time the Landau damping ceases because of trapping, and one then gets a slow decay due only to collisions. This collisionless transit-time magnetic pumping can also be related to the radial drifts of particle orbits in a tokamak in response to a changing radial electric field, i.e. a kind of neoclassical enhancement of the polarization drift [STIX, 1973; HINTON and ROBERTSON, 1984; CALLEN, 1973].

In this section damping rates for magnetic pumping are derived from the toroidal gyrofluid equations derived in Chapter 2. It is shown that in the banana and plateau regimes the toroidal gyrofluid equations accurately capture transit-time magnetic pumping. The damping rate in the Pfirsch-Schlüter is also shown to agree with neoclassical theory, for completeness.

As discussed in Section 5.3.1, the most important flows are those with radial scales on the order of the turbulence scale size or longer. We see $k_r \rho_i \approx 0.1 - 0.2$ in our nonlinear simulations, so we will concentrate on the limit $k_r \rho_i \ll 1$, where magnetic pumping dominates over collisional viscous damping. Let us consider the dynamics of a potential perturbation which is constant of a flux surface, $\Phi = \Phi(r)$. The discussion closely follows [HASSAM and KULSRUD, 1978], but extends their approach into collisionless regimes. The radially varying potential leads to a perpendicular $\mathbf{E} \times \mathbf{B}$ flow, $\mathbf{v}_E = (c/B)\hat{\mathbf{b}} \times \nabla \Phi$. Restricting the discussion to circular concentric flux surface geometry for simplicity, we have: $\hat{\mathbf{b}} = b_z[\mathbf{e}_\phi + (\epsilon/q)\mathbf{e}_\theta]$, $\epsilon = r/R_0$, $b_z^{-1} = \sqrt{1 + \epsilon^2/q^2}$, $\mathbf{e}_\phi$ is the toroidal direction, and $\mathbf{e}_\theta$ is the poloidal

direction. The magnetic field strength is $B = B_0 R_0/R$, where B_0 is the field on axis, at $R = R_0$. In addition to the perpendicular flow, there may be a parallel flow $u_\parallel(r,\theta)$. In the small k_r limit which we consider here, $\Phi \gg p$, so the diamagnetic flow contribution is negligible. Both the perpendicular $\mathbf{E}\times\mathbf{B}$ flow and parallel flow have toroidal and poloidal components:

$$\mathbf{v}_E = \frac{c}{B}\frac{\partial\Phi}{\partial r} b_z \left(\mathbf{e}_\theta - \frac{\epsilon}{q}\mathbf{e}_\phi\right), \tag{5.18}$$

$$u_\parallel \hat{\mathbf{b}} = u_\parallel b_z \left(\mathbf{e}_\phi + \frac{\epsilon}{q}\mathbf{e}_\theta\right). \tag{5.19}$$

The toroidal and poloidal components of the total flow $\mathbf{v} = u_\parallel\hat{\mathbf{b}} + \mathbf{v}_E = v_\theta \mathbf{e}_\theta + v_\phi \mathbf{e}_\phi$ are:

$$v_\phi = (u_\parallel - \frac{\epsilon}{q}\frac{c}{B}\frac{\partial\Phi}{\partial r})b_z, \tag{5.20}$$

$$v_\theta = (u_\parallel \frac{\epsilon}{q} + \frac{c}{B}\frac{\partial\Phi}{\partial r})b_z. \tag{5.21}$$

Let us consider the time evolution of these flows, as described by the 4+2 toroidal gyrofluid equations, given in Section 2.6. The quasineutrality constraint for adiabatic electrons, Eq. (2.9), is $\tau(\Phi - \langle\Phi\rangle) = \bar{n}_i + (\Gamma_0 - 1)\Phi$, where Φ is normalized to e/T_i, $\bar{n}_i$ to n_{i0}, and $\tau = T_i/T_e$. It is convenient to introduce the notation $h = R/R_0 = 1 + \epsilon\cos\theta$, so the flux surface average is $\langle\Phi\rangle = (2\pi)^{-1}\oint d\theta h\Phi(r) = \Phi$. For $k_r\rho_i \ll 1$, $\bar{n}_i = n$ and $\Gamma_0 = 1 - k_r^2\rho_i^2$, so:

$$\langle\Phi\rangle = \frac{\langle n\rangle}{\langle k_r^2\rho_i^2\rangle}. \tag{5.22}$$

We now normalize k_r to ρ_{i0}, where $\rho_{i0} = v_{ti}mc/eB_0$, so $\rho_i = \rho_{i0}h$ and $\langle\Phi\rangle = \langle n\rangle / k_r^2\langle h^2\rangle$. Since we have assumed circular concentric surfaces, k_r is independent of θ. Now consider the evolution of the flux surface averaged toroidal angular momentum, $\langle h v_\phi\rangle$. Using Eq. (5.20),

$$\frac{\partial}{\partial t}\langle h v_\phi\rangle = \frac{\partial}{\partial t}\langle h u_\parallel b_z\rangle - \frac{\partial}{\partial t}\left\langle h\frac{\epsilon}{q}\frac{c}{B}\frac{\partial\Phi}{\partial r}b_z\right\rangle, \tag{5.23}$$

In the normalized units of Chapter 2 and Eq. (5.22), this becomes:

$$\frac{\partial}{\partial t}\langle h v_\phi\rangle = b_z\frac{\partial}{\partial t}\langle h u_\parallel\rangle - i\frac{b_z\epsilon}{qk_r}\frac{\partial\langle n\rangle}{\partial t}, \tag{5.24}$$

so we need to find $\partial \langle h u_\parallel \rangle / \partial t$ and $\partial \langle n \rangle / \partial t$ from the gyrofluid equations.

Considering perturbations with $k_y = 0$, so $\omega_* = 0$, but with slow parallel variation so $\partial/\partial\theta \neq 0$ (the y coordinate is perpendicular and θ is the parallel coordinate, as discussed in Chapter 4), the density and parallel velocity equations, Eqs. (2.91) and (2.92) become:

$$\frac{\partial n}{\partial t} + B\nabla_\parallel \frac{u_\parallel}{B} + 2i\omega_d \Phi + i\omega_d (p_\parallel + p_\perp) = 0, \tag{5.25}$$

$$\frac{\partial u_\parallel}{\partial t} + B\nabla_\parallel \frac{p_\parallel}{B} + \nabla_\parallel \Phi + p_\perp \nabla_\parallel \ln B + i\omega_d (q_\parallel + q_\perp + 4u_\parallel) = 0. \tag{5.26}$$

The parallel derivatives, $\nabla_\parallel = \hat{\mathbf{b}} \cdot \nabla = (b_z/qR_0)\partial/\partial\theta$, when normalized, become $\nabla_\parallel = (b_z \epsilon_n/q)\partial/\partial\theta$, where $\epsilon_n = L_n/R_0$. Furthermore, in these variables, $i\omega_d = (cT/eB^3)\mathbf{B} \times \nabla B \cdot \nabla = -ik_r b_z \epsilon_n \sin\theta$, and $\nabla_\parallel \ln B = (\epsilon_n \epsilon b_z/hq)\sin\theta$. Flux surface averaging the density equation yields:

$$\frac{\partial \langle n \rangle}{\partial t} = -\frac{1}{2\pi} \int d\theta h \left[\frac{b_z \epsilon_n}{q} \frac{B_0}{h} \frac{\partial}{\partial \theta} \frac{u_\parallel}{B} - ik_r b_z \epsilon_n \sin\theta (2\Phi + p_\parallel + p_\perp) \right]. \tag{5.27}$$

The $u_\parallel$ term vanishes on flux surface averaging, leaving:

$$\frac{\partial \langle n \rangle}{\partial t} = \frac{ik_r b_z \epsilon_n}{2\pi} \int d\theta \sin\theta (2\Phi + p_\parallel + p_\perp). \tag{5.28}$$

Averaging the parallel velocity equation leads to:

$$\frac{\partial}{\partial t} \langle h u_\parallel \rangle = -\frac{1}{2\pi} \int d\theta h^2 \frac{b_z \epsilon_n}{q} \left[\frac{\partial}{\partial \theta} (p_\parallel + \Phi) + \frac{\epsilon}{h} (p_\parallel - p_\perp) - ik_r q \sin\theta (q_\parallel + q_\perp + 4u_\parallel) \right]. \tag{5.29}$$

Using the identity:

$$\int d\theta h^2 \frac{\partial}{\partial \theta} (p_\parallel + \Phi) = 2 \int d\theta h \epsilon \sin\theta (p_\parallel + \Phi), \tag{5.30}$$

Eqs. (5.28) and (5.29) can be combined. The k_r independent terms cancel, and:

$$\frac{\partial}{\partial t} \langle h v_\phi \rangle = \frac{ik_r b_z \epsilon_n}{2\pi} \int d\theta h^2 \sin\theta (q_\parallel + q_\perp + 4u_\parallel) \approx 0, \tag{5.31}$$

since we are considering the $k_r \rho_i \to 0$ limit.

Similarly, we can find the time evolution of the flux surface averaged parallel flow, $\langle u_\parallel / h \rangle \propto \langle \mathbf{v} \cdot \mathbf{B} \rangle$, which to zeroth order in k_r is given by:

$$\frac{\partial}{\partial t} \left\langle \frac{u_\parallel}{h} \right\rangle \approx \frac{1}{2\pi} \int d\theta \frac{b_z \epsilon_n \epsilon \sin\theta}{qh} (p_\parallel - p_\perp). \tag{5.32}$$

The parallel flow is damped by the difference between $p_\parallel$ and $p_\perp$. In neoclassical parlance, this expresses the fact that the parallel flow is damped by the parallel viscous stress $\mathbf{B}\cdot\nabla\cdot\boldsymbol{\pi}$ [HIRSHMAN, 1978], where the stress tensor has the CGL form $\boldsymbol{\pi} = (p_\parallel - p_\perp)(\hat{\mathbf{b}}\hat{\mathbf{b}} - \mathbf{I}/3)$ [CHEW *et al.*, 1956]. Keep in mind that the density and velocity gyrofluid equations are exact moments of the gyrokinetic equation in this limit (small $k_\perp$), so these equations for the toroidal and parallel flows are capturing the true physics. (In the six moment model closures are not introduced until the $p_\parallel$ and $p_\perp$ equations.)

The evolution of $\delta p = p_\parallel - p_\perp$ is found by subtracting the parallel and perpendicular pressure equations, Eqs. (2.93) and (2.94). Because $k_r \ll 1$, but $\Phi \sim n/k_r^2$, we keep $\omega_d\Phi$ terms but drop ω_d terms involving the fluid moments, yielding:

$$\frac{\partial}{\partial t}\delta p = -B\nabla_\parallel\frac{q_\parallel}{B} + B^4\nabla_\parallel\frac{q_\perp}{B^4} - 2\nabla_\parallel u_\parallel - u_\parallel\nabla_\parallel \ln B - i\omega_d\Phi - \nu_{ii}\delta p. \tag{5.33}$$

At this point it is convenient, but not necessary, to assume that the flows are incompressible. Incompressibility is enforced by setting $\partial n/\partial t = 0$ in Eq. (5.25), which forces the divergence of parallel flow to balance the divergence of $\mathbf{E}\times\mathbf{B}$ flow, $\nabla\cdot\mathbf{v}_E = 2i\omega_d\Phi$:

$$B\nabla_\parallel\frac{u_\parallel}{B} = -2i\omega_d\Phi. \tag{5.34}$$

This removes the fast parallel sound wave time scale and simplifies the analysis. Using incompressibility in Eq. (5.33), some of the $u_\parallel$ and $\omega_d\Phi$ terms cancel. The remaining $u_\parallel$ and $\omega_d\Phi$ terms can be written in terms of the poloidal flow using $v_\theta = u_\parallel\epsilon b_z/q + ik_r h b_z\Phi$, from Eq. (5.21). The evolution of δp is then given by:

$$\frac{\partial}{\partial t}\delta p = -B\nabla_\parallel\frac{q_\parallel}{B} + B^4\nabla_\parallel\frac{q_\perp}{B^4} - 3v_\theta\frac{\epsilon_n\sin\theta}{h} - \nu_{ii}\delta p, \tag{5.35}$$

Thus δp is driven by poloidal flow and damped by ion-ion collisions and parallel heat flows. Collisions relax the distribution function toward a Maxwellian, which causes isotropization of $T_\parallel$ and $T_\perp$, damping δp. The physical mechanism by which poloidal flow drives δp is a bit more subtle. Consider a poloidal flow which brings plasma from the outer midplane to the inner midplane, where B is larger. Because $\mu = v_\perp^2/2B$ is conserved, as B increases, $T_\perp$ increases. Similarly, from conservation of canonical toroidal angular momentum, $T_\parallel$ decreases, so poloidal flow drives a difference between $p_\parallel$ and $p_\perp$. This δp in turn damps the parallel flow, as shown by

Eq. (5.32). Since the toroidal flow is constant, this parallel flow damping leads to poloidal flow damping, as follows. Again using incompressibility, hv_θ is independent of θ. Then with some manipulation, $u_\parallel/h$ can be written in terms of $\langle hv_\theta \rangle$ and $\langle hv_\phi \rangle$:

$$\frac{u_\parallel}{h} = \frac{q}{\epsilon b_z}\left(\left\langle \frac{1}{h^2}\right\rangle - \frac{b_z^2}{\langle h^2\rangle}\right)\langle hv_\theta\rangle + \frac{b_z}{\langle h^2\rangle}\langle hv_\phi\rangle . \tag{5.36}$$

Evaluating the flux surface averages to lowest order in ϵ, $\langle h^2\rangle \approx 1+\frac{3}{2}\epsilon^2$ and $\langle 1/h^2\rangle \approx 1+\frac{1}{2}\epsilon^2$, leads to:

$$\frac{u_\parallel}{h} = (1+2q^2)\frac{\epsilon}{q}\langle hv_\theta\rangle + \langle hv_\phi\rangle . \tag{5.37}$$

Since the toroidal flow is constant, $\partial\langle hv_\phi\rangle/\partial t \approx 0$, Eq. (5.32) becomes:

$$\frac{\partial}{\partial t}\left\langle \frac{u_\parallel}{h}\right\rangle = (1+2q^2)\frac{\epsilon}{q}\frac{\partial}{\partial t}\langle hv_\theta\rangle = \frac{1}{2\pi}\int d\theta \frac{b_z\epsilon_n\epsilon\sin\theta}{qh}(p_\parallel - p_\perp). \tag{5.38}$$

In the Pfirsch-Schlüter regime (easiest, but least relevant to present day experiments), collisions keep $q_\parallel$ and $q_\perp$ small. Considering slow evolution compared to the sound wave time scale, we can look at the average evolution of δp by ignoring $\partial\delta p/\partial t$. Then δp in Eq. (5.35) is determined by the balance between the drive from the poloidal flow and the damping from collisional isotropization:

$$\delta p = -3v_\theta\frac{\epsilon_n\sin\theta}{\nu_{ii}h}. \tag{5.39}$$

Plugging this into Eq. (5.38), using the fact that hv_θ is independent of θ, and integrating over θ to lowest order in ϵ yields:

$$(1+2q^2)\frac{\epsilon}{q}h\frac{\partial v_\theta}{\partial t} = -3hv_\theta\left\langle \frac{b_z\epsilon_n^2\epsilon\sin^2\theta}{q\nu_{ii}h^4}\right\rangle , \tag{5.40}$$

The flux surface average on the right hand side can now be evaluated, which to lowest order in ϵ gives a poloidal damping rate of:

$$\gamma = -\frac{3}{2}\frac{\epsilon_n^2}{(1+2q^2)\nu_{ii}}. \tag{5.41}$$

Here both γ and ν_{ii} have been normalized to v_{ti}/L_n. In dimensional form, this is:

$$\gamma = -\frac{3}{2}\frac{v_{ti}^2}{(1+2q^2)\nu_{ii}R^2} = -\frac{3}{2}\frac{\omega_{ti}^2}{(2+1/q^2)\nu_{ii}}, \tag{5.42}$$

where $\omega_{ti} = v_{ti}/qR$. This expression matches the Pfirsch-Schlüter result of [HASSAM and KULSRUD, 1978] exactly.

Now consider the less collisional plateau and banana regimes. Here the ν_{ii} term in Eq. (5.35) is negligible, and the dominant balance is between the heat flux terms, which damp δp, and poloidal flow, which drives δp. In these "collisionless" regimes, the heat fluxes primarily come from the Landau damping terms in the gyrofluid equations. For low frequencies, Eq. (2.95) and (2.96) reduce to $\sqrt{2}D_\parallel|k_\parallel|q_\parallel \approx -(3+\beta_\parallel)\nabla_\parallel T_\parallel$ and $\sqrt{2}D_\perp|k_\parallel|q_\perp \approx -\nabla_\parallel T_\perp$. Using $k_\parallel \approx 1/qR$ (in our dimensionless units, $k_\parallel$ is normalized to L_n, so $k_\parallel \approx \epsilon_n/q$), this approximately leads to:

$$\delta p \approx -3\sqrt{\frac{\pi}{2}}\frac{v_\theta q \sin\theta}{h} \tag{5.43}$$

Plugging this into Eq. (5.38) gives:

$$(1+2q^2)\frac{\epsilon}{q}h\frac{\partial v_\theta}{\partial t} = -3\sqrt{\frac{\pi}{2}}h v_\theta \left\langle \frac{b_z \epsilon_n \epsilon \sin^2\theta}{h^4} \right\rangle . \tag{5.44}$$

Evaluating the flux surface average to lowest order in ϵ yields the collisionless poloidal flow damping rate from the toroidal gyrofluid equations:

$$\gamma = -\frac{3}{2}\sqrt{\frac{\pi}{2}}\frac{q\epsilon_n}{1+2q^2}, \tag{5.45}$$

which in dimensional form is:

$$\gamma = -\frac{3}{2}\sqrt{\frac{\pi}{2}}\frac{\omega_{ti}}{(2+1/q^2)}. \tag{5.46}$$

This matches the plateau results of [HIRSHMAN, 1978] and [STRINGER, 1973] within a factor of 1.5, and also agrees with [STIX, 1973] if $(1+2q^2)$ is replaced by 1, since he was working in slab geometry, with modulated B.

In the banana regime, the neoclassical calculation of the poloidal flow damping rate is not as straightforward as in the plateau regime. Using the static values for the parallel viscosity coefficients, [HIRSHMAN, 1978] found:

$$\gamma = -\frac{q^2\nu_{ii}}{1.29\epsilon^{3/2}(1+2q^2)}, \tag{5.47}$$

which is the same expression in dimensional and dimensionless form. This large damping rate violates the assumption $\omega \ll \nu_{ii}$ which calls the use of the static

viscosity coefficients into question; a point which [HIRSHMAN, 1978] emphasized. Earlier works found $\gamma \propto -\nu_{ii}/\epsilon$ [STIX, 1973] and $\gamma \propto -\nu_{ii}$ [ROSENBLUTH *et al.*, 1971]. Later neoclassical expressions for the poloidal flow damping rate were derived without using the static parallel viscosity coefficients and found $\gamma \propto -\nu_{ii}$ [SHAING and HIRSHMAN, 1989], $\gamma \propto -\nu_{ii}/\epsilon^{1/2}$ [TAGUCHI, 1991], and $\gamma \propto -\nu_{ii}/\epsilon$ [HSU *et al.*, 1994]. Since ϵ is small, these results are extremely different. These last three works, instead of using the static parallel viscosity coefficients, solve for the time dependent distribution function, f_i. However, when solving for f_i they order $\partial f_i/\partial t \sim C(f_i) \ll \omega_{ti} f_i$, so these calculations miss any collisionless damping processes which occur on a faster time scale. As [STIX, 1973] argued, collisionless transit-time magnetic pumping dominates for short time scales, $t < \omega_{bi}^{-1}$. The analytic damping rate calculated from the toroidal gyrofluid equations in the banana and plateau regimes, Eq. (5.45), is consistent with this. Dimits' interpretation of poloidal flow damping in collisionless gyrokinetic particle simulations is also based on Stix's transit-time magnetic pumping picture [DIMITS, 1994]. The gyrofluid damping rates are compared to the neoclassical results of [HIRSHMAN, 1978] in Fig. 5.9. The results agree in the plateau and Pfirsch-Schlüter regimes. In the banana regime, transit-time magnetic pumping dominates for times $t \lesssim \omega_{ti}^{-1}, \omega_{bi}^{-1}$, and at later times the damping is governed by collisional processes.

The analytic gyrofluid results for the flow damping rates in Eqs. (5.41) and (5.45) are now compared with numerical solutions of the full toroidal gyrofluid equations without making any of the approximations used above. A flow with both toroidal and poloidal components is initially imposed and is linearly evolved in time. The parameters used are $k_r \rho_{i0} = 0.01$, $\epsilon = 0.1$ and $q = \epsilon_n = 1$; the scaling of Eqs. (5.41) and (5.45) with q and ϵ_n have also been checked, but are not shown here. Fig. 5.10 and 5.11 show the linear damping of these flows for the Pfirsch-Schlüter, plateau, and banana regimes. Here incompressibility is not enforced, so there are oscillations during the damping of the flow; it is not a purely exponential decay. The analytic gyrofluid expressions above compare favorably with the full numerical solutions. In the plateau and banana regimes, after an initial rapid damping phase, a finite poloidal flow is maintained which is damped on a slower collisional time scale. In contrast to the neoclassical banana regime results (valid only for longer time scales), no significant differences are seen between the plateau and banana damping rates in this initial strong damping phase.

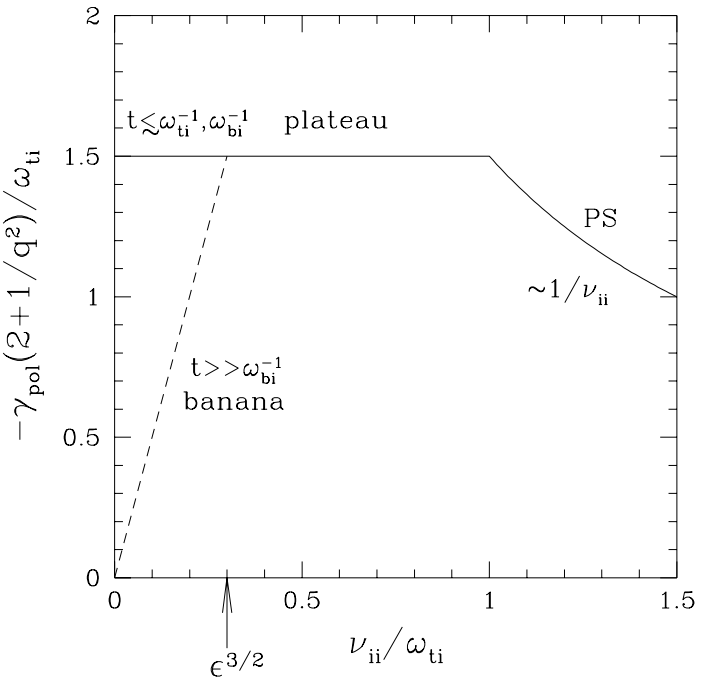

Figure 5.9: Poloidal flow damping rates in various collisional regimes. The gyrofluid results (solid) match the neoclassical results in the Pfirsch-Schlüter and plateau regimes. For short time scales ($t \lesssim \omega_{ti}^{-1}, \omega_{bi}^{-1}$), transit-time magnetic pumping dominates in the banana regime. The neoclassical result of [Hirshman, 1978] (using static parallel viscosity coefficients) is also shown in the banana regime (dashed). Because the neoclassical calculations assume that the distribution function evolves on a collisional time scale, they miss the rapid collisionless damping, and are only valid for $t \gg \omega_{bi}^{-1}$.

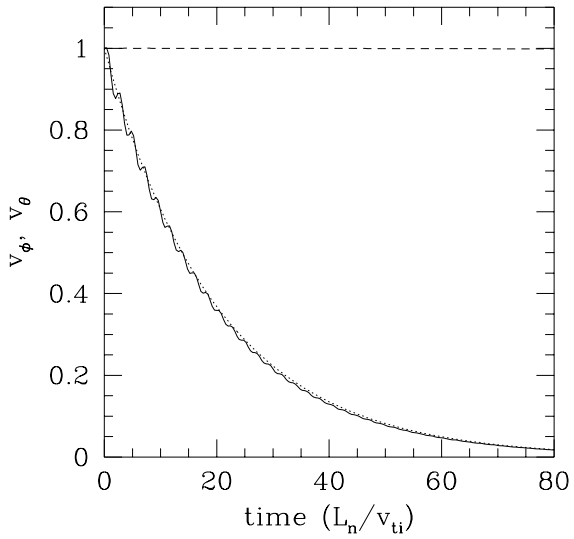

Figure 5.10: Poloidal flow damping in the Pfirsch-Schlüter regime, $\nu_{ii}/\omega_{ti} = 10.0$. The poloidal flow (solid) from simulations agrees with the analytic result Eq. (5.41) (dotted). The toroidal flow (dashed) is constant, demonstrating that toroidal angular momentum is well conserved.

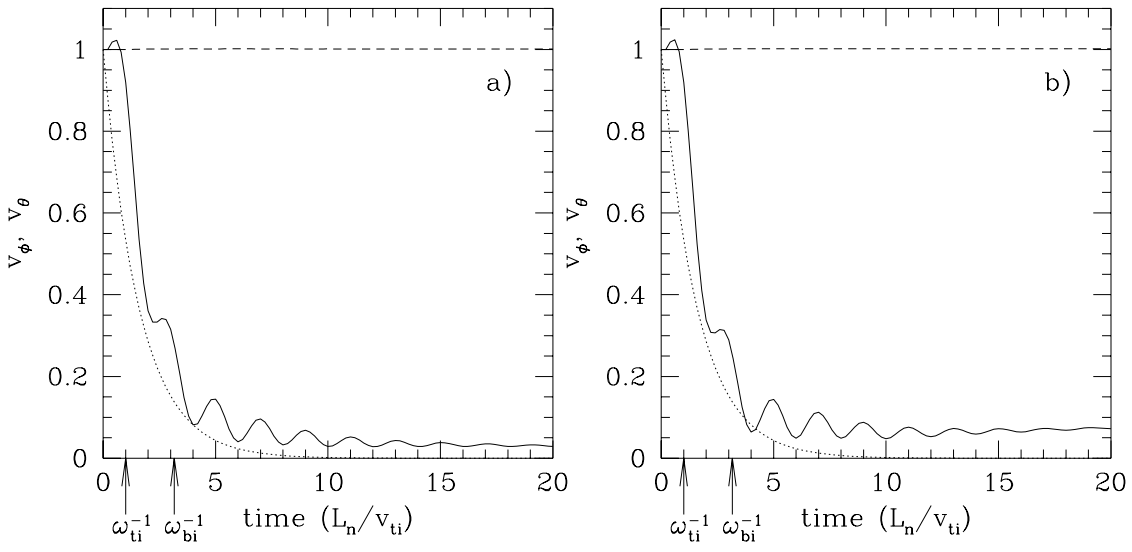

Figure 5.11: Poloidal flow damping in (a) the plateau regime, $\nu_{ii}/\omega_{ti} = 0.1$, and (b) the banana regime, $\nu_{ii}/\omega_{ti} = 0.001$. The poloidal flow (solid) from simulations agrees with the analytic gyrofluid result Eq. (5.45), and the toroidal flow (dashed) is again well conserved. Transit-time magnetic pumping dominates for short time scales $t \lesssim \omega_{ti}^{-1}\omega_{bi}^{-1}$, and at later times the damping is governed by collisional processes.

For the short time scales of the turbulence, transit-time magnetic pumping is the dominant poloidal flow damping process in the banana and plateau regimes. The small scale $\mathbf{E} \times \mathbf{B}$ flows are randomly generated by the turbulence, and damped according to Eq. (5.45). A bounce time later, when Eq. (5.45) is no longer valid, the turbulence has evolved into a different state, generating new flows. Because the turbulence is quite sensitive to balance between the nonlinear generation and the linear damping of the poloidal flow, it is important that the gyrofluid equations accurately model this process. Things get slightly more complicated for $k_r \rho_i \sim \mathcal{O}(1)$, and it is more difficult to check our models in this regime. Future work is needed to fully resolve this issue, but it appears that the toroidal gyrofluid equations are accurately modeling this process.

5.4 Nonlinear Simulation Results with Trapped Electrons

Although the adiabatic electron assumption may lead to a reasonable description of ITG driven turbulence in some regimes (e.g., when the electrons are very collisional so trapped electrons are wiped out, but not so collisional that the parallel dynamics are affected), in general, nonadiabatic electron effects should be taken into account. It is conceivable that if $\chi_i \gg \chi_e, D$, the electrons could be passively advected by toroidal ITG driven turbulence with little effect on the ion transport, but in general $\chi_i \sim \chi_e \sim D$. Clearly when $\chi_e > \chi_i$, nonadiabatic electron effects will be important. Further, electrons are typically in the banana regime ($\nu_{*e} < 1$), except in the collisional extreme edge and in the extreme core where the trapped fraction $\sqrt{\epsilon}$ is small, indicating that collisions are usually not large enough to completely wipe out the nonadiabatic electron response. Again, $D, \chi_e \neq 0$ guarantees that the electrons are significantly nonadiabatic.

In this section, the effects of nonadiabatic electrons are investigated with nonlinear simulations. These results should be considered preliminary. The effect of electron collisionality on the predicted transport is shown in Fig. 5.12 for the parameters $\eta_i = \eta_e = 3$, $q = 1.5$, $\hat{s} = 1$, $\epsilon_n = 1/3$, $\epsilon = 1/6$ and $T_i = T_e$, corresponding to the linear results in Fig. 3.5. For high collisionality, $\nu_{\text{eff}} L_n / v_{ti} = 10$ ($\nu_{*e} = 2$), the electron response is nearly adiabatic. The ion thermal flux, $\chi_i \approx 4\rho_i^2 v_{ti}/L_n$,

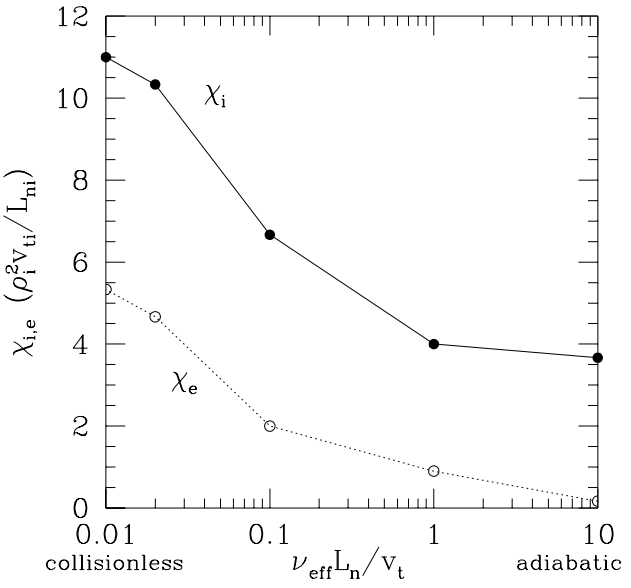

Figure 5.12: Fully nonlinear simulation results with trapped electrons, varying electron collisionality, for ITG driven turbulence at $\eta_i = \eta_e = 3$. As ν_{*e} is reduced, the electrons become destabilizing, until $\chi_i \sim 3\chi_i^{\text{adiabatic}}$ in the collisionless limit.

is the same as obtained with adiabatic electrons and χ_e is very small. As ν_{eff} is reduced, the electrons become destabilizing. In the collisionless limit, $\nu_{*e} = 0.002$, $\chi_i \approx 11\rho_i^2 v_{ti}/L_n$ and $\chi_e \approx 5\rho_i^2 v_{ti}/L_n$. Although for these parameters the turbulence is driven by toroidal ITG modes ($\eta_i = 3$, $L_{Ti}/R = 0.1$), electrons increase χ_i by up to a factor of three over simulations with adiabatic electrons.

Fig. 5.13 shows results from another set of nonlinear simulations showing the effect of ∇T_i. Beginning with the reference case $\eta_i = \eta_e = 3$, $q = 1.5$, $\hat{s} = 1$, $\epsilon_n = 1/3$, $\epsilon = 1/6$, $T_i = T_e$, and $\nu_{*e} = 0.02$, ∇T_i is reduced by lowering η_i holding $L_{ne} = L_{ni}$ and L_{Te} fixed. These nonlinear runs correspond to the linear results in Fig. 3.6. If the electrons are adiabatic, when η_i is reduced below the adiabatic η_i^{crit}, the plasma is stable and the turbulent flux vanishes (solid squares in Fig. 5.13). With trapped electrons at low electron collisionality, below the adiabatic η_i^{crit} the turbulence is driven by unstable trapped electron modes. The ion heat flux $Q_i = \langle v_{Er} p_i \rangle$ drops below Q_e for $\eta_i < \eta_i^{\text{crit}}$, consistent with the quasilinear ratios where $Q_i > Q_e$ for the toroidal ITG mode and $Q_i < Q_e$ for the TEM [Rewoldt

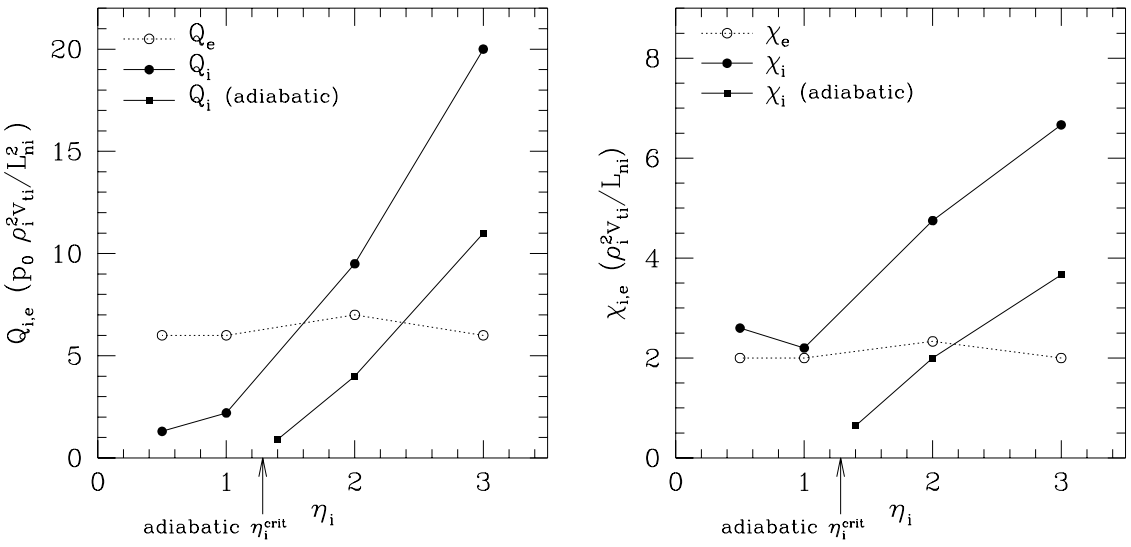

Figure 5.13: Nonlinear simulations predict χ_i/χ_e in experimental range even for $\eta_i < \eta_i^{\rm crit}$ adiabatic at low electron collisionality. At $\nu_{*e} = 0.02$, as η_i is reduced holding $\eta_e = 3$ fixed, Q_i drops below Q_e as the ITG mode evolves into TEM, but since ∇T_i is getting weaker, χ_i stays above or comparable to χ_e. Lowering η_e reduces χ_i and χ_e (weaker TEM drive).

and TANG, 1990]. However, since $Q = \chi \nabla T$, because ∇T_i is decreasing, χ_i stays above or comparable to χ_e. The relative magnitudes of χ_i and χ_e are within the experimental range, where typically $\chi_i \sim \chi_e$. The parameters of this scan were specifically chosen to investigate strongly driven TEM turbulence at $\eta_i < \eta_i^{\rm crit}$. A physically more realistic scan would not hold $\eta_e = 3$ fixed; $\eta_e = \eta_i$ is more likely. When the scan is repeated decreasing both η_e and η_i simultaneously, both χ_i and χ_e are reduced in the TEM regime, by roughly a factor of three.

These nonlinear results show that the most striking effect of trapped electrons is to soften the $\eta_i^{\rm crit}$ or $L_{Ti}^{\rm crit}/R$ threshold which exists with adiabatic electrons. When the turbulence is driven by trapped electron modes, below $\eta_i^{\rm crit}$, Q_i is reduced, so in this sense there is still a threshold for the ion heat transport, but it is not a sharp threshold at low collisionality. For the moderate ν_{*e} of many L-modes, there is marginal behavior, but at lower ν_{*e} there may still be a fairly strong TEM drive with less marginal features. Mapping out precisely when this happens is now pos-

sible with our simulations with trapped electrons. As shown above, the TEM drive can strongly affect both ion and electron transport. It is thus expected that both χ_i and χ_e will depend on electron collisionality and *electron* density and temperature gradients in low collisionality regimes, particularly when η_i is low and the TEM dominates.

Chapter 6

Comparison with Experiment

DIRECT COMPARISONS of the toroidal nonlinear simulations with experiment are presented in this chapter. Recent comparisons between experiment and a transport model based on simulations with our toroidal gyrofluid code and linear fully kinetic calculations have shown good agreement in the core ($r/a < 0.85$) of L-mode type discharges [DORLAND *et al.*, 1994b; KOTSCHENREUTHER *et al.*, 1994a]. These comparisons used an interpolation formula for χ_i, parameterized to fit our toroidal gyrofluid simulation results with adiabatic electrons. This formula also uses an interpolation formula for the marginal L_{Ti}/R found from linear fully kinetic calculations with adiabatic electrons. (As discussed in Section 5.4, a critical L_{Ti}/R does not always rigorously exist with nonadiabatic electrons, but threshold like behavior may still occur in many cases.) This fit to χ_i was then used in a predictive power balance code to predict temperature profiles, and T_i and χ_i from the fit (using the predicted T_i) were compared with experiment. Many L-mode ($\sim$ 50) shots were simulated in this manner, finding encouraging agreement. In this Chapter, a simpler, more direct approach is taken. Measured temperature and density profiles are used as inputs for the toroidal gyrofluid simulations with trapped electrons, and the resulting χ_i's and χ_e's are compared with those inferred from power balance. This comparison is presented here to roughly demonstrate where we stand, and should be considered qualitative.

The specific shot chosen is TFTR L-mode #65018, and the input parameters are taken from SNAP try 3. This shot is very similar to #65012 in [SCOTT *et al.*, 1993]. The primary ion species is deuterium, heated by 14MW of deuterium neutral

beam injection. The major radius is $R_0 = 245$cm, the minor radius is $a = 80$cm, and the toroidal field strength on axis is $B_0 = 4.8$T. The Shafranov shift is not terribly large, 11.8cm at the magnetic axis, so the simulations use concentric circular flux surface geometry. In this shot the impurity concentration is small, $Z_{\rm eff} = 1.73$. At $r = 0$, the beam density is $n_b/n_e = 0.15$, and the hydrogen and carbon impurity densities are $n_H/n_e = 0.071$ and $n_C/n_e = 0.024$, with carbon making largest contribution to $Z_{\rm eff}$ and to the impurity charge density. Metal impurities are negligible. The calculated beam density decreases monotonically towards the edge. Because of this relatively low impurity and beam concentration, in the simulations impurities and beams are neglected. The measured $Z_{\rm eff}$ (assumed independent of minor radius) is used to calculate the electron-ion collision frequency.

The profiles taken from SNAP are shown in Figs. 6.1-6.3. Since $\eta_i = L_{ni}/L_{Ti}$ varies from 1.5 to 4, the turbulence in this shot is driven by the toroidal ITG mode. Several small flux tube simulations, centered at different r/a, are run using the local measured parameters as input. The chosen numerical parameters vary slightly with the physical parameters to ensure adequate resolution. In particular, the simulations find a strong q dependence of the peak in the nonlinear fluctuation spectrum. At the edge where q is large, the spectrum peaks at lower k_θ, so larger simulation domains are required to resolve these long wavelengths. The results from these nonlinear simulations are shown in Fig. 6.4 and compared against χ_i and χ_e from power balance. Also shown is the predicted χ_i from [BIGLARI *et al.*, 1989], $\chi_i = [k_\theta \rho_i q(1+\eta_i)/(\tau \hat{s})]\, \rho_i^2 v_{ti}/L_n$. Since $k_\theta \rho_i$ is not determined from this theory, $k_\theta \rho_i = 0.2$ is used. Using $k_\theta \rho_i$ found from the simulations would exacerbate the difference between this theory and experiment, since $k_\theta \rho_i$ from the simulations decreases with increasing minor radius. In the core ($r/a < 0.2$), all modes are stable for the measured parameters, but just barely; a small increase in ∇T_i would destabilize the toroidal ITG mode and give a small χ_i. (This shot had sawteeth, which might be complicating things in this region, since the $q = 1$ surface is at about $r/a = 0.25$.)

There is a tendency for the predicted χ from the simulations, $\chi^{\rm sim}$, to over- and undershoot $\chi^{\rm PB}$ calculated from power balance. This is related to the dependence of the χ's on ∇T, and the fact that the measured ∇T, as a gradient, is more susceptible to experimental uncertainties than local quantities. The experimentally

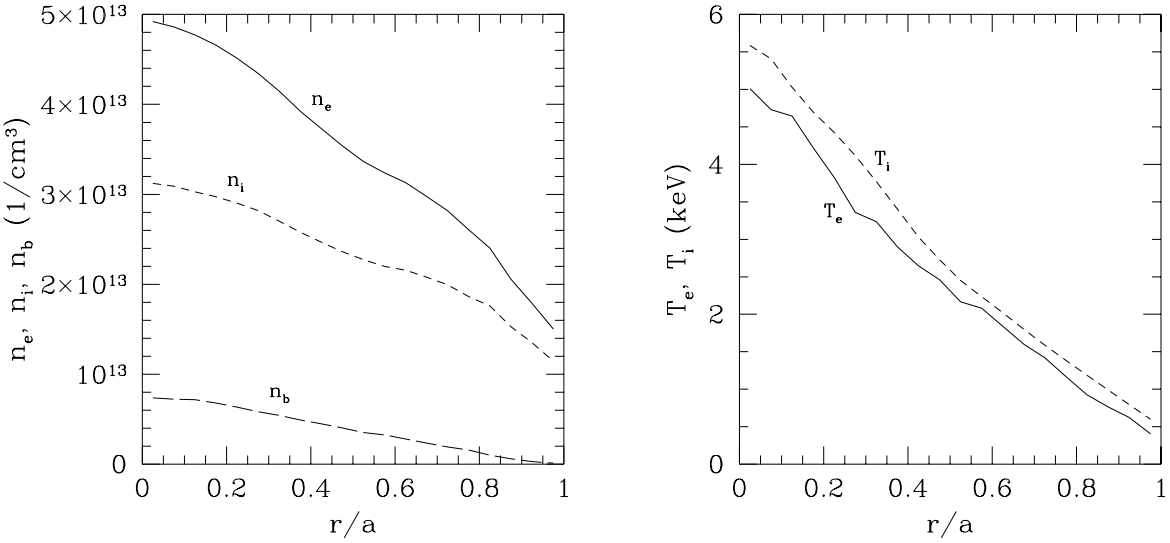

Figure 6.1: Measured electron (solid) and ion (dashed) density and temperature profiles, and beam density (long dashes) for #65018 from SNAP.

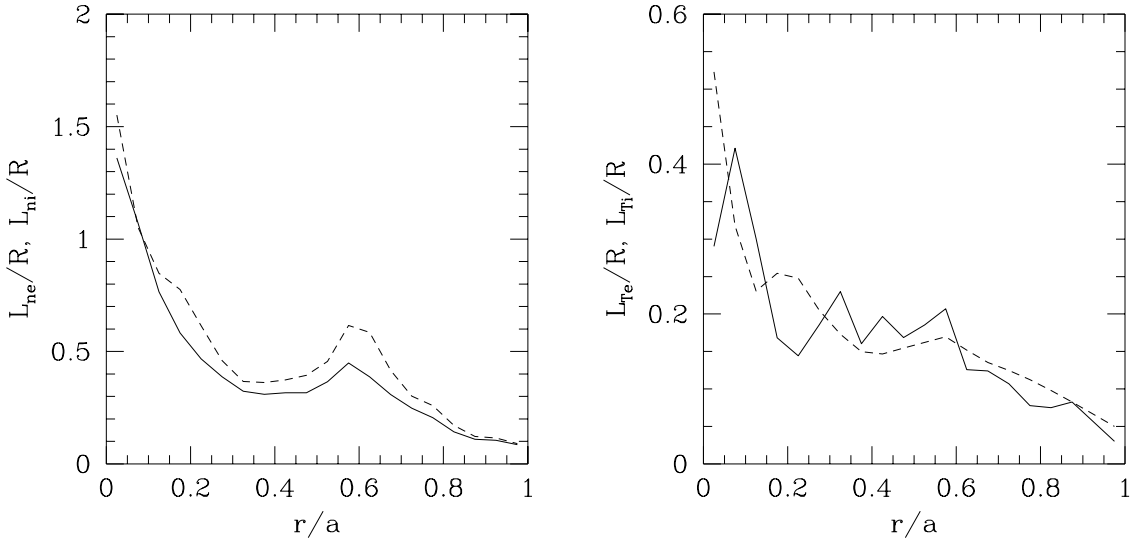

Figure 6.2: Electron (solid) and ion (dashed) density and temperature scale lengths.

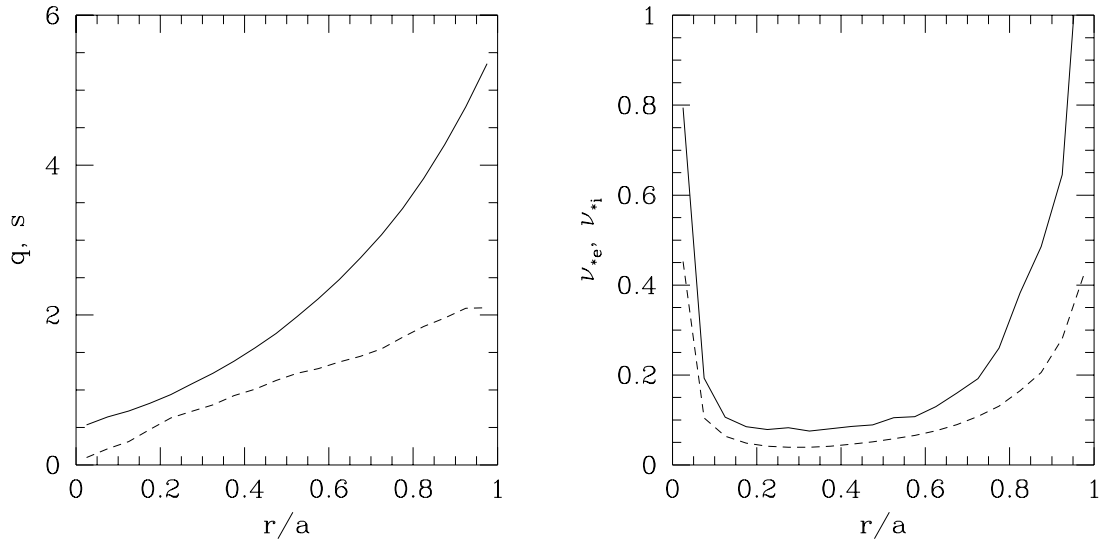

Figure 6.3: Safety factor, q (solid), shear, $\hat{s}$ (dashed), electron (solid) and ion (dashed) collisionality for #65018.

inferred heat flux, Q_i, is fairly smooth. Since $\chi^{\rm PB} \propto Q_i/\nabla T_i$, if the measured ∇T_i is slightly lower than its actual value, $\chi^{\rm PB}$ a will be slightly higher than the actual χ_i. The simulation $\chi^{\rm sim}$ is proportional to ∇T_i, since the turbulence here is primarily driven by the ion temperature gradient. Since the simulations use ∇T_i as an input, if ∇T_i is slightly low, $\chi^{\rm sim}$ will be low. Therefore, small errors in ∇T_i push $\chi^{\rm sim}$ and $\chi^{\rm PB}$ in opposite directions. Taking this into account, Fig. 6.4 shows reasonable agreement between the toroidal gyrofluid results and the experimental results in the core region, $r/a < 0.7$, for both χ_i and χ_e. The heat transport is reduced in the core where the toroidal ITG mode is more weakly driven than, for example, at $r/a = 0.5$.

Outside $r/a = 0.7$, the predicted χ_i is clearly too low. There are a few possible explanations which could make the predicted edge transport increase, due to effects which are not included in these simulations. Increased damping of the turbulence-generated sheared flows near the edge would increase the flux (see Fig. 5.5). Increased flow damping could possibly come from collisional friction with impurities or from drag due to charge exchange, although the latter is probably quite weak. Another mechanism which would increase the edge transport is inverted im-

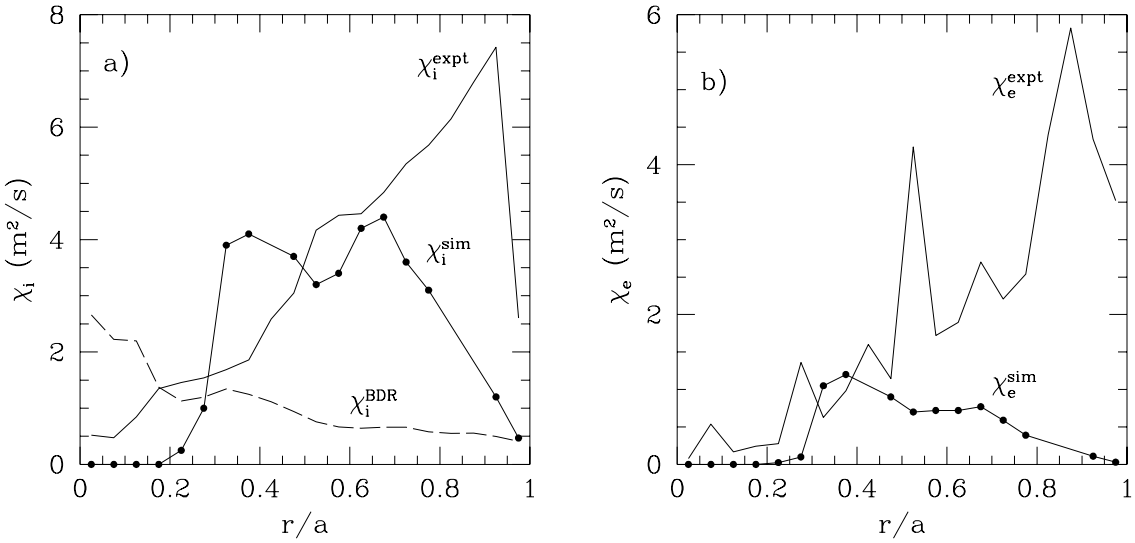

Figure 6.4: (a) Comparison of predicted and experimental $\chi_i(r)$. (b) Comparison of $\chi_e(r)$. The dots are from the simulations and the solid lines without dots are calculated from power balance (SNAP). Also shown is the theoretical χ_i from [Biglari *et al.*, 1989].

purity density gradient drive, as discussed in Section 1.2 [DORLAND *et al.*, 1994a]. The radial variation of impurity density is difficult to measure; it is probably easier to find some signature of impurity density gradient driven turbulence in the simulations, and then look for this signature in fluctuation measurements. Another possibility is Kelvin-Helmholtz type drive from sheared equilibrium flows, but it seems unlikely that the flows in the edge are large enough to drive these instabilities. Another possibility is that the large fluctuations at the edge are not generated locally, but are propagating into the edge from more strongly driven core regions [MATTOR and DIAMOND, 1994]. Finally, perhaps some increased drive at the edge could come from the Shafranov shift. Near the edge the flux surfaces are compressed, increasing the local gradient in the bad curvature region. Clearly all these mechanisms are speculative at this point, and should be studied in more detail.

The predicted electron heat flux is in reasonable agreement with experiment in the core, $r/a < 0.5$, but is too low in the edge. In the region $0.5 < r/a < 0.7$, where χ_i matches fairly well, the predicted electron flux may be low due our approximate collision model. As discussed in Section 3.4, we have approximated the velocity dependence of $\nu_e(v)$. Over most of the minor radius, the collisionality for this shot is near $\nu_{\rm eff} L_n/v_{ti} \approx 1$, where our trapped electron model underestimates the nonadiabatic electron response. (See the right hand side of Fig. 3.5.) Incorporating the velocity dependence of $\nu_e(v)$ could remedy part of this discrepancy.

Overall, this seems to be a reasonable level of agreement. The gyrofluid equations appear to be accurate enough to properly capture the small linear drive in the core, where the plasma is near marginality, without resorting to fully kinetic linear theory. Small changes in ∇T_i and ∇T_e could make the agreement virtually exact for $r/a < 0.7$. To demonstrate this, comparison of this shot with the IFS-PPPL χ_i interpolation formula based on our toroidal gyrofluid simulations with adiabatic electrons and linear fully kinetic calculations is shown in Fig. 6.5(a). This interpolation formula for χ_i found by [DORLAND *et al.*, 1994b]:

$$\chi_i = \frac{\rho_i^2 v_{ti}}{R} \left(\frac{R}{L_{Ti}} - \frac{R}{L_{Ti}^{\rm crit}} \right)^{1,1/2} \mathcal{F}, \tag{6.1}$$

is quite similar to the results with trapped electrons (Fig. 6.4) for this moderate collisionality. In Eq. (6.1), $\mathcal{F} = q/(2+\hat{s})\cdots$, is a complicated function of local dimensionless parameters, and $R/L_{Ti}^{\rm crit}$ is determined from kinetic calculations

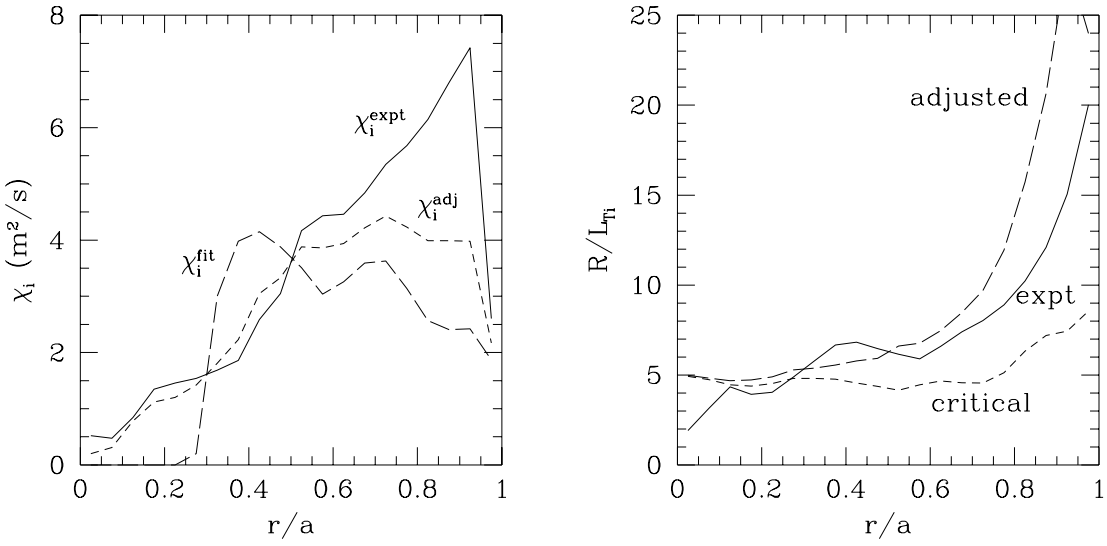

Figure 6.5: (a) Comparison of experimental $\chi_i(r)$ (solid) and and the IFS-PPPL $\chi_i(r)$ (long dashes). Also shown is the IFS-PPPL $\chi_i(r)$ using an $L_{Ti}(r)$ profile adjusted so the predicted heat flux matches the experimental heat flux (short dashes). (b) Measured (solid) and adjusted (long dashes) R/L_{Ti}. In the core, the adjusted R/L_{Ti} is only slightly above the critical R/L_{ti} (short dashes).

[KOTSCHENREUTHER *et al.*, 1994b]. If $L_{Ti}(r)$ is adjusted so the predicted heat flux, Q_i, matches the measured heat flux, $\chi_i(r)$ is in much better agreement, as shown by the $\chi_i^{\rm adj}$ in Fig. 6.5(a). This is similar to the results which would be obtained from the predictive transport code used in [DORLAND *et al.*, 1994b]. Fig. 6.5(b) shows the measured R/L_{Ti}, the adjusted R/L_{Ti}, and $R/L_{Ti}^{\rm crit}$. The adjusted R/L_{Ti} is only slightly above marginal in the core, since the measured heat flux there is small. Fig. 6.6 shows the T_i profile obtained by integrating the adjusted $L_{Ti}(r)$ inward, using the measured T_i at $r/a = 0.8$ as a boundary condition. Thus, only a relatively small change in $T_i(r)$ is needed to get the predicted χ_i to agree. This is an example of usual marginal stability effects as emphasized again in [DORLAND *et al.*, 1994b]. A good sawtooth model might further improve the T_i fit in the core.

This encourages us to add more physics to these simulations to try to explain a wider range of experimental conditions. With nonadiabatic electrons, at sufficiently small ν_{*e}, there is often no rigorous critical L_{Ti} beyond which the modes

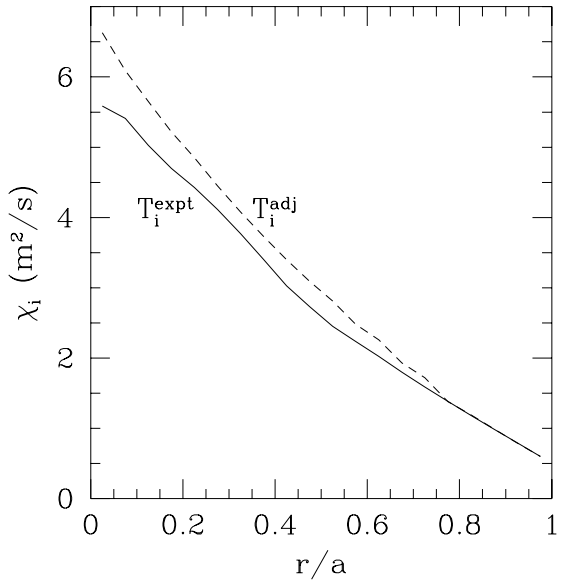

Figure 6.6: T_i profile obtained by integrating the adjusted L_{Ti} inward, using the measured T_i at $r/a = 0.8$ as a boundary condition. Only small changes from the measured T_i profile are necessary to make the heat fluxes agree.

are completely stabilized, but there can still be threshold-like behavior where the modes are weaker. For the moderate ν_{*e} of many of the L-modes looked at in [DORLAND *et al.*, 1994b], there is marginal behavior (as in Fig. 6.4(a)), but at lower ν_{*e} there may still be a fairly strong TEM drive with less marginal features. Mapping out precisely when this happens is now possible with our simulations with trapped electrons, and is important work for the future.

There are many experimental transport scalings which appear to contradict microinstability based theories, especially the scaling with current (I_p), B, and ion mass. There is some evidence, however, that the I_p and B scalings are not inconsistent with our results. The q dependence of Eq. (6.1) can lead to I_p scaling. The detailed comparisons in [KOTSCHENREUTHER *et al.*, 1994a] also compare favorably with the current ramp experiments of [ZARNSTORFF *et al.*, 1991]. Although our simulations and Eq. (6.1) are gyro-Bohm, this gyro-Bohm scaling with B can be partially masked by marginal stability effects, leading to a more Bohm-like behavior, as seen in experiments. While the comparisons discussed in this chapter and in [DORLAND *et al.*, 1994b; KOTSCHENREUTHER *et al.*, 1994a] seem to be on the right track, these issues must be carefully addressed.

Chapter 7

Conclusions

SEVERAL ADVANCES toward an understanding of turbulent transport in tokamaks are made in this thesis. The primary thrust of this work is the development of nonlinear toroidal simulations which predict fluctuation and transport levels that compare favorably with experiment. These simulations rely on more accurate fluid equations for the ions and new bounce averaged trapped electron equations. Together, these equations provide an accurate description of most of the physics considered relevant for microinstability driven turbulence. This reduced fluid model is sufficiently simple to solve directly in high resolution numerical simulations. These simulations implement a reduced flux tube geometry for further numerical efficiency, and fully incorporate toroidal effects. Toroidal effects are found to significantly enhance thermal transport and fluctuation levels over sheared slab predictions, bringing the predictions up to experimentally measured levels. In addition, the nonlinear fluctuation spectrum is peaked at long wavelengths, and is anisotropic in k_r and k_θ due to the ballooning nature of this turbulence, in agreement with experiment. Finally, the trapped electron fluid equations provide the first high resolution toroidal nonlinear simulations which simultaneously include toroidal ITG modes and trapped electron modes, and allow calculation of the full transport matrix: ion and electron heat fluxes and particle fluxes.

7.1 Summary

Toroidal ion gyrofluid equations are derived with improved models of the important kinetic effects associated with toroidicity. Special care is taken to derive closure approximations which, though similar to those of [Waltz *et al.*, 1992], are well behaved in the mixed limit where both toroidal drifts and parallel free streaming are important, i.e. where both $k_\parallel$ and ω_d are non-zero. The four moment toroidal gyrofluid model of [Waltz *et al.*, 1992] is extended to six moments, including the $\mu\hat{\mathbf{b}}\cdot\nabla B$ mirroring terms. This keeps the parallel velocity equation exact, important for accurate poloidal flow damping rates. Including the $\mu\hat{\mathbf{b}}\cdot\nabla B$ terms also incorporates trapped ion effects to some level of approximation (the growth rate in the very low $k_\theta\rho_i$ trapped ion mode regime is within a factor of two of full gyrokinetics). New toroidal FLR terms are treated which arise from the variation of B (in the argument of J_0) with major radius, and generalize the FLR model of [Dorland and Hammett, 1993] to toroidal geometry. An improved four moment model is also presented, which is simpler and numerically less demanding than the six moment model. Impurity and (Maxwellian) beam dynamics are equally well described by these toroidal gyrofluid equations, and have been incorporated into the code by Dorland.

New bounce average fluid equations for trapped electrons are derived, incorporating sophisticated models of the trapped electron toroidal precession resonance and pitch-angle scattering from collisions. Because these equations are bounce averaged, the fast parallel electron time scale is removed, allowing high resolution toroidal simulations simultaneously including drive from toroidal ITG modes and trapped electron modes. Including nonadiabatic electron dynamics also allows predictions of electron heat transport and particle transport. Both the toroidal ion gyrofluid and trapped electron equations are carefully benchmarked against fully kinetic linear theory, in the local limit and in fully nonlocal eigenmode calculations.

A reduced flux tube coordinate system is presented which exploits the elongated nature of microinstability driven turbulence. A slab gyrofluid code [Dorland, 1993] is extended to toroidal geometry using this coordinate system and the comprehensive toroidal gyrofluid equations derived here. These simulations find that the effects of toroidal geometry are quite important. The fluctuation levels and transport are about 25 times larger than sheared slab simulations, bringing

the predicted transport up to measured levels. The fluctuation spectra from these simulations are peaked at $k_\theta \rho_i \approx 0.1-0.2$ for typical parameters and are anisotropic in k_r and k_θ, similar to BES fluctuation measurements on TFTR [Fonck *et al.*, 1993].

The importance of turbulence-generated small-scale sheared $\mathbf{E} \times \mathbf{B}$ flows on toroidal ITG turbulence is demonstrated. The damping of the (large) poloidal component of these flows is shown to be a sensitive control of the turbulence level. The damping of these flows within the six moment gyrofluid model is carefully investigated. For the relevant short time scales of the turbulence, the toroidal gyrofluid model is shown to be accurate.

Direct comparison of these toroidal simulation results with L-mode experiments are found to be encouraging. The predicted ion and electron heat transport in the core, $r/a < 0.7-0.8$, are in reasonable agreement with those calculated from power balance. The transport in the edge, $r/a > 0.7-0.8$, is too low, and possible mechanisms to explain this discrepancy are discussed.

7.2 Future Directions

The gyrofluid equations are an approximation to the full nonlinear gyrokinetic equation, and break down in some regimes. For example, the weak turbulence wave-kinetic equation derived from the gyrofluid equations successfully reproduces the gyrokinetic wave-kinetic equation in the limit $\omega \gg k_\parallel v_{ti}$, but fails to recover the ion-Compton scattering rate very near marginal stability, in the limit $\gamma \ll \omega \ll k_\parallel v_{ti}$ [Mattor, 1992; Dorland, 1993]. The nonlinear validity of the gyrofluid equations in strong turbulence regimes has not yet been unambiguously verified on fundamental grounds. However, gyrofluid simulations have been compared against technically more accurate gyrokinetic particle simulations, finding similar behavior in a sheared slab [Parker *et al.*, 1994; Dorland, 1993]. The toroidal simulations developed in this thesis have been benchmarked with toroidal gyrokinetic particle simulations (though not as extensively as the sheared slab simulations), and find reasonable agreement [Parker *et al.*, 1994]. Very recently, the toroidal gyrokinetic particle simulations of [Dimits *et al.*, 1994] appear to predict lower transport by about a factor of 2.5. While in principle gyrokinetic simulations are more accurate, since

they solve the more fundamental gyrokinetic equation directly, there are a number of issues which need investigation: particle noise, particle filtering, resolution, and geometry (we implement field-line coordinates in a somewhat different way than [DIMITS *et al.*, 1994], which tends to emphasize resolution in different parts of k-space). Detailed comparisons with gyrokinetics is worthy of further study, to track down the causes of this discrepancy.

Closing the fluid hierarchy with linear closures naively appears to introduce an error of $\mathcal{O}(\Delta\omega_{NL}/k_\parallel v_{ti})$, which is typically $\mathcal{O}(1)$. Here $\Delta\omega_{NL} \sim \mathbf{v}_E \cdot \nabla$ is some measure of the nonlinear decorrelation rate. In this sense it is very interesting that gyrofluid models work as well as they do nonlinearly, but there are physical reasons behind this. Each gyrofluid equation, as a moment of the gyrokinetic equation, is an exact nonlinear conservation law: closure approximations are introduced into higher moment equations in a way which preserves the conservative form the equations. As more moments are retained, more details of the distribution function are accurately described. Smith has demonstrated convergence in the number of moments for the nonlinear plasma echo problem [HAMMETT *et al.*, 1993], though it required many moments in that case. In the strong turbulence limit, it seems unlikely that many moments need to be kept, since the broad spectrum of modes should average out sharp velocity space variations in the distribution function. Our equations retain the dominant ($\mathbf{E} \times \mathbf{B}$) nonlinearities and provide accurate physics based models of the linear drive and dissipation. Future work should continue to test the validity of the gyrofluid approximation, both through comparisons with kinetic simulations and through purely theoretical simplified problems.

The toroidal ion gyrofluid equations and trapped electron fluid equations presented here are both derived in the electrostatic limit. Recent work has begun including electromagnetic effects [WALTZ *et al.*, 1994b; HAMMETT *et al.*, 1994]. The main difficulty here is that magnetic fluctuations are driven by parallel current fluctuations, and since trapped particles do not carry current, passing electrons need to be evolved (they can no longer be considered adiabatic). Resolving the fast electron parallel motion seriously slows down the numerical calculations. Some trick analogous to bounce averaging would be useful.

The nonlinear simulation results in this thesis are in axisymmetric, low-β, high aspect ratio magnetic geometry. Including the effects of general magnetic ge-

ometry is a straightforward next step. It is of great interest to investigate the effects of elongation and triangularity on the transport, both to compare with existing non-circular tokamaks and to optimize the design of future experiments. The derivation of both the toroidal ion gyrofluid equations and the trapped electron fluid equations is valid for general geometry. Further, the flux tube simulation geometry in Chapter 4 is formulated in general geometry. All that is required is a pre-processor which would take the equilibrium magnetic field described by Eq. (4.1) and calculate the metric coefficients in Eqs. (4.5) and (4.6). These metric coefficients would then be used as further input for the toroidal gyrofluid code.

Although these toroidal gyrofluid simulations are relatively fast, an analytic formula for χ_i, χ_e, and D would be more desirable. In addition to aiding comparisons with experiment, analytic formulas (even if they are approximate) usually offer more insight than purely numerical results. Our focus to date has been to add more physics to our equations and simulations until we are confident that they are experimentally relevant. Now that it appears we are reaching this point, it would be very interesting to investigate the nonlinear dynamics in the simulations in more detail, to try to develop an analytic model for the transport. While the interpolation formula for χ_i in [Dorland *et al.*, 1994b] represents a significant step towards a reduced description of the simulation results, a model for the transport in terms of a simplified renormalized dispersion relation would be more satisfying. [Dorland *et al.*, 1994b] have found that much of the variation in χ_i is captured by $\max(\gamma/k_\perp^2)$ (different from $\max(\gamma)/k_\perp^2$ because of the $k_\perp$ dependence of γ), but the residual variation is still described by a numerical fit to the simulation results. This residual variation presumably includes physics involving sheared-flow generation and damping, and it would be nice to have an analytic model of this.

The electron equations have been implemented in the nonlinear simulations only quite recently; a more careful investigation of electron heat fluxes and particle fluxes is clearly called for. Further study of TEM driven turbulence is required to accurately describe supershots and ohmic plasmas. We can now study several important questions: Why is the convective multiplier as low as 3/2 in supershots? When are there particle pinches? What is the helium ash diffusion coefficient? We can also study advanced tokamak configurations with trapped electron mode stabilization due to reversed shear or high-β, which are predicted to have improved

confinement. A complete transport model must be able to predict density as well as temperature profiles. Nonadiabatic electron dynamics are thus an essential ingredient.

Appendix A

Old Toroidal Gyrofluid Equations

The equations used in the nonlinear simulations in Chapter 4 are briefly summarized here, since they are an earlier version of those derived in Chapter 2. Since the aim of the simulations in Chapter 4 is to test various assumptions implicit in flux tube simulation, the simpler four moment model is used, using adiabatic electrons and ignoring collisions and particle trapping (i.e. $\nabla_\parallel B = 0$). The four moment equations here use less accurate toroidal closure coefficients and FLR approximations than those in Section 2.7. Using the normalizations and definitions in Chapter 2, the dynamical equations are:

$$
\begin{aligned}
\frac{dn}{dt} &+ \nabla_\parallel u_\parallel - \left(1 + \frac{\eta_\perp}{2}\hat{\nabla}_\perp^2\right) i\omega_* \Psi + \left(\frac{1}{2}\hat{\nabla}_\perp^2 \mathbf{v}_\Psi\right) \cdot \nabla T_\perp = -i\omega_d \left(p_\parallel + p_\perp + 2\Psi\right), \\
\frac{du_\parallel}{dt} &+ \nabla_\parallel (p_\parallel + \Psi) = -4i\omega_d u_\parallel - 2i\omega_d \nu_{5i} u_\parallel - 2|\omega_d|\nu_{5r} u_\parallel, \\
\frac{dT_\parallel}{dt} &+ 2\nabla_\parallel u_\parallel + \sqrt{2}|k_\parallel|\chi_\parallel T_\parallel - \eta_\parallel i\omega_* \Psi = \\
&- 2i\omega_d \left[(3 + \nu_{1i})T_\parallel + \nu_{2i} T_\perp + n + \Psi\right] - 2\nu_{1r}|\omega_d| T_\parallel - 2\nu_{2r}|\omega_d| T_\perp, \\
\frac{dT_\perp}{dt} &+ \sqrt{2}|k_\parallel|\chi_\perp \left(T_\perp + \frac{1}{2}\hat{\nabla}_\perp^2 \Psi\right) - \left[\frac{1}{2}\hat{\nabla}_\perp^2 + \eta_\perp (1 + \hat{\hat{\nabla}}_\perp^2)\right] i\omega_* \Psi \\
&+ \left(\frac{1}{2}\hat{\nabla}_\perp^2 \mathbf{v}_\Psi\right) \cdot \nabla n + (\hat{\hat{\nabla}}_\perp^2 \mathbf{v}_\Psi) \cdot \nabla T_\perp = -2\nu_{3r}|\omega_d| T_\parallel - 2\nu_{4r}|\omega_d| T_\perp \\
&- 2i\omega_d \left[\nu_{3i} T_\parallel + (2 + \nu_{4i}) T_\perp + \frac{n}{2} + \frac{1}{2}(1 + \frac{3}{2}\hat{\nabla}_\perp^2)\Psi\right].
\end{aligned}
$$

The total time derivative includes the main $\mathbf{E} \times \mathbf{B}$ nonlinearities. The parallel closure coefficients are $\chi_\parallel = 2/\sqrt{\pi}$ and $\chi_\perp = 1/\sqrt{\pi}$. The toroidal closure coefficients have both dissipative and reactive pieces, and written in the form $\nu = (\nu_r, \nu_i) =$

$\nu_r + i\nu_i|\omega_d|/\omega_d$, they are $\nu_1 = (1.93, -.39)$, $\nu_2 = (.24, 1.29)$, $\nu_3 = (-1.40, .47)$, $\nu_4 = (-.14, -1.75)$, and $\nu_5 = (.76, -.98)$.

The adiabatic electron response is given by $n_e = \tau\,(\Phi - \langle\Phi\rangle)$, where $\langle\Phi\rangle(\psi) = (\int d\alpha dz J|\nabla\psi|\Phi)/\ (\int d\alpha dz J|\nabla\psi|)$ is a flux surface average. In circular concentric geometry, this becomes $\langle\Phi\rangle = (4\Delta y\, z_0)^{-1} \int dy\, dz (R/R_0)\Phi(x, y, z)$, and is only non-zero for the $k_y = 0$ components. The gyrokinetic quasineutrality constraint is $n_e = \bar{n}_i + (\Gamma_0 - 1)\Phi$, where the expression used for $\bar{n}_i$ is related to the ion guiding center density and perpendicular temperature by the FLR closure relation in [Dorland and Hammett, 1993], yielding:

$$\tau\,(\Phi - \langle\Phi\rangle) = \frac{\Gamma_0^{1/2}}{D(b)}\left[N(b)\,n + \frac{1}{2}\hat{\nabla}_\perp^2 T_\perp\right] + (\Gamma_0 - 1)\,\Phi.$$

Where $\tau = T_i/T_e$, and explicit forms for the functions $N(b)$, $D(b)$, are given in [Dorland and Hammett, 1993].

Since this equation involves both Φ and $\langle\Phi\rangle$, it is woth noting the procedure used to determine Φ, given n and $T_\perp$. In general, the coefficients in this equation can be functions of the field line coordinate, so writing $\Phi = \langle\Phi\rangle + \delta\Phi$, and solving for $\delta\Phi$ gives:

$$\delta\Phi = \frac{\bar{n}_i + (\Gamma_0 - 1)\langle\Phi\rangle}{\tau + 1 - \Gamma_0}.$$

Averaging both sides, since $\langle\delta\Phi\rangle = 0$, and solving for $\langle\Phi\rangle$ gives:

$$\langle\Phi\rangle = \langle\frac{\bar{n}_i}{\tau + 1 - \Gamma_0}\rangle / \langle\frac{(1 - \Gamma_0)}{\tau + 1 - \Gamma_0}\rangle.$$

Now that $\langle\Phi\rangle$ is determined, we use this expression in the quasineutrality constraint to obtain Φ.

Bibliography

Adam, J. C., Tang, W. M., and Rutherford, P. H. (1976). Destabilization of the Trapped-Electron Mode by Magnetic Curvature Drift Resonances. *Phys. Fluids* **19**, 561.

Bakshi, P., Bellew, W., Ganguli, G., and Satyanarayana, P. (1977). Presented at the 1977 Sherwood Theory Conference.

Beer, M. A., Cowley, S. C., and Hammett, G. W. (1994). Field-aligned Coordinates for Nonlinear Simulations of Tokamak Turbulence. Submitted to Phys. Plasmas, PPPL-3040.

Beer, M. A., Hammett, G. W., Dorland, W., and Cowley, S. C. (1992). Nonlinear Ballooning Gyrofluid Simulations of Toroidal ITG Turbulence. *Bull. Am. Phys. Soc.* **37**, 1478.

Beer, M. A., Hammett, G. W., Liu, Q. P., , Parker, S. E., and Dorland, W. (1993). Trapped Ion and Neoclassical Effects on Toroidal ITG Turbulence. *Bull. Am. Phys. Soc.* **37**, 2101.

Biglari, H., Diamond, P. H., and Rosenbluth, M. N. (1989). Toroidal Ion-Pressure-Gradient-Driven Drift Instabilities and Transport Revisited. *Phys. Fluids B* **1**, 109.

Biglari, H., Diamond, P. H., and Terry, P. W. (1990). Influence of Sheared Poloidal Rotation on Plasma Edge Turbulence. *Phys. Fluids B* **2**, 1.

Brizard, A. (1992). Nonlinear Gyrofluid Description of Turbulent Magnetized Plasmas. *Phys. Fluids B* **4**, 1213.

Callen, J. D. (1973). Private communication, as cited in Stix, 1973.

Carreras, B. A., Lynch, V. E., and Garcia, L. (1991). Electron Diamagnetic Effects on the Resistive Pressure-Gradient-Driven Turbulence and Flow

Generation. *Phys. Fluids B* **3**, 1438.

Catto, P. J. and Tsang, K. T. (1978). Trapped Electron Instability in Tokamaks: Analytic Solution of the Two-Dimensional Eigenvalue Problem. *Phys. Fluids* **21**, 1381.

Cheng, C. Z. and Chen, L. (1981). Ballooning-Mode Theory of Trapped-Electron Instabilities in Tokamaks. *Nucl. Fusion* **21**, 403.

Chew, G. F., Goldberger, M. L., and Low, F. E. (1956). Boltzmann Equation and the One-Fluid Hydrodynamic Equations in the Absence of Particle Collisions. *Proc. Roy. Soc.* **A236**, 112.

Cohen, B., Williams, T. J., Dimits, A. M., and Byers, J. A. (1993). Gyrokinetic Simulations of $E \times B$ Velocity-shear Effects on Ion-Temperature Gradient Modes. *Phys. Fluids B* **5**, 2967.

Connor, J. W., Hastie, R. J., and Taylor, J. B. (1979). Shear, Periodicity, and Plasma Ballooning Modes. *Proc. R. Soc. London A* **365**, 1.

Connor, J. W., Taylor, J. B., and Wilson, H. R. (1993). Shear Damping of Drift Waves in Toroidal Plasmas. *Phys. Rev. Lett.* **70**, 1803.

Coppi, B., Furth, H. P., Rosenbluth, M. N., and Sagdeev, R. Z. (1966). Drift Instability Due to Impurity Ions. *Phys. Rev. Lett.* **17**, 377.

Coppi, B. and Pegoraro, F. (1977). Theory of the Ubiquitous Mode. *Nucl. Fusion* **17**, 969.

Coppi, B. and Rewoldt, G. (1974). New Trapped-Electron Instability. *Phys. Rev. Lett.* **33**, 1329.

Coppi, B., Rosenbluth, M. N., and Sagdeev, R. Z. (1967). Instabilities Due to Temperature Gradients in Complex Magnetic Field Geometries. *Phys. Fluids* **10**, 582.

Cordey, J. G. (1976). Effects of Particle Trapping on the Slowing-down of Fast Ions in a Toroidal Plasma. *Nucl. Fusion* **16**, 499.

Cowley, S. C., Kulsrud, R. M., and Sudan, R. (1991). Considerations of Ion-Temperature-Gradient-Driven Turbulence. *Phys. Fluids B* **3**, 2767.

Diamond, P. H. and Kim, Y.-B. (1991). Theory of Mean Poloidal Flow Generation by Turbulence. *Phys. Fluids B* **3**, 1626.

Dimits, A. M. (1993). Fluid Simulations of Tokamak Turbulence in Quasiballooning Coordinates. *Phys. Rev. E* **48**, 4070.

Dimits, A. M. (1994). Private communication.

Dimits, A. M., Byers, J. A., Williams, T. J., Cohen, B. I., Xu, X. Q., Cohen, R. H., Crotinger, J. A., and Shestakov, A. E. (1994). Gyrokinetic and Global Fluid Simulations of Tokamak Microturbulence and Transport. In *Plasma Physics and Controlled Nuclear Fusion Research, 1994*, International Atomic Energy Agency, Vienna. IAEA-CN-60/D-P-I-5.

Dominguez, R. R. and Rosenbluth, M. N. (1989). Local Kinetic Stability Analysis of the Ion Temperature Gradient Mode. *Nucl. Fusion* **29**, 844.

Dong, J. Q., Horton, W., and Dorland, W. D. (1994). Isotope Scaling and η_i Mode with Impurities in Tokamak Plasmas. Submitted to Phys. Plasmas, IFSR 654.

Dong, J. Q., Horton, W., and Kim, J. Y. (1992). Toroidal Kinetic η_i-mode Study in High-Temperature Plasmas. *Phys. Fluids B* **4**, 1867.

Dorland, W. (1993). *Gyrofluid Models of Plasma Turbulence.* PhD thesis, Princeton University.

Dorland, W. and Hammett, G. W. (1993). Gyrofluid Turbulence Models with Kinetic Effects. *Phys. Fluids B* **5**, 812.

Dorland, W., Hammett, G. W., Hahm, T. S., and Beer, M. A. (1992). Nonlinear and Linear FLR Effects in Gyrofluid Turbulence Simulations. *Bull. Am. Phys. Soc.* **37**, 1478.

Dorland, W., Hammett, G. W., Hahm, T. S., and Beer, M. A. (1993). Nonlinear Gyrofluid Model of ITG Turbulence. In Horton, W., Wakatani, M., and Wootton, A., editors, *Ion Temperature Gradient Driven Turbulent Transport.* American Institute of Physics, New York.

Dorland, W., Horton, W., and Hammett, G. W. (1994a). Direct Numerical Simulation of Inverted Density Profile ITG Turbulence. Presented at the 1994 Sherwood Theory Conference.

Dorland, W., Kotschenreuther, M., Beer, M. A., Hammett, G. W., Waltz, R. E., Dominguez, R. R., Valanju, P. M., Miner, W. H., Dong,

J. Q., Horton, W., Waelbroeck, F. L., Tajima, T., and LeBrun, M. J. (1994b). Comparisons of Nonlinear Toroidal Turbulence Simulations with Experiment. In *Plasma Physics and Controlled Nuclear Fusion Research, 1994*, International Atomic Energy Agency, Vienna. IAEA-CN-60/D-P-I-6.

Dubin, D. H. E., Krommes, J. A., Oberman, C., and Lee, W. W. (1983). Nonlinear Gyrokinetic Equations. *Phys. Fluids* **26**, 3524.

Fonck, R. J., Cosby, G., Durst, R. D., Paul, S. F., Bretz, N., Scott, S., Synakowski, E., and Taylor, G. (1993). Long-Wavelength Density Turbulence in the TFTR Tokamak. *Phys. Rev. Lett.* **70**, 3736.

Frieman, E. A. and Chen, L. (1982). Nonlinear Gyrokinetic Equations for Low-Frequency Electromagnetic Waves in General Plasma Equilibria. *Phys. Fluids* **25**, 502.

Gang, F. Y. and Diamond, P. H. (1990). A Nonlinear Bounce-Kinetic Equation for Trapped Electrons. *Phys. Fluids B* **2**, 2976.

Garbet, X., Laurent, L., Roubin, J. P., and Samain, A. (1993). Radial Propagation of Turbulence in Tokamaks. In *Plasma Physics and Controlled Nuclear Fusion Research, 1992*, volume 2, page 213, International Atomic Energy Agency, Vienna.

Glasser, A. H. (1977). Ballooning Modes in Axisymmetric Toroidal Plasmas. In Coppi, B. and Sadowski, W., editors, *Proceedings of the Finite Beta Theory Workshop*, page 55. U. S. Department of Energy, Varenna.

Greene, J. M. and Johnson, J. L. (1962). Stability Criterion for Arbitrary Hydromagnetic Equilibria. *Phys. Fluids* **5**, 510.

Gross, E. P. and Krook, M. (1956). Model for Collision Processes in Gases: Small-Amplitude Oscillations of Charged Two-Component Systems. *Phys. Rev.* **102**, 593.

Guzdar, P. N., Chen, L., Tang, W. M., and Rutherford, P. H. (1983). Ion-Temperature-Gradient Instability in Toroidal Plasmas. *Phys. Fluids* **26**, 673.

Hahm, T. S. (1988). Nonlinear Gyrokinetic Equations for Tokamak Microturbulence. *Phys. Fluids* **31**, 2670.

Hahm, T. S. (1994). Rotation Shear Induced Fluctuation Decorrelation in a Toroidal Plasma. *Phys. Plasmas* **1**, 2940.

Hahm, T. S. and Tang, W. M. (1989). Properties of Ion Temperature Gradient Drift Instabilities in H-mode Plasmas. *Phys. Fluids B* **1**, 1185.

Hamaguchi, S. and Horton, W. (1990). Fluctuation Spectrum and Transport from Ion Temperature Gradient Driven Modes in Sheared Magnetic Fields. *Phys. Fluids B* **2**, 1833–1851.

Hammett, G. W. (1986). *Fast Ion Studies of Ion Cyclotron Heating in the PLT Tokamak*. PhD thesis, Princeton University.

Hammett, G. W., Beer, M. A., Cummings, J. C., Dorland, W., Lee, W. W., Mynick, H. E., Parker, S. E., Santoro, R. A., Artun, M., Furth, H. P., Hahm, T. S., Rewoldt, G., Tang, W. M., Waltz, R. E., Kerbel, G. D., and Milovich, J. (1994). Advances in Simulating Tokamak Turbulent Transport. In *Plasma Physics and Controlled Nuclear Fusion Research, 1994*, International Atomic Energy Agency, Vienna. IAEA-CN-60/D-2-II-1.

Hammett, G. W., Beer, M. A., Dorland, W., Cowley, S. C., and Smith, S. A. (1993). Developments in the Gyrofluid Approach to Tokamak Turbulence Simulations. *Plasma Phys. Controlled Fusion* **35**, 973.

Hammett, G. W. and Perkins, F. W. (1990). Fluid Models for Landau Damping with Application to the Ion-Temperature-Gradient Instability. *Phys. Rev. Lett.* **64**, 3019–3022.

Hasegawa, A. and Mima, K. (1977). Stationary Spectrum of Strong Turbulence in Magnetized Nonuniform Plasma. *Phys. Rev. Lett.* **39**, 205.

Hasegawa, A. and Wakatani, M. (1987). Self-Organization of Electrostatic Turbulence in a Cylindrical Plasma. *Phys. Rev. Letters* **59**, 1581.

Hassam, A. B. and Kulsrud, R. M. (1978). Time Evolution of Mass Flows in a Collisional Tokamak. *Phys. Fluids* **21**, 2271.

Hazeltine, R. D. and Newcomb, W. A. (1990). Inversion of the Ballooning Transformation. *Phys. Fluids B* **2**, 7.

Hinton, F. L. and Robertson, J. A. (1984). Neoclassical Dielectric Property

of a Tokamak Plasma. *Phys. Fluids* **27**, 1243.

Hirshman, S. P. (1978). The Ambipolarity Paradox in Toroidal Diffusion, Revisited. *Nucl. Fusion* **18**, 917.

Horton, W., Choi, D.-I., and Tang, W. M. (1981). Toroidal Drift Modes Driven by Ion Pressure Gradients. *Phys. Fluids* **24**, 1077.

Horton, W., Estes, R. D., and Biskamp, D. (1980). Fluid Simulation of Ion Pressure Gradient Driven Drift Modes. *Plasma Physics* **22**, 663.

Horton, W., Lindberg, D., Kim, J. Y., Dong, J. Q., Hammett, G. W., Scott, S. D., and Zarnstorff, M. C. (1992). Ion-Temperature-Gradient-Driven Transport in a Density Modification Experiment on the Tokamak Fusion Test Reactor. *Phys. Fluids B* **4**, 953.

Hsu, C. T., Shaing, K. C., and Gormley, R. (1994). Time Dependent Parallel Viscosity and Relaxation Rate of Poloidal Rotation in the Banana Regime. *Phys. Plasmas* **1**, 132.

Kadomtsev, B. B. and Pogutse, O. P. (1966). Plasma Instability Due to Particle Trapping in a Toroidal Geometry. *Zh. Eksp. Teor. Fiz.* **51**, 1734. [Sov. Phys.-JETP **24**, 1172 (1967)].

Kadomtsev, B. B. and Pogutse, O. P. (1970). Turbulence in Toroidal Systems. In Leontovich, M. A., editor, *Review of Plasma Physics*, volume 5, page 249. Consultants Bureau, New York.

Kessel, C., Manickam, J., Rewoldt, G., and Tang, W. M. (1994). Improved Plasma Performance in Tokamaks with Negative Magnetic Shear. *Phys. Rev. Lett.* **72**, 1212.

Kim, J. Y., Kishimoto, Y., Horton, W., and Tajima, T. (1994). Kinetic Resonance Damping Rate of the Toroidal Ion Temperature Gradient Mode. *Phys. Plasmas* **1**, 927.

Kotschenreuther, M., Berk, H. L., Denton, R., Hamaguchi, S., Horton, W., Kim, C.-B., LeBrun, M., Lyster, P., Mahajan, S., Miner, W. H., Morrison, P. J., Ross, D., Tajima, T., Taylor, J. B., Valanju, P. M., Wong, H. V., Xiao, S. Y., and Zhang, Y.-Z. (1991). Novel Computational Techniques to Predict Transport in Confinement Devices, and Applications

to Ion-Temperature-Gradient Driven Turbulence. In *Plasma Physics and Controlled Nuclear Fusion Research, 1990*, volume 2, page 361, International Atomic Energy Agency, Vienna.

Kotschenreuther, M., Berk, H. L., Lebrun, M., Dong, J. Q., Horton, W., Kim, J.-Y., Kishimoto, Y., Ross, D. W., Tajima, T., Valanju, P. M., Wong, H. V., Miner, W., Barnes, D. C., Brackbill, J. U., Ling, K. M., Nebel, R. A., Nystrom, W. D., Byers, J. A., Cohen, B. I., Dimits, A. M., Lodestro, L. L., Mattor, N., Smith, G. R., Williams, T. J., Kerbel, G. D., Dawson, J. M., Sydora, R. D., Carreras, B. A., Dominguez, N., Hedrick, C. L., Leboeuf, J.-N., Naitou, H., and Kamimura, T. (1993). Simulations for Confinement in Near Fusion Experiments. In *Plasma Physics and Controlled Nuclear Fusion Research, 1992*, volume 2, page 11, International Atomic Energy Agency, Vienna.

Kotschenreuther, M., Dorland, W., Beer, M. A., and Hammett, G. W. (1994a). Quantitative Predictions of Tokamak Energy Confinement from First Principles Kinetic Simulations. APS invited talk, to be published in Phys. Plasmas (1995).

Kotschenreuther, M., Rewoldt, G., and Tang, W. M. (1994b). Comparison of Initial Value and Eigenvalue Codes for Kinetic Toroidal Plasma Instabilities. Submitted to Comp. Phys. Commun., PPPL-2986.

Kotschenreuther, M. and Wong, H. V. (1991). Private communication.

Kruskal, M. D. and Kulsrud, R. M. (1958). Equilibrium of a Magnetically Confined Plasma in a Toroid. *Phys. Fluids* **1**, 265.

Lee, G. S. and Diamond, P. H. (1986). Theory of Ion-Temperature-Gradient-Driven Turbulence in Tokamaks. *Phys. Fluids* **29**, 3291.

Lee, W. W. (1983). Gyrokinetic Approach in Particle Simulation. *Phys. Fluids* **26**, 556.

Lee, W. W. (1987). Gyrokinetic Particle Simulation Model. *J. Comput. Phys.* **72**, 243.

Lee, W. W. and Tang, W. M. (1988). Gyrokinetic Particle Simulation of Ion Temperature Gradient Drift Instabilities. *Phys. Fluids* **31**, 612.

Lee, Y. C. and Van Dam, J. W. (1977). Kinetic Theory of Ballooning Instabilities. In Coppi, B. and Sadowski, W., editors, *Proceedings of the Finite Beta Theory Workshop*, page 93. U. S. Department of Energy, Varenna.

Linsker, R. (1981). Integral-Equation Formulation for Drift Eigenmodes Cylindrically Symmetric Systems. *Phys. Fluids* **24**, 1485–1491.

Liu, C. S., Rosenbluth, M. N., and Tang, W. M. (1976). Dissipative Universal Instability Due to Trapped Electrons in Toroidal Systems and Anomalous Diffusion. *Phys. Fluids* **19**, 1040.

Liu, Q. P. and Cheng, C. Z. (1993). The Development of a Nonlinear Toroidal Gyrokinetic-Vlasov Simulation. *Bull. Am. Phys. Soc.* **38**, 2102.

Mattor, N. (1991). Toroidal Ion Temperature Gradient-Driven Weak Turbulence. *Phys. Fluids B* **3**, 1913.

Mattor, N. (1992). Can Landau-Fluid Models Describe Nonlinear Landau Damping? *Phys. Fluids B* **4**, 3952.

Mattor, N. and Diamond, P. H. (1994). Drift Wave Propagation as a Source of Plasma Edge Turbulence. *Phys. Rev. Lett.* **72**, 486.

Mazzucato, E. and Nazikian, R. (1993). Radial Scale Length of Turbulent Fluctuations in the Main Core of TFTR Plasmas. *Phys. Rev. Lett.* **71**, 1840.

Parker, S. E., Dorland, W., Santoro, R. A., Beer, M. A., Liu, Q. P., Lee, W. W., and Hammett, G. W. (1994). Comparisons of Gyrofluid and Gyrokinetic Simulations. *Phys. Plasmas* **1**, 1461.

Parker, S. E., Lee, W. W., and Santoro, R. A. (1993). Gyrokinetic Simulation of Ion Temperature Gradient Driven Turbulence in 3D Toroidal Geometry. *Phys. Rev. Lett.* **71**, 2042.

Perkins, F. W. (1990). Issues in Tokamak/Stellarator Transport and Confinement Enhancement Mechanisms. Technical Report PPPL-2708, Princeton Plasma Physics Laboratory.

Perkins, F. W., Barnes, C. W., Johnson, D. W., Scott, S. D., Zarnstorff, M. C., Bell, M. G., Bell, R. E., Bush, C. E., Grek, B., Hill, K. W., Mansfield, D. K., Park, H., Ramsey, A. T., Schivell, J., Stratton, B. C., and Synakowski, E. (1993). Nondimensional Transport Scaling in

the Tokamak Fusion Test Reactor: Is Tokamak Transport Bohm or Gyro-Bohm? *Phys. Fluids B* **5**, 477.

Press, W. H., Flannery, B. P., Teukolsky, S. A., and Vetterling, W. T. (1986). *Numerical Recipes*. Cambridge University Press, Cambridge.

Rewoldt, G. and Tang, W. M. (1990). Toroidal Microinstability Studies of High-Temperature Tokamaks. *Phys. Fluids B* **2**, 318.

Rewoldt, G., Tang, W. M., and Hastie, R. J. (1987). Collisional Effects of Kinetic Electromagnetic Modes and Associated Quasilinear Transport. *Phys. Fluids* **30**, 807.

Roberts, K. V. and Taylor, J. B. (1965). Gravitational Resistive Instability of an Incompressible Plasma in a Sheared Magnetic Field. *Phys. Fluids* **8**, 315.

Romanelli, F. (1989). Ion Temperature-Gradient-Driven Modes and Anomalous Ion Transport in Tokamaks. *Phys. Fluids B* **1**, 1018.

Romanelli, F. and Briguglio, S. (1990). Toroidal semicollisional microinstabilities and anomalous electron and ion transport. *Phys. Fluids B* **2**, 754.

Rosenbluth, M. N., Rutherford, P. H., Taylor, J. B., Frieman, E. A., and Kovrizhnikh, L. M. (1971). Neoclassical Effects on Plasma Equilibria and Rotation. In *Plasma Physics and Controlled Nuclear Fusion Research, 1971*, volume 1, page 495, International Atomic Energy Agency, Vienna.

Rudakov, L. I. and Sagdeev, R. Z. (1961). On the Instability of a Nonuniform and Rarefied Plasma in a Strong Magnetic Field. *Dokl. Akad. Nauk. SSSR* **138**, 581. [Sov. Phys. Dokl. **6**, 415 (1961)].

Scott, S. D., Barnes, C. W., Mikkelsen, D. M., Perkins, F. W., Bell, M. G., Bell, R. E., Bush, C. E., Ernst, D. E., Fredrickson, E. D., Grek, B., Hill, K. W., Janos, A. C., Jobes, F. C., Johnson, D. W., Mansfield, D. K., Owens, D. K., Park, H., Paul, S. F., Ramsey, A. T., Schivell, J., Stratton, B. C., Synakowski, E. J., Tang, W. M., and Zarnstorff, M. C. (1993). Nondimensional Transport Studies in TFTR. In *Plasma Physics and Controlled Nuclear Fusion Research, 1992*, volume 3, page 427, International Atomic Energy Agency, Vienna.

Shaing, K. C. and Hirshman, S. P. (1989). Relaxation Rate of Poloidal

Rotation in the Banana Regime in Tokamaks. *Phys. Fluids B* **1**, 705.

Stix, T. H. (1973). Decay of Poloidal Rotation in a Tokamak Plasma. *Phys. Fluids* **16**, 1260.

Stringer, T. E. (1973). Growth of Ambipolar Electric Field in a Toroidal Plasma. *J. Plasma Physics* **10**, 433.

Stringer, T. E. and Connor, J. W. (1971). Generalized Equations for Plasma of Arbitrary Collision Frequency in Weakly Inhomogeneous Magnetic Field. *Phys. Fluids* **14**, 2177.

Taguchi, M. (1991). Relaxation Rate of Poloidal Rotation in the Banana Regime. *Plasma Phys. and Controlled Fusion* **33**, 859.

Tang, W. M. (1974). Effect of Toroidal Gradient Drifts on the Dissipative Trapped Ion Instability. *Phys. Fluids* **17**, 1256.

Tang, W. M. and Rewoldt, G. (1993). Long-wavelength Microinstabilities in Toroidal Plasmas. *Phys. Fluids B* **5**, 2451.

Tang, W. M., Rewoldt, G., and Chen, L. (1986). Microinstabilities in Weak Density Gradient Tokamak Systems. *Phys. Fluids* **29**, 3715.

Tang, W. M., White, R. B., and Guzdar, P. N. (1980). Impurity Effects on Ion-Drift-Wave Eigenmodes in a Sheared Magnetic Field. *Phys. Fluids* **23**, 167.

Taylor, J. B., Connor, J. W., and Wilson, H. R. (1993). Structure and Damping of Toroidal Drift Waves (and Their Implications for Anomalous Transport). *Plasma Phys. Controlled Fusion* **35**, 1063.

Terry, P. W., Anderson, W., and Horton, W. (1982). Kinetic Effects on the Toroidal Ion Pressure Gradient Drift Mode. *Nucl. Fusion* **22**, 487.

Terry, P. W., Leboeuf, J.-N., Diamond, P. H., Thayer, D. R., Sedlak, J. E., and Lee, G. S. (1988). Radial Fluctuation Scale of Ion Temperature Gradient Driven Turbulence. *Phys. Fluids* **31**, 2920.

Waltz, R. E. (1986). Numerical Simulation of Turbulent Heat Flows. *Phys. Fluids* **29**, 3684.

Waltz, R. E. (1988). Three-Dimensional Global Numerical Simulation of Ion Temperature Gradient Mode Turbulence. *Phys. Fluids* **31**, 1962.

Waltz, R. E. (1989). Turbulent Transport in Tokamaks. In Ichikawa, Y. H. and Kamimura, T., editors, *Nagoya Lectures in Plasma Physics and Controlled Fusion*, page 257. Tokai University Press, Tokyo.

Waltz, R. E. and Boozer, A. H. (1993). Local Shear in General Magnetic Stellarator Geometry. *Phys. Fluids B* **5**, 2201.

Waltz, R. E., Dominguez, R. R., and Hammett, G. W. (1992). Gyro-Landau Fluid Models for Toroidal Geometry. *Phys. Fluids B* **4**, 3138.

Waltz, R. E., Kerbel, G. D., and Milovich, J. (1994a). Toroidal Gyro-Landau Fluid Model Turbulence Simulations in a Nonlinear Ballooning Mode Representation with Radial Modes. *Phys. Plasmas* **1**, 2229.

Waltz, R. E., Kerbel, G. D., Milovich, J., and Hammett, G. W. (1994b). Advances in the Simulation of Toroidal Gyro-Landau Fluid Model Turbulence. APS invited talk, to be published in Phys. Plasmas (1995).

White, R. B. (1989). *Theory of Tokamak Plasmas.* North Holland, Amsterdam.

Xu, X. Q. and Rosenbluth, M. N. (1991). Numerical Simulation of Ion-Temperature-Gradient-Driven Modes. *Phys. Fluids B* **3**, 627.

Zarnstorff, M. C., Barnes, C. W., Efthimion, P. C., Hammett, G. W., Horton, W., Hulse, R. A., Mansfield, D. K., Marmar, E. S., McGuire, K. M., Rewoldt, G., Stratton, B. C., Synakowski, E. J., Tang, W. M., Terry, J. L., Xu, X. Q., Bell, M. G., Bitter, M., Bretz, N. L., Budny, R. V., Bush, C. E., Diamond, P. H., Fonck, R. J., Frederickson, E. D., Furth, H. P., Goldston, R. J., Grek, B., Hawryluk, R. H., Hill, K. W., Hsuan, H., Johnson, D. W., McCune, D. C., Meade, D. M., Mueller, D., Owens, D. K., Park, H. K., Ramsey, A. T., Rosenbluth, M. N., Schivell, J., Schmidt, G. L., Scott, S. D., Taylor, G., and Wieland, R. M. (1991). Advances in Transport Understanding Using Perturbative Techniques in TFTR. In *Plasma Physics and Controlled Nuclear Fusion Research, 1990*, volume 1, page 109, International Atomic Energy Agency, Vienna.

Zarnstorff, M. C., Batha, S., Janos, A., Levinton, F. L., , and the TFTR Group (1993). Search for Radial Structures on TFTR. In Callen,

J. D., Gorini, G., and Sindoni, E., editors, *Local Transport Studies in Fusion Plasmas*, page 257. Societa Italiana di Fisica, Bologna.

Zweben, S. and Medley, S. S. (1989). Visible Imaging of Edge Fluctuations in the TFTR Tokamak. *Phys. Fluids B* **1**, 2058.